Dust and Gas in Protoplanetary Discs

Dissertation

zur Erlangung des akademischen Grades
doctor rerum naturalium (Dr. rer. nat.)

vorgelegt dem Rat der Physikalisch-Astronomischen Fakultät
der Friedrich-Schiller-Universität Jena

von Diplom-Astronom Dmitry Semenov
geboren am 20 Februar 1978 in Sankt-Petersburg (Rußland)

Gutachter

1. ———————————— Prof. Dr. Thomas Henning (Jena/Heidelberg)
2. ———————————— Prof. Dr. Tom Millar (Manchester, UK)
3. ———————————— Prof. Dr. Ewine van Dishoeck (Leiden, NL)

Tag des Rigorosums: 2005

Tag der öffentlichen Verteidigung: 2005

"Do not keep saying to yourself, if you can possibly avoid it, 'But how can it be like that?' because you will get 'down the drain' into a blind alley from which nobody has yet escaped. Nobody knows how it can be like that."

<div align="center">Richard Feynman</div>

<div align="center">"Astronomy", Alain of Lille (XII century)</div>

Contents

List of Figures

List of Tables

Chapter 1

Introduction

Nowadays the study of planet formation attracts particular attention in astrophysics since the recent discovery of extrasolar planets (e.g., Marcy and Butler, 2000). Up to now (September 2004) more than 100 exoplanets orbiting solar-like stars have been detected, with masses ranging from one Neptune mass to ten Jupiter masses and average star-planet distances between $\sim 1\%$ and a factor of 3 that of the Sun-Earth separation (e.g., Butler et al., 2004; Jones et al., 2002; McArthur et al., 2004). This is a strong indication that formation of planets is a common phenomenon which is tightly related to the more general process of star formation and evolution. However, many details of this process remain unclear.

Stars form in cold and relatively dense molecular cloud cores via gravitational contraction. A widely accepted scenario of low-mass (Sun-like) star formation separates four main evolutionary stages (Lada, 1999). First, a region in a molecular cloud starts to collapse when its density exceeds a certain critical value due to external factors, and thermal and magnetic pressures cannot counteract against the gravitation any longer (Class 0 protostar; $t = 0$). After $t \sim 10^4\text{-}10^5$ years, due to the conservation of angular momentum, the initially slowly rotating uniform core is transformed into a young stellar object embedded in a flattened disc-like structure which is further surrounded by an extended spherical envelope (e.g., Larson, 2003). The intense accretion of matter on the central "star" leads to the formation of a pair of collimated high-speed polar outflows (Class I object). After about 10^6 years of contraction, most of the envelope material is accumulated in a dense protoplanetary disc with mass of about 1% of the solar mass, and the central star becomes visible (Class II source). Such a young star emits a lot of UV photons and X-rays, thus further modifying the surroundings (e.g., Waters and Waelkens, 1998). Finally, this prominent disc is entirely dissipated within about 10^7 years, showing only a small amount of dust and almost no gas ("debris-disc", Class III object).

It is natural to ask the question in what form almost all matter of the initial disc has been accumulated. It has been proposed that a significant fraction of the matter in the debris-discs might be locked in large metre- and kilometre-sized planetary bodies (planetesimals) or even planets (e.g., Cameron, 1995). There are some observational hints which support this suggestion (see, e.g., Wahhaj et al., 2003; Wilner et al., 2002). Therefore, in order to understand the evolutionary scenario of the planet formation in our Solar system and other systems, it is imperative to study the physics, chemistry, and dynamics of dust and gas in protoplanetary discs. The main scope of the present thesis is to investigate the evolution and properties of dust and gas in Class II objects.

What can we learn about these circumstellar discs from observations, laboratory experiments, and theoretical models?

(Sub-) millimetre observations of molecular emission lines with (arrays of) radiotelescopes are used to probe the chemical composition, physical parameters, and dynamical properties of the gas in such systems (e.g., Bujarrabal et al., 1997; Piétu et al., 2003; Thi et al., 2001). However, it is not possible to extract the full information from these data without a proper modelling of the physical disc structure, time-dependent chemistry, and transport of the radiation in molecular lines. Increasing computer power and the development of sophisticated numerical algorithms during the last years have

made possible a more realistic modelling of the disc hydrodynamical and chemical evolution (e.g., Aikawa et al., 2002; Ilgner et al., 2004; Millar et al., 2003; van Zadelhoff et al., 2003) as well as of the line radiative transfer (e.g., Hogerheijde and van der Tak, 2000; Pavlyuchenkov and Shustov, 2004). Such a powerful combination of theory and observations offers an unique way to analyse the relevant observational data not only qualitatively but also quantitatively (e.g., Guilloteau and Dutrey, 1998; Hogerheijde, 2001; Semenov et al., 2005).

Experimental studies of the coagulation of small compact grains into larger (fractal) bodies shed light on the efficiency of this process under the disc conditions, as well as on grain structures to be expected in young discs (e.g., Beckwith et al., 2000; Blum et al., 2002; Wurm and Blum, 2000). The laboratory investigations of (isotopic) composition and properties of meteoritic materials and cometary and interplanetary dust particles provided particularly important information concerning the physical conditions and grain properties in the Solar nebula at the earliest stage of its evolution (e.g., Bernatowicz et al., 1996; Brownlee et al., 2003; Messenger, 2000; Schramm et al., 1989).

The composition of solids in protoplanetary discs is studied through the multi-wavelength measurements of their spectral energy distributions (e.g., Bouwman et al., 2001). From these data one can infer more information regarding temperature structure in discs and estimate their masses (e.g., Boogert et al., 2002; Bouwman et al., 2000; Tuthill et al., 2002), provided the radiative (optical) properties ("opacities") of dust grains can be accurately represented (e.g., Pollack et al., 1994). To date this is only possible with an elaborated theoretical approach, though one also needs the laboratory data.

In this thesis, the following problems regarding the evolution of the gas and dust in protoplanetary discs are addressed.

In Chapter 2, I deal with the modelling of absorption and scattering of light by ensembles of dust grains having various sizes, composition, porosities, and shapes, and calculate frequency-dependent opacities. Using the latter quantities, the Rosseland and Planck mean opacities of the dust and gas mixture are computed and the results are compared with other studies. In addition, I investigate how the adopted opacity table may influence the modelling of the hydrodynamical disc structure.

I summarise the basics of astrochemical modelling in Chapter 3: what kind of processes control the chemical evolution of protoplanetary discs, what the role of dust grains is, what the initial conditions are, and where the main numerical difficulties arise. In addition, I describe the chemical model that is applied in the next two chapters.

In Chapter 4, I present a technique to reduce chemical networks by removing those reactions which are not particularly important for the chemical evolution of selected molecules under predefined ranges of physical conditions. This method is applied to investigate what chemical processes control the evolution of the ionisation degree in different regions of a protoplanetary disc. Also, column densities of observationally important molecules are calculated and compared to other recent theoretical studies and observational data. The relevance of the obtained results to the magneto-hydrodynamical modelling of protoplanetary discs is discussed.

Finally, I confront a theoretical disc model with observations in Chapter 5, where I develop and describe the first self-consistent model of the physical, chemical, and dynamical structure of the circumstellar matter orbiting around the intermediate-mass star AB Aur using available observational data. A robust heuristic modelling approach is elaborated and applied to constrain the orientation, size, physical structure, mass, and dynamical state of this system. General conclusions about the evolutionary status of the AB Aur system are provided.

Final conclusions are drawn in Chapter 6.

Chapter 2

Opacities for protoplanetary discs

(Based on the paper by Semenov, Henning, Helling, Ilgner, & Sedlmayr 2003, *A&A*, **410**, 611)

2.1   A link between disc hydro-models and opacities

A nowadays accepted concept of the formation of the Solar system is based on the suggestion that an accretion disc forms after the collapse of a primordial cloud. Originally proposed by Laplace (1796) and Kant (1798), this hypothesis was given a solid mathematical basis by the papers of Weizsäcker (1943), Shakura and Sunyaev (1973), and Lynden-Bell and Pringle (1974). The evolution of the Solar nebula during the first ~ 10 Myr can be roughly divided into three main stages (Ruden and Pollack, 1991). In the *formation* stage, $t \sim 0.1$ Myr, a rotating disc is formed out of the infalling matter from the collapsing envelope (Cassen and Moosman, 1981), with a mass comparable to the mass of the proto-Sun as it has not yet accreted the bulk of the matter. Such massive discs are gravitationally unstable on large scales. This instability causes an efficient global redistribution of the angular momentum (Shu et al., 1990). At later times, when external supply from the surrounding cloud fades off, the evolution of the angular momentum in the disc is regulated by (M)HD-driven turbulent viscosity. During this *viscous* stage, mass in the disc is transported inward, whereas the angular momentum is transported outward, which steadily spreads disc matter over larger radii (Lynden-Bell and Pringle, 1974). It is during this stage pristine tiny ISM-like dust grains start to coagulate into large complex (fractal) aggregates, eventually growing up to cm-sizes (e.g., Beckwith et al., 2000). Then, they decouple from the gas and sediment toward the disc midplane, changing the entire disc structure (Dubrulle et al., 1995; Schmitt et al., 1997; Schräpler and Henning, 2004; Weidenschilling, 1980). Finally, during the last *clearing* phase of the evolution ($t \sim 10$ Myr), most of these dust aggregates in the nebula are locked up in metre-sized and larger bodies (planetesimals) or even already planets, while the gas is partly dispersed and partly accumulated by giant (Jupiter-like) planets (Hayashi et al., 1985).

Infrared observations of several young stellar clusters and star-forming regions have revealed that the initial disc fraction in these systems is high, $\gtrsim 80\%$, and rapidly decreases with increasing cluster age, such that 50% of the stars within the clusters lose their discs in $\lesssim 3$ Myr, with an overall disc lifetime of $\lesssim 10$ Myr (e.g., Haisch et al., 2001). These observations support the proposed evolutionary scenario for a protoplanetary disc around a low-mass star.

Therefore, in order to understand how planets in the Solar system and around other stars have been formed, it is crucial to investigate the properties of dust and gas in a protoplanetary nebula in detail. In this chapter, I focus on the *viscous* stage of the disc evolution and study the optical properties of dust particles having various sizes, structures, and topologies. Why is it so important to examine the optical characteristics of dust grains? The answer is that this quantity regulates the radiative transport in the disc, which in turn controls the global energy redistribution, thus determining the physical structure of the entire disc.

Let us consider a simple accretion model of a thin Keplerian disc in which the angular momentum

is conserved and stellar radiation is not taken into account. It has been found that the global evolution of such disc is governed by a single equation for the surface density (e.g., Lynden-Bell and Pringle, 1974; Papaloizou et al., 1999):

$$\frac{\partial \Sigma}{\partial t} = \frac{3}{r}\frac{\partial}{\partial r}\left(r^{1/2}\frac{\partial}{\partial r}(\Sigma\langle v\rangle r^{1/2})\right), \tag{2.1}$$

where $\Sigma(r, t)$ is the surface density of the disc at the radius r and evolutionary time t, $\langle v\rangle$ is the vertically averaged viscosity, $\langle v(r)\rangle\Sigma(r) = \int_z \rho(r, z)v(r, z)dz$. Usually, the kinematic viscosity is parameterised through the so-called α-prescription (Shakura and Sunyaev, 1973) that relates this value to the global disc parameters: $v \sim \alpha H^2\Omega$, where $H(r)$ is the vertical scale height of the disc, $\Omega(r) = GM_*/r^3$ is the angular Keplerian velocity for the central star of mass M_*, and α is a parameter of the order of ~ 0.01.

However, to follow the evolution of the disc described by Eq. (2.1), one has to specify $\langle v\rangle$ as a function of Σ. This can be done by solving equations describing vertical structure of the disc, namely, the equation of the pressure equilibrium, energy balance, and equation of state.

The equation of hydrostatic equilibrium in vertical direction for every radius r is

$$\frac{1}{\rho}\frac{\partial P}{\partial z} = -\Omega^2 z, \tag{2.2}$$

where P is the local pressure related to the local temperature T and density ρ through the equation of state of an ideal gas:

$$P = \frac{\rho kT}{\mu m_H}. \tag{2.3}$$

Here k is the Boltzmann constant, μ is the mean molecular weight, and m_H is the mass of a hydrogen atom. Finally, the energy equation states that the energy loss rate by radiation is equilibrated by the rate of energy production via viscous dissipation:

$$\frac{\partial \mathcal{F}}{\partial z} = \frac{9}{4}\rho v\Omega^2, \tag{2.4}$$

where $\mathcal{F}$ is the radiative flux of energy through a surface of constant z:

$$\mathcal{F} = \frac{-16\sigma T^3}{3\kappa\rho}\frac{\partial T}{\partial z}, \tag{2.5}$$

where σ is the Stefan-Boltzmann constant, and $\kappa = \kappa(\rho, T)$ is the mean (frequency-averaged) opacity. Obviously, it is this physical parameter that determines the physical structure of the disc in vertical direction.

These ordinary differential equations of the first order for three variables $\mathcal{F}(z)$, $\rho(z)$, and $T(z)$ have to be iteratively solved at each radius r for the input parameters (the viscosity α and mass accretion rate $\dot{M} = 3\pi\langle v\rangle\Sigma$) together with three boundary conditions. It can be done, e.g., by using the Runge-Kutta method with adaptive mesh for the integration in z-direction and Newton-Raphson method to achieve convergence of the iterations (e.g., Papaloizou et al., 1999).

The disc model without a central star is certainly not correct for outer (less dense) disc regions, where the stellar radiation becomes a dominant energy source and thus governs the vertical disc structure (Kenyon and Hartmann, 1987). In this case, Eq. (2.5) is not appropriate and one has to cope with the problem of radiative transfer in the disc using frequency-dependent (monochromatic) opacities.

Modern computational facilities allow considering a wide range of disc models with different physics included up to full 2D or even 3D (M)HD models (e.g., Fromang et al., 2004; Klahr and Bodenheimer, 2003). In some of these models the stellar radiation is taken into account to reconstruct accurately the disc vertical structure, and thus time-consuming 2D/3D continuum radiative transfer is applied, though at the price of using less developed hydrodynamics, if any (e.g. Dullemond and Dominik, 2004; Millar et al., 2003). The reason why in other studies the mean opacities are still utilised is that the corresponding disc models incorporate advanced (magneto-) hydrodynamics that prohibits the use of multi-D radiative transfer from the computational point of view.

There are two basic definitions of the mean opacity, which are used in hydrodynamics. The diffusion approximation (Mihalas, 1978) accurately describes the energy transport in optically thick regions of the medium, and, therefore, harmonic averaging is applied to translate the monochromatic opacity κ_ν into the *Rosseland mean opacity* κ_R:

$$\kappa_R = \frac{4\sigma T^3}{\pi \int_0^\infty \frac{1}{\kappa_\nu} \frac{\partial B_\nu(T)}{\partial T} d\nu}, \tag{2.6}$$

where $B_\nu(T) = (2h\nu^3/c^2)/(exp(h\nu/kT) - 1)$ is the Planck function, h is the Planck constant, and c is the speed of light. In optically thin regions this approximation is not valid, and the *Planck mean opacity* should be used:

$$\kappa_P = \frac{\pi}{\sigma T^4} \int_0^\infty \kappa_\nu B_\nu(T) d\nu. \tag{2.7}$$

In the general case, the monochromatic opacity of a medium can be written as $\kappa_\nu = \kappa_\nu^{dust} + \kappa_\nu^{gas}$.

As it can be understood from the definitions (2.6) and (2.7), the main difference between these two physical quantities is that it is *impossible* to sum up mean opacities of various dust and gas species one by one in the case of the Rosseland mean, while for the Planck mean opacity this can be done easily. Another major difference is that the Planck mean value is sensitive to the spectral regions with the highest values of the monochromatic opacity around the peak of the Planck function (e.g., strong absorption lines or bands), whereas the Rosseland mean opacity depend on the most transparent regions (e.g., continuum intervals between *all possible* atomic and molecular lines). These two factors make it difficult to compute the Rosseland mean opacity for a gas and dust mixture.

In this chapter, I deal with physical conditions typical of protoplanetary discs around low-mass young stellar objects. Virtually everywhere within the disc dust grains are the main opacity source, as they absorb radiation much more efficiently than the gas. However, for hotter domains ($T \gtrsim 1\,500$ K), where even the most stable dust materials cannot survive, it is inevitable to take absorption and scattering due to molecular species into account.

Recently, several extensive models describing the properties and evolution of dust grains in protostellar cores and protoplanetary discs have been proposed by Pollack et al. (1994), Henning and Stognienko (1996), Schmitt et al. (1997), and Gail (2001, 2002). Henning and Stognienko (1996) studied the influence of particle aggregation on the dust opacity in the early evolutionary phases of protoplanetary discs. They concluded that the distribution of iron within the particles is a major factor in determining the optical properties. Schmitt et al. (1997), for the first time, investigated collisional coagulation of dust grains in accretion discs coupled to the hydrodynamical evolution of these objects. They reported significant alteration of the thermal disc structure caused by the modification of the opacity due to dust growth. Gail (2001, 2002) considered annealing and combustion processes leading to the destruction of silicate and carbon dust grains consistently with the evolution of a steady-state accretion disc. They found that the modification of the dust composition in the inner regions due

to these processes and its consequent transport toward outer disc domains affect the opacity and, eventually, the entire disc structure.

A number of papers deal with the computation of gas opacities in atmospheres of cool stars, protostars, and stellar winds (e.g., Alexander and Ferguson, 1994; Helling et al., 2000). Helling et al. (2000) calculated gas opacities for wide ranges of density, temperature, and various chemical compositions, based on up-to-date spectral line lists of the Copenhagen SCAN database, and studied the importance of the molecular opacity for the dynamics of the stellar winds of cool pulsating stars. An extension of this work will be used to construct an opacity table for protoplanetary discs.

The main goal of this chapter is to define a model, applicable in a wide range of temperatures and densities based on both the best estimates of the dust composition and properties and recent improvements in molecular line lists. In addition, I study how frequency-dependent (monochromatic) and Rosseland and Planck mean opacities depend on the properties of dust grains and compare them with other opacity tables. Furthermore, I investigate how different opacity models affect the hydrodynamical structure of accretion discs. Due to its high relevance for hydrodynamical simulations, this opacity table can be retrieved in electronic form from: `http://www.astro.uni-jena.de/Laboratory/labindex.html`.

The organisation of this chapter is the following. I introduce the opacity model in Section 2.2. The influence of the grain properties on the resulting monochromatic and Rosseland mean opacities is described in Section 2.3.1. The Rosseland and Planck mean opacities are compared to other recent opacity tables in Section 2.3.2. I study how different opacity models affect the hydrodynamical structure of active accretion discs in Section 2.3.3. A summary and conclusions follow.

2.2   The model

Given the complexity of the problem and the fact that opacities have been extensively calculated and used over the last decades both for stellar atmosphere modelling and hydrodynamical simulations of discs (e.g., Bell and Lin, 1994; Seaton et al., 1994), it is worth to extend and update these results using recent progress in our understanding of the composition of solids and gases in protoplanetary discs and the Solar nebula, improvements in computational schemes, and achievements of laboratory experiments.

Briefly, I extend the opacity models of Pollack et al. (1994) and Henning and Stognienko (1996) by considering composite and multishell (porous) dust grains, a set of updated optical constants for the silicates, new estimates on the mass fractions of dust constituents, and gas opacities obtained from the Berlin group (Ch. Helling).

2.2.1   Dust opacities

2.2.1.1   Composition model and grain sizes

I adopt the dust composition model for accretion discs from Pollack et al. (1994, see Section 2.3 therein), which is based on an analysis of a wide range of theoretical, laboratory, and observational dust data. This composition model has been frequently used, for instance, in the evolutionary disc modelling or estimates of their masses from millimetre observations (e.g., D'Alessio et al., 2001; Greaves et al., 1998; Jura and Werner, 1999).

How can one determine composition and abundances of various materials in space? The gas-phase abundances of the elements in the interstellar medium can be measured from UV spectra of background objects. Then, these values can be used to estimate the total amount of the elements in the

Table 2.1. Mass fractions f_j and densities ρ_j of dust constituents in the opacity model

Material (grain species j)	NRM f_j	ρ_j	IRS f_j	ρ_j	IPS f_j	ρ_j
Olivine	$2.64\,10^{-3}$	$(3.49\,\mathrm{g\,cm^{-3}})$	$3.84\,10^{-3}$	$(3.59\,\mathrm{g\,cm^{-3}})$	$6.30\,10^{-4}$	$(3.20\,\mathrm{g\,cm^{-3}})$
Iron	$1.26\,10^{-4}$	$(7.87\,\mathrm{g\,cm^{-3}})$	0		$7.97\,10^{-4}$	$(7.87\,\mathrm{g\,cm^{-3}})$
Pyroxene	$7.70\,10^{-4}$	$(3.40\,\mathrm{g\,cm^{-3}})$	$4.44\,10^{-5}$	$(3.42\,\mathrm{g\,cm^{-3}})$	$1.91\,10^{-3}$	$(3.20\,\mathrm{g\,cm^{-3}})$
Troilite	$7.68\,10^{-4}$	$(4.83\,\mathrm{g\,cm^{-3}})$	$3.80\,10^{-4}$	$(4.83\,\mathrm{g\,cm^{-3}})$	$7.68\,10^{-4}$	$(4.83\,\mathrm{g\,cm^{-3}})$
Refractory organics	$3.53\,10^{-3}$	$(1.50\,\mathrm{g\,cm^{-3}})$	$3.53\,10^{-3}$	$(1.50\,\mathrm{g\,cm^{-3}})$	$3.53\,10^{-3}$	$(1.50\,\mathrm{g\,cm^{-3}})$
Volatile organics	$6.02\,10^{-4}$	$(1.00\,\mathrm{g\,cm^{-3}})$	$6.02\,10^{-4}$	$(1.00\,\mathrm{g\,cm^{-3}})$	$6.02\,10^{-4}$	$(1.00\,\mathrm{g\,cm^{-3}})$
Water ice	$5.55\,10^{-3}$	$(0.92\,\mathrm{g\,cm^{-3}})$	$5.55\,10^{-3}$	$(0.92\,\mathrm{g\,cm^{-3}})$	$5.55\,10^{-3}$	$(0.92\,\mathrm{g\,cm^{-3}})$

solid phase by comparing these results to the solar (cosmic) elemental abundances (e.g., Anders and Grevesse, 1989). Moreover, in cold disc regions gas-phase molecules may freeze out onto dust grains and form icy mantles, whose abundances can be determined by solid-state IR spectroscopy (e.g., van Dishoeck, 2004; Whittet et al., 1996), or constrained from chemical models (van Dishoeck and Blake, 1998, see also Chapter 2). IR spectroscopy is also capable in characterising the chemical composition of refractory dust components (e.g., Bouwman et al., 2001). In addition, the dust composition can be directly inferred from the properties of meteorites, interplanetary dust particles (IDPs), asteroids, and comets, though these results must be taken with care as there is evidence that some of these materials have been (partly) processed during the early stages of the solar nebula's formation.

In the Pollack's model, the main dust constituents are amorphous pyroxene ($[Fe,Mg]SiO_3$) and olivine ($[Fe,Mg]_2SiO_4$), volatile (mostly CH_3OH and H_2CO_x, $x > 1$) and refractory organics ("CHON" material, C:H:O:N=1:1:0.5:0.12, found in the coma of the Halley comet, see Jessberger et al., 1988), amorphous water ice, troilite (FeS), and metallic iron. Since it is not clear yet what fraction of iron can be locked in these silicates, I vary the relative iron content in the silicates by considering "iron-rich" (IRS) silicates with Fe/(Fe+Mg)=0.4, "normal" silicates (NRM) with Fe/(Fe+Mg)=0.3, and "iron-poor"(IPS) silicates with Fe/(Fe+Mg)=0 (see also Henning and Stognienko, 1996). The absolute amount of metallic iron in all these models is kept constant as it is restricted by the cosmic abundance. Consequently, this leads to the absence of solid iron in the iron-rich case and enhanced mass fraction of Fe in the iron-poor case. In addition, such a variety of silicate models allows to study the influence of iron content within the grain constituents on the extinction properties of dust.

I re-estimated the absolute abundances of the silicates ($Fe_xMg_{1-x}SiO_3$, $Fe_{2x}Mg_{2x-2}SiO_4$), iron, and troilite (FeS) in the cases of the IPS and IRS compositions from the Fe-stocheometric fractions. The mass fractions of all dust constituents and their densities are summarised in Table 2.1.

The composition of dust particles in the Pollack's model depends on the local gas temperature (see their Table 3). I adopt the corresponding sublimation temperatures and suppose that destruction of dust materials occurs in a narrow range of temperatures ($\sim$ 10–30 K). Given that the evaporation of

Table 2.2. Dust composition as a function of temperature ($\rho \approx 10^{-10}$ g cm^{-3})

Region	T_{low} [K]	T_{high} [K]	Dust component(s)
I		$\lesssim 155$	Ice, organics, troilite, silicates, and iron
II	~ 165	~ 270	No ice
III	~ 280	~ 410	No ice and volatile organics
IV	~ 440	~ 675	Silicates, iron, and troilite
V	~ 685	$\sim 1\,500$	Silicates and iron
VI	$\gtrsim 1\,700$		No grains, only gas species

silicates and iron happens at approximately the same conditions, I assume that they evaporate in one wide temperature range, ~ 100 K. Note that dust grains can also be destroyed by other processes (see Gail, 2001). Six principal temperature ranges for dust composition are listed in Table 2.2.

I assume that for the fifth temperature range the absolute amount of solid iron grows due to the destruction of troilite. The corresponding mass fractions of metallic iron are 6.15×10^{-4}, 2.42×10^{-4}, and 1.29×10^{-3} for the NRM, IRS, and IPS silicate models, respectively.

I take into account the dependence of the evaporation temperatures of ice, silicates, and iron on gas density. For lower/higher densities, these values are lower/higher. For instance, for $\rho \approx 10^{-18}$ g cm^{-3} the evaporation temperature of water ice is only 90 K, whereas iron evaporates at ≈ 710 K. Note that if one considers a condensation sequence of all these dust materials, it results in higher values of the condensation temperatures compared to the evaporation temperatures (hysteresis behaviour).

The optical constants for all dust components but the silicates are adopted from Henning and Stognienko (1996): `www.astro.uni-jena.de/Laboratory/labindex.html`. The optical constants for the IPS, IRS, and NRM silicates are taken from the publicly available database "Optical Data of Cosmic Dust Analogues": `www.astro.uni-jena.de/Laboratory/Database/silicates.html`.

As for the size distribution, I apply a modified MRN (Mathis et al., 1977) function suggested by Pollack et al. (1985):

$$
\begin{aligned}
n(r) &\propto r^{-3.5}, \ 0.005\mu\text{m} \leq r < 1\mu\text{m}, \\
n(r) &\propto r^{-5.5}, \ 1\mu\text{m} \leq r < 5\mu\text{m},
\end{aligned}
\tag{2.8}
$$

where r is the radius of a dust particle. The modification consists of the inclusion of large ($\gtrsim 0.5\mu$m) dust grains. Such particle growth is expected to proceed at early phases of the protoplanetary disc evolution due to the coagulation of small dust grains (see, for instance, Mizuno et al., 1988). I do not consider other size distributions because the overall effect of the particle sizes on the dust opacities is well investigated (e.g., Beckwith et al., 2000; Pollack et al., 1985). Thus, the dust opacities studied in this chapter are appropriate for young (Class II) protoplanetary discs, but probably not for more evolved (e.g., Class III) systems.
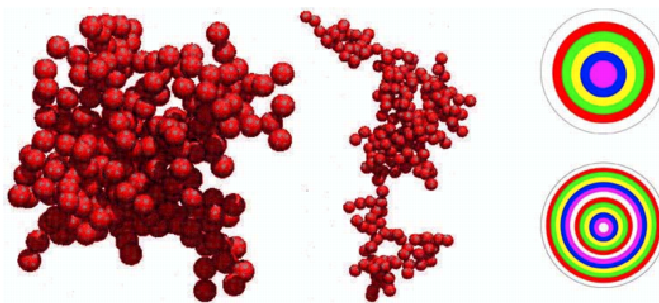
Figure 2.1. In the left panel a typical ballistic particle-cluster aggregate (BPCA) is shown. The ballistic cluster-cluster aggregate (BCCA) is presented in the middle panel. An "onion-like" (multishell) spherical particle is schematically depicted in the top right panel, whereas a "composite" (many-many layered) sphere is shown in the bottom right panel.

2.2.1.2 Grain structure and topology

In many studies of the dust properties in protoplanetary discs, the grains are still assumed to be spherical particles (e.g., Natta et al., 2001). However, it becomes evident from theoretical investigations and laboratory experiments that the dust agglomeration is an efficient process in dense and relatively cold environments, like protostellar cores or protoplanetary discs (e.g., Blum et al., 2002; Kempf et al., 1999; Kesselman, 1980; Nuth and Berg, 1994; Ossenkopf and Henning, 1994; Wurm and Blum, 1998, 2000). Agglomeration leads to the formation of irregular particles consisting of hundreds or thousands of tiny subgrains. Usually, dust aggregates of two extreme kinds are considered, depending on the coagulation process, namely, BPCA (ballistic particle-cluster aggregation) and BCCA (ballistic cluster-cluster aggregation). The laboratory and theoretical studies reveal that the BPCA aggregates are sphere-like particles with a fractal dimension of about 3. They have a compact "core" and a more rarefied "mantle". The BCCA process results in the formation of filamentary grains with complicated structure. They have fractal dimension of roughly 1.5–2 (Stognienko et al., 1995). Examples for these two kinds of aggregates are shown in Fig. 2.1.

During the evolution of parent objects, chemical and physical processes can further modify the properties of dust grains. For instance, accretion of volatile materials on dust surfaces and their subsequent chemical processing are efficient in outer regions of protoplanetary discs and in protostellar clouds (e.g., Brown et al., 1988; Greenberg, 1967; Hartquist and Williams, 1990; Hasegawa and Herbst, 1993; van Dishoeck and Blake, 1995; Willacy et al., 1994). This results in a well-defined "core-mantle" or, more probably, an "onion-like" grain structure (see Fig. 2.1, top right panel). In accretion discs, dust can be further transported by the accretion flow toward hotter regions, where their volatile mantle materials evaporate, and sputtering, annealing, and combustion processes may change even stronger the properties of the grains (e.g., Bauer et al., 1997; Finocchi et al., 1997; Gail, 2001, 2002). Therefore, the real astronomical grains should have a complicated structure and topology.

Unfortunately, modern computational methods and facilities allow only the consideration of somewhat simplified (but still reasonable) types of dust grains. I focus on the following particle types:

1. Homogeneous and composite aggregates;

2. Homogeneous, composite, and porous composite spherical particles;

3. Multishell and porous multishell spherical particles.

An aggregate dust particle is defined as a cluster of small spherical sub-grains stick together (Fig. 2.1, left panel). A particle is called "homogeneous" if it consists of only one dust component. On the contrary, "composite" means that a particle incorporates a fine mixture of various materials (Fig. 2.1, bottom right panel). In addition, I consider a model of "multishell" grains, where each particle includes all constituents distributed within concentric spherical shells (heterogeneous particle, see Fig. 2.1, top right panel). To study the influence of the porosity on the extinction properties of dust grains, I fill composite and multishell spherical particles with vacuum. It is reasonable to assume that the optical behaviour of these porous multishell and porous composite particles may resemble that of more realistic kinds of dust grains. As it has been recently demonstrated by Voshchinnikov et al. (2004), the layered approach to model the optical characteristics of composite interstellar grains indeed gives reliable results.

2.2.1.3   Computational methods

The scheme to compute the optical constants of aggregate particles is adopted from HS; it is described in Appendix A and briefly summarised below.

The main idea of this computational method is to account for the fractal distribution of dust constituents within the aggregates, which allows to calculate effective optical constants of these particles, and consequently their optical properties with a simple light scattering theory (e.g., Mie theory for homogeneous spheres).

I assume that aggregates are in the form of the BPCA (50%) and BCCA (50%) particles consisting of $0.01\mu m$ spherical sub-grains. Then, the spectral representation of inhomogeneous media (Bergman, 1978) and the discrete multipole method (DMM) are elaborated to calculate effective optical constants of aggregates (Stognienko et al., 1995). Shortly, I use the DMM to calculate the spectral function of the aggregated particles of a special topology, when their sub-grains touch each other only at one point. Next, I account for the interaction strength between the sub-grains (percolation), which varies with the size and type of the aggregates, by an analytical expression. Finally, using all these information, the effective optical constants of the homogeneous aggregates are calculated by the spectral representation.

In the case of the composite aggregates, I use the Bruggeman mixing rule (Bruggeman, 1935) to "mix" the optical constants of all individual dust constituents into the optical constants of the "average" (composite) material, and then apply the spectral representation to take into account the fractal nature of the aggregate particles and compute their effective optical constants as in the case of the homogeneous aggregates.

The optical properties of the dust aggregates are calculated from the derived effective optical constants with the usual Mie theory (Mie, 1908). The fractal shape of an aggregate implies its larger geometrical cross section compared to that of the sphere of the same volume. This effect is taken into account by scaling up the calculated absorption and scattering efficiencies with the derived filling factors. It should be noted that this numerical approach is valid in the static limit only, which means that the scale of inhomogeneities within the particles must be small compared to the wavelength. Given the $0.01\mu m$ size of the sub-grains and the shortest considered wavelength of $0.1\mu m$, this condition is satisfied.

To model (porous) composite and (porous) multishell dust particles, I adopt the numerical approach developed by Voshchinnikov and Mathis (1999). In this method, the composite grains are represented as spheres with many concentric shells, where each shell includes several layers of randomly distributed dust materials (see Fig. 2.1). The multishell grains are modelled exactly as the composite ones but each shell includes only one layer of a dust constituent. Then a generalised multilayered

Mie theory is used to calculate their optical properties. As it has been shown by Voshchinnikov and Mathis (1999) and Voshchinnikov et al. (2004), convergence in the optical behaviour of the multishell particles is achieved if the number of shells exceeds 3 and dust materials within shells are randomly ordered. I found that this number must be at least 20, because the highly absorbing material troilite is used that induces interference within the shells and prevents fast convergence. Thus, in this case, a typical composite grain is modelled as a spherical particle with about hundred shells. On the contrary, a multishell grain is represented by a spherical particle with only a few shells.

I modify somewhat the dust model for the case of multishell and composite spherical particles. I mixed the silicates and iron into one material with the Bruggeman mixing rule. A similar mixture of silicates, sulphides, and metals (GEMS, Glass with Embedded Metals and Sulphur) is found to be a common component of interplanetary dust particles (Rietmeijer and Nuth, 2000). However, the main reason for this change is the convergence failure of the applied numerical method for the case of multishell grains with iron layers (for further explanation, see Gurvich et al., 2005, 2001).

I assume that each dust component has a total volume fraction in a particle according to its mass fraction and density, as specified in Table 2.1. For example, for the first temperature range and in the case of IPS silicate mineralogy, the mixture of iron and silicates occupies 8.9%, troilite – 1.6%, refractory organics – 23.4%, volatile organics – 6%, and water ice – 60% of the entire particle volume, respectively. These values are similar in the case of NRM and IRS models. Thus, if the temperature is low, organics and ice are the dominant components of the dust grains.

Unlike the case of composite particles, for the multishell spherical grains it is assumed that the distribution of dust materials is not random but follows their evaporation sequence. Thus, for the first temperature range in the protoplanetary disc, multishell spherical grains consist of a refractory core made of a mixture of silicates and iron and subsequent shells of troilite, refractory organics, volatile organics, and water ice. For higher temperatures, the number of shells is smaller since some materials are evaporated. In total, the number of shells in the case of multishell spherical particles varies from 2 to 5. For the fifth temperature range ($T > 700$ K), where all troilite is converted to solid iron, I let this iron form an additional layer on the grain surface. It is an extreme and probably physically unjustified case, but this allows to study the influence of the formation of a highly absorbing surface layer on resulting opacities.

The porosity of particles is treated in a simple manner by the addition of 50% of vacuum (by volume) inside.

With the two computational approaches described above, I calculated the ensemble-averaged absorption (C_{abs}) and scattering (C_{sca}) cross sections as well as albedo and the mean cosine of the scattering angle ($\langle \cos \Theta \rangle$) for all kinds of dust grains. The dust monochromatic opacities for every temperature range were computed by the following set of expressions (Pollack et al., 1985):

$$C_i(r, \nu) = C_{i,\text{abs}}(r, \nu) + C_{i,\text{sca}}(r, \nu) \cdot (1 - \langle \cos \Theta \rangle), \tag{2.9}$$

$$\kappa_i(\nu) = \frac{\displaystyle\int_0^\infty n_i(r) C_i(r, \nu)/V_i(r) r^3 dr}{\displaystyle\int_0^\infty n_i(r) r^3 dr}, \tag{2.10}$$

and

$$\kappa(\nu) = \sum_i^N \frac{\alpha_i}{\rho_i} \kappa_i(\nu). \tag{2.11}$$

Here i is of N dust materials present at the current temperature, ν is the frequency, r is the grain radius, $n_i(r)$ is the size distribution function, $V_i(r)$ is the particle volume, ρ_i is the density of the i-th dust component, and α_i is its mass fraction.

Then, the Rosseland and Planck mean opacities were computed (Eqs. 2.6 and 2.7) for temperatures below $\sim 1\,500$ K and a density range between 10^{-18} g cm^{-3} and 10^{-7} g cm^{-3}. A convenient analytical representation of the Rosseland and Planck mean opacities for every temperature range is provided as a 5-order polynomial fit. This representation allows to calculate the Rosseland and Planck mean opacities accurately ($\sim 1\%$) and quickly (~ 1 s) for any given temperature and density values within the model applicability range, which is important for computationally expensive hydrodynamical simulations. The corresponding fit coefficients along with all relevant data can be found on the opacity Web page: `http://www.astro.uni-jena.de/Laboratory/labindex.html`.

2.2.2   Gas opacities

The opacity of inner disc parts is dominated by various gaseous species. Here, the temperature is too high for dust to exist.

Compared to the calculation of dust opacities, the calculation of accurate Rosseland and Planck mean gas opacities is more challenging due to the huge variation in frequency, temperature, and density of the absorption coefficient of numerous molecules, atoms, and ions. In addition, the body of data to be handled often amounts to several millions of absorption lines per a molecule.

Missing data for absorption lines are critical for the calculation of Rosseland mean gas opacity since it is dominated by transparent spectral regions. Therefore, each Rosseland mean is always only a lower limit of the correct value. The opposite is true for the case of the Planck mean opacity – missing data for weak lines or bands cause an overestimation of the strong lines. Therefore, a Planck mean is always an upper limit of the case of ideally complete data.

The dust opacity model for protoplanetary discs outlined in the previous sections is supplied by a new table of gas opacities assembled on the basis of Helling (1999, Copenhagen SCAN data base) and Schnabel et al. (2001, HITRAN data base). This model is presented in Helling et al. (2000) and Semenov et al. (2003) and only a short summary is given here.

The Rosseland and the Planck mean gas opacities are calculated from opacity sampled lines lists. The data for the line absorption coefficients used in Helling et al. (2000) (CO, TiO, SiO, H_2O, CH, CN, C_2, C_3, HCN, C_2H_2) were supplemented by data from the HITRAN 96 database (CH_4, NH_3, HNO_3, H_2CO, CO_2, N_2O, O_3, SO_2, NO_2, HO_2, H_2, O_2, NO, OH, N_2). The opacity sampling of the latter was carried out by Schnabel et al. (2001). The set of continuum opacities and scattering includes continuum absorption from H I, H$^-$, H+H, H_2^-, H_2^+, He$^-$, He I, C I, Mg I, Al I, Si I as well as Thompson scattering on free electrons and Rayleigh scattering. Collision-induced absorption has been considered for H_2-H_2 and H_2-He.

The number densities of ions, atoms, and molecules are computed from an updated chemical equilibrium routine, including 14 elements and 155 molecules based on the JANAF table (electronic version of Chase, Jr et al. 1986; for more detail see Helling et al. 2000). The elemental abundances are chosen according to Anders and Grevesse (1989), but have been updated for various elements (see Helling et al., 2000).

Using this model, the Rosseland and Planck mean gas opacities were computed for temperatures between 500 K and 10 000 K and for gas densities between $\sim 10^{-18}$ g cm^{-3} and $\sim 10^{-7}$ g cm^{-3}. In contrast to the dust opacity, no simplified analytical expression can be found for the gas mean opacities due to their sensitive dependence on temperature and density. Therefore, I apply a second-order interpolation to calculate the gas opacities from tabulated values.
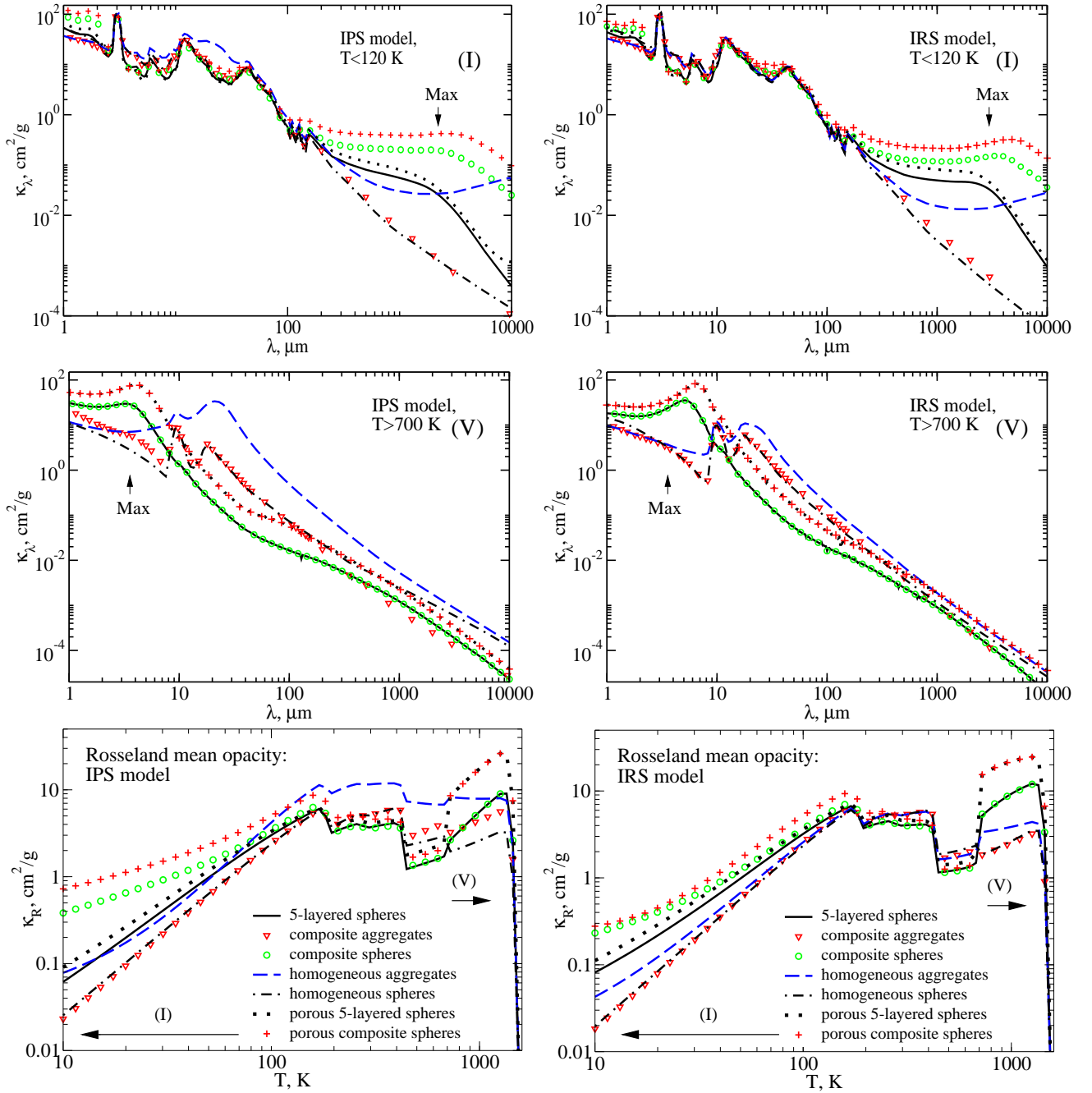
Figure 2.2. The monochromatic (upper two rows) and Rosseland mean (bottom row) dust opacities calculated for the temperature range $T \in [10, 1\,500]$ K (C/O= 0.43) in the case of IPS (left panels) and IRS (right panels) silicate dust model. The following dust particles are indicated: multishell spheres – solid line, composite aggregates – triangles, composite spheres – circles, homogeneous aggregates – dashed line, homogeneous spheres – dot-dashed line, porous multishell grains – dotted line, and porous composite spheres – pluses. The shorthand **Max** denotes the peak wavelength of the Planck function for a considered temperature range. The **(I)** and **(V)** mark the first ($T \lesssim 120$ K) and fifth ($T \gtrsim 700$ K) temperature ranges (see Table 2.2).

2.2.3 Opacity table

To assemble the entire opacity table, I take into account either only dust opacities for low temperatures, $T \lesssim 1\,500$ K, or only gas opacities for higher temperatures. As has been shown by many

authors (e.g., Lenzuni et al., 1995), it is an accurate approach because dust dominates the absorption properties of matter whenever it is present. However, for the dust-to-gas transitional range (T from $\sim 1\,400$ K to $1\,600$ K), where the last grain population evaporates, it is necessary to calculate the opacity of dust and gas simultaneously. Fortunately, in this narrow temperature range the resulting Rosseland and Planck mean opacities are going down by several orders of magnitude, so one can use a simple linear interpolation without introducing significant errors.

2.3 Computed monochromatic and mean opacities

In this section, I present the opacities for all considered dust models and discuss the differences between these results. Second, I compare the Rosseland and Planck mean opacities with other recent opacity models. Finally, I study the influence of the adopted opacity model on the disc structure.

2.3.1 Opacities and dust models

The monochromatic (κ_λ) and Rosseland mean opacities (κ_R) computed for all dust models are presented in Fig. 2.2. I compared the IPS (left panels) and the IRS (right panels). The NSM (Fe/(Fe+Mg) =0.3) opacities are not discussed here as they closely resemble the IRS case (Fe/(Fe+Mg)=0.4). The most prominent trends in behaviour of the monochromatic and Rosseland mean dust opacities can be summarised as follows:

1. There is a significant difference in the calculated κ_λ values between the aggregates, (porous) composite and (porous) multishell spherical particles for $\lambda \lesssim 10\mu$m and $\lambda \gtrsim 100\mu$m, and consequently for the Rosseland mean opacity for the first ($T \lesssim 120$ K) and fifth ($T \gtrsim 700$ K) temperature ranges;

2. For intermediate temperatures, the resulting κ_R opacity does not show profound variations with the applied dust models, except for the case of the IPS homogeneous aggregates. This is because the corresponding κ_λ values do not differ significantly in the spectral interval 10μm $\lesssim \lambda \lesssim$ 100μm;

3. The difference between opacity curves is in general smaller for the case of the IRS silicate model compared to the IPS model;

4. Addition of vacuum to compact composite and multishell spherical particles leads to significant modification of their opacities.

In the first low-temperature range, organics and water ice are the most abundant materials according to the compositional model (Table 2.1). At that temperatures ($T \sim 10$–$\lesssim 120$ K), the main contribution to the Rosseland mean opacity comes from the monochromatic opacity in the wavelength range of about 30–400μm, as calculated by the following expression (Henning and Stognienko, 1996):

$$\lambda_{\max} = 3\,600\mu\text{m} \cdot \frac{\text{K}}{T}. \tag{2.12}$$

In this spectral range, iron and troilite have higher values of the refraction index (m_λ) compared to the other materials. For instance, at $\lambda = 100\mu$m, iron has $m_{100\mu\text{m}}^{\text{Fe}} = 95.02 + i \cdot 181.95$, troilite has $m_{100\mu\text{m}}^{\text{FeS}} = 8.5 + i \cdot 0.73$, whereas organics and water ice have $n_{100\mu\text{m}}^{Org} = 2.14 + i \cdot 0.15$ and

$n^{Ice}_{100\mu m} = 1.82 + i \cdot 0.05$, respectively. Furthermore, for troilite and especially for iron these values rapidly increase with wavelength. Hence, the optical properties of a dust grain become sensitive to the absolute amount and distribution of Fe and FeS inside the particle, and consequently different light scattering theories may give different results and should be used with caution (see, e.g., Stognienko et al., 1995; Voshchinnikov et al., 2004).

However, the refractive index of the composite aggregates does not show a peculiar behaviour at long wavelengths, and changes only little between the silicate models. The main reason is that this refractive index is modelled in such a way that all dust constituents are well mixed within a particle. Therefore, as the total iron abundance is small and kept constant, the resulting refractive indices for aggregates are nearly the same for all compositional models. Consequently, the optical properties of the composite aggregates are not sensitive to the actual topology of particles and adopted silicate model. Indeed, as it is clearly seen in Figure 2.2, the dust opacity values of the composite aggregates are close to the κ_λ and κ_R of the homogeneous spheres. The maximum deviation of these opacity curves is achieved in the case of the IPS silicates for temperatures higher than $\sim$ 700 K (which corresponds to $\lambda_{max} \lesssim 5\mu m$). At these short wavelengths the κ_λ curve for the composite aggregates lies above the monochromatic opacity of the composite spheres (Fig. 2.2, second row, left panel). Here, the absolute amount of metallic iron is increased due to conversion of FeS to Fe. Overall, the opacities of the composite aggregates do not depend much on the adopted silicate model.

In contrast, the opacities of the homogeneous aggregates do demonstrate strong variations with the compositional model. In the case of the IRS silicates (right panels) the monochromatic and Rosseland mean values of the homogeneous aggregates lie closer to the κ_λ and κ_R of the composite aggregates then for the IPS compositional model.

HS has showed that this is caused by the presence of bare iron aggregates in the case of the IPS homogeneous aggregate model. Due to the extremely high absorptivity induced by the strong interactions between individual aggregate sub-grains, the optical properties of such iron clusters determine the overall behaviour of the resulting opacities. Note, that in the case of the IRS composition, all iron is locked inside silicates and the absolute amount of troilite is reduced by a factor of two compared to the IPS and NRM models. In the absence of a population of highly absorbing grains, the opacity values of the IRS homogeneous aggregates are close to those of the IRS composite aggregates. However, at temperatures higher than $\sim$ 700 K, troilite is converted to solid iron, which increases the κ_λ and thus κ_R values of the homogeneous aggregates with respect to those of the composites.

The situation is different for the case of the (porous) composite and (porous) multishell spherical particles. As it was mentioned in Section 2.2.1.3, I changed the compositional model in this case and locked all solid iron in silicates using the Bruggeman rule of the effective medium theory. Thus, the only material with a high absorptivity at long wavelengths which remains in all compositional models is troilite. The metallic iron is another highly absorbing dust component, but it is present at $T > 700$ K only.

Voshchinnikov and Mathis (1999) have shown that conventional EMTs are approximate in the case of small composite spherical particles, $x = 2\pi r |m_\lambda|/\lambda \ll 1$, when one of the grain constituents has a large refractive index (see Fig. 3b therein). Given a typical radius $r = 0.1\mu m$ of the dust grains, a typical wavelength of $\lambda = 100\mu m$ for the first temperature range, and the high refractive index of troilite at that wavelength, $|m_\lambda| \approx 10$, this condition is satisfied. This is a main reason why I adopted the approach of VM to model a composite grain as a spherical particle with many concentric layers (see also Voshchinnikov et al., 2004, 2003). Note that there is an interference between the layers, which makes the optical properties of such composite particles to be different from those of composite grains with well mixed dust materials. This is especially true if one of the dust components has a high absorptivity, e.g. troilite in the first temperature range and iron in the fifth range. Therefore,

one may expect the difference between the monochromatic (and Rosseland mean opacity) values of the composite spheres and composite aggregates, particularly for $\lambda \gtrsim 30\mu$m and $\lambda \lesssim 5\mu$m ($T \lesssim 120$ K and $T > 700$ K).

As it is clearly seen in Fig. 2.2, indeed the opacity values in the case of the composite spherical particles are higher than for the composite aggregates. For instance, at $T = 10$ K this difference can reach factors of 20 and 10 for the κ_R in the case of IPS and IRS compositions, respectively. This temperature corresponds to the peak wavelength, $\lambda_{max} \approx 360\mu$m (Eq. 2.12), for the weighting function in the expression (2.6). At this wavelength, the monochromatic dust opacity of the composite spheres is larger than that of the composite aggregates by factors of 10 and 4 for the IPS and IRS models, respectively.

For shorter wavelengths (higher temperatures), the monochromatic and thus Rosseland mean opacity curves of the composite spheres and aggregates are close to each other till $\lambda \approx 5\mu$m ($T \sim 700$ K) is reached. In this temperature range, I assumed that iron forms a layer on the surface of the composite spherical grains. Such a layer "screens out" all underlying materials and totally dominates the optical behaviour of the entire particle. Due to this fact, the dust opacity values of the composite spheres in the fifth temperature range are nearly the same for both the IPS and IRS compositions.

The multishell spherical particles have a restricted number of layers compared to the composite spheres, namely, from 2 to 5, depending on the temperature range. The troilite layer is assumed to be the first layer after the iron-silicate core and thus troilite is hidden inside. It prevents a strong interference between the subsequent particle shells, contrary to the case of the composite spheres. Then one may expect that the κ_λ and thus κ_R values of the multishell spheres should be lower than those of the composite spherical particles, especially for the IPS model. As it can be clearly seen in Fig. 2.2, this is true for $T \lesssim 120$ K ($\lambda \gtrsim 30\mu$m), whereas for higher temperatures (shorter wavelengths) both opacity curves almost coincide. Hence, the actual distribution of dust materials within a multilayered spherical particle is not that important for the relevant monochromatic dust opacity at $\lambda \gtrsim 30\mu$m and consequently Rosseland mean opacity at $T \lesssim 120$ K.

The addition of vacuum inside the compact composite and multishell spherical grains leads to a significant increase of the calculated opacities for the first and fifth temperature ranges ($\lambda \gtrsim 30\mu$m and $\lambda \lesssim 5\mu$m). First, the density of the porous grains becomes lower than the density of the compact particles, and thus the overall opacities increase (Eq. 2.11). Second, for the porous spheres the relevant extinction efficiencies are higher compared to those of the compact spherical particles because an interference between the highly absorbing troilite layers is more intense in the former case due to a larger number of these layers. This interference is even stronger for the composite spheres since they have more concentric troilite layers compared to the multishell grains (see Fig. 2.1, right panel). Note that in the fifth temperature range, both composite and multishell spheres have a similar topology, namely, a silicate core covered by an iron mantle. Therefore, the resulting Rosseland mean opacities behave similarly.

As it is clearly seen in Fig. 2.2, the κ_R values of the porous composite spheres are higher than those of the compact composite spherical particles at $T < 120$ K and $T > 700$ K by a factor of several for both the IPS and IRS compositions. In contrast, for intermediate temperatures, the opacities of porous and compact composite spheres are closer to each other. The main reason for such a coherent behaviour is that the corresponding monochromatic opacity curves are similar for these two cases of the grain mineralogy.

Given that the same layered approach is applied to construct the composite and multishell particles, the situation with dependence of the relevant opacity values on wavelength, temperature, and dust composition is similar (see Fig. 2.2).
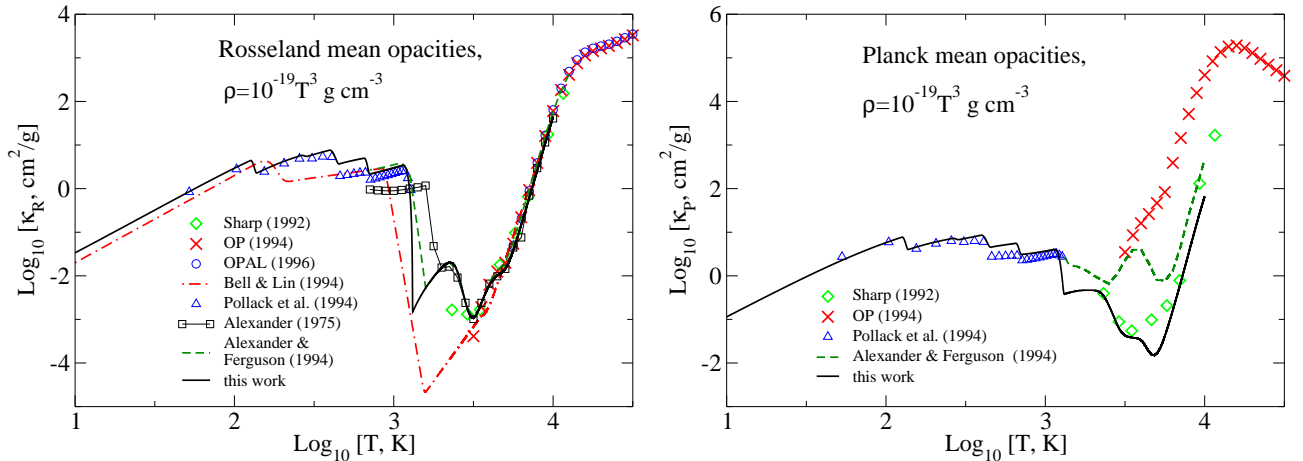
Figure 2.3. The Rosseland (left panel) and Planck (right panel) mean opacities calculated for the whole temperature range considered ($T \in [10, 10^5]$ K) and gas density that scales as $10^{-19} \times T^3$ g cm^{-3} (C/O= 0.43). Depicted are the mean opacities composed of the NRM composite aggregates in the low temperature range and the gas opacity for the higher temperatures (solid line). In comparison, opacity tables of the OP project (Seaton et al. 1994, crosses), OPAL project (Iglesias & Rogers 1996, circles), Bell & Lin (1994, dot-dashed line), Pollack et al. (1994, open triangles), Alexander (1975, line with open squares), Alexander & Ferguson (1994, dashed line), and Sharp (1992, diamonds) are shown.

The important results of this section are the following. The monochromatic opacity values of various dust models show a factor of ~ 100 spread at long wavelengths, $\lambda \gtrsim 100\mu$m, and the corresponding mean opacities differ by more than an order of magnitude at $T \lesssim 120$ K. Moreover, the slopes of the κ_λ curves vary at $\lambda \gtrsim 100\mu$m from one dust model to another. I demonstrated that the inclusion of a highly absorbing material or vacuum in a dust particle modifies its optical properties to a large degree and results in higher opacity values, though this depends on the adopted particle topology and mineralogical composition.

2.3.2 Comparison to other studies

In Fig. 2.3, the Rosseland (left panel) and Planck (right panel) mean opacities of the NRM composite aggregates ($T \lesssim 1\,500$ K) and gas opacities ($T \gtrsim 1\,700$ K) are compared with other opacity models. These values are plotted *simultaneously* for temperatures between ~ 10 K and 10^5 K and for gas densities that scaling as $10^{-19} \times T^3$ g cm^{-3}.

As it is clearly seen in Fig. 2.3 (left panel), the discrepancy between the Rosseland mean values provided by various models is negligible at high temperatures ($T \gtrsim 3\,000$ K). On the contrary, the Planck mean opacity values differ by a few orders of magnitude in this temperature range. The reason is that the Rosseland mean is much less sensitive to differences in the material data than the Planck mean due to the harmonic nature of the averaging process (see discussion in Section 2.1). However, the Planck mean heavily depends on the adopted values of the band and line strengths, which vary for different line lists and on the adopted chemical equilibrium constants (K_p). The latter quantities can cause differences in the resulting opacity values because they affect the abundances of gas-phase species. The same effect can be caused by the neglect of the metal ions in the chemical equilibrium calculations (see, e.g. Helling et al., 2000). However, it is not straightforward to decide which line list is the most correct (for a discussion see Jørgensen, 2003). I nevertheless demonstrate the difficulties arising from the comparison of the Planck mean opacities calculated by different authors because it has – to my knowledge – not been pointed out clearly in the literature. Only comparisons of Rosseland

mean opacities are presented, e.g. by Alexander and Ferguson (1994, AF).

The κ_P values of the Opacity Project (OP) are much larger than all the other opacity models since it combines more atomic opacity sources (see e.g. Table 3.3 in Helling, 1999). This model does not contain molecules for temperatures 1 500–5 000 K, which become dominant absorbers in this temperature range. The difference between the Planck mean opacity values in the case of the AF model and my gas model is caused by different molecular line data and a different set of the adopted chemical species. The same is true for the κ_P values of Sharp (1992), which lie somewhat in between the Planck mean opacities of the applied model and the values of Alexander & Ferguson.

For temperatures lower than about 1 500 K, dust grains are the main opacity source. As it has been shown by Pollack et al. (1994), in this case the difference between the Rosseland and Planck mean opacities computed for the same model is small, $\sim 30\%$ (see Fig. 4b therein). The reason is that both opacities are dominated by continuum absorption and scattering, but not the spectral lines. In what follows, I focus on the low-temperature Rosseland mean opacities only ($T \lesssim 3\,000$ K).

The Rosseland mean opacity values κ_R computed for the model of Bell and Lin (1994, BL) strongly deviate from the κ_R calculated for other models. For example, this difference can reach a factor of hundred for $T \sim 1\,500$–$1\,800$ K. The reason is that the BL data are a modification of the old analytical Lin and Papaloizou (1980) opacities that are based on the opacity tables of Alexander (1975) and Cox and Stewart (1970a,b) supplemented by the data from Alexander et al. (1989) for $T < 3\,000$ K. The model of Bell & Lin includes dust grains of two types, namely, homogeneous icy and metallic spherical grains. Since I used the more advanced dust compositional model of PHB and different sets of optical constants and evaporation temperatures, this causes lower κ_R values in the case of the BL model compared to the other models for $T \lesssim 1\,500$ K. For higher temperatures, $\sim 1\,500$–$3\,000$ K, this deviation is huge, ~ 100 times. As it has been shown by AF, the reason is that Bell & Lin truncated monochromatic opacities of water, which is one of the main absorbers at such temperatures, at a too short wavelength in their calculations. The missing opacity data strongly affect the resulting Rosseland mean opacity.

The opacity curves of all other models do not show such a strong difference between each other. The NRM aggregate model differs from the model of Pollack et al. by taking into account an aggregate nature of cosmic dust grains and a new set of optical constants for silicates, but dust size distribution, composition, and evaporation temperatures are the same. However, the difference between the Rosseland mean opacities of these two models can reach about a factor of two (see also Fig. 5a in Henning and Stognienko, 1996).

The κ_R values for the opacity model of Alexander (1975) are lower for the dust-dominated temperature range ($T \lesssim 1\,500$ K) and higher for the dust-to-gas transitional range (1 500 K $\lesssim T \lesssim 1\,700$ K), compared to the adopted model, by factors of 5 and 100, respectively. As mentioned above, the reason is that I used an approximation to compute κ_R in that temperature range, where the last dust grains evaporates, which is not too accurate approach. On the contrary, the opacity model of Alexander assumes the presence (but not evaporation!) of small $0.1\mu m$ spherical silicate grains in an approximate way, assuming that all dust is homogeneously condensed when the gas becomes saturated. Since here a phase transition takes place, a supersaturated gas would be needed, which results in higher molecular abundances than AF derive from their equilibrium consideration (for a discussion see, e.g., Woitke and Helling, 2003). Moreover, the condensation begins at higher temperature than the value I assumed for the evaporation of the last grain constituents due to the hysteresis behaviour. Finally, the model of AF neglects the presence of other refractory materials, like iron, in the dust-dominated temperature range ($T \lesssim 1\,500$ K), which makes the relevant Rosseland mean opacity values lower than provided by my model.

On the contrary, the model of AF does consider several dust materials, namely, iron, silicate, car-
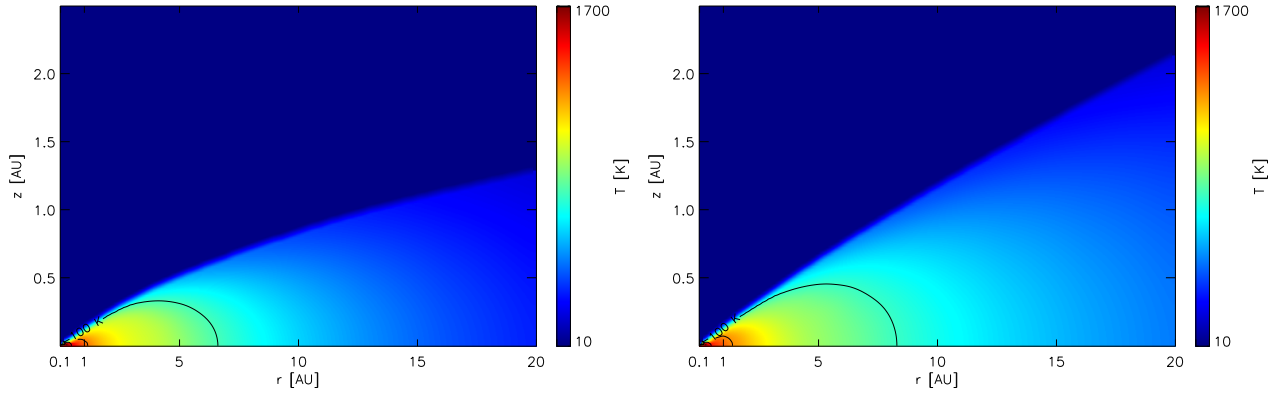
Figure 2.4. Hydrodynamical structure of the accretion disc derived with the BL opacity model (left panel) and in the case of IPS homogeneous aggregates (right panel). The solid line indicate temperature of 100 K.

bon, and SiC in the form of small ellipsoidal grain particles. Therefore, the corresponding Rosseland mean dust opacities nearly coincide with the values of my opacity model. Luckily, the same is true even for the dust-to-gas transitional range, where the reference opacity model is supposed to give only approximate values.

2.3.3 Opacities and disc structure

I compare the thermal structure of a proto-planetary disc around a low-mass star computed with two different opacity tables in Fig. 2.4. The 1 + 1D model of an active steady-state accretion disc of Ilgner (2003) was used with the following input parameters: $M_\star = 1 M_\odot$, $\dot{M} = 10^{-7} M_\odot$ yr^{-1}, and $\alpha = 0.01$ (see also Eqs. 2.1–2.5). Here, $M_\star$ is the stellar mass, $\dot{M}$ is the mass accretion rate, and α is the parameter describing the kinematic viscosity.

The thermal structure shown in the left panel was obtained with the Rosseland mean opacity table of Bell and Lin (1994). In the right panel, I present the same disc structure but for the case of the IPS homogeneous aggregate model (IPSHA) supplemented by the gas mean opacity. I choose these two opacity models as the overall difference between them is the largest among the different models (compare solid and dash-dotted lines in Fig. 2.3).

Figure 2.5. Midplane temperature of the accretion disc obtained with the BL opacity model (dashed line) and IPS (solid line) and IRS (dotted line) homogeneous aggregate dust models.

It is clearly seen that the higher values of the Rosseland mean opacity in the case of the IPSHA model leads to a hotter and more extended disc structure. For instance, the scale height of the disc at 20 AU is equal to 1.3 AU for the former and 2.1 AU for the latter opacity models, respectively. Consequently, the disc density is in general higher at the same vertical coordinate for the BL opacity model compared to that of the IPSHA model, though the disc surface density is the same for both these models.

The temperature difference is also prominent. For example, the midplane temperature of 100 K, which roughly corresponds to the ice melting point, is reached at 6.5 AU for the model of Bell & Lin,

whereas in the case of the IPSHA model it corresponds to ≈ 8 AU.

To confirm the findings, I did a similar comparison with another code. I used a full 2D hydrodynamical code designed to simulate the interaction of the protoplanetary disc with a protoplanet (D'Angelo, 2001). The parameters of the model were as follows: $M_\star = 1 M_\odot$, $M_d = 0.01 M_\odot$, $\nu = 10^{15}$ cm^2 s^{-1}, $\mu = 2.39$, and $\gamma = 1.4$, where M_d is the total disc mass, ν is the kinematic viscosity, μ is the mean atomic weight of the gas, and γ is the adiabatic exponent.

The Bell & Lin opacity model together with IPS and IRS homogeneous aggregate models were chosen for the comparison. The midplane temperature for all three opacity models is shown in Fig. 2.5. It is clearly seen that the difference in the temperature values between all models can reach about 50% for the disc radii $r_d \lesssim 2$ AU, where $T \gtrsim 250$ K. Note that this difference is smaller at larger distances, $r_d \sim 10$ AU, where temperature is lower.

As expected, in the case of the BL model the midplane temperature is the lowest almost everywhere, whereas for the IPS homogeneous aggregates it is the highest and the IRS temperature values lie in between (Fig. 2.5). The reason is the same as for the 1 + 1D disc model, namely, lower opacity values of the BL model compared to both the IPS and IRS opacities and higher values of IPS opacity in comparison with those of BL and IRS models. Note that at $T \sim 130$ K ($r \sim 2$ AU) all the temperature curves are close to each other. This is due to the adopted ice evaporation temperatures that are slightly lower in my case compared to the model of Bell & Lin. This leads to nearly the same opacity values for all three models at a restricted (~ 10 K) range of temperatures around $T \sim 130$ K (Fig. 2.4). For $r \gtrsim 10$ AU the temperature curves are close to each other because the corresponding opacity models have similar values at low temperatures.

Thus, I demonstrated that the difference in the Rosseland opacity tables applied in hydrodynamical calculations leads to deviations in the resulting disc structure. As it has been shown by Markwick et al. (2002), the temperature distribution is a crucial factor for the chemical evolution in the inner parts of accretion discs. Therefore, proper opacity modelling is an important issue in order to follow the dynamical and especially chemical evolution of protoplanetary discs.

2.4 Summary and conclusions

I compiled the monochromatic and Rosseland and Planck mean dust and gas opacities for the temperature range $T \in [5, 10^4]$ K and for gas densities $\rho \in [10^{-18}, 10^{-7}]$ g cm^{-3} that are appropriate for the conditions in protoplanetary discs. The absorption and scattering due to dust grains of different compositions, shapes and topological structures and the absorption provided by over 30 atoms, molecules, ions were taken into account. The corresponding well-documented numerical code together with representative data and figures are electronically available: `http://www.astro.uni-jena.de/Laboratory/labindex.html`.

It was found that the topological distribution of highly absorbing materials, such as iron and troilite, within dust grains dominates the relevant optical properties to a large degree. Particularly, the composite and porous composite spherical grains have remarkably high monochromatic opacities at $\lambda \gtrsim 100 \mu$m and $\lambda \lesssim 10 \mu$m, and consequently the Rosseland mean opacities at $T \lesssim 120$ K and $T \gtrsim 700$ K, even in comparison with the homogeneous aggregated particles. I demonstrated that at intermediate temperatures the monochromatic and Rosseland mean opacities of distinct grain models are close to each other. It was shown that the difference between the opacity values of various dust models is smaller in the case of the composition with a smaller amount of solid iron and troilite. I found that porous composite and porous multishell spherical particles show higher opacity values in comparison with their compact analogues. Therefore, I conclude that the factor of $\gtrsim 10$ difference in the monochromatic dust opacities at $\lambda = 1$ mm should be taken into account if one simulates the spectral energy distribution of protoplanetary discs or estimates their masses from measured continuum

flux at these millimetre wavelengths.

I also performed a comparison of my results with other recent opacity models. I found a significant difference between the opacity models in the case of the Planck mean and a good agreement between them for the Rosseland mean at $T \gtrsim 1\,500$ K, where gas species are the main opacity sources. For lower temperatures, where opacities are dominated by dust grains, there is a discrepancy (a factor of ~ 3 at most) in both the Rosseland and Planck mean values for all considered models.

I demonstrated that differences in the Rosseland mean opacity values provided by distinct opacity models affect the hydrodynamical structure of steady-state accretion discs. Namely, higher values of the Rosseland mean opacity lead to a hotter and more extended disc structure in the case of $1 + 1$D and 2D disc modelling. Thus, these differences introduce an additional uncertainty factor in the chemical modelling of protoplanetary discs. A disc chemical model is presented and discussed in the next chapter.

Chapter 3

Chemical evolution of protoplanetary discs

In this chapter, I briefly summarise the basics of astrochemical modelling and present the chemical model applied in the next two chapters.

The first interstellar species, CN, CH$^+$, and CH, have been identified by absorption spectroscopy at visual wavelengths in 1937-1941 (Adams, 1941; Dunham, 1937; Dunham and Adams, 1941). To date, more than 130 gas-phase species have been detected in space, with atomic masses ranging from 2 (molecular hydrogen) to 147 (HC$_{11}$N), see `http://astrochemistry.net`. Many of these species are organic molecules. The most notable example is the simplest amino acid glycine (NH$_2$CH$_2$COOH) tentatively identified by Kuan et al. (2003). Moreover, solid-state features of abundant ices, like CO and NH$_3$, residing on grain surfaces in cold and dense environments, have been discovered by IR spectroscopy (van Dishoeck, 2004). Such a chemical complexity and the great variety of the observed molecules imply that much more relevant species, which have not been detected yet, must be involved in the processes of their formation and destruction. Therefore, if one aims at the understanding by what chemical pathways all these observed species might have been produced, it is unavoidable *to model* the chemical evolution of a much larger number of species. This can be done by solving a system of time-dependent kinetic equations describing chemical processes thought to proceed efficiently under cosmic conditions, namely, gas-phase reactions, reactions on dust surfaces, and gas-grain interactions.

Modern astrochemical reaction databases may include up to about 400 species involved in 4 000 gas-phase reactions and contain information about reaction rate coefficients (e.g., Aikawa and Herbst, 1999b; Le Teuff et al., 2000; Millar et al., 1991, 1997; Smith et al., 2004; Terzieva and Herbst, 1998b). Among these thousands of reactions, only $\sim$ 10–20% have been studied in the laboratory or calculated theoretically (see, e.g., Millar and Williams, 1988). The rate values often have significant uncertainties of an order of magnitude or even larger (e.g., Herbst, 1980; Millar et al., 1997).

Nowadays two publicly available databases are widely applied in astronomy, namely, the UMIST[1] 95 (University of Manchester, T. Millar's group, see Millar et al., 1997) and OSU[2] 03 (Ohio State University, E. Herbst's group, see Smith et al., 2004) networks. Both databases comprise different sets of the gas-phase reactions, with the rates that are not always the same (see discussion in Amin et al., 1997; Semenov et al., 2004a). In addition, several databases of surface reactions have been compiled (e.g., Allen and Robinson, 1977; Hasegawa and Herbst, 1993; Hasegawa et al., 1992; Tielens and Hagen, 1982).

Despite the fact that these databases contain thousands of reactions, all these reactions fall into only four classes of chemical processes, which are listed in Table 3.1 (after van Dishoeck and Black, 1988): The role of every process is discussed below.

The first simple astrochemical models have been developed to describe the chemistry in interstellar clouds either by considering pure gas-phase reactions (Bates and Spitzer, 1951; Black and

---

[1] `http://visier.cfa.harvard.edu/viz-bin/VisieR?-source=J/A+AS/121/139`
[2] `http://www.physics.ohio-state.edu/~eric/research_files/cddata.july03`

Table 3.1. Types of chemical reactions in space

Bond formation	
$A + B \rightarrow AB + h\nu$	Radiative association
$A^- + B \rightarrow AB + e^-$	Associative detachment
$A + B \| grain \rightarrow AB + grain$	Surface formation
$A + B + body \rightarrow AB + body$	Termolecular
Bond destruction	
$AB + h\nu \rightarrow A + B$	Photodissociation
$AB + CRP \rightarrow A + B$	Dissociation by cosmic ray particles
$AB + body \rightarrow A + B + body$	Collisional dissociation
$AB^+ + e^- \rightarrow A + B$	Dissociative recombination
Bond rearrangement	
$A + BC \rightarrow AB + C$	Neutral-neutral
$A^+ + BC \rightarrow AB^+ + C$	Ion-molecule
$A^+ + BC \rightarrow A + BC^+$	Charge transfer
Ionisation	
$AB + h\nu \rightarrow AB^+ + e^-$	Photoionisation
$AB + CRP \rightarrow AB^+ + e^-$	Ionisation by cosmic ray particles

Dalgarno, 1973; Herbst and Klemperer, 1973) or surface processes (Hollenbach and Salpeter, 1971; Tielens and Hagen, 1982). Under the cold and "dark" conditions of dense molecular clouds and outer disc regions ($T \sim 10$–30 K, $n_H \sim 10^4$–10^8 cm^{-3}, low ionising radiation), the chemical processes are necessarily dominated by two-body gas-phase reactions without activation barriers (exothermic reactions), creating more complex molecules. In the absence of effective desorption mechanisms, these molecules freeze out and stay on dust grains, eventually forming thick icy mantles on which surface reactions take place. In the inner disc parts density is so high ($n_H \gtrsim 10^{10}$ cm^{-3}) that even three-body processes become important (e.g., Aikawa et al., 2002). In more harsh environments, like diffuse clouds and disc atmospheres ($T \gtrsim 100$ K, high ionising radiation), many chemical reactions with barriers (endothermic reactions) proceed efficiently (e.g., Millar, 2000; van Dishoeck and Blake, 1998). Furthermore, durig the last couple of years it has been recognised that many (multiply-) deuterated species exist in space, thus one has to take the processes of deuterium fractionation into account (e.g., Bacmann et al., 2003; Millar et al., 1989; Parise et al., 2004; Roberts and Millar, 2000). This nearly triples the amount of species and reactions to be considered. Accordingly, modern chemical models may include up to 1 000 species involved in more than 10 000 reactions (e.g., Aikawa and Herbst, 1999a, 2001; Bettens and Herbst, 1996).

Because the chemical evolution of protoplanetary discs is a major topic of this thesis, I shall restrict myself to this particular topic. The organisation of this chapter is the following. First, I describe basics of the gas-phase and dust surface reactions in Sections 3.1 and 3.3. In Section 3.2 processes of accretion of gas-phase molecules onto dust surfaces, recombination of ions on grains,

the sticking probabilities, and desorption mechanisms in the discs are overviewed. The chemical model applied in the next chapters is also presented in these sections. In Section 3.4 I shortly explain why and how deuterium fractionation can lead to the production of an enormous amount of deuterated species in cold regions. The problem of initial conditions in astrochemical modelling is raised and discussed in Section 3.5. Finally, I describe in Section 3.6 how a system of equations of chemical kinetics can be solved for given physical and initial conditions. A summary follows.

3.1 Gas-phase reactions

According to the compilation in Table 3.1, many chemical processes in space involve two reactants and proceed entirely in the gas phase. The rate at which new gas-phase products AB form in reactions between colliding species A and B can be written as $\alpha_{AB} n(A) n(B)$. Here n is the particle density of a reactant (in cm^{-3}) and α_{AB} is the reaction rate coefficient (in $cm^3\,s^{-1}$) describing the probability of this reaction to occur under given physical conditions. In general, the rate values depend on the local gas temperature only and are usually parameterised as follows (assuming the Maxwellian velocity distribution):

$$\alpha_{AB} = \alpha_0 \left(\frac{T}{300\ K}\right)^{\beta} \exp\left(-\frac{\gamma}{T,K}\right), \tag{3.1}$$

where α_0 is the value of the reaction rate at the room temperature of 300 K, the parameter β characterises the temperature dependence of the rate, and γ is the activation barrier (in Kelvin). For exothermic reactions the latter parameter is essentially zero. Note that this convenient parameterisation (Arrhenius form) of the reaction rates is usually adopted in astrochemical modelling.

In the chemical model, I adopt the UMIST 95 ratefile for the gas-phase chemistry (Millar et al., 1997). It contains information about 3864 reactions among 395 atomic and molecular species made of 12 elements H, He, C, N, O, S, Si, Na, Mg, Fe, P, and Cl. Consequently, discussion in this section is based on this set of chemical reactions.

3.1.1 Bond formation processes

The processes leading to the formation of molecular bonds are radiative association, associative detachment, termolecular reactions, and surface reactions. The latter process is discussed below. The termolecular reactions involve three reactants and thus are only important for the inner disc regions, where $n \gtrsim 10^{10}\ cm^{-3}$ (e.g., Le Teuff et al., 2000). Since the reaction rates of three-body processes are poorly known, these reactions are neglected in the chemical model.

Contrary, the reactions of associative detachment are not efficient in dense environments despite their high rate values ($\alpha_0 \sim 10^{-9}\ cm^{-3}\,s^{-1}$), mainly due to low abundances of negative ions (the most abundant is the H^- ion, $n_{H^-} \lesssim 10^{-12}\ cm^{-3}$). Overall, these reactions play only a minor role in cosmic chemistry (e.g., van Dishoeck, 1998). The UMIST 95 database contains about 45 exothermic reactions of this type, e.g., $H^- + H \rightarrow H_2 + e^-$ ($\alpha = 1.3 \cdot 10^{-9}\ cm^{-3}\,s^{-1}$).

The most important process for the formation of new, more complex chemical species is the radiative association. When two species collide, they form eventually a larger unstable molecule ("collisional complex"), which can stabilise itself by emitting a photon of sufficient energy (e.g., Bates, 1951; Herbst and Klemperer, 1973; Williams, 1972). The reactions of radiative association can be divided in two subclasses (e.g., Bates and Herbst, 1988). The first type of radiative association occurs when an alternative ion-molecule reaction channel is not competitive. This class includes reactions between molecular hydrogen acting as a neutral reactant and atomic or molecular ion. For

example, at low temperatures reaction between C^+ and H_2 leads to the production of CH_2^+ via radiative association ($\alpha_0 = 4.0 \cdot 10^{-16}$ cm^{-3} s^{-1} and $\beta = -0.2$, Herbst, 1985) rather than to $CH^+ + H$ because the latter ion-molecule pathway has a barrier of about 4 640 K (Adams et al., 1984). In the second type of radiative associations the neutral reactant is a heavy molecule, which leads to the formation of complex molecular ions (e.g., Huntress and Mitchell, 1979). The UMIST 95 database contains about 75 radiative association reactions of both types, e.g. $CH_3^+ + CH_3OH \rightarrow C_2H_6OH^+$ ($\alpha_0 = 7.8 \cdot 10^{-12}$ cm^{-3} s^{-1} and $\beta = -1.1$ Herbst, 1987).

However, the rates of radiative association processes have uncertainties of one or two order(s) of magnitude(s) and often even larger. The main reason is that the radiative association is a slow process and the corresponding reaction rates cannot be accurately measured in the laboratory due to the competition by other faster processes, like ternary association. On the other hand, it is also difficult to compute these quantities because one has to deal with the modelling of the radiative stabilisation of a complex molecular product. Thus, one may only wonder how all these uncertainties in the reaction rates affect the results of chemical modelling since the radiative association is among the most important routes to produce complex species.

3.1.2 Ionisation and bond destruction processes

As soon as new species are formed, they can either be dissociated or ionised by stellar and interstellar UV photons, stellar X-rays, cosmic ray particles (CRP), CRP-induced UV photons, due to decay of short-living radionuclides, and by reactions of dissociative recombination and collisional dissociation.

The latter destruction mechanism is only working for the disc regions in the closest vicinity of the young star subjected to the strong stellar wind, because it requires high temperatures of more than $\sim 2\,500$ K and high densities, $n \gtrsim 10^8$ cm^{-3} (e.g., Dalgarno and Roberge, 1979). There are a handful of these endothermic reactions in the UMIST 95 database, e.g. $H + H_2 \rightarrow 3H$, with $\alpha_0 = 4.67 \cdot 10^{-7}$ cm^{-3} s^{-1}, $\beta = -1$, and $\gamma = 55\,000$ K (Millar et al., 1997).

The decay of extinct radioactive nuclides, like ^{26}Al, ^{40}K and ^{129}I, with short half-lives of $\lesssim 0.1$-100 Myr is considered to be an important ionisation source in the deep disc interiors (see Table 3 in Finocchi and Gail, 1997). Among these elements, ^{26}Al is the most abundant one and thus it determines the total ionisation rate ζ_{RN}. In the model, I adopt the constant value through the disc, $\zeta_{RN} = 6.1 \cdot 10^{-18}$ s^{-1} (Umebayashi and Nakano, 1981).

The two processes outlined above play a minor role in the global chemical evolution of protoplanetary discs. In contrast, photo- and CRP-ionisation and dissociation of neutral molecules followed by rapid dissociative recombination of newly created molecular ions have a great impact on the chemistry.

3.1.2.1 Photodissociation and ionisation

The chemical processes in the upper disc layers are regulated by stellar and interstellar UV radiation. These energetic (912 Å–3 000 Å) photons are able to break molecular bonds and destroy many neutral species or ionise them. Some molecules, like CO, H_2, and CN, dissociate at short wavelengths only ($\lambda \lesssim 1\,100$ Å), while for other species (e.g., NaH) photodissociation occurs at wavelengths long ward of 3 000 Å (van Dishoeck, 1998). One should also mention that some species (e.g., H_2) dissociate entirely by absorbing the UV photons of specific energies (line dissociation), whereas other molecules dissociate by the continuum (e.g., CH_4) or in both continuum and lines (e.g., C_2). Moreover, dissociation may proceed in different ways, namely, direct photodissociation, predissociation, coupled

states dissociation, and spontaneous radiative dissociation (for a brief introduction, see van Dishoeck, 1988).

To calculate the photodissociation rate of a molecule, one has to integrate the frequency-dependent photodissociation cross section together with the UV spectrum (continuum dissociation) or/and sum it up with all possible line photodissociation rates, which depend on the oscillator strengths, dissociation efficiencies, and intensity of the UV radiation (see Eqs. 1–2 in van Dishoeck, 1988). In contrast, photoionisation proceeds via continuum absorption only. The most complete database of the depth-dependent photo rates have been computed by van Dishoeck (1988), assuming the mean interstellar UV field of Draine (1978) and that UV photons penetrate into a slab region in perpendicular direction (1D plane-parallel model).

Many authors have estimated the average interstellar UV field in the vicinity of the Sun (e.g. Draine, 1978; Habing, 1968; van Dishoeck, 1988). It can be described as a diluted radiation from an early B star ($T_{\mathrm{eff}} \sim 30\,000$ K) located at a distance of ~ 10 pc, with a cut-off at 912 Å due to absorption by interstellar atomic hydrogen (e.g., van Dishoeck, 1994). I adopt the standard mean interstellar UV field ($G = 1$) of Draine (1978) in the form suggested by van Dishoeck (1988, see their Eq. 3).

As it has been revealed from observations, young low-mass stars possess relatively intense UV radiation. It is above the photospheric level and higher than expected from the effective stellar temperatures. This fact is related to the on-going process of accretion of the circumstellar matter on the central star(s) (see, e.g., Herbig and Goodrich, 1986; Imhoff and Appenzeller, 1987; Mannings et al., 2000; Montmerle et al., 1993). Following these observations, it has been assumed in various studies of the disc chemistry that the unattenuated stellar UV flux at the distance of 100 AU from the star reaches a value of about 10^4 times higher than the intensity of the interstellar radiation field (e.g., Aikawa and Herbst, 2001; Markwick et al., 2002; Willacy and Langer, 2000). Accordingly, I utilise the same value $G_* = 10^4 \cdot G$ in the chemical model. However, recently Bergin et al. (2003) have shown that the strength of a realistic stellar far-ultraviolet (FUV) field is signicantly lower than this value and that the radiation field is dominated by strong line emission, most notably the Lyman α radiation. This necessitates the use of an UV radiation transfer and frequency-dependent photodissociation cross sections data in the chemical model in order to represent adequately the realistic dissociation rates, which is left for the future.

In order to calculate the extinction of the UV radiation at any given disc location, I use a simple equation (1D slab model):

$$A_{\mathrm{V}} = \frac{N_{\mathrm{H}}}{1.59 \cdot 10^{21}} \frac{\mathrm{mag}}{\mathrm{cm}^{-2}}, \tag{3.2}$$

where N_{H} is the column density of hydrogen nuclei between the point and the star (see, e.g., Aikawa et al., 2002), and the factor $1.59 \cdot 10^{21}$ cm^{-2} is the hydrogen column density to reach the visual extinction $A_{\mathrm{V}} = 1$ mag, assuming uniform 0.1μm spherical grains made of astrosilicate (Draine and Lee, 1984) and dust-to-gas mass ratio of 1%. The extinction of the interstellar UV radiation is computed in a similar way but in vertical direction only. Note that the stopping length for penetrating UV photons corresponds to the optical depth $A_{\mathrm{V}} \sim 5$–10, and thus $N_{\mathrm{H}} \sim 10^{22}$ cm^{-2} ($\approx 10^{-2}$ g cm^{-2}).

The expression 3.2 does not account for the scattering of the stellar UV photons, which penetrate the disc at small incident angles in respect to the surface. As it has been demonstrated by Bergin et al. (2003) and van Zadelhoff et al. (2003), the scattering allows UV photons to propagate closer to the "dark" disc interior. Still, this is a second-order effect in comparison with the direct dust attenuation.

There are about 150 photoreactions in the UMIST 95 database (mostly from van Dishoeck, 1988), e.g. CH$_3$ + hν → CH + H$_2$ ($\alpha_0 = 2.5 \cdot 10^{-10}$ cm^3 s^{-1} and $\gamma = 1.9$). The corresponding photorates are parameterised as

$$\alpha = \alpha_0 \cdot G \exp(-\gamma A_{\mathrm{V}}). \tag{3.3}$$

Here G represents the intensity of the unshielded interstellar (or stellar) UV radiation field, A_V is the dust extinction at visible wavelengths, and γ is the parameter describing the increased extinction of dust at short wavelengths (Millar et al., 1997). Note that the latter two factors are different for different grain populations (Roberge et al., 1991).

One still has to consider the self- and mutual-shielding of H_2 and CO. Both these molecules are so abundant that they can shield themselves and each other from the UV radiation.

The photodissociation of H_2 occurs through discrete absorption in Werner and Lyman bands in the wavelength range between 912 Å and 1 110 Å with an efficiency of $\sim 10\%$ (e.g., Dalgarno and Stephens, 1970). Given the fact that these lines become optically thick when the hydrogen column density reaches $\sim 10^{14}$ cm^{-2}, it is unavoidable to take into account the effect of the H_2 self-shielding in the disc chemical modelling. To calculate the H_2 shielding, I use an analytical expression (37) from Draine and Bertoldi (1996)

$$F_{\rm sh}(H_2) = \frac{0.965}{(1 + x/b_5)^2} + \frac{0.035}{(1 + x)^{0.5}} \exp\left[-8.5 \cdot 10^{-4} (1 + x)^{0.5}\right], \tag{3.4}$$

where $x = N(H_2)/5 \cdot 10^{14}$ cm^{-2} and $b_5 = 3 \sqrt{T/100\,{\rm K}}$ cm s^{-1}. The unattenuated dissociation rate of H_2 for the interstellar UV radiation ($G = 1$) is taken as $3.4 \cdot 10^{-11}$ cm^3 s^{-1}.

The photodissociation of CO molecules is dominated by discrete absorption at $\lambda \lesssim 1120$ Å (van Dishoeck, 1988). Since hydrogen molecules dissociate in the same wavelength range, one has to account for mutual shielding by coincidental lines of H_2 and dust extinction when calculating the CO self-shielding. This is a complex task and there is no convenient analytical representation similar to Eq. (3.4). Therefore, I follow the approach of van Zadelhoff et al. (2003) and compute the CO self-shielding by interpolating the values from Table 11 of Lee et al. (1996), where a set of shielding factors is given as a function of the H_2 and CO column densities and visual extinction by dust grains. As initial guess for the CO column densities in the medium under consideration, I use those of H_2 and scale them by a constant factor, $CO/H_2 = 6 \cdot 10^{-5}$. The adopted unattenuated photodissociation rate of CO molecules is $2.0 \cdot 10^{-10}$ cm^3 s^{-1}.

3.1.2.2 CRP- and CRP-induced dissociation and ionisation

The cosmic ray particles (CRP) consist of relativistic ($\gtrsim 1$ Mev per nucleon) protons, electrons, positrons, and heavier ions. Due to a high penetration ability, they serve as a significant ionisation source in many astrophysical objects, like dense clouds or protoplanetary discs (e.g., Dalgarno and McCray, 1972; Millar, 2000). Cosmic rays with energies below about 1 Gev are not likely reached the disc surface because they are absorbed in the interstellar medium, and can also be scattered on stellar winds in vicinity of the central star (e.g., Dolginov and Stepinski, 1994). When cosmic ray particles propagate through the disc, they lose their initial energy by ionising and dissociating the disc matter, though even the most energetic CRP cannot propagate till the midplane due to high surface density of the inner disc region ($r \lesssim 30$ AU). In contrast to UV photons and X-rays, the stopping length for CRP is much larger, ~ 96 g cm^{-2} ($\approx 10^{26}$ cm^{-2}) (Umebayashi and Nakano, 1981). The UMIST 95 database contains 10 processes of this type, with the rates that proportional to the total CRP ionisation rate, $\alpha \approx \zeta_{\rm CR}$ (e.g., He + CRP $\rightarrow$ He$^+$ + e$^-$, $\alpha = 1/2 \cdot \zeta_{\rm CR}$).

The exact value of the cosmic-ray ionisation rate $\zeta_{\rm CR}$ is poorly known, $\zeta_{\rm CR} \sim 10^{-17}$–$5 \cdot 10^{-17}$ s^{-1}. In the chemical model, I adopt $\zeta_0 = 1.3 \cdot 10^{-17}$ s^{-1} (Umebayashi and Nakano, 1981) and use the standard expression to compute the cosmic-ray ionisation rate through the disc (see, e.g., Finocchi and Gail, 1997):

$$\zeta_{\rm CR} = \frac{1}{2}\zeta_0 \left[\exp\left(-\Sigma_1(z, r)/100\right) + \exp\left(-\Sigma_2(z, r)/100\right)\right], \tag{3.5}$$

where $\Sigma_1(z, r)$ is the surface density (g cm^{-2}) *above* the point with height z at radius r, $\Sigma_2(z, r)$ is the surface density *below* the point with height z at radius r.

In dense disc interior, a secondary diffuse UV field is generated due to excitation of molecular hydrogen by collisions with energetic ($\sim$ 30 MeV) secondary electrons, which are produced due to the cosmic-ray ionisation of H$_2$ (the so-called Prasad-Tarafdar mechanism, see Prasad and Tarafdar, 1983). In the absence of the direct stellar and interstellar UV radiation in these heavily obscured disc regions, the CRP-induced UV photons become an important chemical factor. The UMIST 95 database includes 68 CRP-induced photoreactions with rates taken from Gredel et al. (1987, 1989) (e.g. H$_2$O + CRP-hν → OH + H with γ = 971),

$$\alpha = \zeta_{CR}\gamma/(1 - \omega),\tag{3.6}$$

where γ describes the probability per cosmic-ray ionisation that this particular photoreaction takes place and ω is the dust albedo in the far UV, typically 0.6 at 1 500 Å (Millar et al., 1997).

3.1.2.3 Ionisation and dissociation by stellar X-rays

It is well known from the X-ray satellites, like *ROSAT*, *ASCA*, and *Chandra*, that young stars are strong emitters of magnetic-powered X-rays (2–10 keV), with X-ray luminosities being 10 to more than 10^4 times (10^{29}–10^{31} erg s^{-1}) larger than that of the Sun (Feigelson and Lawson, 2004; Feigelson and Montmerle, 1999; Montmerle et al., 1983; Tsuboi et al., 1999). The stellar X-ray emission is an important chemical factor since it has a penetration depth of $\sim 10^{25}$ cm^{-2} (Glassgold et al., 1997a), which is larger than that of UV photons but smaller than that of cosmic ray particles. Similar to CRP, they ionise and dissociate chemical species and produce a number of secondary energetic electrons, which in turn collide, ionise, and dissociate molecules (e.g., Maloney et al., 1996). The X-ray photoprocesses are not included in the UMIST 95 ratefile, likely because the relevant reactions have been scarcely studied (see Lepp and Dalgarno, 1996; Maloney et al., 1996; Neufeld et al., 1994). I assume that the X-ray photoreactions proceed exactly like those induced by cosmic ray particles and substitute the CRP reaction rates in the UMIST 95 (ζ_{CR}) by the sum of ζ_{CR} and ζ_X. Here the X-ray ionisation rate in the disc, ζ_X, is computed according to Glassgold et al. (1997a,b) with parameters for their high depletion case. The source of X-rays is assumed to be located at $z = 12\,R_\odot$ above the stellar photosphere Glassgold et al. (1997a).

3.1.2.4 Dissociative recombination

The molecular ions are efficiently destroyed in the reactions of dissociative recombination with electrons and negative ions. These processes are especially fast at low temperatures, with typical rates of about 10^{-7} cm^{-3} s^{-1} at 10 K, because of the long-range Coulomb attraction between positive ions and negative species. Therefore, the corresponding reaction rates have a negative dependence on the gas temperature, $\beta \approx -0.5$ (Millar et al., 1997). While these rates can be computed (e.g., Bates and Herbst, 1988) and measured (e.g., Spanel and Smith, 1994) rather accurately, a major uncertainty is the branching ratios of the reaction products. Millar et al. (1988) have shown that the uncertainties in the branching ratios may introduce additional uncertainty in the calculated abundances of complex molecules (see also Semaniak et al., 2001), which should be taken into account in the chemical modelling. The UMIST 95 database contains 440 ($\sim$ 11%) reactions of the dissociative recombination type between electrons and positive molecular ions (e.g., HCO$^+$ + e$^-$ → CO + H with $\alpha_0 = 1.1 \cdot 10^{-7}$ cm^{-3} s^{-1}, $\beta = -1$, and no activation barrier).

3.1.3   Bond rearrangement processes

3.1.3.1   Ion-molecule reactions

A common factor in all astrochemical databases is that the chemistry is dominated by ion-neutral processes, which control the formation and destruction pathways for most of the species. For example, among the full set of 3 864 reactions included in the UMIST 95 database (Millar et al., 1997), $\approx 2\,700$ are ion-neutral reactions ($\approx 70\%$). Why is this particular class of reactions so important?

Most of these reactions are exothermic; their rate coefficients are relatively high, $\sim 10^{-9}$ cm^{-3} s^{-1}, and do not depend on the gas temperature ($\beta = 0$) or even increase at low temperatures ($\beta < 0$), see e.g. (Le Teuff et al., 2000; Millar et al., 1997). For exothermic reactions the simple Langevin theory applies that relates the rate coefficient α with the isotropic polarisability of the neutral molecule δ and the reduced mass μ (see, e.g., Clary, 1988): $\alpha = 2\pi \sqrt{\frac{\delta}{\mu}}$. Obviously, the Langevin rate does not depend on temperature. A good example for such a reaction in the UMIST 95 database is protonation of formaldehyde by protonated molecular hydrogen, $H_3^+ + H_2CO \rightarrow H_3CO^+ + H_2$, with the rate $\alpha_0 = 6.3 \cdot 10^{-9}$ cm^{-3} s^{-1}. For molecules that possess a large dipole moment, the rate values may even increase toward low (~ 10 K) temperatures (i.e. low velocities) due to the long-range Coulomb attraction between positive ions and negatively charged side of the molecules. An example of such a reaction is protonation of a long carbon chain: $H_3^+ + C_4H_3 \rightarrow C_4H_4^+ + H_2$ with $\alpha_0 = 2.3 \cdot 10^{-9}$ cm^{-3} s^{-1} and $\beta = -0.5$ (see Le Teuff et al., 2000; McEwan et al., 1999). Furthermore, the effect of the long-distant attraction and thus the reaction rate value is even larger for reactions between negatively and positively charged ions, e.g. $H_3^+ + H^- \rightarrow 2H_2$ with $\alpha_0 = 2.3 \cdot 10^{-7}$ cm^{-3} s^{-1} and $\beta = -0.5$ (mutual neutralisation).

3.1.3.2   Neutral-neutral reactions

Although the ion-molecule reactions have been shown to be particularly rapid at low temperatures by both laboratory measurements and theoretical calculations since many years (e.g., Dalgarno and Black, 1976), it was not until recently when it was realised that a more limited number of neutral-neutral reactions can also be fast under interstellar conditions. Especially, the rates of some radical-radical reactions are controlled by the long-range attraction force and thus increase toward low temperatures (see, e.g., Smith, 1988). The UMIST 95 chemical set includes 394 (10%) of such reactions, particularly, those between radicals and radicals, radicals and open-shell atoms, and radicals and unsaturated molecules (Clary, 1988; van Dishoeck, 1998). The typical rate coefficient for these reactions is $\sim 10^{-11}$-$\sim 10^{-10}$ cm^{-3} s^{-1}, i.e., only about an order of magnitude lower than for the ion-molecule processes. However, it is difficult to measure accurately the rates of the fast neutral-neutral reactions at low temperatures in the laboratory. Thus, their rate values have been mostly calculated (e.g., Clary et al., 1994; Smith et al., 2004). Examples of these three subtypes of neutral-neutral reactions from the UMIST 95 database are: (1) $O + OH \rightarrow O_2 + H$, $\alpha_0 = 4.34 \cdot 10^{-11}$ cm^{-3} s^{-1}, $\beta = -0.5$, and $\gamma = 30$ K (two open-shell species); (2) $CN + O_2 \rightarrow OCN + O$ with $\alpha_0 = 2.5 \cdot 10^{-11}$ cm^{-3} s^{-1}, $\beta = -0.76$, and $\gamma = 10$ K (two radicals); and (3) thermally neutral $CH_3 + HCO \rightarrow CH_4 + CO$, $\alpha_0 = 2.0 \cdot 10^{-10}$ cm^{-3} s^{-1} and $\gamma = 0$ K (a radical and an unsaturated molecule).

3.2   Gas-grain interactions

The dust in protoplanetary discs is not only a fundamental physical factor determining their thermal and density structure (see previous chapter), but it is also an important chemical ingredient. Dust

grains are relatively underabundant in respect to hydrogen, but they have much larger geometrical cross sections for interactions. In cold disc regions, grains mainly serve as a passive sink for heavy molecules and electrons and provide free electrons to dissociate colliding positive ions, thus participating in global chemical and (re-) charging processes in the disc. Their surfaces can also act as catalyst for otherwise prohibited reactions, whose products can be returned back into the gas phase by several desorption mechanisms. All these processes are briefly outlined in this section.

3.2.1 Accretion and sticking on dust grains

The accretion rate $k_{ac}(i)$ of the i-th species onto dust grains is given by

$$k_{ac}(i) = \pi a_d^2 v_{th}(i) n_d S,$$

where $v_{th}(i) = \sqrt{8kT_{gas}/\pi m_i}$ is the thermal velocity for the i-th species, n_d is the number of dust grains per unit volume, T_{gas} is the gas temperature, m_i is the atomic mass of the i-th species, and k is the Boltzmann constant.

When a molecule or an atom happens to strike a dust grain in cold disc regions ($T \sim 10$ K), it should definitely stick to the surface. Most probably, S is close to unity for all molecules (except for H_2, H, and He) sticking to 0.1μm dust grains at $T = 10$ K because usually molecular kinetic energy is much smaller than the binding energy to the grain surface ($E_{kin} \ll E_D$), and the timescale for a molecule to loose excess kinetic energy after touching a grain is very short (see, e.g., d'Hendecourt et al., 1985).

However, the effective sticking probability for a grain depends on its surface properties, namely, the distribution of passive and active sites for chemisorbing and physisorbing of newly frozen species. Chemisorption implies the formation of a chemical bond between a surface species and a grain, and thus is characterised by relatively large desorption energies of $\sim 10\,000$ K. Physisorption is caused by van der Waals forces implying weak binding (typically, $\sim$ a few 100 K), and therefore physisorbed species can be returned to the gas more easily (e.g., Williams, 1993).

The sticking coefficients can be measured (see, e.g., Mattera, 1978) or computed (e.g., Buch and Zhang, 1991; Jones and Williams, 1985). However, caution should be taken in implementing measured values because fast re-evaporation may occur during the experiment for species with low binding energies, i.e., atoms and radicals (d'Hendecourt et al., 1985).

Therefore, I assume that $S = 1$ for all species except for H_2, H, and He. For atomic hydrogen, I estimate the sticking coefficient from Eq. (3.7) by Hollenbach and McKee (1979), while those for helium and molecular hydrogen are assumed to be zero. However, at higher temperatures S is likely to be smaller (Burke and Hollenbach, 1983). To account for this tendency, I multiply the initial $S = 1$ for neutrals by an additional factor equal to the fraction of molecules of a given kind that have thermal energy lower than the desorption energy for this species (assuming Maxwellian velocity distribution).

3.2.2 Desorption processes

Since the sticking of heavy molecules proceeds with almost 100% efficiency, there must be some mechanisms to return these species back into the gas phase as it is required by their relatively high observed abundances (e.g., Charnley et al., 1990). The desorption processes, which are taken into account in my chemical model, are thermal evaporation, cosmic ray induced desorption, and photodesorption. There are also other desorption mechanism that are only shortly mentioned (for a review, see Tielens and Hagen, 1982).

3.2.2.1   Thermal desorption

Thermal desorption is the simplest desorption mechanism. When a dust grain achieves a certain temperature T_d, an individual molecule in the mantle leaves the grain if it acquires more energy than its binding energy (e.g., Leger et al., 1985; Williams, 1993). The thermal evaporation rate $k_{th}(i)$ of the i-th surface species is

$$k_{th}(i) = \nu_0 \exp(-T_D(i)/T_d), \tag{3.7}$$

where $kT_D(i)$ is the binding energy for physical adsorption of the i-th species to the dust surface and ν_0 is the characteristic vibrational frequency for the adsorbed species given by Hasegawa et al. (Eq. (3) from 1992).

3.2.2.2   CRP-induced desorption

When cosmic rays penetrate into the disc, they deposit energy in each grain they hit, which causes a modest heating and thus evaporation of volatile surface molecules (e.g., Hartquist and Williams, 1990; Leger et al., 1985; Watson and Salpeter, 1972). The cosmic ray desorption rate $k_{cr}(i)$ of the i-th surface species has been estimated by Hasegawa and Herbst (1993) as

$$k_{cr}(i) = 3.16 \cdot 10^{-19} \nu_0 \exp(-T_D(i)/T_{crp}), \tag{3.8}$$

where T_{crp} is the peak temperature of the grain due to CRP-heating.

This expression is based on the assumption that a cosmic ray particle (usually an iron nucleus) deposits on average 0.4 MeV into a dust grain of the adopted radius, impulsively heating it to 70 K for cold 0.1μm silicate dust. As in a disc much higher dust temperatures are expected, I used data from Leger et al. (1985) to take into account the dependence of the cosmic ray heating on the initial dust temperature. The peak temperature is approximated as

$$T_{crp} = (4.36 \cdot 10^5 + T_d^3)^{1/3}. \tag{3.9}$$

This expression predicts that a grain heats up to 76 K at $T_d = 10$ K and gives almost no heating for $T_d \gtrsim 100$ K.

The values of T_D for most species are taken from Hasegawa and Herbst (1993). There are some species in the UMIST 95 database for which desorption energies are not given in that paper. For these species, T_D is interpolated from values of chemically identical species or estimated as

$$T_D = 50A_i, \tag{3.10}$$

with A_i being the corresponding atomic number, which is a good approximation for species from Table 4 of Hasegawa and Herbst (1993). The adopted desorption energies are listed in Table B.1.

3.2.2.3   Photodesorption

In less opaque disc regions (e.g., disc surface), penetrating UV photons may lead to photoevaporation of surface species. The probability per one UV photon for a surface species to be evaporated is described by the so-called photoevaporative yield Y. For some simple molecules, like H_2O, CH_4, and NH_3, the values of these yields have been measured in the laboratory (e.g., Bourdon et al., 1982; Greenberg, 1973; Westley et al., 1995), which results in controversial values between $\sim 10^{-10}$ and 10^{-5}.

In the disc chemical model, I take into account photodesorption processes with the rate given by

$$k_{\text{ph}} = \left[G_{\text{S}} \exp(-2A_{\text{V}}^{\text{S}}) + G_{\text{IS}} \exp(-2A_{\text{V}}^{\text{IS}}) \right] Y \pi a_{\text{d}}^2, \tag{3.11}$$

where G_{S} and G_{IS} are intensities of the stellar and interstellar UV radiation expressed in units of the mean interstellar radiation field. A_{V}^{S} and A_{V}^{IS} are the corresponding visual extinctions in the direction to the star and in the vertical direction, and Y is the photodesorption yield for which I adopted the expression

$$Y = 0.0035 + 0.13 \exp(-336/T_{\text{d}}), \tag{3.12}$$

derived by Walmsley et al. (1999) from the experimental data obtained by Westley et al. (1995).

3.2.2.4 Other desorption mechanisms

There are other desorption mechanisms which have been proposed to resolve the problem of high observed molecular abundances in dense and cold molecular cloud cores, namely, chemical (explosive) desorption and X-ray induced desorption (see, e.g., d'Hendecourt et al., 1982; Greenberg, 1973; Leger et al., 1985).

The first mechanism is based on the suggestion that surface exothermic reactions between frozen radicals can lead to explosive desorption of mantle material (e.g., Greenberg, 1973). These radicals are likely produced by UV irradiation, and explosions are triggered when grain temperature rises to a critical value either due to grain-grain collisions or cosmic ray heating (Williams, 1993). The laboratory experiments of d'Hendecourt et al. (1982) have revealed that for CO films deposited on metal surface, this critical temperature is around 27 K. Since it is difficult to distinguish this process from thermal evaporation, I do not take it into account.

The X-ray induced desorption is similar to CRP-induced desorption mechanism. However, the X-rays are able to heat entirely only small grains, $\lesssim 0.05\mu m$ (e.g., Leger et al., 1985; Najita et al., 2001). The X-ray induced desorption is not efficient for large $0.1\mu m$ grains adopted in my chemical model. Therefore, it is neglected.

3.2.3 Grain charge

In a dark and dense environment, like a protoplanetary disc midplane, grains play an important role in ion recombination and can be the dominant charged particles in some disc regions. The charge of grains can sensitively depend on the grain size distribution, icy mantle composition, physical conditions etc. (e.g., El-Nawawy et al., 1992; Nishi et al., 1991). As most of the disc regions are shielded from direct stellar and interstellar radiation, photoelectric effects producing positively charged grains are effective only for the hot inner disc interior and disc surface (e.g., Watson, 1974). In the rest of the disc, grains are negatively charged because of the larger velocity of electrons compared to that of positive ions (e.g., d'Hendecourt et al., 1985). This means that at least a simplified treatment of grain charging processes must be included in the chemical model in order to compute fractional ionisation of the disc correctly.

I consider neutral, positively charged (+1), and negatively (-1) charged grains separately (e.g., d'Hendecourt et al., 1985). A grain attains a negative charge or looses a positive charge colliding with free electrons. The probability of electron sticking to grain surfaces is assumed to decrease exponentially with dust temperature T_{d}, so that the sticking coefficient is around 0.5 at $T_{\text{d}} \sim 10-20$ K, close to the value obtained by Umebayashi and Nakano (1980), and is essentially zero at higher temperatures. Via dissociative recombination of a gas-phase ion, a grain looses one electron and becomes neutral

or positively charged. The corresponding set of dissociative reactions on grains is created using the UMIST 95 dissociative reactions of molecular ions with electrons and their branching ratios (Millar et al., 1997). The collisional rates between electrons and positively charged grains are multiplied by a factor correcting for the long-distant Coulomb attraction, $C_{ion} = 1 + e^2/ka_dT_d$, where $a_d = 0.1\ \mu m$ is the grain radius (Umebayashi and Nakano, 1980).

Then, the total rate coefficients are calculated by

$$k_{dr}(i) = \sum_j \alpha_j \pi a_d^2 v_{th}(i) n_d C_{ion}, \tag{3.13}$$

where T_d is the dust temperature (Rawlings et al., 1992). Here the summation is over different recombination channels; the quantity α_j denotes the probability of a particular channel. I assume that the sticking probability $S = 1$ for all ions and that products of these reactions return to the gas phase immediately.

3.3 Surface reactions

The surfaces of dust grains serve as a natural catalyst for many reactions that otherwise cannot proceed efficiently in the gas phase. The most notable example of such a reaction is the formation of molecular hydrogen which occurs almost entirely on dust surfaces, as it has been inferred from observations of H_2 in diffuse clouds (e.g., Jura, 1975; Stantcheva and Herbst, 2004). There is also increasing observational evidence that certain gas-phase species are produced on the surfaces of dust grains and then desorbed back in the gas (e.g., NH and CH_3OH in diffuse clouds, Meyer and Roth 1991 and Shalabiea and Greenberg 1994).

The study of surface chemistry has started with the pioneering investigations of Hollenbach and Salpeter (1971) and Watson and Salpeter (1972), who mainly focused on the surface formation of H_2 and some simple saturated species such as H_2O, CH_4, and NH_3 (see Hasegawa et al., 1992). Later, Allen and Robinson (1977) have considered a large set of surface association reactions without barrier. Tielens and Hagen (1982) have studied the chemical evolution of surface species on large grains and considered the effect of various migration rates for light atoms and heavy molecules. A comprehensive model of surface chemistry has been presented by Hasegawa et al. (1992) and Hasegawa and Herbst (1993), who have also published their full set of surface reactions with rates. Recently, Stantcheva and Herbst (2004) have presented a gas-grain model in which the gas-phase chemistry is treated by the standard rate equation approach, whereas the surface chemistry is modelled stochastically, and compared these results with the deterministic model that uses the rate equation method for both the gas-phase and surface chemistry.

Let us consider a large $0.1 \mu m$ silicate grain that has about 10^6 sites for accretion of molecules from the gas. An atom or light molecule may migrate over the surface from site to site by thermal hopping, when its energy exceeds the barriers for particle motions and if it is not chemisorbed (e.g., Hollenbach and Salpeter, 1971). However, for cold grains with $T \sim 10$ K and the lightest species (e.g., H, H_2) this process become less efficient than the direct quantum mechanical tunnelling through the potential barriers (e.g., Williams, 1993). This leads to enhanced conversion of the surface CO, O_2, H_2CO, etc. to their more hydrogenated analogues (e.g., Tielens and Hagen, 1982).

Migrating species may find another surface species and react. Then exothermic reactions occur and lead to the formation of product species in an excited state, which usually results in the ejection of the molecule from the surface back in the gas (e.g., Williams, 1993). The surface reaction rate can be calculated similar to the gas-phase rate by taking into account diffusion timescale for a species

to migrate over the surface (the so-called "diffusion-limited" regime) and the probability for this particular reaction to occur after an encounter (which is 100% for exothermic reaction without a barrier), see Eq. (5) in Hasegawa et al. (1992). Given the large potential barriers for most complex species, significantly large surface rates correspond to reactions with light species, namely, atoms and diatomic molecules (e.g., Tielens and Hagen, 1982). However, the standard rate equation approach to estimate the surface rates become questionable in a situation when reactions occur much faster than the accretion rate of molecules on grain surfaces (the so-called "accretion-limited" regime), and thus some species have average surface abundances smaller than one (e.g., Charnley et al., 1997; Stantcheva and Herbst, 2004).

In this case, one has to deal with stochastic methods, like Monte-Carlo approach (e.g., Tielens and Hagen, 1982) and the master equation approach (e.g., Biham et al., 2001; Green et al., 2001), or use semi-empirical modifications of the standard rate equations ("modified rate approach", e.g., Caselli et al., 1998; Stantcheva et al., 2001). Unfortunately, with these methods it is not possible to consider surface chemistry of more than a handful of species. Therefore, I follow the standard rate equation approach.

The surface reactions as well as their rates are taken from the set compiled by Hasegawa et al. (1992) and Hasegawa and Herbst (1993) with the appropriate correction for different gas densities. The activation energy of 1000 K is adopted for the O + CO surface reaction (Hasegawa and Herbst, 1993). The set of adopted surface reactions is listed in Table B.2.

3.4 Deuterium fractionation

Several tens of (multiply-) deuterated species in space have been detected over the last few decades, with abundances that are comparable with those of non-deuterated analogues and which have much higher D/H ratio than the cosmic value of $\sim 0.01\%$ (e.g., see Table I in Millar, 2003). Such over-abundance of deuterated species is possible due to a particular reaction, $H_3^+ + HD \rightarrow H_2D^+ + H_2 + 232$ K, which has zero-point energy difference implying that the forward reaction is exothermic and thus more probable in cold environments ($T \lesssim 30$ K) than the slightly endothermic backward reaction (e.g., Millar et al., 1989). Consequently, this leads to the formation of H_2D^+ ions in large amounts, $H_2D^+/H_3^+ \gg HD/H_2$. This ion is reactive and thus it triggers the production of other, more complex deuterated species via both the gas-phase and surface reactions (see, e.g., Roberts et al., 2002, 2003; Roberts and Millar, 2000). For example, recent observations of prestellar cores by Bacmann et al. (2003) have revealed that simple organic deuterated molecules, like DCO^+ and deuterated methanol, can be as abundant as their main isotopomers. Moreover, Ceccarelli et al. (2004) have detected H_2D^+ in the DM Tau and TW Hya discs and argued that it is likely the most abundant ion and thus a good tracer of the ionisation degree in protoplanetary discs (see also the next chapter).

However, there is no unique approach to model deuterium chemistry because the rates and branching ratios of many relevant reactions are not well studied. Usually, these missed values are taken to be equal to those of the analogous reactions involving the main H-bearing species (e.g., Le Teuff et al., 2000; Millar, 2003). In the chemical model, I utilise a small set of deuterium reactions from Bergin et al. (1999). This set includes primal formation and destruction routes relevant to the chemical evolution of OD and HDO. It consists of about 60 gas-phase and 10 gas-grain reactions among 11 gas-phase species including accretion onto and desorption from dust surfaces of D, OD, and HDO species. The elemental abundance of deuterium, D/H=$1.52 \cdot 10^{-5}$, is taken from Piskunov et al. (1997).
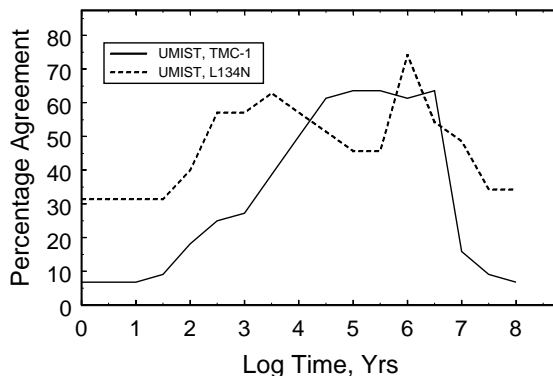
3.5   Initial conditions for chemistry

The problem of the initial conditions for chemical models of star-forming regions remains an open issue. The modelling of pre-protostellar objects commonly starts with a purely atomic or partly ionised initial composition, while in reality the initial abundances even for a moderately dense medium must reflect its previous evolution. Even though the atomic or ionic initial composition can be adequate in pre-protostellar objects, the situation is different in protoplanetary discs, where the chemical composition at the beginning of the modelling is obviously more advanced. One way to cope with this problem is to use "sliding" ini-

Figure 3.1. Percentage agreement between calculated and observed gas-phase abundances.

tial conditions, when the initial abundances are set to be mostly atomic at the outer radius of the disc. Then, a chemical model is run, and the final abundances at a given radius are used as initial abundances at the next radius, closer to the disc centre (Bauer et al., 1997; Willacy et al., 1998). Another approach is to compute the input abundances with the model of a dark cloud, out of which the disc has evolved (e.g., Aikawa and Herbst, 1999b; Aikawa et al., 2002). Willacy et al. (1998) have compared both methods and found that they provide almost similar results because in a dense environment reasonable molecular abundances are reached within a fraction of a year even with the atomic initial composition.

He	1.95(−1)	C	1.57(−4)
N	4.94(−5)	O	3.60(−4)
S	1.83(−7)	Si	1.95(−8)
Na	4.50(−9)	Mg	2.18(−8)
Fe	5.48(−9)	P	4.32(−10)
Cl	2.00(−9)		

Table 3.2. Cosmic elemental abundances in respect to hydrogen

To simplify the modelling and analysis of the results, I adopted the second approach. The choice of a cloud model in Aikawa et al. (2002) and in previous papers of this group is based on the analysis of the Ohio New Standard Model performed by Terzieva and Herbst (1998a,b). These authors have developed a simple criterion that allows estimating how good the chemical model is in reproducing the chemical composition of a given object. Adopting a fixed density of $2 \cdot 10^4$ cm^{-3} and a gas temperature of $10\,$K, Terzieva and Herbst (1998b) have found that with the pure gas-phase chemistry, the chemical composition of the two typical molecular clouds, namely, TMC-1 and L134N, is best reproduced after about $3 \cdot 10^5$ years

of the evolution. Aiming to reproduce the observed low abundances of water and molecular oxygen, Roberts and Herbst (2002) added surface chemistry to this model and found that the consistency interval can be shifted toward later time, $t \sim 10^6$ years.

As I use the UMIST 95 ratefile, I perform a similar analysis for this database. The observed abundances for TMC-1 and L134N are taken from Ohishi et al. (1992) and Langer et al. (1997). Following Terzieva and Herbst (1998a), I assume that an abundance of a given molecule is consistent with observational data if it lies within an order of magnitude of the observed abundance. When the observed abundance is an upper limit, I assume that the computed abundance is in agreement with observations if it is less than or equal to 10 times this upper limit. With the same density, temperature, and the surface chemistry included, I find that for my chemical model the agreement is best at $t \sim 10^6$ years (Fig. 3.1). The "low-metal" set of abundances is adopted for this computation (Lee et al., 1998), which is compiled in Table 3.2. The 'low-metal' means that Na, Si, Mg, Fe,

P, and Cl are initially depleted onto dust grains with depletion factors of 10^3, $5 \cdot 10^3$, $6 \cdot 10^3$, and $1.1 \cdot 10^4$. The cosmic abundances for all elements but P and Cl are taken from Aikawa et al. (1996) and for Cl and P from Grevesse and Sauval (1998). I use the set of gas-phase and surface abundances obtained with the above model for $t = 10^6$ years as the initial conditions. The brief outline of this set is the following (abundances relative to the number of hydrogen nuclei are given in parentheses): The primary carbon-bearing compound is surface formaldehyde ($3.7 \cdot 10^{-5}$) which also accounts for a significant fraction of the overall oxygen content, being second only to surface water ($7.8 \cdot 10^{-5}$). Gas-phase oxygen and carbon are locked in CO molecules ($2.8 \cdot 10^{-5}$). A fraction of oxygen is also present in atomic ($1.1 \cdot 10^{-5}$) and molecular ($8.7 \cdot 10^{-6}$) form. Gas-phase nitrogen is contained mainly in N_2 molecules ($9.7 \cdot 10^{-6}$), while in icy mantles the main N-bearing species are HCN and HNC ($\sim 10^{-6}$ each) with a slightly lower amount of CH_2NH, NH_3, and NO. Sulphur is distributed almost equally between gas and dust phases. In the gas phase it is locked in CS molecules ($2.9 \cdot 10^{-8}$). Surface sulphur is bound in H_2S ($2.2 \cdot 10^{-8}$) and H_2CS ($1.5 \cdot 10^{-8}$). Even though the density is not so high, metals are already significantly depleted. Surface abundances of Mg, Fe, and Na constitute about 1/3 of their total abundances. The dominant ions are HCO^+ ($3.8 \cdot 10^{-9}$), H_3^+ ($3.5 \cdot 10^{-9}$), Mg^+ ($1.9 \cdot 10^{-9}$), C^+ ($1.3 \cdot 10^{-9}$), and Fe^+ ($1.2 \cdot 10^{-9}$).

3.6 Chemical modelling

All chemical processes discussed above can be mathematically formalised by the equations of chemical kinetics. In essence, each equation describes the change of concentration of a gas-phase or surface species due to the gas-phase and surface reactions and gas-grain interactions. For a surface species i, the kinetic equation is (e.g., Herbst, 1993):

$$\frac{dn_s(i)}{dt} = \Sigma_l \Sigma_j k_{lj} n_s(l) n_s(j) - n_s(i) \Sigma_j k_{ij} n_s(j) + R_{acc}(i) - k_{des}(i) n_s(i),$$ (3.14)

where the first term describes the production of the species i, second term accounts for its destruction, and last two terms describe accretion and desorption of the species i. For a gas-phase species, the equation is essentially the same, with the last two terms having opposite signs in respect to those in Eq. 3.14.

The equations of chemical kinetics form a system of ordinary differential equations (SODE). The rates k_{lj} of all chemical reactions in the model have so different scales that the corresponding SODE is stiff and requires a special mathematic algorithm for integration.

I use the code DVODE, which is based on the Variable Coefficient method to solve systems of stiff and non-stiff differential equations (Brown et al., 1989). This code utilises variable time step and error control techniques to preserve numerical accuracy during the integration. The input parameters for a given calculation are the gas density (in $g\,cm^{-3}$) and temperature (in Kelvin), the

Figure 3.2. The computational time needed to simulate the chemical evolution in a disc location with chemical networks of various sizes.

factor G_* by which the stellar UV radiation is enhanced above the interstellar radiation field $G = 1$, the visual extinctions toward the central star and in vertical direction (in respect to the disc midplane), the cosmic ray and X-ray ionisation rates, ζ_{CR} and ζ_X, and shielding factors for H_2 and CO regarding the stellar and interstellar UV radiation. The accuracy of calculated time-dependent abundances is con-

trolled by two parameters, namely, absolute and relative errors, which are chosen as $\epsilon_{abs} = 2.2\,10^{-16}$ and $\epsilon_{rel} = 10^{-8}$, respectively. I found that the relative error $\epsilon_{rel} \gtrsim 10^{-8}$–$10^{-5}$ is enough to give reliable estimations of the molecular abundances yet save computational time.

For numerical computations, I use the Pentium IV 2.4 GHz PC (1 Gb RAM) with Intel Fortran 8.0 compiler installed on SuSe Linux 9.2. The typical time necessary to run a model for 10^6 years of evolution in a disc location is only a few minutes in the case of the gas-phase chemistry and can reach half an hour if the gas-grain interactions and dust surface reactions are taken into account. Therefore, a disc model with one hundred of grid points requires about one day of computational time.

It is interesting to investigate how this time depends on the number of species considered in a chemical model. This effect is illustrated in Fig. 3.2. As can be clearly seen, this time grows approximately as the third power of the number of species. Thus, the disc chemical models with full deuterium chemistry included become computationally prohibitive. In this case, special methods designed to decrease amount of species and reactions in the chemical model without loosing accuracy in the calculated time-dependent abundances of pre-selected molecules can help to make this task manageable.

3.7 Summary

The basics of astrochemical modelling were overviewed using the UMIST 95 database as a guideline. I discussed why the gas-phase reactions of radiative association and surface reactions lead to the formation of new, more complex chemical species, which in turn can either be dissociated or ionised by stellar and interstellar high-energy sources (UV radiation, X-rays, CRP) and then dissociatively recombine with grains and electrons, or create new molecular ions via the ion-molecule chemistry. The roles of the gas-grain interactions and deuterium fractionation in the cosmic chemistry were also outlined. I briefly explained how the rate coefficients have been obtained for every particular class of reactions and showed typical examples of such reactions, their rate values, and the total number in the UMIST 95 database. Finally, the problem of initial conditions in the astrochemical modelling was discussed in detail, and a numerical recipe to solve the system of differential equations of chemical kinetics was given.

Chapter 4

Reduction of chemical networks

(Based on the papers by Wiebe, Semenov, & Henning 2003, *A&A*, **399**, 197 and Semenov, Wiebe, & Henning 2004, *A&A*, **417**, 93)

4.1   Need for the reduction of chemical networks

As it has been demonstrated in the previous chapter, the modelling of the chemical evolution of protoplanetary discs is still a challenging computational task despite the significant growth of computer power over the last years. This is even more true if one aims at the simultaneous self-consistent modelling of the dynamical and chemical evolution of these systems.

The mathematical formulation of the chemical processes is realised by differential equations of chemical kinetics. They contain terms for chemical reactions expected to proceed efficiently under cosmic conditions. Along with abundances of all involved species, these terms depend on the rate coefficients that are summarised in special databases, typically containing hundreds of species and thousands of reactions (e.g., Millar et al., 1997; Smith et al., 2004). Of course, one can only wonder if these databases contain all the information about reactions needed to reproduce observed molecular abundances that are determined with a limited accuracy. The opposite question to ask is if all this information is always needed.

In many astronomically interesting cases, it is enough to follow the evolution of a limited number of species only. Intuitively, it seems to be apparent that to predict an abundance of N_2H^+, for example, one can afford computing C_{10} abundance with less accuracy or even ignore this molecule altogether. Given the fact that the calculated abundances suffer from the intrinsic uncertainties in the reaction rates (Vasyunin et al., 2004), the approach to save the computational time by using smaller sets of species and reactions is viable.

In many cases, modelling of the chemical evolution of a parcel of gas in a limited pre-defined range of physical conditions is not too time-consuming and thus one probably will not be eager to sacrifice any accuracy even for the sake of several orders of magnitude gain in computational speed. However, in the case of dynamical modelling with changing density, temperature, UV intensity etc., a reduced chemical network may help to distinguish between feasible and non-feasible problems. One possible application for reduced chemical networks could be the modelling of the evolution of weakly-magnetised accretion discs, when it is necessary to compute the fractional ionisation self-consistently. In addition, reduced networks could be applied for analysing the chemical evolution of selected molecules under specified conditions. The generally smaller, but still accurate networks would also make computationally manageable the problem of self-consistent coupling between the chemistry and mixing processes (turbulence, radial transport, convection, etc.) in the protoplanetary discs.

Recently, Ruffle et al. (2002) and Rae et al. (2002) have made a first attempt to reduce astrochemical networks by the so-called "objective reduction techniques" developed in combustion chemistry.

Briefly, they have shown that it is possible to quantify the reduction task by introducing a certain criterion that would allow in each particular case to indicate, abundances of which species must be followed in order to have a reasonable estimate for an abundance of a molecule under investigation. For static conditions typical of diffuse clouds, they have isolated the species set that contains tens instead of hundreds species, which significantly decreases the computational time and introduces only a factor of two uncertainty in the predicted CO abundance and fractional ionisation.

Complementary to their scheme, I developed a robust method to reduce *simultaneously* the number of species and reactions in chemical networks. In collaboration with D. Wiebe, I applied this method and the "objective reduction techniques" to perform a similar analysis of the UMIST 95 database including surface reactions in order to find if it is possible to reduce the number of species and/or reactions in this network in respect to ionisation degree and carbon monoxide under conditions typical of diffuse and dense molecular clouds (Wiebe et al., 2003). It has been found that the abundances of CO and fractional ionisation can be accurately computed with significantly reduced networks in the case of pure gas-phase chemistry. For instance, to follow with < 15% uncertainty the evolution of the CO abundance in a dense cloud, it is enough to take into account only 8 species involved in 9 reactions. In contrast, for gas-grain chemistry with surface reactions the reduction task is found to be more difficult, though still possible, with typical acceleration factors being about a factor of 10. It is proved that the "reaction-based" reduction method is more efficient and accurate compared to the "objective techniques", but more time-consuming as well.

The first aim of this chapter is to describe the reaction-based reduction technique in detail. Then, this reduction method is utilised to investigate what processes govern the chemical evolution of the ionisation degree in various parts of a protoplanetary disc, and at what times. Finally, the column densities of the observed species are computed and compared with other studies and observational data in order to verify the reliability of the adopted chemical model.

The organisation of this chapter is the following. The reaction-based reduction technique is presented in Section 4.2. The chemical processes responsible for the fractional ionisation in various parts of the disc are outlined in Section 4.3, where I also present the disc model. In Section 4.4 column densities of observed species are tabulated and compared with other studies and observational data. Results of the analysis and their relevance to the MHD modelling are discussed in Section 4.5. A summary and final conclusions follow.

4.2   Reduction method

To reduce a number of species and reactions in a chemical network, one has to provide a mathematical method designed to estimate the significance of particular species or reactions to the evolution of the species under consideration. One such method is outlined in this section.

The so-called "reaction-based" reduction allows to select *simultaneously* only those species and reactions from the entire chemical network that are *necessary* to compute abundances of "important" species with a specified accuracy. This approach is also useful if one aims at the search of essential destruction and formation pathways for selected species, where a smaller number of chemical reactions makes the thorough analysis easier.

The basic idea of the reaction-based reduction is to search for the production and destruction reactions, most important for the evolution of (an) important species, and determine their relative significance. This is done via the analysis how sensitive the net formation and loss rate of a given species is to the presence of particular reactions at certain time.

At the beginning, the chemical model is computed with the full network in order to obtain abundances of all species during the entire evolutionary time span.

Second, the *important* species are specified. Further, the algorithm estimates the weights of all species w_s and reactions w_r in order to quantify their importance for the evolution of the species under investigation by an iterative process.

At the first iteration, weights of important species are set to 1 and weights of all other species and all reactions are set to 0. At the ith iteration all possible formation and destruction pathways of the current species s_i are found and their significance values $w_r^i(j)$ ($j = 1 \div K$) are specified as

$$
w_r^i(j) = \max \left\{ w_r^{i-1}(j), \ \frac{k_j n_{r_1}(j) n_{r_2}(j)}{\displaystyle\sum_{l=1,N_r(i)} k_l n_{r_1}(l) n_{r_2}(l)} w_s(i) \right\}.
\tag{4.1}
$$

Here k_j is the rate of the jth reaction, $n_{r_1}(j)$ and $n_{r_2}(j)$ are the abundances of the first $r_1(j)$ and second $r_2(j)$ reactants, $N_r(i)$ is the number of those reactions, in which s_i is a reactant or a product, and $w_s(i)$ is the weight of the species s_i.

Consequently, a new set of species, which are found at that iteration to be *necessary* for the evolution of the important species and were not considered at previous iterations, is formed. Their weights w_s are estimated as the maximum possible values of the weights w_r of the reactions they are involved in. Then these species are added to the set of necessary species, and the last two steps of weighting are repeated again. This process is performed for several stages during the computational time.

The iterations are stopped after all species and all time steps are considered. Then one obtains a reduced chemical network from the full network by choosing only those reactions that have weights w_r exceeding a pre-defined cut-off threshold ϵ: $\log w_r \geq \epsilon$.

The cut-off value must be chosen to satisfy the requested accuracy of the computed abundances of the important species, which is usually set to $\gtrsim$ 30–50% or even higher. Usually, it is hard to guess immideately the largest ϵ value, so one has to deal with an iterative approach, starting from a reasonably low value of $\sim 10^{-10}$. If such an intermediate smaller chemical network is found, then the full procedure described above is repeated again for this set of reactions, now being the new "full" network, but with a slightly higher value of the cut-off parameter. This iterative approach to reduce the initial full network through subsequently smaller networks by steadily increasing the cut-off allows to find the smallest possible reduced network. The iterations are finished when there is a difference between the abundances of the important species computed with the initial (complete) and last reduced network greater than the requested accuracy value for any particular time step. These optimised reduced networks are especially useful for the analysis of the chemical evolution of the species under investigation as they contain only their primal formation and destruction pathways, and none of unimportant reactions.

4.3 Ionisation state of a protoplanetary disc

4.3.1 Importance of the ionisation fraction for disc evolution

In this section, I apply the reaction-based reduction method described above to study the chemistry of the fractional ionisation in a protoplanetary disc. Why I focus on this particular quantity instead of dealing with other interesting species?

Ionisation in protoplanetary discs is an important quantity which enables the angular momentum transport to occur via magnetohydrodynamic (MHD) turbulence driven by the magnetorotational instability (MRI; Balbus and Hawley, 1991). From this point of view, a disc is conventionally divided

into the "active" layer, adjacent to the disc surface, and the "dead" zone, centred on the midplane. The active part of the disc is irradiated by high energy stellar/interstellar photons and cosmic rays. There, the fractional ionisation is so high that the magnetic field is well coupled to the gas. Due to this coupling, the active layer is unstable to MRI, and the developing turbulence allows the accretion to occur (e.g., Fleming and Stone, 2003; Gammie, 1996). In contrast, the shielded midplane region is almost neutral, decoupled from the magnetic field, and thus quiescent.
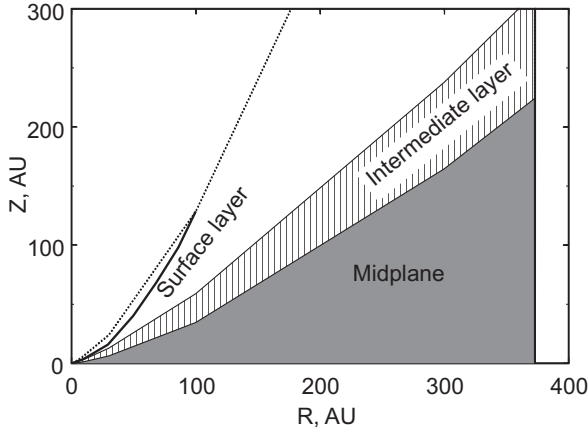
Figure 4.1. Three layers of a disc with distinctively different sets of chemical processes responsible for the value of the fractional ionisation x_e. The thick solid line is the upper boundary of the surface layer where $x_e = 10^{-4}$, while dotted line depicts the disc upper limits.

The location of the boundary between these two regions may prove to be very sensitive to the disc physical properties and chemical composition (e.g., Fromang et al., 2002). The non-ideal MHD simulations require the self-consistent calculation of the fractional ionisation together with dynamical modelling, which is a demanding computational task. This is why in the state-of-the-art MHD modelling of protoplanetary discs an oversimplified chemical scheme is usually assumed with a few ions and a network that includes only ionisation and recombination reactions, often neglecting the presence of dust grains (Fleming and Stone, 2003; Fromang et al., 2002; Sano et al., 2000). The medium is believed to be in chemical equilibrium, so that the fractional ionisation x_e can be expressed as (e.g., Gammie, 1996)

$$x_e(eq) = \sqrt{\frac{\zeta}{\beta n_H}}, \qquad (4.2)$$

where ζ is the ionisation rate, β is a typical recombination coefficient, and n_H is the hydrogen number density. This approach may indeed be valid if only the cosmic ray ionisation is taken into account and only gas-phase chemical processes are considered. However, dust plays an important role in the evolution of the fractional ionisation, being an efficient electron donor for recombining ions and a sink for neutrals in cold disc parts. Moreover, newly born stars possess a relatively high X-ray flux with photon energies from about 1 to 5 keV (e.g., Igea and Glassgold, 1999) as well as a high UV flux (e.g., Bergin et al., 2003). These factors give rise to a more complicated chemistry relevant for the ionisation degree. In particular, different ions dominate the fractional ionisation at different times and in different parts of the disc. Therefore, the straightforward application of Eq. (4.2) for evaluating the ionisation degree can be fraught with errors in some disc locations.

In order to check the validity of Eq. (4.2), I analyse the detailed ionisation structure of a protoplanetary disc computed with the UMIST 95 database and surface chemistry included. I adopt a reference disc model to serve as a guide to the range of possible physical conditions that may be encountered in real protoplanetary discs. Within this model, I choose several representative disc locations and investigate in detail, which chemical processes control the time-dependent ionisation degree. My primal intention is to show that the oversimplified treatment of the ionisation in a protoplanetary disc as an equilibrated ionisation-recombination cycle can lead to the x_e values that differ by more than an order of magnitude from values computed with all the available information on the disc chemical evolution.

In each of the selected disc locations the chemical model described in Section 4.3.3 is followed over 10^6 years. Resulting dominant ions in various disc layers are listed in Table 4.1. The reaction-

Table 4.1. Dominant ions in the midplane, intermediate layer, and surface layer at $t = 1$ Myr

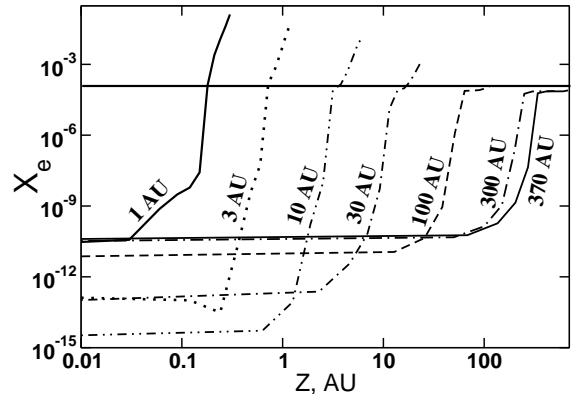| R, AU	1	3	10	30	100	300	373
Midplane	Na^+	$HCNH^+$	HCO^+	HCO^+	N_2H^+	H_3^+	H_3^+
Intermediate layer	Mg^+	HCO^+, S^+, H_3^+, NH_4^+, etc.	HCO^+	HCO^+	HCO^+	HCO^+	HCO^+
Surface layer	C^+ H^+	C^+ H^+	C^+	C^+	C^+	C^+	C^+

based reduction method is then used to find out those processes that determine the x_e value. In addition, I show some representative reduced networks for the midplane and surface layer.

4.3.2 Disc model

As a basis for calculations, I adopted the steady-state disc model of D'Alessio et al. (2001). The central star is assumed to be a classical T Tau star with an effective temperature $T_* = 4\,000$ K, mass $M_* = 0.5 M_\odot$, and radius $R_* = 2 R_\odot$. The disc has a radius of 373 AU, an accretion rate $\dot{M} = 10^{-7}\,M_\odot$ yr^{-1}, and viscosity parameter $\alpha = 0.01$. It is illuminated by UV radiation from a central star and by interstellar UV radiation. The intensity of the stellar UV field is described with the standard G factor, which is scaled in a way that the unattenuated stellar UV field at $R = 100$ AU is a factor of 10^4 stronger than the mean interstellar radiation field (Draine, 1978). The intensity of the stellar and interstellar UV radiation at a given disc point is calculated as described in Section 3.1.2.1 (Eq. 3.2).

Figure 4.2. Fractional ionisation as a function of height above the disc plane. Lines are labelled with the corresponding radii.

In addition to the UV field, three other ionisation sources are considered: cosmic ray ionisation (ζ_{CR}), decay of radionuclides (ζ_R), and stellar X-ray ionisation (ζ_X). The region under investigation spans a range of radii from 1 to 373 AU. I do not consider regions closer to the star to avoid the necessity to account for dust destruction, collisional ionisation, and three-body interactions, etc. Even when the close vicinity of the star is excluded, the disc is still characterised by a wide range of all relevant physical parameters: gas temperatures T are $10 - 600$ K, densities are $10^{-20} - 10^{-10}$ g cm^{-3}, G are $10^2 - 10^8$, A_V varies from 0 to more than 100 mag, and ionisation rates are $10^{-18} - 10^{-10}$ s^{-1}.

To organise the study, I divide the entire disc into three regions, namely, the midplane, the intermediate layer, and the surface layer. This division is similar to that outlined by Aikawa and Herbst (1999b). The midplane is the part of the disc near the symmetry plane, which is opaque to both X-ray and UV photons and is ionised primarily by cosmic ray particles and due to decay of short-living

radionuclides. If one goes up from the midplane, the fractional ionisation first stays the same as in the midplane, but then at some height it starts to grow in response to increasing X-ray intensity. I take this turn-off height to be the lower boundary of the intermediate layer (and the upper boundary of the midplane region). In the adopted model this height is approximately given by $z_L = 0.05\,r^{1.42}$ AU. With increasing height, the fractional ionisation grows first slowly, then much faster, in response to a decreasing opacity of the medium to the UV radiation. The point, where transition between slow and fast growth occurs, is assumed to be the upper boundary of the intermediate layer and the lower boundary for the third, surface layer. This boundary is approximated by $z_U = 0.17\,r^{1.27}$ AU. One also has to keep in mind that the fractional ionisation is important in dynamical calculations, only if it is small, as high ionisation means that the ideal MHD equations can be used. Thus, I set the upper boundary of the surface layer to a position where the ionisation degree exceeds $\sim 10^{-4}$. It must be noted that this simple picture may not be appropriate if diffusion processes of the disc matter are taken into account (Ilgner et al., 2004).

The disc structure is depicted in Figure 4.1. The upper boundary of the surface layer is shown schematically (thick solid line), as at $R \gtrsim 100$ AU it extends beyond the disc limits (dotted line) for the adopted cut-off fractional ionisation of 10^{-4}. In Figure 4.2 I show the dependence of the fractional ionisation on the height above the disc plane computed with the chemical model for seven representative radii R.

4.3.3 Chemical model

The adopted chemical model is already described in Chapter 3. Briefly, I utilise the UMIST 95 ratefile (Millar et al., 1997) for the gas-phase chemistry and the surface reaction set compiled by Hasegawa et al. (1992) and Hasegawa and Herbst (1993). As there are multiple ionisation sources in the protoplanetary disc, the cosmic ray ionisation rate is replaced by the sum $\zeta_{CR} + \zeta_X + \zeta_R$ in expressions for rates of chemical reactions with cosmic ray particles (CRP) and cosmic ray induced photoprocesses. Given the high intensity of the impinging UV radiation, photodesorption of surface species is taken into account along with thermal and CRP-induced desorption. I assume that gas-phase species stick onto dust surfaces with the probability $S = 0.3$, apart from H_2, He ($S = 0$), and H (S is calculated by Eq. (3.7) in Hollenbach and McKee, 1979).

4.3.4 Results

4.3.4.1 Ionisation in the midplane

The midplane of the disc is characterised by high density, high optical depth, and a relatively low ionisation rate. Neither the UV radiation from a central star, nor the interstellar UV radiation is able to penetrate into this region. The ionisation rate is close to 10^{-17} s^{-1}. At the point closest to the star, ζ is dominated by X-ray ionisation, further away from the centre the attenuated cosmic rays and radionuclides are the only ionising factor. The temperature drops from ~ 600 K at $R = 1$ AU to about 8 K at the disc edge. In the same distance interval, the gas density goes down from 10^{-10} g cm^{-3} to less than 10^{-14} g cm^{-3}. Detailed physical conditions for the midplane are given in Table 4.2.

*4.3.4.1.1 Dark, hot chemistry* The chemistry of the point M1 is extremely simple. In essence, it involves only five species, that are neutral and ionised magnesium, neutral and ionised NO, and electrons.

The reduced network for this point is shown in Table 4.3. At the beginning of the computation the electron abundance decreases from the initial value of $\sim 10^{-9}$ to the new equilibrium value of

Table 4.2. Physical conditions in the midplane

Point	R, AU	ρ, g cm^{-3}	T, K	ζ_{CR}, s^{-1}	ζ_X, s^{-1}
M1	1	2.1(−10)	614.	8.8(−19)	7.5(−18)
M2	3	4.7(−11)	193.	2.3(−18)	4.0(−23)
M3	10	8.5(−12)	52.	5.0(−18)	1.2(−25)
M4	30	7.3(−13)	29.	9.4(−18)	5.4(−27)
M5	100	4.8(−14)	16.	1.2(−17)	3.8(−28)
M6	300	4.8(−15)	9.	1.3(−17)	4.0(−29)
M7	370	3.3(−15)	8.	1.3(−17)	2.6(−29)

about 10^{-11}, determined by the electron exchange between Mg, Mg$^+$, NO, and NO$^+$, and then remains nearly constant. With the full network, the dominant ion is Na$^+$, but it serves mainly as a passive sink for positive charges. This is why it is taken out of the reduced network. It suffices to include ionised magnesium, which is one of the most abundant ions in the initial abundance set.

NO$^+$ + Mg	$\rightarrow$	Mg$^+$ + NO
Mg$^+$ + e^-	$\rightarrow$	Mg + $h\nu$
NO + $h\nu_{CR}$	$\rightarrow$	NO$^+$ + e^-
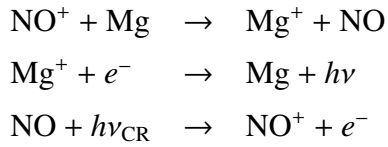
Table 4.3. Reduced network for dark, hot chemistry in the disc midplane

It is worth to mention here the apparent similarity of this network to the one that determines x_e in dense interstellar clouds (Oppenheimer and Dalgarno, 1974) in the sense that it consists of a representative metal, a representative molecular ion, and the charge transfer reaction between them. The explanation is that at such high temperature the chemistry mostly proceeds in the gas-phase. Thus, the ionisation degree is determined by the gas-phase reactions. However, due to much higher density these reactions are different from those described in Oppenheimer and Dalgarno (1974). The major difference is that the reaction of H$_2$ ionisation by cosmic rays is not important in the considered point. A modest electron supply is provided by NO ionisation by cosmic ray induced photons. The importance of the NO$^+$ ion is caused by its chemical inertness. Due to this inertness, most of the time its abundance exceeds that of other ions, involved in charge transfer reactions with magnesium, by more than an order of magnitude. With this 5×3 network, the error in the fractional ionisation does not exceed 40% during the entire computation time of 1 Myr. By adding a few more species to the reduced network, it is possible to decrease this uncertainty to 20%. These species account for the rapid destruction of the two other initially abundant ions, HCO$^+$ and H$_3^+$.

The chemistry of the point M2 is also simple, but in a totally different way. At this lower temperature of ~ 200 K, magnesium is irreversibly depleted onto dust grains. While at earliest times ($t < 3$ years) the evolution of the electron abundance is governed by recombination of Mg$^+$, later the fractional ionisation is equilibrated and determined by a simple network involving H, H$_2$, H$_2^+$, and H$_3^+$. Included reactions are H$_2$ ionisation by cosmic rays, H$_3^+$ formation, H$_3^+$ and Mg$^+$ recombination, accretion of Mg onto dust grains, and grain charging processes. The error in the fractional ionisation does not exceed 10% during almost the entire computation time, reaching 40% only at the very beginning of the computation due to neglected Na$^+$ and Fe$^+$ ions. Note that the equilibrated electron concentration $x_e \sim 10^{-13}$ at this point is several times lower than the abundance of charged grains.

Table 4.4. Reduced network for dark, cold chemistry in the midplane

$H_2 + CRP$	$\rightarrow$	$H_2^+ + e^-$	$H_2^+ + H_2$	$\rightarrow$	$H_3^+ + H$
$H_3^+ + N_2$	$\rightarrow$	$N_2H^+ + H_2$	$H_3^+ + e^-$	$\rightarrow$	$H_2 + H$
$HCO^+ + e^-$	$\rightarrow$	$CO + H$	$N_2H^+ + e^-$	$\rightarrow$	$N_2 + H$
$Fe^+ + g^-$	$\rightarrow$	Fe	$Mg^+ + g^-$	$\rightarrow$	Mg
$H_3^+ + g^-$	$\rightarrow$	$H_2 + H$	$HCO^+ + g^-$	$\rightarrow$	$CO + H$
$N_2H^+ + g^-$	$\rightarrow$	$N_2 + H$			

Thus the net charge density at these conditions is determined mainly by grain charging processes.

Dominant ions in a model of the disc interior, which is similar to the one used here, are determined by Markwick et al. (2002). In the second part of their Table 1 they present ions that define the x_e value for various heights and at $R \leq 10$ AU, when X-rays are taken into account. The difference with my results is obvious. In the present model dominant ions in the inner part of the midplane are Na^+, $HCNH^+$, and HCO^+, while in the model by Markwick et al. (2002) everywhere in the midplane the fractional ionisation is determined by the complex CH_3CO^+ ion. I attribute this discrepancy to the different treatment of the surface dissociative recombination of ions as well as to different treatment of grain charges. In the Markwick et al. model all grains are assumed to participate in recombination reactions, with products of recombination sticking to grain surfaces, while in my model these products are returned to the gas immediately (see, e.g., discussion in Tielens, A. G. G. M., 1993, Section 6.5.2 therein). Thus, in their model metals recombine with dust grains, stick to them, and are not easily returned to the gas-phase. In my model, in the point closest to the star, all dust grains are positively charged, so they do not contribute to the recombination rate at all. Also, when a metal ion happens to encounter a rare negative or neutral grain, it looses the charge but remains in the gas-phase (e.g., Watson and Salpeter, 1972). Higher above the midplane and further from the star, where details of the gas-grain interaction are less important, dominant ions in both models are almost the same, i.e., $HCNH^+$ and HCO^+.

4.3.4.1.2 Dark, cold chemistry The ionisation at the points M3 and M4 displays a similar behaviour. In a cold and dense environment metals are depleted onto dust grains almost immediately, and the gas-phase fractional ionisation drops to a very low equilibrium value – about $3 \cdot 10^{-15}$ in M3 and about $8 \cdot 10^{-14}$ in M4. These values are determined by three almost equally important cycles, that are ionisation and recombination of helium, formation and destruction of HCO^+, and formation and destruction of H_3^+. The reduced network, consisting of these species and processes, reproduces the fractional ionisation with a few per cent accuracy in all but earliest times. The electron abundance at $t < 0.1$ yrs in the absence of metals is determined by a more complicated set of processes, with the fractional ionisation being reproduced within 50% uncertainty by a network of about 40 species. Again, charged grains determine the total charge density at these points.

The dominant ions at points M5, M6, and M7 are N_2H^+, HCO^+, and H_3^+. The reduced network for the entire outer part of the disc consists of about 25 species and of a comparable number of reactions, which govern abundances of these ions. At earlier times Mg^+ and Fe^+ are important as electron suppliers, so in addition to N_2H^+ and HCO^+ chemistry, the reduced network includes also neutral and ionised metals. Among the included reactions are metal sticking to grains, cosmic ray ionisation of molecular hydrogen, H_3^+ formation, charge transfer between metals and H_3^+, and dissociative recom-

Table 4.5. Physical conditions in the intermediate layer

R, AU	ρ, g cm^{-3}	T, K	ζ, s^{-1}
1	4(−12)–2(−10)	140–520	3(−13)–4(−10)
3	4(−15)–6(−12)	80–120	2(−15)–2(−12)
10	1(−15)–4(−14)	50–90	8(−16)–2(−13)
30	6(−17)–1(−14)	30–80	4(−17)–6(−15)
100	4(−18)–1(−16)	30–60	7(−17)–1(−15)
300	2(−18)–2(−17)	20–40	1(−17)–7(−17)
370	1(−18)–1(−17)	20–40	1(−17)–4(−17)

bination of ions with grains and electrons. The network responsible for x_e at the outer disc edge is presented in Table 4.4. It also includes reactions of adsorption and desorption of neutral components that are not shown for brevity.

4.3.4.2 Ionisation in the intermediate layer

The intermediate layer differs from the midplane by a much higher X-ray ionisation rate. Ranges of physical conditions for the intermediate layer are summarised in Table 4.5. They imply that many molecules are abundant in the gas phase in this disc domain due to shielding of the UV radiation and effective desorption by X-rays. From the chemical point of view, the characteristic feature of the intermediate layer is that a chemo-ionisation equilibrium is sometimes not reached during the entire considered 1 Myr time span.
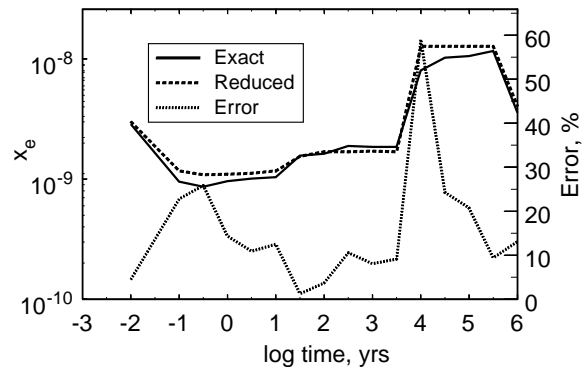
4.3.4.2.1 Warm, X-ray driven chemistry Similar to the midplane, the part of the intermediate layer closest to the star ($R < 3$ AU) is characterised by temperatures of a few hundred K. As the grain icy mantles are absent, the chemistry in this region is driven by the gas-phase reactions. Dominant ions are metals, HCO$^+$, and HCNH$^+$. Apart from these components, the reduced network contains CO and neutral metals as well as neutral and ionised N and neutral O along with their hydrides [N,O]H$_n$ and [N,O]H$_n^+$, involved in synthesis and destruction of the hydrogen saturated molecules NH$_3$ and H$_2$O. Also included are N$_2$, He, He$^+$, which are needed closer to the bottom of the layer (where T is high and ζ is relatively low), and HCN, HNC, HCN$^+$, O$_2$, and O$_2^+$ which are important further away from the midplane (where T is low and ζ is high). The fractional ionisation computed with this reduced network differs from the one computed with the full network by less than 40% during the entire time span.

Again comparing my data for the intermediate layer to those by Markwick et al. (2002) I find that at $3 < R < 10$ AU the results generally agree with each other, especially given the fact that the sampling of the inner part of the disc is much more detailed in the Markwick et al. model. Again, in the innermost point I find a dominant metal ion in the model compared to molecular ions HCNH$^+$ and H$_4$C$_2$N$^+$ in their model. I believe that the origin of this difference is the same as described above.

The ionisation degree further out from the star (at $R > 30$ AU) is established by the evolutionary sequence which consists of the following stages. Initially, the more abundant HCO^+ and H_3^+ species are destroyed almost immediately and attain abundances of the order of 10^{-11} at $t \sim 10^{-3}$ years. Metal ions are neutralised slower through recombination with negatively charged grains and electrons and stick to dust surfaces. The overall electron concentration x_e decreases from $\sim 3 \cdot 10^{-9}$ cm^{-3} at $t = 0$ to 10^{-9} cm^{-3} at $t \sim 0.3$ yrs. Then, few equilibrium states are reached with a sequence of molecular ions, mainly, NH_4^+, H_3CO^+, and HCO^+. Equilibrium abundance of the respective next ion in this sequence is higher and is reached later, thus the time dependence of the fractional ionisation has a step-like appearance. The "second birth" of HCO^+ is caused by H_2CO coming from icy mantles. Formaldehyde reacts with H_3^+ to form H_3CO^+, which is the dominant ion at $0.1 < t < 30$ yrs. One of the recombination channels for H_3CO^+ maintains its equilibrium, restoring H_2CO. The other two channels lead directly and indirectly to CO production and eventually increase the abundance of this molecule up to the point where a new equilibrium state is reached for HCO^+. This ion eventually dominates the fractional ionisation in the outer part of the intermediate layer. Direct formation of HCO^+ in the reaction of H_3^+ with CO is damped initially in favour of H_3^+ reaction with H_2CO both because of the lower initial CO abundance and because the latter reaction has a higher rate coefficient $\alpha = 6.3 \cdot 10^{-9}$ cm^3 s^{-1} compared with $\alpha = 1.7 \cdot 10^{-9}$ cm^3 s^{-1} for H_3^+ + CO reaction.

To reproduce the step-like x_e behaviour, one needs a reduced network that includes a few tens of species involved in cycles of synthesis and destruction of the above ions. This network reproduces the nature of the equilibrium stages and their length with an uncertainty that does not exceed 20%. This simple picture is not appropriate closer to the star ($3 < R < 30$ AU), where the density is high enough and the temperature is low enough to allow effective gas-dust interaction. At the same time, a high ionisation rate leads to an increased abundance of helium ions, which significantly alters the late-time evolution of the fractional ionisation. An example of this evolution is shown in Figure 4.3. It corresponds to the case with $n_H = 8.4 \cdot 10^{10}$ cm^{-3}, $T = 74$ K, and $\zeta = 2 \cdot 10^{-13}$. The "exact" solution is shown with the solid line. The initial decrease of the electron

Figure 4.3. Evolution of the fractional ionisation in the intermediate layer at $R = 3$ AU. The solid line shows the exact solution. The dashed line corresponds to the reduced network consisting of 112 species and 195 reactions. The dotted line (right Y-axis) shows the relative uncertainty in the fractional ionisation computed with the reduced network.

abundance is followed by a few steps corresponding to different equilibrium states. The last one, that of HCO^+, is reached after approximately 300 yrs of evolution. If there were no relatively abundant ionised helium, the fractional ionisation would stay constant from that moment. It is this ion, coupled to high density and low temperature, which causes a new development. At $t \sim 3 \cdot 10^4$ yrs the ionisation degree increases by about an order of magnitude up to $\sim 10^{-8}$ cm^{-3}, and another equilibrium state is reached, with S^+ being a dominant ion and a dominant sulphur-bearing species.

In the initial abundance set sulphur is mostly bound in the CS and H_2S molecules that are destroyed by He^+, producing either S^+ or S (as well as C, C^+, and H_2). Passing through a few reactions, the most important of which is the reaction with CH_4, sulphur is reunited with carbon in a CS molecule. This process is well equilibrated, when the abundance of methane is high, and leads to a negligible S^+ abundance at $t < 10^4$ yrs. However, as the time goes by, some carbon atoms (both free and incorporated into CH_4) are taken out of this cycle due to formation of long carbon chains in reactions

of C^+ with methane and other hydrocarbons. After 3000 yrs the cycle is broken entirely. As the abundance of methane and other light carbon-bearing species goes down, that of ionised sulphur grows, causing almost an order of magnitude increase in the fractional ionisation.

Further evolution of x_e is implicitly controlled by gas-phase and surface reactions involving carbon chains. The reduction method allows to find which of them are most important, as shown in Figure 4.4. The main route for synthesis and destruction of long carbon chains in the depicted scheme starts with an acetylene molecule containing only two carbon atoms, which is rapidly converted to C_5H_2 molecules. This molecule then either transforms to even longer chains, or proceeds further down the cycle to C_5H^+ that recombines to C_4H. This species starts a chain of slow reactions with atomic oxygen that degrade it to C_3H, C_2H, and CH. Eventually, destruction of carbon chains leads to the new growth of methane abundance and to the slow decrease of the fractional ionisation. Ionised sulphur is consumed in

Figure 4.4. Main routes governing synthesis and destruction of long carbon chains. Surface reactions are indicated by dashed lines.

the reaction with CH_4 and eventually is converted back to CS. The abundance of H_3^+ determines the ionisation degree at the end of the computation. Conversion of C_5H_2 molecules into longer chains (the lower part of Figure 4.4) slows down the methane abundance restoration. The reduced network must include almost all species with six carbon atoms to reproduce properly the time scale of this process. It must be noted that three key reactions of this carbon chain cycle proceed on dust grain surfaces. These are reactions of hydrogen addition to C_5H, C_6, and C_6H (shown with dashed lines). Without these reactions the sequence of carbon chain synthesis would be terminated by the C_5N molecule that lacks effective destruction pathways at given conditions. Exhaustion of atomic and ionised carbon would keep the ionised sulphur at high level, reached at $t \sim 3000$ years. Thus, I must conclude that at least within the limits of the adopted chemical model some surface reactions are of crucial significance. As far as I know, this is the *first* indication that the surface chemistry may have an "order-of-magnitude" importance for the evolution of fractional ionisation in the protoplanetary discs.
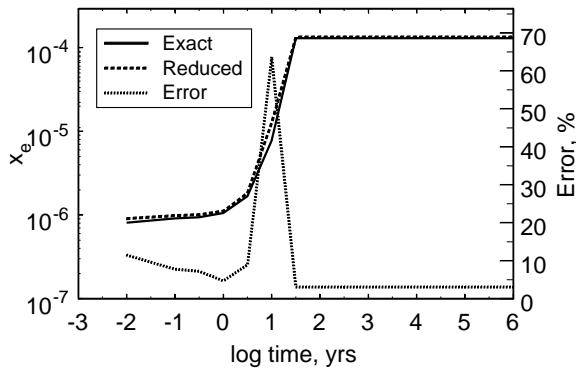
4.3.4.3 Ionisation in the surface layer

The surface layer encompasses those disc regions where the degree of ionisation reaches a value of $\lesssim 10^{-4}$ at the end of the evolutionary time. The corresponding physical conditions imply low densities ($\rho \sim 10^{-19} - 10^{-13}$ g cm^{-3}), moderate temperatures ($T < 250$ K), a high X-ray ionisation rate and low obscuration of the UV radiation. Conditions in the surface layer are given in Table 4.6. Note that the temperature of the disc atmosphere is nearly constant in the vertical direction at any distance from the star. This extreme environment presumes a chemical evolution typical of photon-dominated regions (PDR). The chemistry is dominated by gas-phase processes, while the role of gas-grain interactions is negligible, apart from the desorption of initially abundant surface species. As my definition of the surface layer is based on the fractional ionisation value, it turns out that the layer can be further divided into two chemically distinct zones. Closer to the star ($r \lesssim 10$ AU) x_e is controlled by the X-ray ionisation, while in the outer regions ($r \gtrsim 10$ AU) ionisation is mainly provided by the UV photons.

Table 4.6. Physical conditions in the surface layer

R, AU	ρ, g cm^{-3}	T, K	G_0	A_V^S, mag	A_V^{IS}, mag	ζ, s^{-1}
1	2(−14)–1(−13)	∼ 180	1(8)	> 10	∼ 1	2(−9)
3	2(−16)–1(−15)	∼ 230	7(7)	∼ 1.0	< 0.5	8(−12)
10	1(−17)–8(−17)	140–160	9(5)	< 1	< 0.5	6(−13)
30	3(−18)–1(−17)	80–100	9(4)–1(3)	< 1	< 0.5	5(−14)
100	4(−19)–4(−18)	60–70	5(3)–7(3)	< 1	< 0.5	1(−15)–4(−15)
300	3(−19)–2(−18)	35–40	5(2)–7(2)	< 1	< 0.5	7(−17)–2(−16)
370	1(−19)–1(−18)	30–40	2(2)–4(2)	< 1	< 0.5	5(−17)–1(−16)

Figure 4.5. Evolution of the fractional ionisation in the surface layer at $R = 1$ AU. The exact solution is shown with solid line. Dashed line corresponds to the reduced network consisting of 21 species and 27 reactions. The dotted line (Y-axis) shows the relative uncertainty in the fractional ionisation computed with the reduced network.

4.3.4.3.1 X-ray dominated chemistry   The evolution of the ionisation degree in the hot ($T \sim$ 200 K) part of the surface layer closer to the star is determined by X-ray ionisation of atomic hydrogen. The final equilibrium ionisation degree is well reproduced by the network, consisting of hydrogen-bearing species (H, H$^+$, H$_2^+$, H$_3^+$) only. This equilibrium value is reached after 100 years of evolution. Up to this time x_e is determined by a more complicated set of chemical processes, which includes H$_3^+$ formation, an H$_3$O$^+$ formation and destruction cycle as well as reactions involving CO and HCO$^+$. The primary carbon and oxygen carrier, formaldehyde, adds to this complexity by being desorbed from grain surfaces and destroyed by cosmic ray and X-ray induced photons. The cycles that involve these molecules are not equilibrated. Most reactions with polyatomic species tend to produce atomic hydrogen, which is gradually ionised by intense X-ray radiation. Eventually, all complex molecules are destroyed, and at the end of the computation gas mostly consists of atoms and atomic ions. The entire reduced network comprises 21 species and 27 reactions and is presented in Table 4.7.

The uncertainty does not exceed 60% during the entire computational time (Fig. 4.5). It must be noted that without this simple, but important ion-molecule chemistry the uncertainty at earlier times would exceed an order of magnitude.

4.3.4.3.2 UV-dominated chemistry   The evolution of the ionisation fraction in the distant regions of the surface layer ($r \gtrsim 10$ AU) is similar, but more complicated from the chemical point of view than

Table 4.7. Reduced network for X-ray dominated chemistry in the surface layer

H_2CO^d	$\rightarrow$	H_2CO	H_2O^d	$\rightarrow$	H_2O
$C + h\nu_{CR}$	$\rightarrow$	$C^+ + e^-$	$OH + h\nu_{CR}$	$\rightarrow$	$O + H$
$CO + h\nu_{CR}$	$\rightarrow$	$C + O$	$H_2CO + h\nu_{CR}$	$\rightarrow$	$CO + H_2$
$H + CRP, X\text{-ray}$	$\rightarrow$	$H^+ + e^-$	$H_2 + CRP, X\text{-ray}$	$\rightarrow$	$H_2^+ + e^-$
$H_2^+ + H_2$	$\rightarrow$	$H_3^+ + H$	$H^+ + O$	$\rightarrow$	$O^+ + H$
$H^+ + OH$	$\rightarrow$	$OH^+ + H$	$H_3^+ + O$	$\rightarrow$	$OH^+ + H_2$
$H_3^+ + H_2O$	$\rightarrow$	$H_3O^+ + H_2$	$H_3^+ + CO$	$\rightarrow$	$HCO^+ + H_2$
$O^+ + H$	$\rightarrow$	$H^+ + O$	$O^+ + H_2$	$\rightarrow$	$OH^+ + H$
$OH^+ + H_2$	$\rightarrow$	$H_2O^+ + H$	$H_2O^+ + H_2$	$\rightarrow$	$H_3O^+ + H$
$C^+ + H_2O$	$\rightarrow$	$HCO^+ + H$	$C^+ + O_2$	$\rightarrow$	$O^+ + CO$
$O + OH$	$\rightarrow$	$O_2 + H$	$H^+ + e^-$	$\rightarrow$	$H + h\nu$
$H_3^+ + e^-$	$\rightarrow$	$H_2 + H$	$C^+ + e^-$	$\rightarrow$	$C + h\nu$
$H_2O^+ + e^-$	$\rightarrow$	$O + H_2$	$H_3O^+ + e^-$	$\rightarrow$	$OH + H + H$
$HCO^+ + e^-$	$\rightarrow$	$CO + H$			

Superscript "d" is used to denote surface species

in the case of the X-ray dominated chemistry. As the intensity of stellar X-rays goes down to lower values, UV photons become the main ionising source (see Table 4.6). The typical gas temperature in this part of the disc decreases below 100 K. The entire ionisation process of the region is determined by formaldehyde desorption and destruction. Icy mantles illuminated by UV radiation evaporate, thus delivering H_2CO into the gas phase. This molecule is either destroyed directly by photons ($H_2CO \rightarrow CO, HCO^+$) or ionised and dissociated ($H_2CO \rightarrow H_2CO^+ \rightarrow CO$). HCO^+ dissociatively recombines to CO as well, and this molecule is dissociated by photons producing C and O. The destruction processes proceed so fast that after only a fraction of a year the gas composition is mostly atomic, with C^+ being the dominant ion. When all polyatomic species are destroyed, the fractional ionisation

Table 4.8. Reduced network for UV-dominated chemistry in the surface layer

H_2CO^d	$\rightarrow$	H_2CO	$C^+ + H_2CO$	$\rightarrow$	$H_2CO^+ + C$
$C^+ + e^-$	$\rightarrow$	$C + h\nu$	$HCO^+ + e^-$	$\rightarrow$	$CO + H$
$H_2CO^+ + e^-$	$\rightarrow$	$CO + H + H$	$H_2CO^+ + e^-$	$\rightarrow$	$H_2CO + h\nu$
$C + h\nu$	$\rightarrow$	$C^+ + e^-$	$CO + h\nu$	$\rightarrow$	$C + O$
$H_2CO + h\nu$	$\rightarrow$	$CO + H_2$	$H_2CO + h\nu$	$\rightarrow$	$CO + H + H$
$H_2CO + h\nu$	$\rightarrow$	$H_2CO^+ + e^-$	$H_2CO + h\nu$	$\rightarrow$	$HCO^+ + e^- + H$

Table 4.9. The SIREN chemical network

Gas-phase species:
H, H_2, H_x^+ ($x = 1 \div 3$), He, He^+, CH_x ($x = 0 \div 4$), CH_x^+ ($x = 0 \div 5$),
H_xCO ($x = 0 \div 2$), H_xCO^+ ($x = 0 \div 3$), HOC^+, NH_x ($x = 0 \div 3$),
NH_x^+ ($x = 0 \div 4$), CN, CN^+, HCN, HNC, HCN^+, $HCNH^+$, CH_2CN^+,
NO, NO^+, N_2, N_2^+, N_2H^+, H_xO ($x = 0 \div 2$), H_xO^+ ($x = 0 \div 3$),
Na, Mg, Fe, Na^+, Mg^+, Fe^+

Surface species:
H, CH_x ($x = 0 \div 4$), H_xCO ($x = 0 \div 2$), NH_x ($x = 0 \div 3$), H_xO ($x = 0 \div 2$),
O_2, CN, HCN, HNC, N_2, Na, Mg, Fe

is regulated by an equilibrium ionisation-recombination cycle of atomic carbon. The reduced network consisting of less than 15 species and about 20 reactions leads to less than 20% uncertainty during the entire computational time. An example of such a network for $R = 100$ AU is given in Table 4.8.

4.3.4.4   SIREN chemical network

In each particular region of the disc, the number of species and reactions in reduced networks is limited. However, as it has shown above, these species and reactions are different in various disc locations. Thus, it is natural to try to isolate a universal chemical network which is able to predict the ionisation degree over the entire disc. Such a network would be far from the optimal one, but still more convenient from the computational point of view as it would preclude switching from one network to another in various disc domains, thereby saving significant amount of CPU time. To demonstrate the possibility of a unified approach to chemo-ionisation in a protoplanetary disc, I combine such a generalised network, which I named "SIREN" (SIngle REduced Network). Basically, this network consists of ions that dominate the fractional ionisation at various times and in various disc regions, and molecules which are directly related to these dominant ions. All the selected species are combined to a closed set of 60 gas-phase and 28 surface components, so that in total the SIREN network consists of 88 species involved in 966 reactions (Table 4.9).

The overall accuracy of the SIREN network at $t = 10^6$ years is about 10–100% almost in the entire disc except for the inner part of the intermediate layer, $R < 10$ AU. The neglect of the sulphur chemistry in the SIREN network causes an order of magnitude error in the intermediate layer at $10^4 < t < 10^6$ years, when this chemistry is important as described in Section 4.3.4.2.2. This reduced network provides a total computational time speed gain of about a factor of 50.

4.4   Column densities

A useful product of this study is the complete chemical structure of the disc. Therefore, it would be instructive to compare the study with results of similar investigations. I present the calculated column densities of some species along with observed values and column densities obtained by other groups (Table 4.10) in Table 4.11. The observed values are taken from Aikawa et al. (2002, Table 1).

Table 4.10. Chemical models of protoplanetary discs

Study	Disc model	Gas-phase reactions	Gas-grain reactions	Surface reactions	Cosmic rays	UV radiation	X-rays	S
WL00	CG97	UMIST 95	Yes	Yes	Yes	Yes	No	1
AH99,01	MMSN	NSM	Yes	No	Yes	Yes	Yes	0.03
Aea02, vZea03	DAea01	NSM	Yes	No	Yes	Yes	No	1

References.— (WL00) Willacy & Langer 2000; (CG97) Chiang & Goldreich 1997; (AH99,01) Aikawa & Herbst 1999,2001; (Aea02) Aikawa et al. 2002; (DAea01) D'Alessio et al. 2001; (vZea03) van Zadelhoff et al. 2003

Five theoretical models of the chemical evolution of a protoplanetary disc are considered. The main differences between them are listed in Table 4.10 and discussed below.

Willacy and Langer (2000) used the gas-phase UMIST 95 database, supplied with an additional set of gas-grain processes and surface reactions. They adopted an extrapolated flared T Tau disc model of Chiang and Goldreich (1997), taking into account cosmic rays and stellar UV radiation and assuming a sticking probability $S = 1$. In all the other models, namely, in Aikawa and Herbst (1999b, 2001), Aikawa et al. (2002), and van Zadelhoff et al. (2003), the New Standard Model (NSM) with a set of gas-grain interaction processes is used as the chemical network.

Aikawa and Herbst (1999b, 2001) considered an extrapolated minimum-mass solar nebula model of Hayashi (1981), taking into account stellar X-ray radiation in addition to the UV radiation and cosmic rays and assuming an artificially low sticking probability $S = 0.03$ that compensates for the absence of non-thermal desorption mechanisms. The flared T Tau disc model of D'Alessio et al. (2001) for various accretion rates is used with a sticking probability $S = 1.0$ in Aikawa et al. (2002) and van Zadelhoff et al. (2003). Stellar X-rays are not included in the latter two models.

Column densities of selected species presented in these papers are compared to those computed in this work in Table 4.11. Whenever possible, I took values from tables, otherwise figures were used. In this paper, a disc model with an accretion rate of $10^{-7}\ M_\odot\ \mathrm{yr}^{-1}$ is used, but in Table 4.11 I also present results of time-dependent chemical models for a lower accretion rate, $\dot{M} = 10^{-9}\ M_\odot\ \mathrm{yr}^{-1}$.

To characterise differences between model predictions, I divide all species in three groups by the maximum ratio of their theoretical predicted column densities among the different model (less than 20, less than 200, and the rest). Given the wide variety of conditions and assumptions made in the various models, it is natural to expect that differences in calculated column densities should be significant. However, column densities for many species are close to each other in the different studies. For example, the scatter in HCN column densities does not exceed an order of magnitude. Similarly, ammonia densities in all but one case are a few times $10^{13}\ \mathrm{cm}^{-2}$. Note that I omitted the anomalously high NH_3 column density computed by Aikawa and Herbst (1999b) as this was based on an unrealistic rate for the $H_3^+ + N$ reaction (Aikawa and Herbst, 2001).

Somewhat higher maximum-to-minimum ratios for species in the second group are mainly caused by their low abundances in the Willacy and Langer (2000) model. In the last column of Table 4.11 I give relative variations of their column densities both with and without (in parentheses) Willacy

Table 4.11. The observed and calculated column densities (cm^{-2}) for $r = 370$ AU at $t = 1$ Myr

Species	I	II	III	IV	V	This paper $\dot{M}, M_\odot\,\mathrm{yr}^{-1}$ 10^{-9}	10^{-7}	DM Tau (SD)	Observed LkCa15[a] (IM)	LkCa15[b] (SD)	Max. difference
H$_2$	9(22)	9(21)	1.5(24)	1.3(22)	1.3(23)	4.8(21)	1.4(24)	3.8(21)	...	...	...
H$_2$O	...	...	...	2.7(14)	8.0(13)	2.1(14)	1.6(14)	...	...	...	~ 3
HCN	2(12)	2(12)	2.1(12)	1.4(12)	2.5(12)	1.3(13)	6.7(12)	2.1(12)	$0.02-1.2(15)$	7.8(13)	~ 10
NH$_3$	...	1(13)	...	1.4(13)	...	4.4(13)	1.4(14)	...	...	...	~ 15
C$_2$H	2(12)	8(12)	6.2(12)	8.9(11)	2.0(13)	7.0(12)	1.1(13)	4.2(13)	...	...	$\sim 20\,(10)$
HNC	1(12)	...	2.0(12)	3.0(11)	...	6.9(12)	8.0(12)	9.1(11)	$< 5.4(12)$	...	$\sim 30\,(8)$
CN	1(13)	1(13)	3.8(12)	5.3(11)	3.0(13)	6.4(12)	4.6(12)	$9.5-12(12)$	$9.1-25(13)$	6.3(14)	$\sim 60\,(8)$
N$_2$H$^+$	...	...	1.9(12)	8.1(11)	...	6.0(12)	8.1(13)	$< 7.6(11)$	$< 5.7(12)$	$< 5.9(13)$	$\sim 100\,(40)$
HCO$^+$	3(11)	5(11)	9.0(12)	8.8(10)	9.0(12)	8.4(11)	2.0(11)	$4.6-28(11)$	1.5(13)	1.4(13)	$\sim 100\,(45)$
CS	3(11)	1(12)	4.9(11)	1.0(11)	1.2(12)	5.6(12)	1.1(13)	$6.5-13(11)$	$1.9-2.1(13)$	2.2(14)	$\sim 110\,(35)$
CO	2(15)	8(15)	1.1(18)	7.1(16)	1.2(18)	1.6(16)	2.5(16)	5.7(16)	1.6(18)	9.0(17)	~ 600
H$_2$CO	7(11)	1(12)	2.9(12)	8.7(10)	...	8.0(13)	8.3(13)	$7.6-19(11)$	...	$3.0-22(13)$	$\sim 10^3$
CH$_3$OH	...	...	6.4(08)	7.7(11)	...	4.0(10)	2.9(10)	...	$7.3-18(14)$	$< 9.4(14)$	$< 10^3$

References. — (I) Aikawa & Herbst 1999, Fig. 7, $R = 400$ AU, $t = 9.5 \cdot 10^5$ yrs, high ζ case; (II) Aikawa & Herbst 2001, Fig. 6, $R = 400$ AU, $t = 9.5 \cdot 10^5$ yrs; (III) Aikawa et al. 2002, Table 1, $\dot{M} = 10^{-7}\, M_\odot\,\mathrm{yr}^{-1}$, $R = 370$ AU, $t = 9.5 \cdot 10^5$ yrs; (IV) Willacy & Langer 2000, Table 4, interpolated to $R = 400$ AU, $t = 10^6$ yrs; (V) van Zadelhoff et al. 2003, Fig. 5, $R = 400$ AU; (IM) Interferometric observations, beam size is $\sim 4''$; (SD) single-dish observations, beam size is $\sim 20''$; (a) do not necessarily correspond to $r = 370$ AU; (b) disc size is ~ 100 AU

and Langer (2000) data. If the latter are not taken into account, the ratio of maximum to minimum column density does not exceed 50 for all these molecules. This similarity of column densities and a lack of correlation between them and the column density of molecular hydrogen can be understood as a further manifestation of the "warm molecular layer" (Aikawa et al., 2002) where nearly all gas-phase molecules are concentrated due to a "rich" chemistry. On the other hand, molecular hydrogen is concentrated in the midplane, where all other molecules are frozen out and thus do not contribute to column densities.

The reason why column densities in the calculations of Willacy & Langer are lower in comparison with other studies is probably related to the disc model they adopted. In the model of Chiang and Goldreich (1997) the disc is assumed to consist of only two layers, namely, the dark dense midplane and the less dense surface layer subject to harsh UV radiation. In the cold midplane molecules are mainly locked in icy mantles while in the surface layer they are easily dissociated or ionised by UV photons. In contrast to the disc model of D'Alessio et al. (2001), there is no region similar to the shielded intermediate ("warm molecular") layer, which is the most favourable disc domain for many molecules to have their maximum gas-phase concentrations.

The most striking fact are variations in theoretical CO column densities. As carbon monoxide has its highest abundance in the intermediate layer, one might expect that its abundance is relatively independent of the total gas column density. Thus, the origin of the large discrepancies in CO abundances should lie in physical differences between various models. Looking at Table 4.11, one is tempted to assume that the CO abundance is low in models with surface chemistry (this paper and Willacy and Langer, 2000) or in models with X-ray induced chemistry (this paper and Aikawa and Herbst, 1999b, 2001; van Zadelhoff et al., 2003). In the former case the CO molecule might be transformed to CO_2 and H_2CO, in the latter case it might be destroyed by abundant He^+.

To check, if this is the case, I computed the vertical distribution of CO for $R = 370$ AU without surface reactions and with $\zeta_X=0$. In both cases, I failed to reproduce the high CO column densities obtained by Aikawa et al. (2002) and van Zadelhoff et al. (2003). As I noted above, the low CO column density in the Willacy & Langer model can partly be caused by the disc model they adopted. A possible explanation for the low CO abundance in my model is the fact that I do not take into account self- and mutual-shielding of molecular hydrogen and carbon monoxide, contrary to Aikawa et al. (2002) and van Zadelhoff et al. (2003). Thus, the discrepancy in the computed CO abundance among all considered chemical disc models may be caused by the neglect of the CO shielding in some of these models.

In addition, I include in Table 4.11 observationally inferred column densities for DM Tau (single-dish measurements of Dutrey et al., 1997) and LkCa15 (interferometric data of Qi, C. 2000 and Thi et al. 2001). Note that DM Tau values correspond to column densities averaged over the entire disc (~ 800 AU), while values estimated from the LkCa15 single-dish observations are column densities averaged over a ~ 100 AU disc. For species in the first and second groups, there is a reasonable agreement between my predictions and observational data.

4.5 Discussion

Recent theoretical studies (e.g., Aikawa and Herbst, 1999b, 2001; Aikawa et al., 2002; van Zadelhoff et al., 2003) revealed that the distribution of gas-phase molecular abundances within a steady-state accretion disc in the absence of mixing processes has a three-layer vertical structure. In the dense and cold midplane all species, except the most volatile ones, are frozen out on grain surfaces while in the disc atmosphere (surface layer) they are easily destroyed by high-energy stellar radiation. Therefore, in these disc domains gas-phase abundances of polyatomic species are low. On the contrary, in the

intermediate layer, which is shielded from UV photons but not X-rays and thus still warm enough to allow effective desorption, most molecules remain in the gas phase and drive a complex chemistry resulting in a rich molecular composition. My study confirms such a chemical disc structure. It is a disc domain where most of (sub-) millimetre line emission comes from. As I noted above, this simple picture may not be appropriate when diffusion processes are taken into account (Ilgner et al., 2004).

In the present study I focused on the analysis of chemical processes relevant to the evolution of disc fractional ionisation based on the reduction approach. The size of a reduced chemical network, accurately reproducing electron concentration in a given disc region, can be understood as a quantitative criterion for the complexity of ionisation chemistry. In Figure 4.6 I show the distribution of the number of species in the reduced networks over the disc. This distribution follows a layered structure. In most parts of the disc the chemistry of ionisation is simple either due to the lack of ionising factors, low temperature, and high density (midplane) or due to the

Figure 4.6. The distribution of the number of species in the reduced networks governing fractional ionisation over the disc. The highest and smallest number of species is 115 and 5, respectively.

presence of ionising radiation (surface layer). In these regions, it is sufficient to keep about 10–30 species and few tens of reactions in reduced networks. Between the midplane and the surface layer the intermediate layer is located, where the evolution of ionisation degree is more complicated from the chemical point of view (especially at early times). Here, one has to retain more than fifty species and a comparable number of reactions in the reduced networks.

This layered structure is directly related to the size and location of the so-called "dead zone" within a protoplanetary disc, which is the region where the ionisation degree is so low that the magnetic field is not coupled to the gas. The MHD turbulence cannot develop in this region. Thus, the MRI is not operative, which means the lack of an effective angular momentum transport if no other transport mechanism can be identified. The "dead zone" in accretion discs has been widely investigated (e.g., Fromang et al., 2002; Igea and Glassgold, 1999; Sano et al., 2000).

An important quantity that characterises the coupling between the matter and magnetic field is the magnetic Reynolds number, which can be defined as (Fromang et al., 2002)

$$Re_M = \frac{c_s H}{\eta}, \tag{4.3}$$

where η is the Ohmic resistivity (Blaes and Balbus, 1994)

$$\eta = \frac{234 \cdot T^{0.5}}{x_e}. \tag{4.4}$$

The other quantities are the sound speed c_s, and the thickness of the disc H. The MHD turbulence can be maintained only if this quantity exceeds a certain critical value that depends on the field geometry and other factors. Following Fromang et al., I consider two cases of this limiting value, namely, $Re_M^{crit} = 100$ and $Re_M^{crit} = 1$ and define the "dead zone" as a disc domain where $Re_M < Re_M^{crit}$.

The calculated magnetic Reynolds numbers for the adopted model are shown in Fig. 4.7. The lowest magnetic Reynolds number is $Re_M \sim 10$, which implies that under certain circumstances within the framework of my model the "dead zone" is entirely absent. With another critical value, $Re_M^{crit} = 100$, the "dead zone" occupies the following disc region: 2 AU $< r <$ 20 AU, $z \sim 0.06 \cdot r^{1.27}$
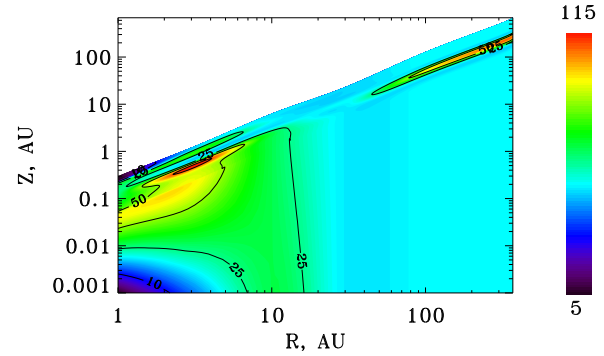
(solid line). This result is roughly consistent with other recent studies. For example, Fromang et al. found that the "dead zone" can extend over 0.7 AU $< r <$ 100 AU, if the viscosity parameter is equal to 10^{-2} and the accretion rate is $10^{-7} M_\odot$ yr^{-1}, whereas Igea and Glassgold (1999) obtained a "dead zone" of somewhat smaller size, $r < 5$ AU.

Apart from defining the location of the "dead zone" in accretion discs, the fractional ionisation determines whether non-ideal MHD equations have to be used to describe the evolution of protoplanetary discs. When the electron abundance is computed for the solution of non-ideal MHD equations, an ionisation equilibrium is often assumed. An expression similar to Eq. (4.2) is then used to calculate the equilibrium fractional ionisation, with different estimates for the gas-phase recombination coefficient β (e.g., Blaes and Balbus, 1994; Fleming and Stone, 2003; Fromang et al., 2002; Gammie, 1996; Regos, 1997; Reyes-Ruiz, 2001).

Figure 4.7. The magnetic Reynolds numbers computed for the adopted disc model and an evolutionary time of 1 Myr. The solid line designates $Re_M^{crit} = 100$. The highest and lowest values are equal to about 10^{13} and 10, respectively.

In Fig. 4.8 I compare the fractional ionisation x_e(eq), computed from Eq. (4.2) with the often used expression for the recombination coefficient $\beta = 8.7 \cdot 10^{-6} T^{-1/2}$ (Glassgold et al., 1986), to the fractional ionisation computed with the full chemical network x_e(full), for some representative points in the midplane and in the intermediate layer. It is not surprising that the ratio of these two quantities exceeds 10 at low ionisation degrees. Here the electron density is small and ion-grain interactions should be taken into account. At moderate ionisation degrees ($10^{-10} - 10^{-8}$), the equilibrium value may differ from the "exact" value by a factor of a few at the end of the computation. At earlier times, the discrepancy is higher.

However, in the midplane the equilibrium state is reached rapidly, with no appreciable changes in x_e after ~ 1000 years of evolution. If one is not interested in time scales less than 1000 years and can afford a factor of a few uncertainty in the fractional ionisation, deep in the disc interior the equilibrium x_e is sufficient, provided grain charging processes are taken into account.

The intermediate layer shows a different behaviour. As I mentioned previously, the equilibrium state is not reached there or is reached very lately. The initial decrease of x_e, caused by HCO$^+$, H$_3^+$, and metal ion recombination, is followed by a step-like increase. Duration of each phase and overall evolution of x_e (see, e.g., Figure 4.3) vary significantly in different parts of the intermediate layer. Surprisingly, the equilibrium x_e from Eq. (4.2) is close to the computed fractional ionisation at $t = 1$ Myr in this point ($1.5 \cdot 10^{-9}$ and $2 \cdot 10^{-9}$, respectively). This is, of course, a mere coincidence, as the equilibrium is not reached there. I emphasise that even if x_e(full) is equilibrated eventually in the intermediate layer and is close to x_e(eq), the latter value does not reflect the ionisation state of the medium for most of the computational time.

In the surface layer not only X-rays control the fractional ionisation, but also UV-radiation. The equation (4.2) is still applicable here but with an important change. In the surface layer x_e is determined mostly by ionised carbon (Table 4.1). Its recombination coefficient is much lower than the value quoted above, thus, $\beta = 8.7 \cdot 10^{-6} T^{-1/2}$ should not be used in this case. If one substitutes in Eq. (4.2) the correct β for C$^+$ ($1.4 \cdot 10^{-13} T^{-0.61}$), the resultant equilibrium x_e is a few times smaller than the "exact" value, mainly because photoionisation is not taken into account. Time, needed to reach the equilibrium x_e in the surface layer does not exceed 100 years.
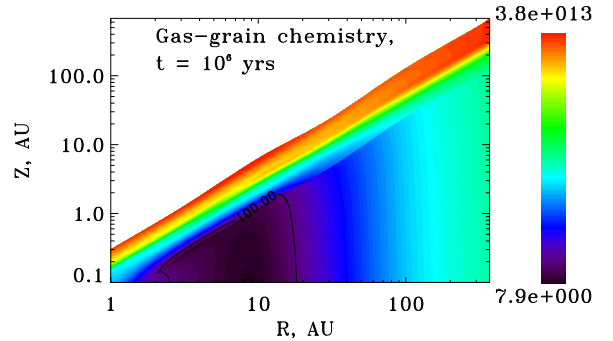
Overall, I conclude that the equilibrium approach is appropriate most of the time and in most parts of the studied disc, but it should be applied with care. This is especially important in less dense discs which are more transparent to X-rays and UV radiation (e.g., debris-discs). In this paper, I used a relatively massive disc model with a narrow intermediate layer. In models with lower accretion rates, the intermediate layer would occupy a greater volume of the disc.

Although the reduced networks presented in this paper provide much better accuracy than the equilibrium approach, while having modest sizes, their usefulness in this respect is limited by the fact that they are computed in the steady-state disc. To make the reduction the real value one needs to consider it in a dynamically evolving medium.

4.6 Summary and conclusions
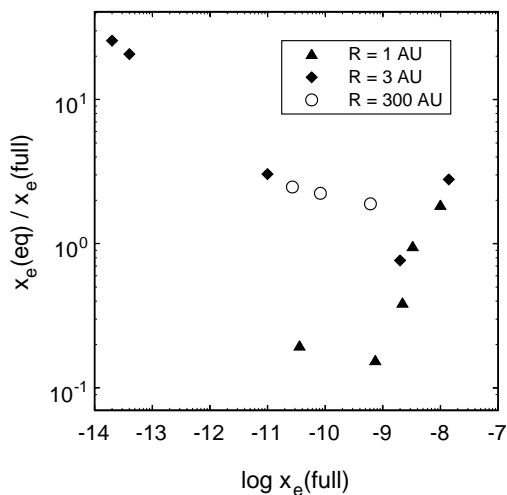
Figure 4.8. Comparison of the equilibrium and time-dependent fractional ionisations at $t = 1$ Myr in the midplane and in the intermediate layer. Symbols correspond to different radii.

In this chapter chemical processes, responsible for the ionisation structure of a protoplanetary disc with a central star, are analysed by means of reduced networks that reproduce the ionisation fraction within a factor of 2 during 10^6 years of evolution. Because of the wide range of physical conditions met in a typical disc, there is a corresponding diversity in the chemical reactions that control the fractional ionisation in different parts of the disc. Generally, it can be divided into three layers. In the midplane the ionisation is provided by cosmic rays and radioactive elements only. Above the midplane, the intermediate layer is located where the ionisation is dominated by X-rays. In the surface layer UV photons are the main ionising factor. In each of these layers, I analyse several representative points and construct reduced chemical networks that are needed to reproduce the time-dependent fractional ionisation. In the midplane, the relevant chemistry is simple. Reduced networks typically include no more than 10 species and a similar number of reactions. The same holds true for the surface layer. The intermediate layer is the most complicated region from the chemical point of view. To compute the fractional ionisation with the targeted accuracy, in some regions one has to take into account carbon chains containing up to 6 carbon atoms and a handful of relevant surface reactions, which leads to reduced networks with over hundred species and reactions. It is demonstrated that the equilibrium approach to compute the disc fractional ionisation is appropriate most of the time in most parts of the studied disc. Also, it is found that the neglect of the shielding processes in the disc chemical modelling may lead to significant errors in the calculated CO abundances.

Chapter 5

Millimetre observations and modelling of AB Aur

(Based on the article by Semenov, Pavlyuchenkov, Schreyer, Henning, Dullemond, and Bacmann 2004, submitted to *ApJ*)

5.1   Why AB Aur?

The aim of the present chapter is to develop the first comprehensive model of the physical, chemical, and dynamical properties of circumstellar material around an intermediate-mass and young (Herbig Ae/Be, Herbig, 1960) star using available observational data. Why is this particular class of stars so interesting?

The Herbig Ae/Be stars are more massive ($M_* \sim 2$–$10 M_\odot$) and thereby hotter ($T \gtrsim 8\,000$ K) analogues of young solar-type stars in their pre-main-sequence phase, $t \lesssim 5$ Myr (Perez and Grady, 1997). Originally, this class of stars has been selected by the following observational criteria: an A or B star ($T \sim 10\,000$–$30\,000$ K) located in a star-forming region (like Taurus or Auriga), which shows the Balmer series of hydrogen in emission and is associated with a reflection nebulosity (Herbig, 1960). Later, this working definition has been extended by The et al. (1994), who have included in their sample of Herbig stars also cooler F-type stars, apparently isolated objects, and stars without the Balmer emission.

With the advent of infrared telescopes, it has been found that the Herbig Ae/Be stars emit IR radiation in excess over the photospheric level, which can be attributed to the reprocessing of stellar radiation by nearby circumstellar dust grains (e.g., Hillenbrand et al., 1992). The spectroscopic observations with the *Infrared Space Observatory* have unravelled that the composition and sizes of solids widely vary among the Herbig Ae/Be systems, from the ISM-like small grains made of amorphous silicates (and coated by ices in cold regions), to larger μm-sized grains, or even thermally processed crystalline silicates similar to the cometary dust (see, e.g., Bouwman et al., 2001; Crovisier et al., 1997; Meeus et al., 2001). This seems to be a strong indication that the process of grain growth accompanied by chemical and topological restructuring may have taking place in some of these objects.

Meeus et al. (2001) have introduced a classification for the Herbig Ae/Be stars based on the spectral shape of the infrared region of their SED. The group I sources show an almost flat SED in the mid-infrared and their continuum can be reconstructed by a combination of a power-law and a black body. The group II sources have a strong decline of the SED towards the far-infrared and require only a power-law contribution to reproduce the continuum. As it has been demonstrated by Dullemond and Dominik (2004), the group I vs. II distinction can be understood as arising from flaring (highly optically thick) vs. self-shadowed (moderately optically thick) discs. They have proposed that the protoplanetary disc starts to evolve with the flaring shape, and later becomes the self-shadowed due to the grain growth.

The dusty environments of the Herbig Ae/Be stars have been investigated at large scales ($\gtrsim$ 1 000 AU) by continuum observations at millimetre wavelengths with single-dish antennas (e.g., Henning et al., 1998). These observations have provided a wealth of information about morphology, column densities and masses of the outer regions of the Herbig systems. The millimetre continuum observations with interferometers allowed to study the dust distributions in inner ($\sim$ 100–500 AU) regions of the Herbig Ae/Be systems (e.g., Di Francesco et al., 1997; Thi et al., 2001).

However, the presence of rotating discs around the Herbig stars has been unambiguously demonstrated by (sub-) millimetre interferometric observations in molecular lines (e.g., Mannings and Sargent, 1997; Piétu et al., 2003). Thus, the Herbig Ae/Be systems belong to the Class II objects, according to the classification of Lada (1999). Also, the observations in molecular lines both with interferometers (e.g., Pietu et al., 2005; Thi et al., 2001) and single-dish radiotelescopes (e.g., Fuente et al., 2002) have been used to study the chemical composition and kinematics of the gas in the Herbig Ae/Be systems.

It is believed that the Herbig Ae stars are precursors of older (Class III, $t \sim$ 10–100 Myr) main-sequence β-Pictoris and Vega-type stars that are surrounded by debris discs with trace amounts of dust ($M_{\mathrm{dust}} \sim 1 M_{\mathrm{earth}}$) and gas ($\lesssim$ 0.1–1 times the dust mass), and possibly harbour planets or planetary-sized bodies (for a review, see Waters and Waelkens, 1998). Therefore, it is of a crucial importance to investigate the properties of the Herbig Ae/Be systems in detail in order to catch the process of planet formation at work. Inevitable, it will shed light on the origin of and initial conditions in our own Solar system and other stellar systems during the first few million years of the evolution, with a particular emphasis to infer any differences and similarities between their evolutionary scenarios.

I focus on AB Aur, which is one of the nearest and best-studied object among the entire class of Herbig Ae stars. The AB Aur system consists of a pre-main-sequence star with spectral type A0Ve+sh (mass $M_* \sim 2.4 M_\odot$, radius $R_* \approx 2.5 R_\odot$, The et al., 1994) located at a distance of $\approx$ 145 pc (van den Ancker et al., 1998, 1997), which is surrounded by a rotating circumstellar disc with radius of about 450 AU (Mannings and Sargent, 1997) and an extended ($r >$ 1 000 AU) envelope (Grady et al., 1999; Nakajima and Golimowski, 1995; Roberge et al., 2001). The age of AB Aur can be roughly estimated by using evolutionary track modelling, giving a value of $t \approx$ 2–5 Myr (DeWarf et al., 2003; Thi et al., 2001).

One of the long-standing mysteries that is related to this object is the value of its inclination angle. Mannings and Sargent (1997) have spatially resolved a disc-like configuration around AB Aur using OVRO (*Owens Valley Radio Observatory*) aperture-synthesis imaging in the ^{13}CO(1-0) line. From the aspect ratio of the disc major and marginally resolved minor semiaxes, $\sim$ 110 AU/450 AU, they have derived a disc inclination angle $\iota \approx 76°$ (almost "edge-on" orientation), which is in close agreement with mid-infrared (MIR) observations of Marsh et al. (1995). However, near-infrared (NIR) interferometric observations by Millan-Gabet et al. (2001, 1999) have revealed that the AB Aur system looks nearly spherically-symmetric at $\sim$ 1 AU scale, implying that the inclination angle is close to 0° ("face-on"). This is in agreement with a value of $\iota <$ 45° deduced from scattered-light *Hubble Space Telescope* (HST) coronographic imaging by Grady et al. (1999) and $\iota \in [27°, 35°]$ estimated by Eisner et al. (2003) using NIR measurements with the *Palomar Testbed Interferometer* (PTI). Recently, using coronographic NIR-imaging with the *Subaru* telescope, Fukagawa et al. (2004) have found an inclination $\iota = 30 \pm 5°$. Moreover, Miroshnichenko et al. (1999) have obtained $\iota = 80°$ in the concept of their best-fit "disc-in-envelope" model to the observed spectral energy distribution (SED). A similar value of 65° has been used by Dominik et al. (2003), who have successfully fitted the AB Aur SED by a flared disc model with a puffed up inner rim. Obviously, there is a general disagreement regarding the disc orientation observed with IR- and mm-interferometers or derived from the SED modelling, though more recent studies point to a face-on configuration. A combination

of high-quality observational data and appropriate theoretical modelling would allow to determine precisely, among many other parameters, the orientation of the AB Aur system.

In this chapter, I report on the results of the observations at millimetre wavelengths and modelling of the AB Aur system. The object was observed by K. Schreyer (AIU Jena) at low resolution ($\sim 10''-30''$) using the IRAM 30-m antenna between 2000 and 2001 and at a higher $\approx 5''$ resolution in the HCO$^+$(1-0) line with the IRAM *Plateau de Bure Interferometer* (PdBI) in 2002. About a dozen rotational transitions of CO, C^{18}O, CS, HCN, HNC, HCO$^+$, DCO$^+$, SiO, and H$_2$CO were detected with the IRAM 30-m telescope. These single-dish and interferometric data as well as supplementary data from the literature form the observational basis for this study.

First, I simulate the time-dependent chemical evolution of the AB Aur system using a gas-grain chemical network and assuming a two-component model of a flared passive accretion disc enshrouded in a diffuse spherical envelope. Second, I apply a 2D non-LTE line radiative transfer code to translate the calculated molecular abundances of CS, CO, and HCO$^+$ to the corresponding synthetic beam-convolved single-dish and interferometric spectra. Next, I compare the observed and synthesised emission lines in a systematic way in order to determine the model parameters. Iterating these three stages of the modelling, I find the best-fit model of the AB Aur disc and envelope and estimate uncertainties of the parameters.

My primary intention is to verify the strength of such an advanced theoretical approach to account for various observed interferometric and single-dish molecular spectra *simultaneously*. As a by-product of this study, many important parameters describing the physical, chemical, and dynamical structure of the AB Aur system can be constrained *independently* from other investigations performed so far.

This chapter is organised as follows. In Section 5.2 I describe results of the single-dish and interferometric millimetre observations of AB Aur performed with the PdBI array and IRAM 30-m antenna. The relevant physical and chemical models of the disc and envelope are presented and discussed in Section 5.3. I briefly outline the algorithm and limitations of the 2D line radiative transfer code "URAN(IA)" and calculate excitation temperatures of several rotational transitions of the CS, CO, and HCO$^+$ molecules in Section 5.4. Using the best-fit model of the AB Aur system, the corresponding interferometric map of the HCO$^+$(1-0) emission and single-dish CO(2-1), HCO$^+$(1-0), HCO$^+$(3-2), C^{18}O(2-1), and CS(2-1) spectra are synthesised and compared with the observed spectra in Section 5.5. In this Section, I also discuss how parameters of the best-fit model and their uncertainties are constrained, and what the evolutionary status of the AB Aur system is. A summary and conclusions follow.

5.2 Observations of AB Aur

5.2.1 IRAM 30-m data

The observations of AB Aur with the IRAM 30-m dish were performed by K. Schreyer (AIU Jena) during two runs in September 2000 and October 2001. Details of these observations are reported elsewhere (see Semenov et al., 2005).

All single-dish detections are compiled in Table 5.1. In total, nine different molecular species were detected: CO, C^{18}O, CS, HCO$^+$, DCO$^+$, H$_2$CO, HCN, HNC, and SiO. The observed intensities (mJy) were converted to the antenna temperatures (Kelvin) and afterwards to the main beam temperatures: $T_{\rm mb} = T_{\rm A}^*/\eta_{\rm mb}$. The beam efficiency values, $\eta_{\rm mb}$, were taken from the IRAM Newsletter, N. 18, 1994 (see also Table 5.1, Col. 10). In addition, the following spectral lines were only marginally detected (with $\lesssim 2$ sigma): CN(J=3/2-1/2, F=5/2-3/2), H$_2$CO($J_{\rm K_p,K_o}$=2$_{1,2}$-1$_{1,1}$), and H$_2$CO($J_{\rm K_p,K_o}$=3$_{0,3}$-
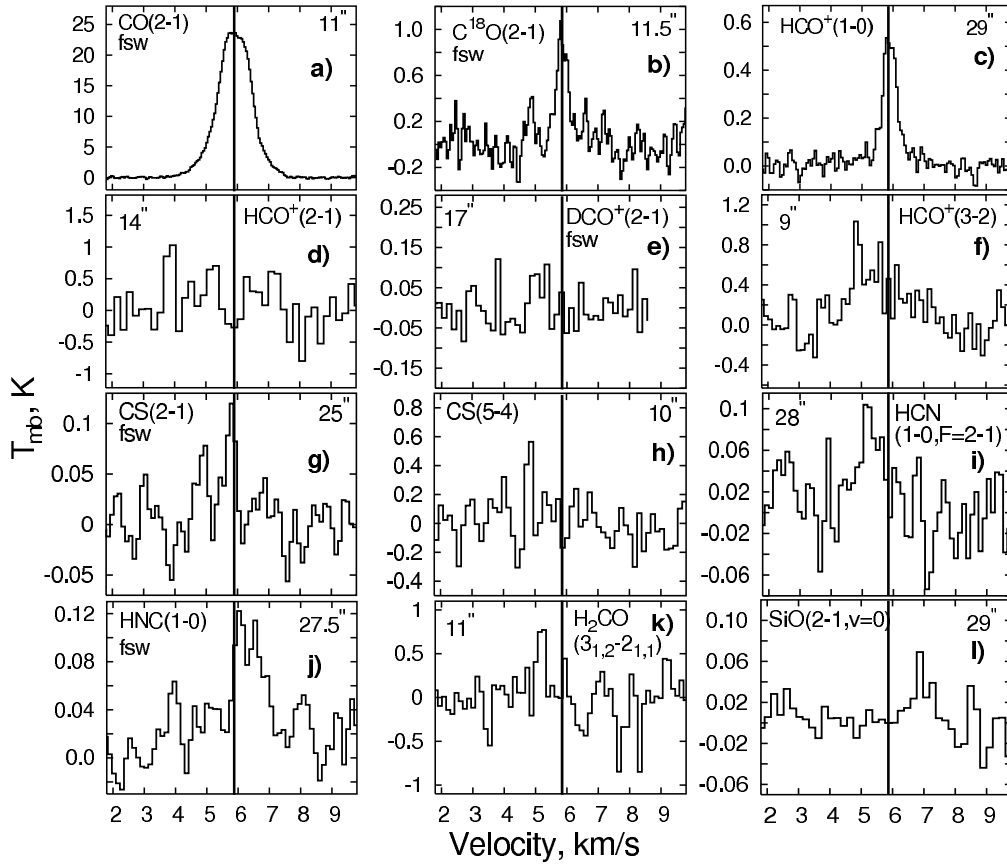
Figure 5.1. Single-dish emission lines observed toward AB Aur with the IRAM 30-m antenna. From the upper left to lower right panel (**a – l**) the following lines are shown: CO(2-1), $C^{18}O$(2-1), HCO^+(1-0), HCO^+(2-1), DCO^+(2-1), HCO^+(3-2), CS(2-1), CS(5-4), HCN(1-0, F=2-1), HNC(1-0), $H_2CO(3_{1,2}-2_{1,1})$, and SiO(2-1, v =0). The intensity values are given in units of the main beam temperature (Kelvin). On every spectrum the corresponding IRAM beam size is indicated in arcseconds. I marked by the shorthand "**fsw**" those measurements that have been done with the 5 MHz frequency shift, otherwise the $240''$ beam wobbling observational mode has been used. The value of the system velocity V_{lsr} = 5.85 km s^{-1} is depicted in each panel by thick vertical line.

$2_{0,2}$). Other observationally interesting lines, like $HC_3N(J$=10-9), $N_2H^+(J$=1-0), $C_2H(J$=3/2-1/2), $CH_3OH(J_{K_p,K_o}$=$2_{1,1}$-$1_{1,0}$), and $CH_3CN(J$=5-4, K=0) were not detected at all.

Spectra of firmly detected lines are shown in Fig. 5.1. As can be clearly seen, they basically exhibit three different types of line profiles. The CO(2-1), $C^{18}O$(2-1), HCO^+(1-0), and CS(2-1) lines are single-peaked, centred at the system velocity (V_{lsr} = 5.85 ± 0.1 km s^{-1}), and narrow, < 1 km s^{-1} (except for CO(2-1) which is broader than 2 km s^{-1}). In contrast, the HCN(1-0, F=2-1) and HNC(1-0) line profiles are slightly broader and apparently have a more complicated asymmetric structure. Furthermore, HCO^+(2-1), HCO^+(3-2), DCO^+(2-1), CS(5-4), and $H_2CO(3_{1,2}-2_{1,1})$ spectra show a narrow single-peaked shape and a blueshift up to $\Delta V \approx -2$ km s^{-1} from the system velocity, whereas SiO(2-1, v =0) has a $\sim$ 1 km s^{-1} redshift.

The reason for such diversity in the observed line profiles is not completely understood. I suppose that the blueshifted single lines could be broad double-peaked asymmetric spectra, with their less intense redshifted wings being lost in the noise. As I show below, all these lines but CO(2-1) are optically thin and their double-peaked appearance would imply that they trace mainly the rotating AB Aur disc but not much of the quiescent envelope material. The asymmetry of these line profiles

Table 5.1. Parameters of the detected single-dish emission lines

Molecule	Transition (J=)	ν (MHz)	T_{mb} (K)	rms (K)	ΔV_{obs} (km s^{-1})	V_{lsr} (km s^{-1})	$\int T_{mb}dv$ (K km s^{-1})	D_v (km s^{-1})	η_{beam}	Beamsize ($''$)
CO	2 – 1[a]	230538.0	25.2	0.176	1.2	5.9	32.5	0.051	0.53	10.8
C^{18}O	2 – 1[a]	219560.3	0.84	0.135	0.4	5.9	0.33	0.053	0.55	11.4
CS	2 – 1[a]	97981.0	0.116	0.030	0.4	5.8	0.045	0.120	0.76	25.2
	5 – 4[a]	244935.1	0.44	0.158	0.20	4.8	0.136	0.048	0.5	10.0
	5 – 4	244935.1	0.73	0.190	0.17	4.7	0.136	0.048	0.5	10.05
HCO$^+$	1 – 0	89188.5	0.54	0.029	0.54	5.9	0.310	0.066	0.78	29.0
	2 – 1[b]	178375.0	1.41	0.417	0.27	3.7	0.404	0.066	0.65	14.0
	3 – 2[b]	267557.6	1.16	0.269	0.26	4.8	0.315	0.044	0.45	9.3
DCO$^+$	2 – 1[a]	144077.3	0.22	0.077	0.17	5.6	0.040	0.081	0.69	17.1
	2 – 1[c]	144077.3	−1.13	0.033	0.17	6.2	−0.024	0.081	0.69	17.1
HCN	1 – 0, F= 0 – 1	88633.9	0.117	0.025	0.65	9.9	0.080	0.132	0.78	28.2
	1 – 0, F= 2 – 1	88631.8	0.201	0.025	0.77	5.1	0.165	0.132	0.78	28.2
HNC	1 – 0[a]	90663.6	0.113	0.020	1.29	6.3	0.155	0.129	0.77	27.6
SiO	2 – 1, v= 0	86847.0	0.091	0.027	0.19	7.0	0.019	0.067	0.78	29.0
H$_2$CO	$K_p, K_o = 2_{1,2} - 1_{1,1}$	140839.5	0.234	0.089	0.25	6.0	0.063	0.083	0.70	17.5
	$K_p, K_o = 3_{1,2} - 2_{1,1}$	225697.8	0.899	0.232	0.27	5.2	0.264	0.133	0.54	11.0

Note. — The Col. (2) lists observed transitions at the rest frequencies from Col. (3). The intensities, noise, and FWHMs of detected lines are presented in Col. (4)–(6), while in Col. (7) the line velocity shifts are specified. The corresponding integrated intensities and achieved spectral resolutions are listed in Col. (8) and Col. (9). Finally, in Col. (10)–(11) the beam efficiencies and sizes are given.

[a]Frequency switching measurements,

[b]Fit is made to the strongest line of a double-peak profile,

[c]Signal is negative due to subtraction of the strong DCO$^+$(2-1) signal arising in the outer cold envelope region from the weaker emission that originates in the inner warm (and thus less deuterated) part of the AB Aur envelope.

can be explained by the misalignment of the emission centre and centre of the IRAM 30-m antenna during the measurements due to the pointing errors, or/and because of the global inhomogeneity of the AB Aur disc (the latter fact was recently established by the Pietu et al., 2005). This idea is partly confirmed by the fact that some of these spectra, like HCO^+(3-2) and CS(5-4), require high densities for the excitation and were measured with small beam sizes of about $10''$ (which is comparable with the $\sim 6''$ disc).

On the other hand, the IRAM beam for the HCO^+(1-0) and CS(2-1) lines is $\gtrsim 25''$, a few times larger than the apparent disc size, and due to a significant beam dilution in this case, both emission lines come from the extended envelope around AB Aur. This suggestion is further supported by the narrow $\sim 1 \text{ km s}^{-1}$ width and central position of these emission lines, typical of cool and quiet gas. This is also certainly true for the CO(2-1) and $C^{18}O$(2-1) lines, though the broad width of the former spectrum indicates that the CO(2-1) emission is contaminated by moving gas along the line of sight to AB Aur.
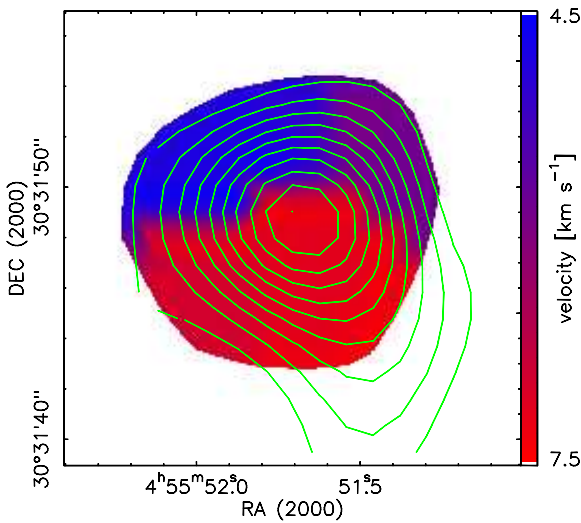
Figure 5.2. Smoothed velocity map (in km s^{-1}) of the AB Aur system observed with the Plateau de Bure interferometer in the HCO^+(1-0) transition at $\sim$ 89 GHz. The distribution of the integrated line intensity within this $\sim 10''$ object is represented by contour lines. The levels are equidistant with 0.05 K km s^{-1} intensity steps. The "butterfly" ("blue-red") symmetric appearance of the map is characteristic of a globally rotating disc-like configuration that is observed close to face-on ($\iota \sim 0°$). The border between these two lobes corresponds to the projection of the disc rotational axis on the sky plane ($V = V_{\text{lsr}}$). It implies that the disc positional angle $\phi \sim 90°$.

There is strong evidence that a large gas reservoir is located within at least $\sim 8'$ around the central star, which is indirectly probed by the DCO^+-(2-1) measurements (see Table 5.1, footnote "c)"). The negative intensity of this line was detected only in the case of the $240''$ on-off observations, which can be easily explained. It is known that deuterium fractionation proceeds most efficiently in cold environments, $T \lesssim 70$ K, (e.g., Bacmann et al., 2003) but not in the inner (warm) parts of protoplanetary discs (see Aikawa and Herbst, 1999a). Consequently, the DCO^+(2-1) signal is stronger for the cold outer region of the envelope at a distance of $\sim 35\,000$ AU ($240''$ offset) than for the warm inner $\lesssim 2\,500$ AU part ($17''$ IRAM beam). Therefore, the measured intensity of this emission line became negative after the on-off subtraction of the strong background signal. Note that the HCN(1-0, F=2-1) single-peaked asymmetrical spectrum was observed with the same $240''$ beam wobbling technique and may suffer from a similar contamination.

It is worth to mention that an extended $\sim 35\,000$ AU region of thermal emission from cold dust grains around AB Aur has been observed by the *IRAS* satellite at 60μm[1] (Wheelock et al., 1991).

5.2.2 Plateau de Bure interferometric data

The AB Aur system was mapped in the HCO^+(1-0) line at 89.18 GHz with the PdBI in March 2002. The synthesised HPBW (Half Power Beam Width) size of the beam was $6.76'' \times 5.09''$ ($= 970 \text{ AU} \times 730 \text{ AU}$ at 144 pc) with a position angle of $94°$ because these observations were obtained with five 15-m antennas using the compact configuration CD (baselines of 20-80 meters). They are described in detail Semenov et al. (2005). As an example, in Fig. 5.2 I show the distribution of the

---

[1]The corresponding map can be found here: `http://skyview.gsfc.nasa.gov/cgi-bin/skvadvanced.pl`

HCO$^+$(1-0) intensity-weighted velocities within the AB Aur system overplotted by the integrated line intensity (contour lines). Though not well spatially resolved with the $\sim 6''$ beam, it appears as a nearly spherically symmetric $\sim 10''$ (1450 AU) structure with a peculiar "two-lobe" (blueshifted and redshifted) velocity pattern. This is a typical sign of a rotating disc-like configuration that is seen close to face-on (e.g., Mannings and Sargent, 1997; Simon et al., 2000). The lack of spatial resolution does not allow to determine the radius of this structure precisely, and only an upper limit can be put on this value, $R_{disc} \lesssim 800$ AU. The border between two velocity lobes (zero-velocity gradient, $V = V_{lsr}$) corresponds to the projection of the disc rotational axis on the plane of the sky. This implies that the disc positional angle is about 90°.

Whether the disc size and orientation are indeed close to these first-order observational estimates is verified by the modelling in the following sections.
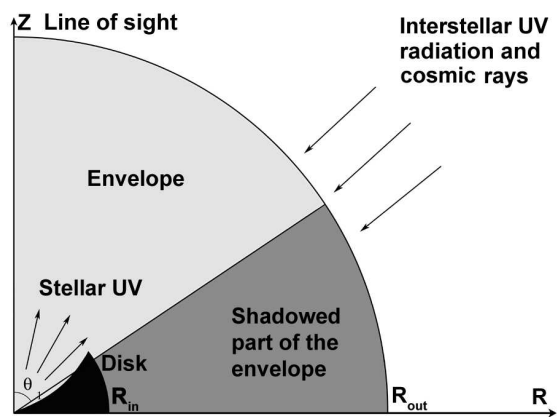
5.3 Model of the AB Aur system

In this section, I describe and discuss the physical model of the AB Aur system in detail. A schematic sketch of this object is presented in Fig. 5.3. It is assumed that the AB Aur system consists of a passive flaring rotating disc surrounded by an infalling spherical envelope. This dense protoplanetary disc shades off a torus-like region in the diffuse envelope from strong stellar UV flux, which allows many complex molecules to form and survive there. In contrast, the composition of the two unshielded envelope lobes is mainly atomic. Since the star directly heats these lobes, they have to be hotter; in a pure hydrostatic equilibrium it would also imply that they are less dense than the shadowed part of the envelope. Thus, an observationally significant amount of molecules is only reached during the chemical evolution of the AB Aur disc and the shielded part of the envelope.

Figure 5.3. A sketch of the AB Aur system. It consists of a passive flared disc (black) surrounded by a spherical envelope (grey). The envelope is divided in the torus-like region shadowed from the star by the disc (dark grey) and two unshielded lobes (light grey).

5.3.1 Disc model

The UV-to-mm surveys of Herbig Ae stars have unveiled that many of these stars are surrounded by circumstellar gas and dust distributed in flattened (disc-like) configurations (e.g., Natta et al., 2001). Indeed, the presence of a compact structure (0.5 AU $\lesssim r \lesssim 500$ AU) around AB Aur has been revealed from IR interferometric measurements (e.g., Eisner et al., 2003; Marsh et al., 1995; Millan-Gabet et al., 2001, 1999), at visual wavelengths by the photometric and polarimetric observations of Grinin and Rostopchina (1996), and from millimetre interferometric observations of Mannings and Sargent (1997). Moreover, the latter authors have reported on the Keplerian rotation of the gas in this object. All these facts indicate that a rotating protoplanetary disc encircles the AB Aur star. Given that the measured mass accretion rate on the central star is low, $\dot{M} \sim 10^{-8} M_\odot$ yr^{-1} (e.g., Grady et al., 1996), the vertical structure of the AB Aur disc is globally sustained by reprocessing stellar radiation (passive disc) but not due to viscous dissipation.

Some clues concerning the dust content of the AB Aur system can be gained from the analysis of

the SED. The emission bands of various dust materials have been detected in the IR spectra of AB Aur with the *Infrared Space Observatory* (ISO), most notably those of iron oxide, PAHs, amorphous silicates, and water ice (van den Ancker et al., 2000). The strong silicate emission band at $9.7\mu m$ points to the presence of a large amount of warm ($\sim$ 100–200 K) and small ($\lesssim 0.1$–$2\mu m$) amorphous silicate grains in this object. Together with the absence of crystalline silicate features in the spectra, it implies that the dust in AB Aur is thermally unprocessed and may still resemble pristine interstellar grains even after a few Myr of the evolution (e.g., Bouwman et al., 2001; Meeus et al., 2001) or the system is younger, $t \sim 2$ Myr (e.g., Pietu et al., 2005).

A large amount of warm dust and gas observed in the AB Aur system (e.g. Thi et al., 2001) cannot be accounted for without invoking a flared geometry of the disc or/and an additional disc heating by the surrounding envelope. The importance of the latter effect is discussed by Vinković et al. (2003). The idea that the disc is flaring is further supported by the results of the detailed modelling of Eisner et al. (2003) and Brittain et al. (2003), who have found that a flared disc model with a puffed up inner rim provides a suitable fit to their NIR and MIR observational data.

Unfortunately, the disc of AB Aur is detected with the PdBI array only in one line and at modest resolution. Thus it is not possible to unravel the disc thermal and density structure in both radial and vertical directions, using these observational data alone. On the other hand, many other parameters of the AB Aur system have been revealed from previous observations. They can be used to construct a physical disc model.

I adopt the passive flared disc model of Dullemond and Dominik (2004). This disc model is calculated using a 2D axisymmetric continuum radiative transfer code and silicate dust opacity data (Draine and Lee, 1984) under the assumption of hydrostatic equilibrium in vertical direction. The *a priori* fixed disc parameters are as follows.

I assume that the dust grains are uniform spheres with radius of $0.3\mu m$, though the additional case of larger $1\mu m$ particles is also considered. In the model, I focus only on a single-size grain distribution instead of a range of dust sizes because otherwise it would significantly slow down the chemical computations and 2D disc modelling, thus making prohibitive efficient fitting of the model parameters. The disc surface density as a function of radius obeys a power law, $\Sigma(r) = \Sigma_0(r/r_0)^p$, with the exponent $p = -5/2$ and the initial value Σ_0 to be constrained. Note that the adopted radial gradient p is somewhat steeper than the usually assumed value between about -2 and -1 (see, Miroshnichenko et al., 1999; Natta et al., 2001). Therefore, I consider two additional models with $p = -3/2$ (minimum-mass solar nebula) and $p = 0$ (uniform disc).

The disc has its inner boundary at 0.7 AU (dust sublimation radius, $T \sim 1\,500$K) and extends up to several 100 AU in radial direction, with its vertical height covering a comparable spatial scale. The ratio of the disc outer radius to the vertical height at which the star is still sufficiently obscured, $A_V \gtrsim 1^m$, is used to estimate what fraction of the entire AB Aur envelope is shadowed (see Fig. 5.3).

I adopt the following parameters of the central star: $T_{eff} = 10\,000$ K, $M_* = 2.4 M_\odot$, $R_* = 2.5 R_\odot$ (see Table 5.2). It is assumed that the disc is illuminated by the UV radiation from the star and by the interstellar (IS) UV radiation. The intensity of the stellar UV flux is calculated using the Kurucz (1993) ATLAS9 of stellar spectra, and utilised to calculate self-consistently the 2D disc physical structure (Dullemond and Dominik, 2004). This intensity is converted to the standard G factor, $G_* \approx 10^5 G$ at the distance of 100 AU, where $G = 1$ corresponds to the mean interstellar UV field of Draine (1978). The penetration of the stellar and interstellar UV radiation into the disc is computed by using 1D plane-parallel scheme presented in Section (3.1.2.1). To calculate the visual extinction by dust grains toward the central star at a given disc location, I use slightly modified expression Eq. (3.2):

$$A_V = \frac{N_H}{N_1(a)} \text{ mag,} \tag{5.1}$$
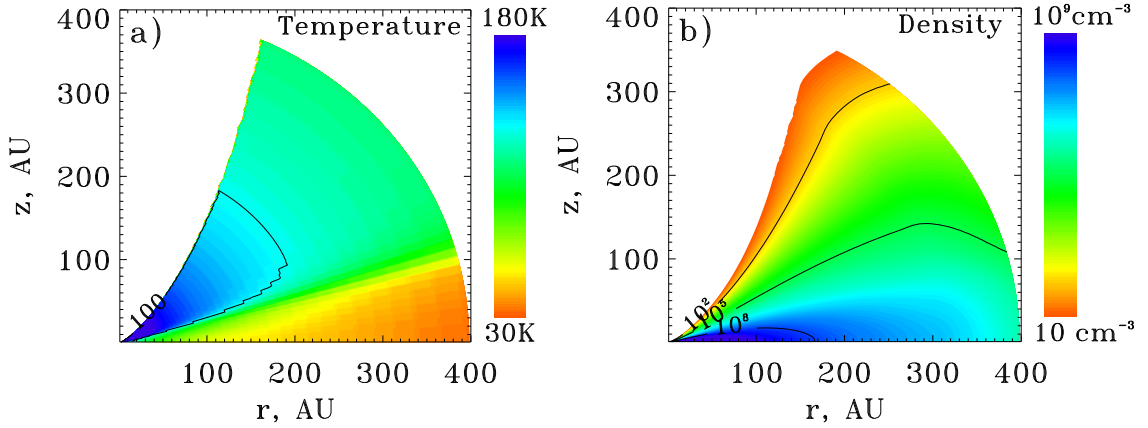
Figure 5.4. The thermal structure of the adopted disc model is shown in the left panel, where the solid curve represents the so-called "snowline" ($T = 100$ K). The relevant density distribution is presented in the right panel. There, three solid lines correspond to the disc regions with number densities of 10^2 cm^{-3}, 10^5 cm^{-3}, and 10^8 cm^{-3} (from the disc surface to midplane, respectively).

where N_H is the total column density of hydrogen nuclei between the point and the star and the column density to reach $A_V = 1$ mag is $N_1(a) = 8.36 \cdot 10^{20}$ cm^{-2} and $9.75 \cdot 10^{21}$ cm^{-2} for the grain radius $a = 0.3\mu$m and 1μm, respectively. The extinction of the interstellar UV radiation ($G = 1$) is computed in the same way but in vertical direction only. I calculate the penetration of cosmic rays (CR) into the disc by Eq. (3.5) in Section 3.1.2.2. Finally, ionisation due to the decay of short-living radionuclides is considered with a total rate $\zeta_{RN} = 6.1 \cdot 10^{-18}$ s^{-1} (Umebayashi and Nakano, 1981).

Overall, a wide range of relevant physical parameters characterises the disc model, namely, temperatures between 35 K and 1 500 K, densities between 10^{-21} g cm^{-3} and 10^{-9} g cm^{-3}, G factors $\gtrsim 10^3$, A_V between 0 and more than 100 mag, and ionisation rates between $\sim 10^{-19}$ s^{-1} and 10^{-17} s^{-1}. The disc thermal and density structure is shown in Fig. 5.4.

The parameters of the best-fit disc model are given in Table 5.3. In Section 5.5 I discuss how they and their uncertainties are derived.

5.3.2 Envelope model

The body of observational data about the extended nebulosity surrounding AB Aur allows to constrain some of its basic parameters prior to the detailed modelling.

The visual extinction observed toward the star is low, $A_V \sim 0.2$–0.5 mag (Fuente et al., 2002; Roberge et al., 2001; van den Ancker et al., 2000, 1997), and can be attributed to light scattering and absorption by dust grains in the nearby envelope and interstellar medium. Thus, the AB Aur envelope is diffuse and its average density has to be low.

The apparent size and morphology of the envelope depends on the spectral region at which observations are performed. For instance, an extended 8′ ($\approx 35\,000$ AU) cloud of cold dust has been observed with the IRAS satellite at 60μm, which is confirmed by the IRAM single-dish observations. At visual wavelengths, the spherically-symmetric envelope has been traced from $r \approx 1\,300$ AU to ~ 365 AU with the HST coronographic imaging by Grady et al. (1999), who have also found that it is highly inhomogeneous from hundreds AU down to tens of AU (spiral arches). They have mentioned that this symmetric (inner) envelope is further surrounded by a large band of the reflection nebulosity which has been detected with ground-based telescopes. An envelope of almost the same structure has been observed by Nakajima and Golimowski (1995) using the *John Hopkins University Corono-*

Table 5.2. Parameters of the central star

Parameter	Symbol	Value	Reference
Distance	r_*	144^{+23}_{-17} pc	1
Temperature	T_{eff}	$10\,000 \pm 500$K	2
Radius	R_*	$2.5 \pm 0.2 R_{\odot}$	3
Mass	M_*	$2.4 \pm 0.2 M_{\odot}$	2
UV flux at 100 AU	G_*	$1.5 \cdot 10^5$	4

References. — (1) van den Ancker et al. 1997; (2) van den Ancker et al. 1998; (3) van den Ancker et al. 2000; (4) This work

graph. They have put a lower limit on the mass of the reflection nebulosity using its visual brightness, $M_{\mathrm{refl}} \sim 2 \cdot 10^{-7} M_{\odot}$ (this seems to be a strong underestimation). Di Francesco et al. (1998) have not resolved the AB Aur envelope with the *Kuiper Airborne Observatory* at 50μm and 100μm and gave an upper limit to its size, $r \lesssim 5\,000$ AU.

At millimetre wavelengths, the global distribution of the circumstellar matter around AB Aur has been probed in several low rotational lines of CO isotopomers with the IRAM 30-m antenna by Fuente et al. (2002). Fuente et al. have estimated the envelope mass within 0.08 pc ($\sim 15\,000$ AU) to be $\sim 1\,M_{\odot}$. They have classified AB Aur as a Class II object according to their notation (a star embedded in the remnant natal cloud), which implies a power-law radial density profile with an $-2 < p < -1$ exponent. With these two limiting cases of the density profile, the derived mass $M_{0.08\mathrm{pc}} = 1 M_{\odot}$, and assuming that the envelope extends down to the dust sublimation radius $r_0 = 0.7$ AU, I find that the typical density at r_0 is between 10^8 and 10^{12} cm^{-3}.

Moreover, Miroshnichenko et al. (1999) have fitted the SED of AB Aur using a model of a flat disc immersed in a spherically-symmetric diffuse envelope. Their best-fit parameters for the AB Aur envelope are the following: the mass is about $0.03 M_{\odot}$, the radial density distribution follows a broken power law, $p = -2$ for 1.2 AU $< r <$ 120 and $p = 0$ for 120 AU $< r <$ 5800 AU with initial density of $\sim 10^8$ cm^{-3}, and the temperature scales with radius as $T(r) = 1\,500$ K $\cdot (r/1.2$ AU$)^{-0.4}$.

Recently, Elia et al. (2004) have fitted the AB Aur SED from UV to the radio domain with a similar model of a pure spherical envelope and assuming large porous grains (dust emissivity $\propto \lambda^{-0.6}$). They have adopted radial power-law temperature ($q = -0.4$) and density ($p = -1.4$) distributions with $T_0 = 1\,500$ K and $n_0 = 3 \cdot 10^9$ cm^{-3} at $r_0 \approx 1$ AU.

Using these observational facts and theoretical constraints on typical density and temperature values to be encountered in the AB Aur envelope, I construct a simple model of the envelope. Since the molecular content of the AB Aur envelope was probed in several lines with the IRAM 30-m antenna, this allows to derive the temperature and density structure of the AB Aur envelope *directly* from these data, but only assuming 1D power-law distributions for $T(r)$ and $\rho(r)$. Thus, extensive modelling of its physical structure with an advanced radiative (hydro-) code can be omitted.

I focus on the inner part of the entire AB Aur envelope and assume that it is spherically symmetric, homogeneous, and has a radius of $R_{\mathrm{out}} = 2\,200$ AU. The latter quantity is restricted by the largest $29''$

Table 5.3. Parameters of the best-fit disc model

Parameter	Symbol	Value
Inner radius	$R_{\mathrm{in}}^{\mathrm{disc}}$	0.7 AU
Outer radius	$R_{\mathrm{out}}^{\mathrm{disc}}$	400 ± 200 AU
Temperature	T_{disc}	30–1 500 K
Surface density at 1 AU	Σ_0	$7.7 \cdot 10^3$ g cm^{-2} ($\pm$ factor of ~ 7)
Surface density profile	p	-2.5
Mass	M_{disc}	$1.3 \cdot 10^{-2} M_\odot$ ($\pm$ factor of ~ 7)
Grain radius	a_{disc}	0.3μm
Gas-to-dust mass ratio	m_{gd}	100

($\approx 2\,200$ AU) IRAM beam size used in the single-dish observations. Given the low inclination of the disc inferred from the interferometric data, the part of the envelope shielded by the disc is also seen close to face-on. It makes no sense to take into account the outer region of the envelope beyond $2\,200$ AU because it is molecularly deficient (apart from H_2 and CO) along the line of sight due to high stellar UV flux (Fig. 5.3, light grey), while in the opposite direction (the disc midplane) the emitting material is out of the largest used IRAM beam. I assume that the inner radius of the AB Aur envelope coincides with the disc outer edge, $R_{\mathrm{in}}^{\mathrm{env}} = R_{\mathrm{out}}^{\mathrm{disc}} \gtrsim 200$–600 AU.

The envelope radial density profile is modelled with a power law, $\rho(r) = \rho_0 \cdot (r/r_0)^{-p}$, where ρ_0 and p are parameters to be constrained. I assume that the shadowed part of the AB Aur envelope is isothermal, than its mean kinetic temperature T_{kin} can be directly estimated from the T_{mb} intensity of the optically thick CO(2-1) line: $T_{\mathrm{kin}} \sim T_{\mathrm{mb}} \approx 20$–40 K (see Table 5.1). The initial guess for the inner envelope temperature is similar to the range $T = 20$–50 K derived by Thi et al. (2001) from the analysis of excitation conditions for several CO low- and high-rotational lines. I assume that gas and dust species are in thermal equilibrium, which is a justified assumption for the inner (dense, cold, and shadowed) part of the envelope.

The gas-grain and grain-grain collisional timescales in the AB Aur envelope are larger than those in the dense disc. This essentially rules out the possibility that a profound grain growth up to cm-sized bodies occurred there during the contraction phase, which is further supported by the fact that the bulk of dust grains in the AB Aur system are smaller than a few microns. Therefore, I assume that dust particles in the envelope are small uniform spheres with radius of 0.1μm.

The approach of the previous subsection is adopted to compute the UV flux in the shadowed part of the envelope, but with some minor modifications. As this region is shielded from the direct stellar radiation, it is only necessary to take into account the penetration of the IS UV photons. Given the low radial density of the envelope ($\Sigma_{\mathrm{env}} \ll 100$ g cm^{-2}), the constant CR-ionisation rate is taken ($\zeta_{\mathrm{CR}} = 1.3 \cdot 10^{-17}$ s^{-1}) whereas ionisation due to the decay of the radionuclides is negligibly low ($\zeta_{\mathrm{RN}} = 0$).

The best-fit parameters of the AB Aur envelope model are compiled in Table 5.4 and discussed in Section 5.5.

Table 5.4. Parameters of the best-fit envelope model

Parameter	Symbol	Value
Inner radius	R_{in}^{env}	400 ± 200 AU
Outer radius	R_{out}^{env}	$2\,200$ AU
Shadowing angle	θ	$25°$
Temperature	T_{env}	35 ± 14K
Density at 400 AU	ρ_0	$9.4 \cdot 10^{-19}$ g cm^{-3} ($\pm$ factor of ~ 7)
Density profile	p	-1.0 ± 0.3
Mass	M_{env}^{sh}	$4 \cdot 10^{-3} M_{\odot}$ ($\pm$ factor of ~ 7)
Grain radius	a_{env}	$0.1\,\mu$m
Gas-to-dust mass ratio	m_{gd}	100

5.3.3   Chemical model

The chemical model adopted in this study is the same as described in Chapter 3, but with a few modifications. In the rates of reactions with cosmic ray particles and CR-induced UV photons the CR-ionisation rate, ζ_{CR}, is replaced either by the sum of $\zeta_{CR} + \zeta_{RN}$ (disc) or left unchanged (envelope). In accordance with the studies by Willacy and Langer (2000), Aikawa et al. (2002), and van Zadelhoff et al. (2003), I assume that the probability of species to stick onto dust grain surfaces is 100%. Finally, I consider deuteration processes by utilizing the reaction set for deuterated species (Section 3.4) and take into account self- and mutual-shielding of H$_2$ and CO molecules (Section 3.1.2.1). The reference network does not include reactions involving C^{18}O. Therefore I scale down the CO abundances calculated *without self-shielding* by the isotopic ratio O/^{18}O=490 (Wilson and Rood, 1994). Overall, this network consists of 560 species made of 13 elements that are involved in 5336 reactions.

   Although Ilgner et al. (2004) have found that the vertical mixing and radial transport may significantly affect the disc chemical evolution under certain conditions, I do not consider these processes in the model because of three main reasons. First, the estimated mass accretion rate on AB Aur is low, therefore the radial transport of matter toward the central star is small. Second, there is observational evidence that turbulence in protoplanetary discs is low, $V_{turb} \lesssim 0.1$–0.2 km s^{-1} (see, e.g. Dartois et al., 2003), and consequently diffusion processes may be less important. The last (but not least) reason, why mixing processes are not considered, is that the chemical model has to be remain numerically manageable.

5.3.3.1   Results of chemical calculations

Using molecular initial abundances described in Section 3.5 and the aforementioned model of the AB Aur system, a set of time-dependent molecular abundances and vertical column densities are computed for 3 Myr of the evolution in every iterative step of the modelling. Below I discuss the results obtained with the final (best-fit) set of model parameters (Tables 5.2–5.4).

   The calculated HCO$^+$ and CO vertical column densities as a function of radius are presented in
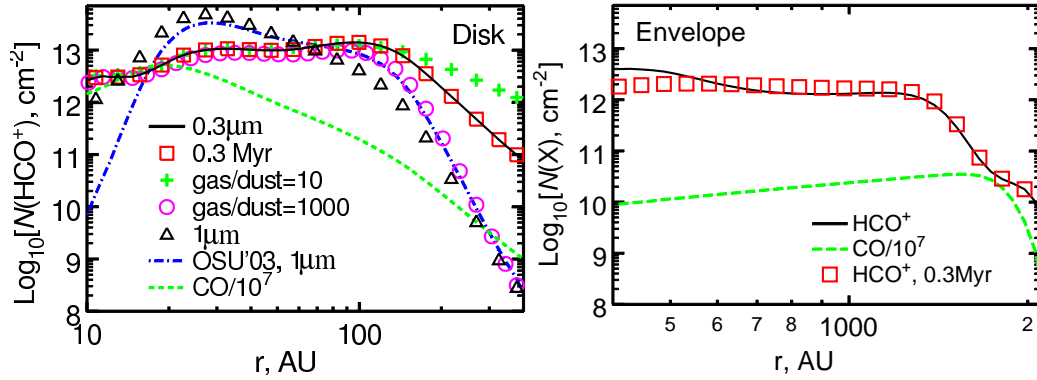
Figure 5.5. Radial distributions of the calculated vertical column densities in the disc (left panel) and envelope (right panel). The thick solid line represents the results for HCO$^+$ obtained with the standard model of the UMIST 95 gas-grain chemistry assuming 0.3μm grains and 3 Myr evolutionary time span, whereas open squares correspond to the case of earlier 0.3 Myr chemistry. The same standard model is used to compute column densities for CO molecules, which are depicted by dashed lines. Note that the CO column densities are scaled by a factor of 10^7. In the left panel, I show the HCO$^+$ disc column densities calculated with the model of larger 1μm dust grains by open triangles, whereas crosses and open circles stand for the results obtained with the standard model, but two different gas-to-dust ratios, 10 and 1000, respectively. Finally, the dashed-dotted line in the left panel corresponds to the HCO$^+$ column densities in the disc after 3 Myr of the evolution that are computed using the OSU 03 gas-grain chemical network with 1.0μm grains.

Fig. 5.5. As can be clearly seen, $N_{CO}(r)$ in general follows the radial decline of the surface density and thus is less steep for the AB Aur envelope than for the disc. The fact that CO column densities are strongly related to the total amount of hydrogen in both the disc and envelope, $N(CO)/N(H) \lesssim 10^{-4}$, merely reflects chemical stability and efficient shielding of CO molecules from dissociating UV radiation. In contrast, the HCO$^+$ column densities as a function of radius show a more complicated behaviour because the chemical evolution of this molecular ion is governed by a larger set of formation and destruction pathways. For instance, a rapid decrease of N_{HCO^+} in the outer parts of the disc and envelope is caused not only by the decline of the surface density, but also due to enhanced recombination rate of HCO$^+$ molecular ions with abundant electrons. These regions are relatively transparent for the impinging UV photons, which dissociate molecules and ionise chemical species (mostly carbon atoms), thereby increasing the electron concentration in the gas-phase and decreasing the HCO$^+$ abundances.

The difference between the chemical evolution of the disc and shielded part of the envelope is the following. The disc has density, temperature, and UV-intensity gradients in both vertical and radial directions, leading to a "layered" chemical structure. The abundances of many gas-phase species peak at the disc intermediate layer where the UV flux is low enough to drive a rich molecular chemistry (e.g., Aikawa et al., 2002; Semenov et al., 2004b). Contrary to the disc, the shadowed envelope region is cold, less dense, and opaque to the stellar UV radiation (but not to the interstellar UV photons). Therefore, many photoreactions and reactions with barriers cannot efficiently proceed there, which results in a more simplified ("dark") chemistry.

I also investigate how various physical and chemical factors influence the evolution of HCO$^+$ in the disc in detail.

First, I consider the standard model of the UMIST 95 chemistry, 0.3μm grains, and $t = 3$ Myr, but two limiting gas-to-dust mass ratios, 10 and 1000. As can be clearly seen, the resulting column densities are nearly the same as in the case of the standard value $m_{gd} = 100$ for $r \lesssim 100$ AU, $N_{HCO^+}(r) \sim 10^{13}$ cm^{-2}. At larger radii, these quantities for $m_{gd} = 1000$ decrease faster with radius than

the column densities computed with the standard chemical model and the difference at $r = 400$ AU reaches about 3 orders of magnitude. Contrary, in the case of $m_{gd} = 10$ the radial decline is shallower than in the standard case, and at $r = 400$ AU the calculated column densities differ by a factor of 10. A similar tendency is seen for the model of larger $1\mu m$ dust particles. In the inner disc regions, 13 AU $< r <$ 60 AU, the corresponding HCO^+ column densities are $\lesssim 10$ times higher than that of the standard model ($m_{gd} = 100$), while at larger radii they decrease with radius like in the case of $m_{gd} = 1000$.

All these trends can be understood if one recalls the fact that the disc at $r \gtrsim 100$ AU has a so low surface density that interstellar UV radiation can easily penetrate and thus controls the chemistry. As I noted above, the HCO^+ abundances strongly depend on the total amount of electrons in the gas phase. In turn, the overall electron concentration in the outer disc regions is related to the value of dust extinction in vertical direction. The higher the extinction is, the lower is the electron concentration (and the higher is the resulting HCO^+ column densities). For a fixed hydrogen column density and two models of uniform grains, the ratio of the corresponding visual extinction values is

$$\frac{A_{V,1}}{A_{V,2}} = \frac{m_{gd,2}}{m_{gd,1}} \frac{a_{d,2}}{a_{d,1}} \frac{Q\mathrm{ext}(a_{d,1},\ V)}{Q\mathrm{ext}(a_{d,2},\ V)}, \tag{5.2}$$

where m_{gd} is the gas-to-dust mass ratio and $Q_{ext}(a_d,\ V)$ is the extinction efficiency factor for a particle with the radius a_d.

According to this equation, the disc with the gas-to-dust ratio of 1000 is 10 times more transparent in vertical direction than in the case of the standard model with $m_{gd} = 100$, while the disc with 10 times more dust grains ($m_{gd} = 10$) is 10 times more opaque. Similarly, in the case of larger $1\mu m$ grains, the total visual extinction is ≈ 6 times smaller than that of the standard $0.3\mu m$ grain model due to ≈ 6 times higher extinction efficiency and about 27 times reduced amount of dust particles in unit volume. Moreover, the ~ 3 times larger radius of $1\mu m$ dust grains in respect to the $0.3\mu m$ particles also implies that Coulomb attraction of positively charged ions and negatively charged dust particles is smaller, leading to less effective grain neutralisation of HCO^+ ions. In turn, this results in the bump of the HCO^+ column density curve at 13 AU $< r <$ 60 AU (Fig 5.5).

Another important question that needs to be clarified is how sensitive the chemical modelling to the adopted set of reactions is. As it has noticed in Chapter 3, there are two chemical databases, which are widely used, namely, UMIST 95 (Millar et al., 1997) and OSU 03 (Smith et al., 2004). These networks comprise hundreds of species and thousands of reactions with the rates that are not always the same. Shortly, the values of the photorates and temperature-dependence in the ion-molecule reaction rates deviate between the UMIST 95 and OSU 03 (see Semenov et al., 2004a).

To answer this question, I repeat the chemical calculations for the disc model with $1\mu m$ dust grains using the OSU 03 network. The corresponding HCO^+ column densities are shown in Fig. 5.5. As can be clearly seen, N_{HCO^+} for the OSU 03 and UMIST 95 models are nearly the same everywhere in the disc except for the inner parts, $r \lesssim 15$ AU. There, the column densities of HCO^+ computed with the OSU 03 model decrease more rapidly with radius than in the case of the UMIST 95 network. As mentioned above, the main reason for that can be the difference in the rates of ion-molecule reactions between these two chemical networks.

Moreover, recently Vasyunin et al. (2004) have shown that computed abundances of HCO^+ ions in dark and diffuse molecular clouds can be uncertain by a factor of ~ 1.8–3 due to uncertainties in the reaction rate coefficients of the UMIST 95 database (see Fig. 1 therein). Given a broad range of physical conditions encountered in the applied disc model, most probably the calculated HCO^+ column densities suffer from the same uncertainty of a factor of ~ 2.

The total computational time for the disc model with 7 radial and 11 vertical grid points is ~ 10

hours on a Pentium IV 2.4 GHz PC, while it takes about several hours to compute the chemical evolution of the envelope model with 28 grid points.

5.4 2D line radiative transfer calculations

In this section, I describe the approach to simulate the radiative transfer in molecular lines and to synthesise their spectra. In essence, the radiative transfer modelling is based on the solution to the radiative transfer (RT) equation coupled with balance equations for molecular level populations (e.g., Rybicki and Hummer, 1991). Prior to the modelling, one needs to provide density, temperature, and velocity distributions as well as molecular abundances in a medium.

I solve the system of the radiative transfer and balance equations with the 2D non-LTE code "URAN(IA)" developed by Pavlyuchenkov and Shustov (2004). It partly uses the scheme originally proposed and implemented in the publicly available 1D code "RATRAN" (Hogerheijde and van der Tak, 2000). The iterative algorithm of "URAN(IA)" is the following.

First, initial molecular level populations and a set of photon random paths through the model grid have to be defined. Using these quantities, the specific intensities $I_\nu(i, j)$ are computed for each cell i by the explicit integration of the RT equation along the pre-defined photon paths $\vec{n}(j)$. For the photon ray-tracing, the code employs a Monte Carlo description. After that, $\vec{n}(j)$ and $I_\nu(i, j)$ are used to calculate the mean line intensity $J_\nu(i)$ in every cell. The computed mean intensities are utilised in the next iteration step to refine the level populations by solving balance equations in all model cells. To accelerate convergence of the entire procedure for optically thick lines, additional internal subiterations for each grid cell (ALI scheme) are included on top of the global iterations. The adopted acceleration scheme relies on the fact that the calculated mean line intensity in every particular cell can be divided into an internal component generated in the cell and external contributions from other cells of the grid. Therefore, subiterations are applied to bring into an agreement the internal mean intensity of the line and corresponding level populations (for more detail, see Hogerheijde and van der Tak, 2000).

The global iterations are performed until the final molecular level populations are obtained. After that, I repeat the calculations again, but with another set of pre-defined random photon paths in order to estimate a typical error of the computed values. In these simulations, the relative errors in the level populations are always smaller than 5%. Finally, the resulting level populations are used to calculate the corresponding excitation temperatures, which are further transformed into synthetic beam-convolved single-dish and interferometric spectra.

There are a few limitations in the code. Since "URAN(IA)" does not contain a realisation of the radiative transfer in the lines with fine structures yet, I can only consider rotational transitions of CO, CS, HCO$^+$ and their isotopomers among the full set of the detected species. The utilised collisional rate data for CO, CS, and HCO$^+$ are taken from Flower and Launay (1985), Green and Chapman (1978), Green (1975), and Monteiro (1985), respectively. I do not take into account the continuum absorption and emission by dust grains, which is a reliable approximation for optically thin and moderately optically thick low-transitional lines (e.g., Leung and Liszt, 1976).

5.4.1 Calculated excitation temperatures

For the line radiative transfer modelling of the AB Aur system I use the set of input parameters compiled in Table 5.5. Standard Keplerian rotation is adopted to represent the regular velocity field of the disc. The quality of the acquired interferometric data does not permit to verify whether the disc

**Table 5.5.** Parameters of the 2D LRT calculations

Parameter	Symbol	Value
Resolution of the numerical grid:	r, θ	
1) Disc model		28×55
2) Envelope model		28×55
3) Disc-in-envelope model		56×55
Error in the level populations		$\lesssim 5\%$
System velocity	V_{lsr}	$5.85 \pm 0.1 \ \mathrm{km\,s^{-1}}$
Microturbulent velocity	V_{turb}	$0.2 \ \mathrm{km\,s^{-1}}$
Disc regular velocity	V_{disc}	$46.2 \cdot (r/1\mathrm{AU})^{-0.5} \ \mathrm{km\,s^{-1}}$
Envelope regular velocity	V_{env}	$0.2 \cdot (r/400\mathrm{AU})^{-1} \ \mathrm{km\,s^{-1}}$
Background temperature	T_{bgr}	$2.73 \ \mathrm{K}$
Spectral resolution	D_ν	$0.04 \ \mathrm{km\,s^{-1}}$
Inclination angle	ι	$17^{+6\circ}_{-3}$
Positional angle	ϕ	$80 \pm 30°$
PdBI HPBW beam		$5.87''$
IRAM HPBW beam		$9.3–29''$[a]

[a]See Table 5.1, Col. (11)

rotation is indeed Keplerian ($V_{\mathrm{disc}}(r) \propto r^{-0.5}$) or follows another power law (see Simon et al., 2000). The AB Aur disc has a much smaller mass in comparison with the stellar mass (e.g., Mannings and Sargent, 1997). Therefore, it is likely that such an assumption is valid, unless the disc is too young to be fully relaxed to the Keplerian state (this possibility is discussed in Pietu et al., 2005).

Little is known about the dynamical state of the AB Aur envelope. Therefore, I consider a steady accretion of the envelope material on the disc (and consequently on the central star), with the regular velocity that can be found from the conservation-of-mass principle and adopted power-law exponent p of the radial density distribution: $V_{\mathrm{env}}(r) \propto r^{-2-p}$. For example, for $p = -1$ the infall velocity decreases as $V_{\mathrm{env}}(r) \propto r^{-1}$. In agreement with recent observations by Thi et al. (2001) and Dartois et al. (2003), the uniform microturbulent velocity $V_{\mathrm{turb}} = 0.2 \ \mathrm{km\,s^{-1}}$ is assumed for both the disc and envelope model.

The computed disc excitation temperatures of the CO(2-1), CS(2-1), HCO$^+$(1-0), and HCO$^+$(3-2) transitions are shown in Fig. 5.6. As can be clearly seen, the excitation temperature T_{ex} for the CO(2-1) line follows the kinetic temperature everywhere in the disc but the surface layer (compare the left panel in Fig. 5.4 with the top left panel in Fig. 5.6). This line is easily excited (critical density $n_{\mathrm{cr}} \sim 10^3 \ \mathrm{cm^{-3}}$) and thus thermalised in most of the disc and envelope regions, $n_{\mathrm{H}} \gtrsim 10^5 \ \mathrm{cm^{-3}}$. Given this fact and the high abundance of CO molecules, CO/H$_2 \lesssim 10^{-4}$, the CO(2-1) line is optically thick with $\tau \sim 10$–1000 in the disc and $\tau \lesssim 10$ in the envelope.
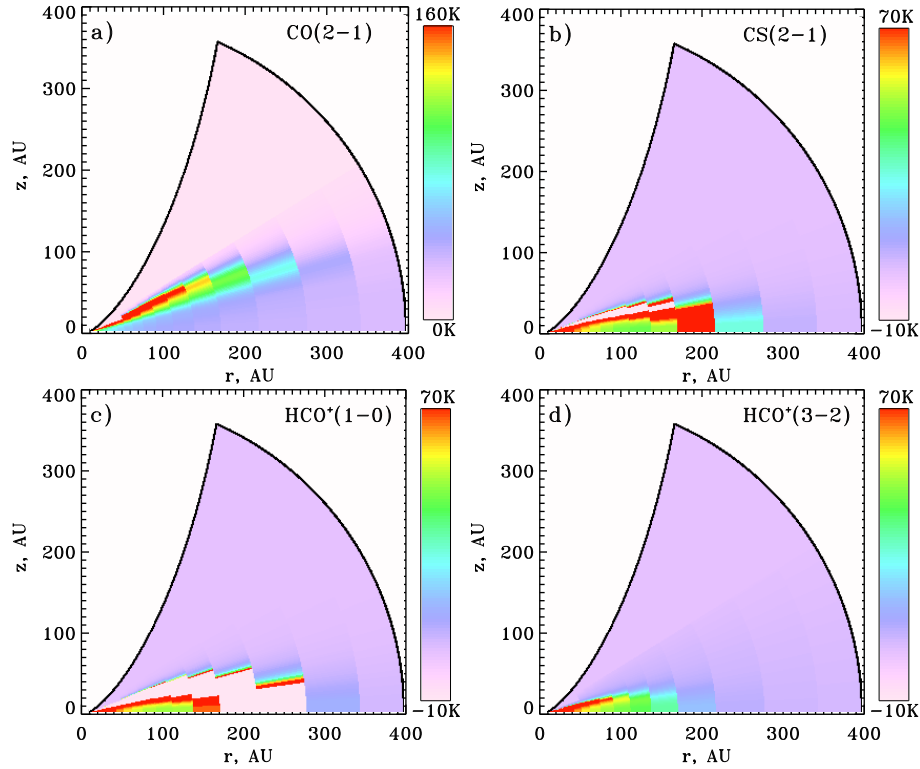
Figure 5.6. Calculated excitation temperatures in the disc for the CO(2-1), CS(2-1), HCO$^+$(1-0), and HCO$^+$(3-2) transitions are presented in the upper left (**a**), upper right (**b**), lower left (**c**), and lower right (**d**) panels. Light areas in the panels (**b**) and (**c**) indicate the disc regions with negative excitation temperature (inversion in the level populations). The plots look somewhat coarse due to a finite discretisation of the applied disc model.

In contrast, the CS(2-1) transition requires about 200 times higher density for thermalisation, therefore its excitation temperature peaks closer to the dense disc interior. The optical thickness of the CS(2-1) line is low, $\tau \sim 10^{-3}$, mainly due to much lower gas-phase CS abundances compared with the amount of CO molecules, $N(CS)/N(CO) \lesssim 10^{-4}$.

The disc excitation temperatures of the HCO$^+$(1-0) and HCO$^+$ (3-2) transitions are shown in the bottom of Fig. 5.6. The 3-2 rotational line is excited at about 10 times higher density than the critical density for HCO$^+$(1-0), $n_{cr} \sim 10^5$ cm^{-3}, leading to the lower excitation temperatures in the former case. Since HCO$^+$ ions are only $\sim$ 10 times more abundant than CS molecules, the HCO$^+$(1-0) and HCO$^+$(3-2) lines have a low optical depth of about 10^{-3}. The disc excitation map for the C^{18}O(2-1) emission is similar to that of CO(2-1) and therefore is not shown.

Note that the CS(2-1) and HCO$^+$(1-0) excitation temperatures show a broad zone in the disc intermediate layer, where $T_{ex} < 0$ (light areas in Fig. 5.6). Here a non-LTE effect plays a role. The inversion in the rotational level populations is caused by a specific ratio between collisional and radiative (de-) excitation probabilities. In those disc parts, where the concentration of CS and HCO$^+$ is low, their levels are excited and de-excited by collisions and only radiatively de-excited (but not excited). Thus, the LTE condition is broken and level populations do not follow the Boltzmann distribution. This effect for the CS molecule has been considered by Liszt and Leung (1977) in detail. However, such inversion does not lead to significant maser amplification of the line intensity even for the most favourable case of the edge-on disc. As soon as the optical depth of the line approaches unity, stimulated radiative transitions become operative. They additionally excite and de-excite the level populations and destroy the inversion.

I do not present the resulting excitation temperatures for the envelope model because the excitation conditions there do not change as strongly as in the case of the disc, and resemble those of the low-density disc surface. Consequently, the CS(2-1) and HCO$^+$(3-2) emission lines are not thermalised anywhere in the envelope, 5 K $\lesssim T_{\text{ex}} \lesssim$ 10 K, whereas HCO$^+$(1-0) is partly thermalised in the inner part at $r \lesssim$ 800 AU: 5 K $\lesssim T_{\text{ex}} \lesssim$ 25 K. Finally, the CO(2-1) and C^{18}O(2-1) lines are thermalised in the entire envelope with $T_{\text{ex}} \approx T_{\text{kin}} \sim$ 30 K.

A typical computation for a 56 × 55 grid model, 11 transitions, and the optically thick CO(2-1) line needs about 2 days on a Pentium IV 2.4 GHz PC. In the extremely optically thin approximation applied to simulate the radiative transfer in the CS(2-1), CS(5-4), C^{18}O(2-1), HCO$^+$(1-0), and HCO$^+$(3-2) lines, the photon ray tracing and ALI scheme are not used. In this case, the level populations are computed within a few seconds. The validity of this approach is verified by comparing once the level populations of the CS(2-1), C^{18}O(2-1), HCO$^+$(1-0), and HCO$^+$(3-2) transitions calculated with the full line radiative transfer and in the limit of the extremely low optical depth. It is found that both methods yield nearly identical results both for the disc and envelope model.

5.5 Results of the line radiative transfer modelling

In this section, I confront the theoretical model of the AB Aur system with the observational data and constrain basic parameters of the disc and envelope. It would be mathematically more correct to compare the interferometric data with the model results in the *uv*-plane in order to avoid the highly non-linear deconvolution procedure (see, e.g. Guilloteau and Dutrey, 1998), but this is only meaningful for low-noise data, when model parameters can be determined with a high accuracy, e.g., by utilising chi-square minimisation. However, I follow a more illustrative way and face the synthesised HCO$^+$(1-0) interferometric map *directly* with the observed line profiles. Another limiting factor for the numerical simulations is the computational time. Typically, it takes about 10–30 minutes to generate one synthetic single-dish spectrum and $\sim$ 2 days to synthesise the entire interferometric map with a 2.4 GHz Pentium IV machine. Together with chemical and non-LTE line radiative transfer calculations, a total computational time for one modelling run can be as long as about 3 days. Therefore, a full χ^2-minimisation in the space of all parameters to be constrained is not feasible for the adopted approach, and one has to estimate these values and their uncertainties with a more robust analysis.

This analysis is based on the *a priori* unknown fact that many model parameters can be constrained *independently* from the others in a subsequent way ("step-by-step"), starting from suitable initial guesses. The most optimal search strategy for the best-fit values of the model parameters was elaborated after several attempts, and is given below. First, I use the first-order estimates for the AB Aur disc orientation and determine more precisely the value of the disc inclination by fitting the width of the central HCO$^+$(1-0) spectrum in the interferometric map. Next, with this best-fit value I derive the disc positional angle by fitting the asymmetry of the observed line profiles out of the map centre. After the best-fit disc orientation is found, I investigate how the radial gradient of the normalised synthetic line intensities depends on the assumed disc radius and choose accordingly the best-fit value of the disc size. Finally, the derived disc orientation and radius allow to constrain the total disc mass because this value defines the absolute intensities of the modelled HCO$^+$(1-0) lines in the interferometric map. The uncertainties of the best-fit disc parameters are found by the same iterative way.

Consequently, I constrain temperature, density structure, and mass of the inner shielded part of the AB Aur envelope using the best-fit disc orientation and radius. First, I determine the temperature of the envelope and its uncertainty by modelling the intensity of the optically thick CO(2-1) line (see Section 5.3.2). Second, with the best-fit envelope temperature, I iteratively find the value of the
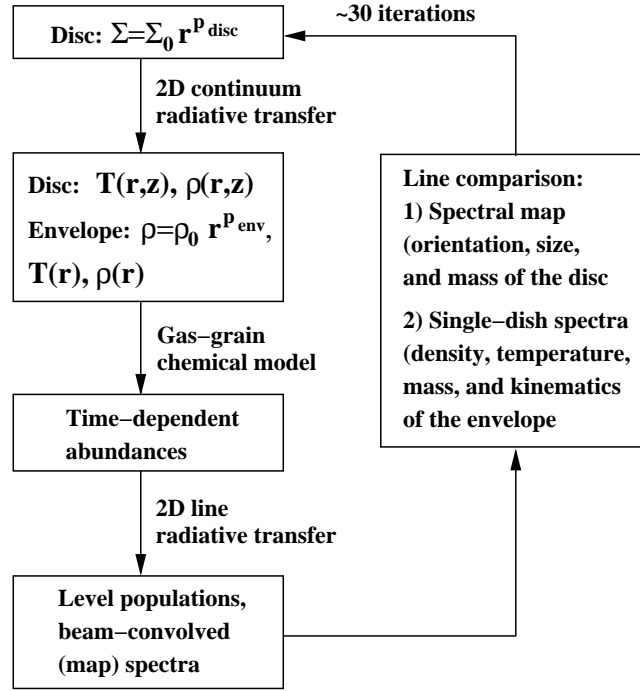
Figure 5.7. The algorithm of the applied modelling approach.

radial density gradient, initial density at the envelope inner radius, and their uncertainties by fitting the observed single-dish HCO^+(1-0), HCO^+(3-2), $C^{18}O$(2-1) and CS(2-1) spectra.

The entire modelling approach is schematically shown in Fig. 5.7.

5.5.1 Interferometric HCO^+(1-0) map

I present the results for the best-fit model of the AB Aur disc, was found after approximately 15 subsequent iteration.

The simulated and observed interferometric HCO^+(1-0) maps are compared in Fig. 5.8. As can be clearly seen, intensities and widths of the synthetic spectra match well the observed values, $T_{mb} \sim$ 0.1 K and $\Delta V_{obs} \approx 2.3$ km s^{-1}. Moreover, the synthesised line profiles in general follow the shape of the observed spectra in the entire interferometric map. This proofs again that the Keplerian law is a reasonable choice for the disc global velocity field. One has to keep in mind that even if the actual velocity field of the AB Aur disc differs from the Keplerian rotation, it will fit the data due to the lack of spatial resolution.

The low intensities of the observed interferometric spectra, $T_{mb} \sim 0.1$ K, suggest that the HCO^+(1-0) line is optically thin. Given a typical excitation temperature in the disc for this transition, $T_{ex} \sim$ 100 K (see Fig. 5.6, lower left panel), the optical depth of HCO^+(1-0) can be roughly estimated as $\tau \sim T_{mb}/T_{ex} \approx 10^{-3}$, exactly the value I have found in Section 5.4.1.

The double-peaked shape of the synthetic line profiles and their asymmetry are the result of the Gaussian convolution with the 5.87″ beam over the inclined disc of a similar size (see Table 5.3). Every HCO^+(1-0) spectrum is a beam-weighted average of the emission generated in various disc regions which have a broad velocity range (from negative to positive values in respect to the system velocity). The central spectrum in the interferometric map has a symmetric profile because disc locations with various velocities contribute equally to the formation of this line. Similarly, all spectra located along the projection of the disc rotational axis on the plane of the sky (zero-velocity line,
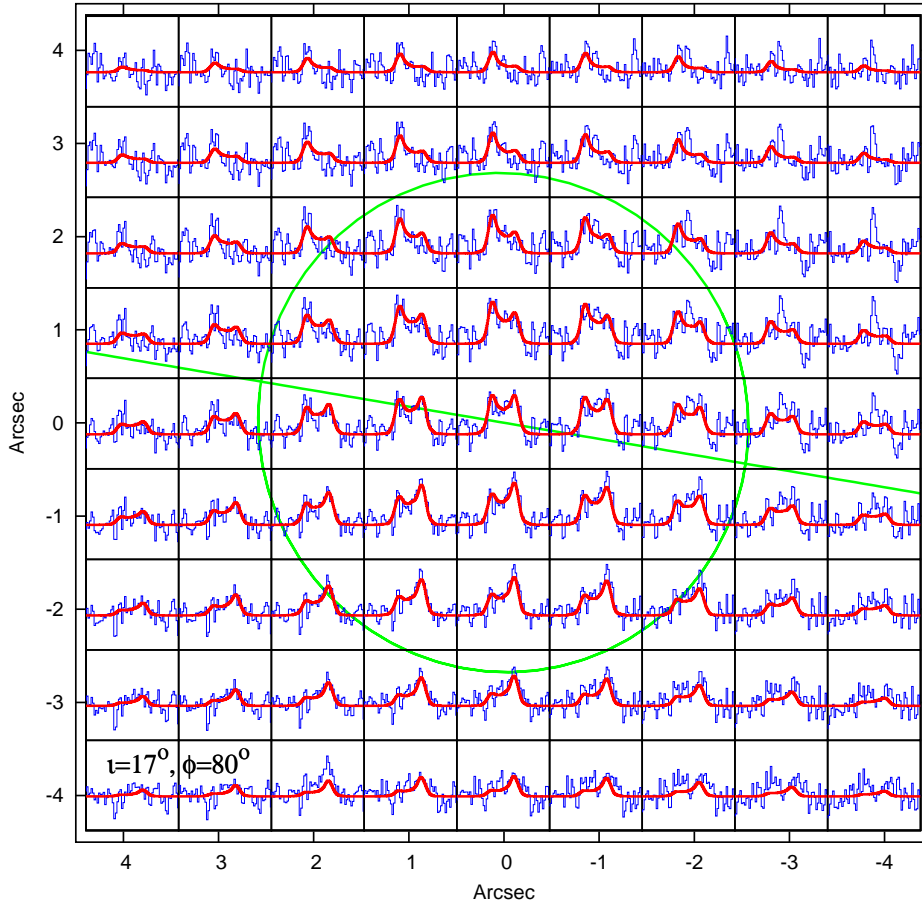
Figure 5.8. Synthetic (thick line) and observed (thin line) HCO$^+$(1-0) interferometric spectra of the AB Aur disc are compared. The vertical (Dec) and horizontal (RA) axes are offsets in arcseconds from the disc centre (standard "N–E" observational orientation). To produce every synthetic spectrum, I convolve it with the Gaussian beam of 5.87″. The intensity of all spectra spans the same $[-0.12\,\mathrm{K}, 0.195\,\mathrm{K}]$ range expressed in units of the main beam temperature (see Table 5.5). The size of the adopted disc model is depicted by a solid circle, while the projection of the disc rotational axis on the plane of the sky is shown by a straight line. The best-fit values of the inclination ($\iota = 17°$) and positional ($\phi = 80°$) angles are indicated in the lower left corner of the plot.

$V = V_{\mathrm{lsr}}$) are also symmetric (compare the line profiles near the straight line and in the perpendicular direction in Fig. 5.8). All other spectra have asymmetric line profiles due to the beam weighting over the disc parts that have a lack of either blueshifted or redshifted emission components. The contrast between the left and right intensity peaks of the HCO$^+$(1-0) lines depends on the orientation of the beam in respect to the zero-velocity line and is maximal in perpendicular direction.

The convolution with a beam size comparable to the size of the adopted disc model leads to the non-zero HCO$^+$(1-0) intensities beyond the disc outer edge (depicted by circle in Fig. 5.8). It is worth to mention here that the convolution with a beam size that is several times smaller than the disc would produce a synthetic map of the narrow single-peaked spectra with different velocity shifts in different disc parts, $|\Delta V| \propto r^{-0.5}$.

Note that there is a region in the interferometric map out of the disc ($x \sim -4''$, $y \sim 2''$), where the observed HCO$^+$(1-0) lines have a peculiar shape, which is far from the modelled one (upper right corner in Fig. 5.8). This shape has a ~ -0.1 K absorption feature with about 2 km s^{-1} offset from the system velocity V_{lsr} and a ~ 0.2 K emission peak centred at V_{lsr}, closely resembling an inverse
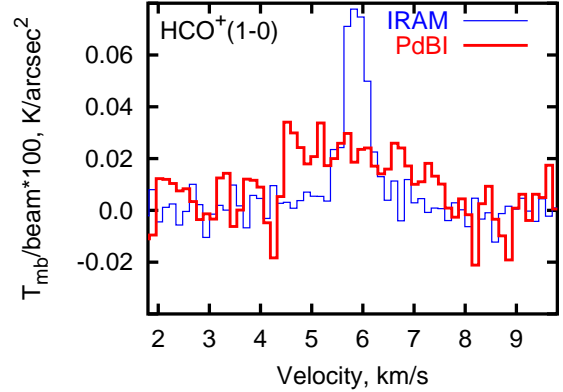
P Cygni profile. It has been checked that the profiles of these "emission-absorption" spectra are stable to the data reduction with various CLEANing parameters and weightings. As I mentioned in Section 5.2.2, the detected HCO^+(1-0) continuum is low, which contradicts with the absolute intensity of the absorption peak. Thus, the absorption peak is not real and likely appeared due to the highly non-linear deconvolution of a low signal-to-noise signal. However, the strength, width, and position of the central peak is consistent with the emission arising in low-velocity envelope regions. Moreover, the peculiarity in the observed profiles is only seen in a part of the full interferometric map.

The presence of a small dense structure in the disc outer region or nearby envelope could be responsible for the appearance of such emission-absorption spectra in the deconvolved interferometric map. Why this structure has to be small and dense can be easily explained: its small ($\lesssim$ 2″) angular extent is a necessary condition to produce the peculiar profiles in a limited area of the whole 12″ × 13″ spectral map only, while a high density contrast is needed for the interferometer to "see" the presence of such an inhomogeneity. Interestingly, Fukagawa et al. (2004) have resolved the AB Aur system using the *Subaru Coronographic Imager and Adaptive Optics* at near-infrared wavelengths and discovered a few spiral arms and a knotty structure associated with a circular inhomogeneous structure of ∼ 580 AU radius (see Figs. 2–3 therein). Thus, it is likely that one of these local and compact structures with enhanced density has been detected during the PdBI observational campaign.
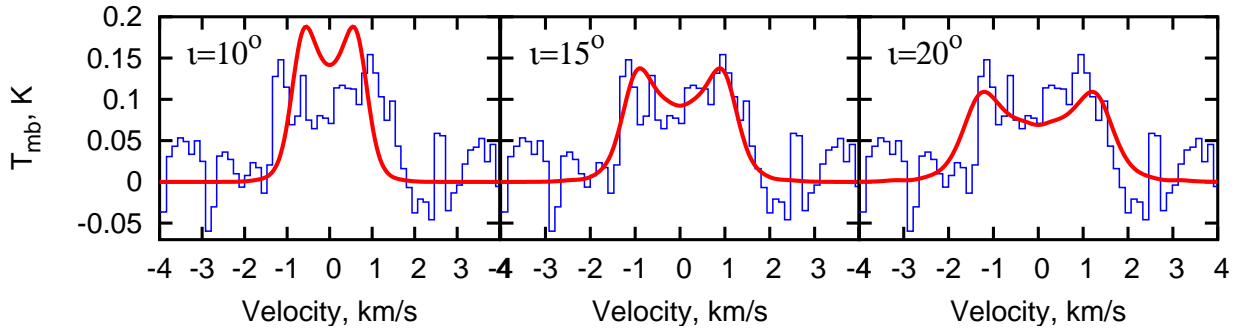

Figure 5.9. Normalised single-dish IRAM spectrum (thin line) of the HCO^+(1-0) emission in comparison with the average HCO^+(1-0) interferometric spectrum (thick line) obtained with PdBI. In the former case, the intensity of the spectrum has been scaled down by the square of the IRAM HCO^+(1-0) beam size of 29″, while in the latter case the intensity has been averaged over a total of 12×13 (1″×1″) various interferometric HCO^+(1-0) PdBI spectra.

The fact that the interferometer probes only dense and compact matter is illustrated in Fig. 5.9, where I compare the observed beam-normalised HCO^+(1-0) IRAM 30-m and averaged PdBI spectra. The IRAM line profile is narrow, ≈ 1 km s^{-1} and single-peaked, while the PdBI spectrum is about 4 km s^{-1} wide and has a double-peaked shape. Furthermore, their normalised intensities differ by a factor of 2. The reason for such a difference in the observed spectra is that the IRAM 30-m antenna has a 29″ beam for the HCO^+(1-0) transition, covers large spatial scales, and therefore is not capable in detecting the emission from the small AB Aur disc due to the huge beam dilution. Instead, the HCO^+(1-0) emission from the surrounding envelope is only observed. Contrary, the ≈ 5″ PdBI beam is sensitive to small spatial scales and thus does not "feel" the emission that comes from the low-density and extended envelope.

5.5.1.1 Disc orientation

First, the disc inclination angle ι is determined by comparing the observed HCO^+(1-0) line profile at the centre of the interferometric map with the corresponding synthetic spectrum. The modelled central line has a symmetric double-peaked profile independent of the actual value of the disc positional angle (see Fig. 5.8, $x = 0$, $y = 0$). However, the line width and intensity do depend on the assumed value of the inclination angle, as shown in Fig. 5.10. It can be clearly seen that a 10° inclination of the disc results in a too narrow (≈ 1 km s^{-1}) modelled spectrum compared with the observed 2.2 km s^{-1}

Figure 5.10. Observed (thin line) and synthesised (thick line) HCO$^+$(1-0) spectra at the centre of the interferometric map. Three different cases are shown, namely, the inclination angle 10° (left panel), 15° (middle), and 20° (right panel). The observed line profile is consistent with a value of the inclination angle between 15° and 20°.

line width (Fig. 5.10, left panel). On the other hand, the disc inclined by $\iota = 20°$ produces a slightly broader spectrum than observed (Fig. 5.10, right panel). Thus, the disc inclination angle has the best-fit value somewhere between these two limits, $\iota \approx 15°$ (middle panel in the Figure). I take 17° as the best-fit inclination angle of the AB Aur disc. Note that a similar approach to constrain the disc inclination was recently presented by Qi et al. (2004), who applied it for the TW Hya disc based on the SMA observations in the CO(2-1) and CO(3-2) lines.

The accuracy of this value is mainly determined by the uncertainty in stellar mass and by the radial gradient of the disc surface density, whereas other model parameters play a minor role.

The width of the modelled central HCO$^+$(1-0) line for a fixed value of the disc inclination angle and density gradient varies as $\sqrt{M_*}$ (Keplerian law). I consider two values of the stellar mass, $M_* = 2.0 M_\odot$ and $M_* = 3.0 M_\odot$, and find that for the low-mass limit of $2.0 M_\odot$ the best-fit disc inclination is 19°, while for the $3.0 M_\odot$ star this value is about 14°.5. In addition, I use two disc models with shallower surface density profiles, namely, $p = -3/2$ (minimum-mass solar nebula) and $p = 0$ (uniform disc). In this case, the HCO$^+$ column densities peak at larger radii than for the reference model with $p = -5/2$. However, I regain that such a modification does not lead to a significant spread in the derived best-fit inclination angle. For the uniform disc model the best-fit value is $\iota = 23°$, whereas for the minimum-mass solar nebula it is 19°. Taking into account all these uncertainty factors, I estimate that the AB Aur disc is inclined by $17^{+6°}_{-3}$.

The value of the disc positional angle is constrained in a similar way. In Section 5.2.2 the first-order observational estimate of $\phi \sim 90°$ has obtained. In order to determine it better, I use the best-fit inclination angle and consider three different values of the positional angle: $\phi = 40°$, 80°, and 120°. The resulting modelled spectra are compared with the observational data at off-central positions of the interferometric map in Fig. 5.11.

The most noteworthy changes in the synthetic HCO$^+$(1-0) lines are seen in two spectra at $x = 2''$, $y = -2''$ (S1) and $x = 2''$, $y = 1''$ (S2). The disc positional angle $\phi = 40°$ can be essentially ruled out because the asymmetry of the observed S1 profile is not properly fitted with this model. Contrary, with $\phi = 120°$ it is not possible to explain the observed shape of the S2 spectrum. Finally, the best fit to the asymmetry of the observed line profiles is obtained with the disc positional angle of 80°. However, this value cannot be constrained as accurately as the disc inclination angle since the noisy observational data can be fitted equally well with any other positional angle between 60° and 100°. Therefore, the best-fit value of the disc positional angle is $\phi = 80 \pm 30°$.

The derived orientation of the AB Aur disc, $\iota = 17^{+6°}_{-3}$ and $\phi = 80 \pm 30°$, is in reasonable agreement with the recent high-resolution NIR observations of Eisner et al. (2003), who have successfully
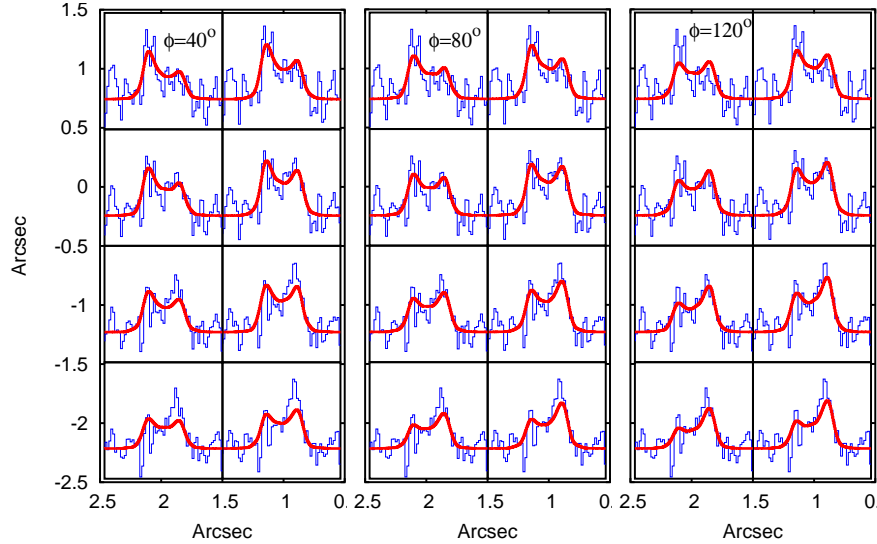
Figure 5.11. Comparison between the observed (thin line) and synthetic (thick line) HCO$^+$(1-0) spectra for a part of the whole interferometric map outside of the disc centre. The inclination angle is fixed, $\iota = 17°$, whereas three different values of the positional angle are considered: $\phi = 40°$ (left panel), $\phi = 80°$ (middle), and $\phi = 120°$ (right panel). The overall comparison of the acquired and modelled line profiles favours to a value of the disc positional angle between 60° and 120°.

reproduced the interferometric visibilities with uniform disc ($\iota = 26^{+10°}_{-19}$, $\phi = 128^{+30°}_{-45}$), accretion disc ($\iota = 27^{+13°}_{-17}$, $\phi = 105^{+34°}_{-20}$), and ring ($\iota = 28^{+10°}_{-18}$, $\phi = 144^{+17°}_{-51}$) models. It is also consistent with the disc inclination of $30 \pm 5°$ and positional angle $\phi = 58 \pm 5°$ determined by Fukagawa et al. (2004) using isophoto fitting of the Subaru coronographic NIR image.

However, a nearly edge-on 76° inclination angle has been derived by Mannings and Sargent (1997) from the analysis of the mid-resolution $\sim 5''$ interferometric image of the AB Aur system obtained with the OVRO array in the ^{13}CO(1-0) line. In many later studies aimed at the modelling of the AB Aur SED this value of the disc inclination has been adopted to constrain the model parameters (see, e.g., Dominik et al., 2003; Miroshnichenko et al., 1999), though Natta et al. (2001) have used a more correct value of 30°. In all these studies the SED of the AB Aur system has been successfully reproduced because the corresponding models possess so large parameter space that a good fit can be found for any given value of the inclination angle by tuning other parameters.

5.5.1.2 Disc radius and mass

With determined values of the AB Aur disc inclination and positional angles, I continue the step-by-step analysis and put constraints on the size and mass of this object.

There is no such controversy in the literature regarding the size of the AB Aur disc as in the case of orientation. The resolved disc radius has been determined as ~ 400–600 AU (Fukagawa et al., 2004; Mannings and Sargent, 1997). I use the value $R_{out}^{disc} = 400$ AU as an initial guess for the modelling (see, however, Natta et al., 2001). A disc model of that size successfully reproduces the radial gradient of the observed HCO$^+$(1-0) intensities (see Fig. 5.8). In addition, I consider a smaller disc with $R_{out}^{disc} = 200$ AU and find that this model still provides a reasonable fit to the radial decline of the observed line intensities, but the width of the synthesised spectra is slightly broader than observed $\Delta V_{obs} \approx 2.3$ km s^{-1}. To get the correct line widths, I adopt a smaller inclination angle of 15°, which is close to the lower limit of the best-fit disc angle, $\iota = 17° - 3° = 14°$. An even smaller 100 AU disc model shows a too rapid decrease of the calculated intensities with radius and hence is not in

agreement with the data.

I cannot determine an upper limit of the disc size by the same way because the gas in the outer disc regions is cold and diffuse. As it has shown in Section 5.4.1, the HCO^+(1-0) transition is hardly excited under these conditions; moreover, the HCO^+ abundances are low (see Fig. 5.5). As a result, the synthetic interferometric spectra almost do not change even if I take into account far-distant disc parts. Thus, as the upper limit I use the largest value of the resolved AB Aur disc, R_{out}^{disc} = 600 AU.

Summarising all these findings, I estimate the best-fit size of the AB Aur circumstellar disc as R_{out}^{disc} = 400 ± 200 AU.

The best-fit disc model with R_{out}^{disc} = 400 AU and ι = 17°, which is shown in Fig. 5.8, has a mass M_{disc} = 1.3 · 10^{-2} $M_\odot$ (Table 5.3). To constrain the latter value, I rely on the fact that the absolute intensities of the calculated HCO^+(1-0) spectra are sensitive to the HCO^+ abundances and thus column densities in the disc due to the low optical thickness of this line:

$$T_{mb} \propto \int_{beam} < T_{ex}(r) > N_{HCO^+}(r) r \exp(-(\frac{r}{r_{beam}})^2) dr \sim$$
$$< T_{ex}(r_{max}) > N_{HCO^+}(r_{max}) r_{max} \exp(-(\frac{r_{max}}{r_{beam}})^2) \Delta r_{max}. \tag{5.3}$$

Here, $< T_{ex}(r) >$ and $N_{HCO^+}(r)$ are the averaged excitation temperature and HCO^+ column densities at a certain radius r, respectively, while the term $r \exp(-(r/r_{beam})^2)$ accounts for convolution with the Gaussian beam of the radius r_{beam}. Using the column densities computed in Section 5.3.3.1 and disc excitation temperatures of the HCO^+(1-0) line calculated in Section 5.4.1, I find that expression (5.3) has a global maximum at $r_{max} \approx 120$ AU (with dispersion $\Delta r_{max} \sim 60$ AU) *independent* of the considered disc model. Thus, the HCO^+ line profiles are mainly determined by the *local* emission generated in the disc regions at r_{max}. Indeed, the width of the observed spectra can be calculated by the following equation:

$$\Delta V_{obs} \approx 2 V_{Kepl}(120 \text{ AU}) \sin(\iota) = 2 \cdot 4.2 \text{ km s}^{-1} \cdot \sin(17°) = 2.47 \text{ km s}^{-1}, \tag{5.4}$$

which is close to the actual value of ≈ 2.3 km s^{-1}.

I find that for 10 times more/less massive discs the modelled HCO^+(1-0) interferometric lines are 7/4.5 times more/less intense than in the case of the best-fit model with M_{disc} = 1.3 · 10^{-2} $M_\odot$ (reference model). At first glance, it seems that the value of the disc mass can be accurately determined since the intensity of the resulting spectra sensitively depends on this parameter. However, the observed HCO^+(1-0) flux suffers from the calibration errors that are $\gtrsim$ 10%. Furthermore, the distance toward AB Aur is derived with $\sim$ 15% uncertainty (see Table 5.2), and hence the flux is uncertain by additional 30%. Thus, the intrinsic uncertainty of the observed line intensities is $\gtrsim$ 40%. Consequently, it results in a factor of $\sim$ 3 uncertainty in the best-fit value of the disc mass. Nonetheless, the spread in M_{disc} is mostly defined by the uncertainties in those parameters of the model which strongly affect the resulting abundances of HCO^+ (see discussion in Section 5.3.3.1) and thus the intensity of the synthesised spectra (Eq. 5.3).

Above all, the disc mass depends on the assumed gas-to-dust ratio because this parameter regulates the total amount of HCO^+ in the disc at large radii, $r \gtrsim 100$ AU (see Fig. 5.5). It is found that for the ratio m_{gd} = 1000 the simulated HCO^+(1-0) interferometric lines have intensities $T_{mb} \sim 0.047$ K, which is 2.1 times lower than observed. Contrary, the model with low gas-to-dust ratio, m_{gd} = 10, produces 4 times more intense lines than the observed spectra with $T_{mb} \sim 0.1$–0.2 K. Thus, such unrealistically high variation of the gas-to-dust ratio introduces a factor of 5 uncertainty in the best-fit disc mass M_{disc} = 1.3 · 10^{-2} $M_\odot$. Moreover, I realise that it also affects the disc inclination angle in a sense that the disc model with m_{gd} = 10 requires ι = 19° to fit the widths of the observed HCO^+(1-0) line profiles, while for the case of m_{gd} = 1000 it is 15°, which is still within the proposed range of

Table 5.6. Disc mass as a function of model parameters

Parameter	Symbol	Value	Disc mass[a]
Gas-to-dust ratio	m_{gd}	10	0.2
Gas-to-dust ratio	m_{gd}	1000	5.0
Grain radius	a_{disc}	1μm	5.0
HCO$^+$ intensities	T_{mb}	$\lesssim$ 0.14 K	0.3
HCO$^+$ intensities	T_{mb}	$\lesssim$ 0.3 K	2.1
HCO$^+$ abundances		2 of standard	0.21
HCO$^+$ abundances		0.5 of standard	1.8
Surface density profile	p	0	0.7
Outer radius	$R_{\text{out}}^{\text{disc}}$	400 AU	1.5

[a]Disc masses are given in units of the best-fit mass $M_{\text{disc}} = 1.3 \cdot 10^{-2} M_{\odot}$.

the disc inclination angle, $\iota \in [14°, 23°]$. Similarly to the case of high gas-to-dust ratio $m_{\text{gd}} = 1000$, the disc model with large 1μm grains shows $\approx$ 2 times less intense spectra than the intensity of the acquired HCO$^+$(1-0) lines. To compensate for this decrease of the modelled line intensity, the disc mass has to be increased by a factor of 5 in respect to the reference value.

The next most important parameter determining the disc mass is the factor of $\sim$ 2 uncertainty of the computed HCO$^+$ abundances. In this case, the intensities of the synthetic lines vary by a factor of $\sim$ 2.4–3.5 compared with the observed values $T_{\text{mb}} \lesssim$ 0.2 K. Therefore, for the model with 2 times increased abundances of HCO$^+$ the corresponding disc mass is only 20% of the standard value $M_{\text{disc}} = 1.3 \cdot 10^{-2} M_{\odot}$, whereas for the case of the 2 times lowered HCO$^+$ abundances the disc mass is 1.8 times higher than for the reference model.

The parameters of the disc model that influence the evaluation of the disc mass to a smaller extent are the size and density distribution. The uniform disc model with the radial gradient of the surface density $p = 0$ and mass $1.3 \cdot 10^{-2} M_{\odot}$ results in 1.2 times higher intensity of the modelled spectra in comparison with the observed line profiles. Consequently, the relevant disc mass constitutes 70% of the mass of the standard model. In contrast, the model with the reduced outer radius $R_{\text{out}}^{\text{disc}} = 200$ AU produces synthetic lines of 1.5 times lower intensity than the observed value of $\lesssim$ 0.2 K. In this case, the best-fit mass of the disc is 50% higher than the reference value of $1.3 \cdot 10^{-2} M_{\odot}$.

All considered model configurations and corresponding estimates of the AB Aur disc mass are summarised in Table 5.6.

Overall, I constrain the AB Aur disc mass to $M_{\text{disc}} \sim 1.3 \cdot 10^{-2} M_{\odot}$ with a factor of 7 uncertainty. This best-fit value is in agreement with $M_{\text{disc}} = 2.1 \pm 0.9 \cdot 10^{-2} M_{\odot}$ determined by Thi et al. (2001) from the 1.3mm flux, assuming dust opacities $\kappa_{1.3\text{mm}} = 0.01$ cm^2 g^{-1} and a gas-to-dust ratio of 100 (see also Mannings and Sargent, 1997).
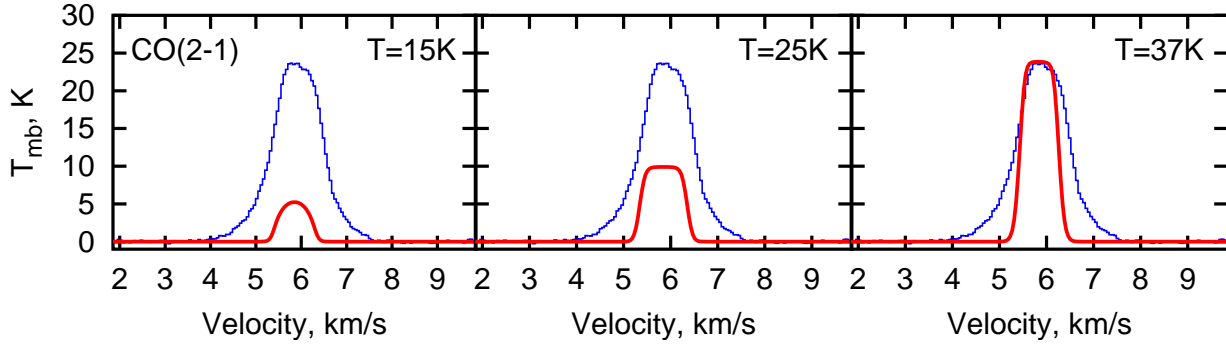
Figure 5.12. Observed (thin line) and synthetic (thick line) single-dish CO(2-1) spectra are compared for three different envelope models. From the left to right panel, the models with a fixed density distribution but different temperature of 15 K, 25 K, and 37 K are presented. As can be clearly seen, the observed line intensity is reproduced only with the latter model. The high intensity ($T_{mb} \approx 25$ K) of the CO(2-1) spectrum suggests that this emission line is optically thick.
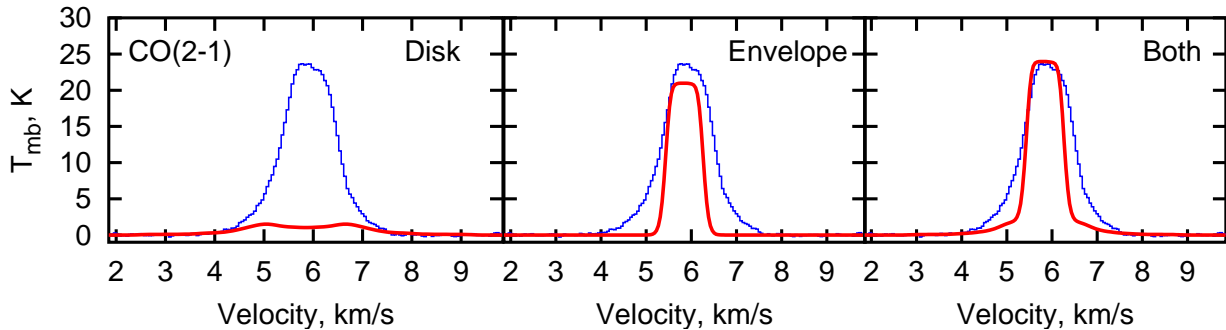
Figure 5.13. Same as in Fig. 5.12 but for three different models. In the left panel, I present the case where only the disc model has been used in the line radiative transfer calculations, whereas in the middle panel the result for the envelope model is shown. Finally, the combination of these two cases (disc-in-envelope model) is shown in the right panel.

5.5.2 Single-dish data

5.5.2.1 Temperature of the envelope

As I have shown in Section 5.4.1, the observed single-dish CO(2-1) line is optically thick and thermalised, $T_{ex} \sim T_{kin}$. Therefore, the intensity of the CO(2-1) synthetic spectrum depends on the assumed value of the envelope temperature and does not depend much on the adopted density structure. I use this fact and consider a grid of the envelope models with various kinetic temperatures within the proposed initial range of T = 20–40 K. In Fig. 5.12, I show the synthetic CO(2-1) line profiles calculated for three different envelope temperatures, namely, T_{kin} = 15 K (left panel), T_{kin} = 25 K (middle panel), and T_{kin} = 37 K (right panel). As can be clearly seen, the observed and modelled CO(2-1) line intensities are nearly the same only in the latter case, whereas for temperatures $T \lesssim 35$ K the computed line intensities are too low. Therefore, the value of 35 K is used in further modelling. The $\sim 40\%$ uncertainty of the best-fit envelope temperature comes from the calibration error of the observed CO(2-1) flux and the distance uncertainty. Finally, I constrain the best-fit temperature of the inner AB Aur envelope to T_{env} = 35 ± 14 K.

In Fig. 5.13, I investigate what the relative contributions of the CO(2-1) emission generated by the disc and envelope on the resulting line profile are. The modelled disc emission shows extremely low intensity $T_{mb} \approx 2$ K compared with the observed value of 24 K, though the width of the synthetic

spectrum is consistent with the observed ≈ 2 km s^{-1} width (left panel). In contrast, the CO(2-1) emission from the envelope has a nearly correct intensity of 21 K, but a too narrow width of 1 km s^{-1} due to low infall velocities adopted in the model, $V(r) \sim 0.1$ km s^{-1} (see the middle panel in the Figure). The combination of both these models, the so-called "disc-in-envelope" model, results in the synthesised CO(2-1) profile with the correct intensity but still too narrow width at signal levels $T_{mb} \sim 5$–10 K (right panel in Fig. 5.13). As discussed in Section 5.2.1, emission arising in moving gas clouds along the line of sight to AB Aur may contaminate the observed CO(2-1) line profile. The chemical stability of CO molecules to dissociative UV radiation and low critical density to excite the 2-1 rotational transition support this suggestion. Recently, Roberge et al. (2001) have studied with HST and FUSE the properties of H$_2$ and CO gases toward AB Aur. They have estimated a CO column density of $N_{CO} = 7.1 \pm 0.5 \cdot 10^{13}$ cm^{-2}, and found that the value of the CO velocity is consistent with the velocity of the star. Thus, this gas is indeed most likely associated with the nearby remnant envelope.

5.5.2.2 Density structure of the envelope

Using the best-fit envelope temperature $T_{env} = 35$ K, I simulate the chemical evolution and line radiative transfer for a grid of the envelope and disc-in-envelope models with various initial densities ρ_0 and density profiles within the range $p \in [-2, 0]$. Then, the mass of the shadowed part of the AB Aur inner envelope can be calculated:

$$M_{env}^{sh} = 4\pi \frac{\theta}{90°} \rho_0 r_0^3 \frac{((r_1/r_0)^{p+3} - 1)}{p + 3}, \tag{5.5}$$

where $\theta = 25°$ is the shadowing angle of the envelope (see Table 5.4), and r_0 and r_1 are the inner and outer envelope radii, respectively.

First, the intensity of the synthetic HCO$^+$(1-0) line is used as a criterion to determine whether the current guess of the initial envelope density ρ_0 (and thus the envelope mass M_{env}^{sh}) is appropriate or not because the observed HCO$^+$(1-0) emission almost entirely comes from the AB Aur envelope (see discussion in Section 5.4.1). The low optical thickness of HCO$^+$(1-0) implies that the corresponding calculated intensity is related to the HCO$^+$ abundances and can be easily scaled up and down by adjusting the mass of the envelope model until the observed intensity $T_{mb} = 0.55$ K is reached.

Second, with the updated envelope model that fits the observed HCO$^+$(1-0) line intensity, I verify whether the radial density gradient of this model is appropriate or not by comparing the observed and modelled HCO$^+$(3-2) to HCO$^+$(1-0) intensity ratios as well as the line profiles of C^{18}O(2-1), CS(2-1), and CS(5-4). The radial gradient of the infall velocity is calculated from the value of the density gradient as $-2-p$, while the initial infall velocity is determined from the observed line widths, $V_{env}(r_0) \sim 0.2$ km s^{-1}.

Iterating these two steps of the modelling about 15 times, the final best-fit model of the AB Aur inner ($r \lesssim 2\,200$ AU) envelope is obtained with the radial density profile $p = -1$ and thus infall velocity law $V_{env}(r) = 0.2 \cdot (r/400\text{AU})^{-1}$ km s^{-1}, initial density $\rho_0 = 9.4 \cdot 10^{-19}$ g cm^{-3} ($n_0 \approx 3.9 \cdot 10^5$ cm^{-3}), and mass $M_{env}^{sh} = 4 \cdot 10^{-3} M_\odot$ (see Table 5.4).

The corresponding synthetic spectra are compared with the observed line profiles in Fig. 5.14. As can be clearly seen, intensities and widths of the synthesised and observed HCO$^+$(1-0), C^{18}O(2-1), and CS(2-1) lines are perfectly matched in the case of the envelope (middle panels) and disc-in-envelope (right panels) models, whereas the contribution from the disc in the resulting spectra is negligible (left panels). In contrast, the observed HCO$^+$(3-2) emission comes partly from the AB Aur disc and partly from the surrounding envelope, therefore a reasonable fit to this line is only produced by the full disc-in-envelope model (see second row of plots in the Figure). Particularly, the broad ~ 2 km s^{-1} width of

the observed HCO^+(3-2) spectrum is not possible to explain without accounting for the emission from the AB Aur disc. Still, the synthetic HCO^+(3-2) spectrum peaks at about $1\,km\,s^{-1}$ higher velocity than the observed emission from the AB Aur envelope, which cannot be explained in the framework of the applied model. A possible explanation for this inconsistency can be the large-scale inhomogeneity of the interior part of the AB Aur system (for more detail, see Pietu et al., 2005).

The uncertainties of the derived parameters are estimated as follows. I adopt the factor of 7 uncertainty for the best-fit value of the envelope mass and initial density at the inner envelope edge based on the results of a similar investigation performed for the AB Aur disc model (see extensive discussion in the previous section). The uncertainty of the determined radial density profile $p = -1.0$ is found to be ± 0.3. This is because an envelope model with $p = 0$ show ~ 2 and 3 times lower intensities of the synthetic $C^{18}O$(2-1) and CS(2-1) lines than the observed values of 1.1 K and 0.11 K, respectively. For a model with $p = -1.5$, the intensity of the calculated HCO^+(3-2) spectrum is about 1.5 times higher than the observed value $T_{mb} \approx 0.9$ K.

Note that in framework of the adopted model of the AB Aur system it is not possible to fit the observed CS(5-4) line profile since the intensity of the synthesised CS(5-4) spectrum is essentially zero. This line is excited at high densities, $n_{cr} \gtrsim 10^6$–$10^7\,cm^{-3}$, which are reached only in inner dense disc regions at $r \lesssim 150$ AU (see Fig. 5.4, right panel). Therefore, the intensity of the modelled CS(5-4) line becomes extremely low after the convolution with the $9''$ (~ 1000 AU) IRAM beam. Consequently, a necessary requirement for a model of the AB Aur system to reproduce the observed CS(5-4) line intensity would be the presence of high-density clumps at $\gtrsim 100$-200 AU distance from the central star.

I find that the intensity, width, and line profile of CS(5-4) can be reproduced with a 5 times more massive model of the AB Aur envelope than the best-fit one. However, in this case all other modelled single-dish lines differ substantially from the observed spectra. Therefore, I tried to match all single-dish data *simultaneously* with a clumpy envelope model. This is possible only in one case: clumps that homogeneously fill 3% of the entire $10''$ IRAM CS(5-4) beam and have about 150 times higher density than the surrounding medium, $n \sim 5 \cdot 10^7\,cm^{-3}$. The total mass of these clumps is approximately equal to the mass of the best-fit envelope model, $M_{clumps} \approx 4 \cdot 10^{-3} M_\odot$, and consequently the mass of the clumpy envelope model is twice that of the reference best-fit model. The applicability of this clumpy envelope model cannot be thoroughly verified with the adopted 2D approach and requires full 3D treatment, which is beyond the scope of the present work.

The density distribution and mass of the best-fit model of the AB Aur envelope are consistent with the values derived by Elia et al. (2004) from the modelling of the SED: $p = -1.4$, $\rho_0 \approx 1.6 \cdot 10^{-18}\,g\,cm^{-3}$ at $r = 400$ AU, and M_{env} within $r \in [400\,AU, 2\,200\,AU]$ of about $2 \cdot 10^{-2} M_\odot$. There is almost no difference between initial densities for both models, the radial density profiles are also similar, but the envelope masses differ by a factor of 5. This is because I focus on the shadowed part of the inner envelope part, which contains only $25°/90° \approx 28\%$ of the volume of the full sphere. If one takes into account 28% of the total envelope mass determined by Elia et al., the resulting value is $5.5 \cdot 10^{-3} M_\odot$, which is close to the $4 \cdot 10^{-3} M_\odot$ mass of the best-fit model.

Similarly, Fuente et al. (2002) have estimated the mass of the AB Aur envelope within 0.08 pc as $1 M_\odot$ and obtained a density profile of $-2 < p < -1$. These values can be translated to the initial density at $r = 400$ AU and mass of the shielded inner part of the envelope: $\rho_0 \approx 1.3 \cdot 10^{-18}\,g\,cm^{-3}$ and $M_{env}^{sh} \approx 6.8 \cdot 10^{-3} M_\odot$ for $p = -1$ and $\rho_0 \approx 3.7 \cdot 10^{-17}\,g\,cm^{-3}$ and $M_{env}^{sh} \approx 5.4 \cdot 10^{-2} M_\odot$ for $p = -2$, respectively. The mass and initial density of the best-fit envelope model ($\rho_0 = 9.4 \cdot 10^{-19}\,g\,cm^{-3}$ and $M_{env}^{sh} = 4 \cdot 10^{-3} M_\odot$) are close to the values of Fuente et al. for the case of $p = -1$, while the steeper density gradient $p = -2$ requires about a 10 times more massive envelope model to match the AB Aur SED.

Table 5.7. Comparison of the AB Aur envelope models

Study	Initial density at 400 AU, g cm^{-3}	Density profile	Mass[a] $M_\odot$	Total mass $M_\odot$
(1)	$2.3 \cdot 10^{-20}$	0	$5 \cdot 10^{-4}$	$1.6 \cdot 10^{-3}$
(2)	$9.4 \cdot 10^{-19}$	-1	$4 \cdot 10^{-3}$	$6 \cdot 10^{-3}$
(3)	$1.3 \cdot 10^{-18}$	-1	$6.8 \cdot 10^{-3}$	$2.5 \cdot 10^{-2}$
(4)	$1.6 \cdot 10^{-18}$	-1.4	$5.6 \cdot 10^{-3}$	$2 \cdot 10^{-2}$
(3)	$3.7 \cdot 10^{-17}$	-2	$5.4 \cdot 10^{-2}$	$2 \cdot 10^{-1}$

[a]Mass of the shadowed ($\approx$ 28% by volume) part of the envelope between 400 AU and 2 200 AU.

References. — (1) Miroshnichenko et al. 1999; (2) This work; (3) Fuente et al. 2002; (4) Elia et al. 2004

Finally, Miroshnichenko et al. (1999) have found by the modelling of the AB Aur SED with a disc-in-envelope model the total mass of the envelope to be $M_{\mathrm{env}} \sim 0.03 M_\odot$. Again, it can be translated to the value of $\sim 5 \cdot 10^{-4} M_\odot$ for the inner shadowed part, which is $\sim$ 10 times lower than in my case. Such a low value of the envelope mass is due to the uniform density distribution ($p = 0$) at $r \gtrsim 120$ AU they have applied in the calculations. This density profile is shallower compared to the other studies mentioned above and my best-fit model, which leads to the strongly underestimated mass of the AB Aur envelope.

Since I focus on the shadowed and inner region of the AB Aur envelope, it is difficult to calculate accurately the total mass of the envelope with my model. The mass of the two unshielded lobes can be roughly estimated from the value of the observed extinction toward AB Aur, $A_{\mathrm{V}} \lesssim 0.5$ mag. For the best-fit model of the shadowed part, the visual extinction is maximal in radial direction, $A_{\mathrm{V}}^{\mathrm{sh}} = 2.5$ mag, which is about 5 times higher than for the unshielded region. If one assumes that this difference stems entirely from the density contrast between the shadowed and unshielded envelope parts and their radial density profiles and dust grain properties are the same, than the total envelope mass between 400 AU and 2 200 AU is

$$M_{\mathrm{env}} \sim (1 + \frac{A_{\mathrm{V}}}{A_{\mathrm{V}}^{\mathrm{sh}}} \frac{90° - \theta}{\theta}) M_{\mathrm{env}}^{\mathrm{sh}}, \tag{5.6}$$

where $\theta = 25°$ is the shadowing angle, $A_{\mathrm{V}} \lesssim 0.5$ mag, $A_{\mathrm{V}}^{\mathrm{sh}} = 2.5$ mag, and $M_{\mathrm{env}}^{\mathrm{sh}} = 4 \cdot 10^{-3} M_\odot$. According to this expression, the total mass of the AB Aur inner ($r \lesssim 2 200$ AU) envelope is $M_{\mathrm{env}} \sim 6 \cdot 10^{-3} M_\odot$. Moreover, assuming that the best-fit density profile of the inner envelope model is also appropriate at larger distances until the cloud outer border at 35 000 AU, I calculate the mass of the *entire* AB Aur envelope, $M_{\mathrm{env}} \approx 1 M_\odot$, which is exactly the value measured by Fuente et al. (2002).

The parameters of the density structure and mass of the envelope models considered above are summarised in Table 5.7.

5.5.3   Evolutionary status of the AB Aur system

In this Section, I discuss the evolutionary nature of the AB Aur system using the results of the modelling.

With the reconstructed best-fit velocity profile of the AB Aur envelope (see Table 5.4), one can estimate *independently* the mass accretion rate in this system:

$$\dot{M}_{\text{acc}} = 3.16 \cdot 10^7 \, \rho_0 \, V_{\text{env}}(r_0) \, 4\pi \frac{\theta}{90°} r_0^2, \tag{5.7}$$

where $\rho_0 = 9.4 \cdot 10^{-19}$ g cm^{-3} is the initial density at the disc outer edge $r_0 = 400$ AU and $\theta = 25°$ is the shadowing angle. According to this expression, the mass accretion rate from the AB Aur envelope onto the disc is $\dot{M}_{\text{acc}} \approx 4 \cdot 10^{-8} M_\odot$ yr^{-1}. This value is close to the measured mass accretion onto the central star, $\dot{M}_{\text{acc}} \sim 10^{-8} M_\odot$ yr^{-1} (see, e.g., Grady et al., 1996).

If one assumes that the mass rate is constant with time and due to the viscous evolution of the disc only, then dispersal timescale for the AB Aur disc is $\tau_{\text{disc}} \sim M_{\text{disc}} / \dot{M}_{\text{acc}} \sim 0.3$ Myr, which is too short in comparison with the ~ 4 Myr age of AB Aur. Thus, accretion from the envelope should play a major role in the evolution of the AB Aur system as a whole. The lifetime of the entire $\sim 35\,000$ AU envelope can be roughly estimated from the same principles, $\tau_{\text{env}} \sim M_{\text{env}} / \dot{M}_{\text{acc}} \approx 1 M_\odot / 4 \cdot 10^{-8} M_\odot$ yr^{-1}, which gives evolutionary timescale of about 25 Myr. Therefore, I conclude that the AB Aur system will remain a Class II object for the next few million years.

However, if the mass accretion in the disc steadily decreases with time and the AB Aur system is in general younger, $t \sim 2$ Myr, the timescale for the disc viscous evolution can become comparable with the age of the system. In this case, the disc may not be relaxed to the Keplerian state yet, implying different rotational profile than classical $V(r) \propto r^{-1/2}$. Too short time for the viscous spreading of the disc matter may also result in a globally irregular disc structure, being an "imprint" of the earlier, more active and non-steady accretion phase (for explanation, see Pietu et al., 2005).

The estimated timescale for dispersal of the AB Aur envelope is in sharp contrast to the free-fall time from the envelope outer edge at $35\,000$ AU on the central star, $\tau_{\text{ff}} = \sqrt{3\pi/32G\rho} \approx 0.3$ Myr. Thus, contraction of the envelope is not free-fall and regulated by additional force(s) acting against gravitation, like thermal pressure, rotation, turbulence, or magnetic field.

The suggestion that the AB Aur envelope fully rotates can be essentially ruled out given the fact that the widths of the observed single-dish lines are narrow, $\lesssim 1$ km s^{-1}. Indeed, it is found that the model with only 20% of the Keplerian rotation representing the regular velocity field in the envelope produces broader synthetic single-dish lines than observed. On the other hand, conservation and redistribution of initial angular momentum of the natal cloud out of which the AB Aur system has been formed should end up in a rotating flattened configuration (see, e.g., Larson, 2003, and references therein). Thus, it explains why the AB Aur envelope is flattened and suggests that the envelope slowly rotates, $V_{\text{rot}} \lesssim 0.1$ km s^{-1}, in addition to the infall.

Furthermore, by fitting the line widths with various microturbulent velocities, I find that turbulence in the envelope should be low, $V_{\text{turb}} \lesssim 0.2$ km s^{-1}, which is smaller than the sound speed, $c_s \approx 0.4$ km s^{-1}. Therefore, these subsonic turbulent motions cannot retard the cloud collapse.

Also, the AB Aur envelope cannot be fully supported against the gravitational contraction by thermal pressure because it is not spherically symmetric, and cold, $T \lesssim 35$ K. Using the equation of state of an ideal gas (2.3) and best-fit density profile $\rho(r) \propto r^{-1}$, the equation of pressure equilibrium (2.2) can be rewritten as

$$\frac{kT}{\mu m_{\text{H}}} = \frac{GM_*}{r}, \tag{5.8}$$

where k is the Boltzmann constant, $\mu = 1.44$ is the mean molecular weight, m_H is the mass of one hydrogen atom, G is the gravitational constant, $M_* = 2.4 M_\odot$ is the stellar mass, and r is the radius. The left (pressure) part of this expression is equal to the right (gravitational) part only for $r \gtrsim 10\,000$ AU, and lower for smaller radii. Consequently, the inner part of the AB Aur envelope is too cold to resist the gravitation force.

Finally, magnetic pressure can slow the collapse, but only if the envelope matter is well coupled to the magnetic field. The computed ionisation fraction for the best-fit AB Aur envelope is about 10^{-8}–10^{-6} and thus the latter requirement is fulfilled.

Therefore, I conclude that slow rotation and magnetic pressure play a major role in the dynamical evolution of the AB Aur envelope by regulating the speed of the collapse. In turn, it defines the accretion rate onto the disc and thus its mass and consequently the lifetime of the *entire* AB Aur system, $t \lesssim 25$ Myr. Also, these two dynamical factors are responsible for the flattened appearance of the envelope. Note that the presence of such asymmetric structures around protoplanetary discs has been predicted by theories of star formation (see, e.g., Larson, 2003) and inferred from observations (e.g., Hogerheijde, 2003). In a more general sense, these findings support the idea of Armitage et al. (2003), who have argued that the observed disc lifetimes between 1 and 10 Myr are mostly determined by the initial mass available for the accretion, but not by the mass of the central star(s).

The instantaneous infall of the envelope matter onto the rotationally supported disc should produce an accretion shock interface, and likely *local* density enhancement at the disc outer edge (Velusamy et al., 2002). Then it is natural to ask whether these disc regions remain stable or not. The gravitational instability in rotating disc-like configurations is suppressed when the so-called Toomre parameter exceeds unity (see discussion in Larson, 2003):

$$Q(r) = \frac{c_s \Omega(r)}{\pi G \Sigma(r)}, \tag{5.9}$$

where c_s is the sound speed, $\Omega(r)$ is the epicyclic velocity at the radius r, G is gravitational constant, and $\Sigma(r)$ being the disc surface density.

Applying this equation to three considered disc models that fit the observations, namely, the uniform disc ($p = 0$), minimum-mass solar nebula ($p = -3/2$), and reference model ($p = -5/2$), I find that the corresponding Q-factors at the disc outer boundary $r = 400$ AU are 0.57, 22, and 300, respectively. It is likely that these values are smaller because of the density enhancement at the disc outer edge due to the mass flow from the envelope. Thus, continuous mass feeding of the AB Aur disc from the surrounding envelope may make it gravitationally unstable. Consequently, the disc will develop prominent spiral arms trailing around through which the matter from the disc edge will be rapidly transported inward, to the inner regions (Larson, 2003).

In Sections 5.5.1 and 5.5.2.2 I have claimed that presence of local high-density (clump-like) structures in the AB Aur system is a necessary requirement to explain the peculiar shape of the HCO^+(1-0) profiles in a region of the PdBI map and the high ratio of the single-dish IRAM CS(5-4) and CS(2-1) spectra. This suggestion is supported by the observations of Fukagawa et al. (2004) that reveal the presence of a few spiral arms and underlying circular inhomogeneous structure in the AB Aur system at $r \lesssim 600$ AU. They have also found that these arms are trailing and concluded from similar arguments that the gravitational instability is caught at work in a protoplanetary disc. Note that spiral density waves like discussed above can also be produced by tidal interactions between the disc matter and hidden low-mass (planetary) companion(s). However, Fukagawa et al. have ruled out such a possibility because otherwise a companion would have been detected. It is worth to mention here that recently Fromang et al. (2004) have simulated the evolution of magnetised self-gravitating discs in 2D and 3D showing amazingly similar spiral pattern (see Fig. 5 therein) as has been observed by Fukagawa et al. (2004).

The continuous replenishment of the AB Aur disc matter by "fresh" material from the envelope via inward accretion by the spiral arms provides a natural explanation for the observational fact that the bulk of dust grains in the disc are pristine and closely resemble the ISM dust (see Bouwman et al., 2001; Meeus et al., 2001), though it can also be due to underestimated youthfulness of this object. This hypothesis explains why some Herbig systems do not show significant grain evolution after several million years of the evolution, while other do, but it should be carefully verified by future observations and modelling.

5.6   Summary and conclusions

The AB Aur system was observed by K. Schreyer at millimetre wavelengths with the IRAM 30-m antenna and Plateau de Bure array during 2000–2002. Overall, nine different molecular species in a dozen rotational transitions were detected at low resolutions $(10$–$30'')$ using the IRAM telescope: CO, $C^{18}O$, CS, HCO^+, DCO^+, H_2CO, HCN, HNC, and SiO. From the measured negative intensity of the $DCO^+(2$-$1)$ line, I found strong evidence that the AB Aur envelope extends up to at least $\sim 35\,000$ AU from the star. In contrast, only the $HCO^+(1$-$0)$ emission from the AB Aur disc has been detected with PdBI at the modest $\sim 5''$ resolution. The symmetric "butterfly" (two-lobe) appearance of the intensity-weighted velocity map is indicative of a rotating $\lesssim 10''$ ($\lesssim 1\,500$ AU) disc that is seen close to face-on with a positional angle of $\sim 90°$. To account for these observational data, I used *for the first time* a coherent modelling of the disc and envelope physical structure, chemical evolution, and radiative transfer in molecular lines.

I modelled the AB Aur disc by the 2D flared passive disc model with vertical temperature gradient and Keplerian rotation, using the 2D continuum radiative transfer code and observational facts and theoretical constraints from the literature. To represent the AB Aur envelope, I adopted the infalling isothermal spherical cloud model with a central region shadowed by the disc and two wide cones transparent to the stellar radiation. For both the disc and envelope models, time-dependent abundances and column densities of observationally important molecules were calculated for 3 Myr of the evolution with the gas-grain UMIST 95 chemical network supplied by dust surface reactions, reactions of deuterium fractionation, and CO and H_2 shielding. After that, the calculated abundances of HCO^+, CO, $C^{18}O$, and CS molecules were translated to the excitation temperatures of the $CO(2$-$1)$, $C^{18}O(2$-$1)$, $HCO^+(1$-$0)$, $HCO^+(3$-$2)$, $CS(2$-$1)$, and $CS(5$-$4)$ transitions by mean of the 2D non-LTE line radiative transfer code. Finally, with the same code I synthesised the beam-convolved $HCO^+(1$-$0)$ interferometric map and single-dish $CO(2$-$1)$, $C^{18}O(2$-$1)$, $HCO^+(1$-$0)$, $HCO^+(3$-$2)$, $CS(2$-$1)$, and $CS(5$-$4)$ lines and compared them *directly* with the observational data. Iterating this modelling scheme about 30 times (each run took ~ 3 days on a Pentium IV 2.4GHz PC), I constrained the parameters of the AB Aur system and their uncertainties by varying the model configurations in a robust step-by-step way.

Overall success of such an advanced and complicated theoretical approach to explain the observational data is surprising. The best-fit disc model reproduces the intensities, widths, and profiles of the observed $HCO^+(1$-$0)$ spectra in the entire interferometric map apart from one corner. There the line profiles show a fake absorption-emission shape that resembles the inverse P Cygni profile. I suggest that this can be *indirect* evidence for a *local* inhomogeneity (density enhancement) of the nearby envelope at $r \gtrsim 600$ AU.

The constrained parameters of the AB Aur disc are the following. The AB Aur disc is in Keplerian rotation and inclined by $\iota = 17^{+6°}_{-3}$, whereas its position angle is $\phi = 80 \pm 30°$. The uncertainties of the derived inclination angle are mainly caused by the uncertainty of the adopted stellar mass and spread in the radial gradient of the disc surface density. The radius of the disc is $R_{out} = 400 \pm 200$ AU and its mass is $M_{disc} = 1.3 \cdot 10^{-2}\,M_\odot$ with a factor of ~ 7 uncertainty. The uncertainty of the constrained

mass is mainly caused by possible variations of the gas-to-dust mass ratio and the size of dust grains in this object.

The best-fit model of the AB Aur disc and inner shadowed part of the envelope (disc-in-envelope model) successfully reproduces the intensities, widths, and profiles of the single-dish CO(2-1), $C^{18}O$(2-1), HCO^+(1-0), HCO^+(3-2), and CS(2-1) spectra with the exception of the CS(5-4) data, which can be fitted only by the model with clumps that have a characteristic density of about $5 \cdot 10^7$ cm^{-3} and homogeneously fill 3% of the full 10″ IRAM beam in the CS(5-4) transition. I found that the large ~ 2 km s^{-1} width of the observed CO(2-1) emission cannot be explained by this model alone and is likely due to contamination by moving gas clouds along the line of sight to AB Aur. The best-fit envelope model has the mean temperature of about 35 ± 14 K, power-law density distribution $\rho \propto r^{-1.0 \pm 0.3}$ with the initial density of $9.4 \cdot 10^{-19}$ g cm^{-3} at 400 AU, mass of the shielded region within $400 < r < 2\,200$ AU, $M_{\mathrm{env}}^{\mathrm{sh}} = 4 \cdot 10^{-3}\ M_\odot$, and total mass of about $6 \cdot 10^{-3}\ M_\odot$ (the latter three quantities are uncertain by a factor of ~ 7). Here, the ± 14 K uncertainty of the average envelope temperature is due to the ~ 10–15% calibration errors in the observed CO(2-1) flux and a ~ 15% uncertainty in the distance to AB Aur.

The many estimated parameters of the AB Aur disc and envelope are in reasonable agreement with other recent studies, especially those which are based on the (sub-) millimetre observations (e.g., Fuente et al., 2002; Pietu et al., 2005; Thi et al., 2001), but disagree with older works based on the SED modelling (e.g., Miroshnichenko et al., 1999).

Furthermore, the applied step-by-step theoretical approach allowed to account for various observed interferometric and single-dish molecular spectra of AB Aur *simultaneously*. I conclude that a comprehensive theoretical modelling of the observed interferometric maps obtained even with modest resolution offers an unique possibility to constrain the masses, sizes, orientation, and dynamical structure of young protoplanetary discs in an *independent* way. The same approach applied to single-dish spectra is capable in determining average temperature, density, and kinematics of the surrounding envelopes

Moreover, the best-fit model predicts that the $\sim 10^{-8} M_\odot$ yr^{-1} mass accretion to be in the AB Aur system is regulated by steady contraction of the envelope, which is only partly supported by rotation and magnetic field acting against gravitation. It also gives a rough estimate of a timescale for dispersal of the entire system, $t \lesssim 25$ Myr. I argued that the continuous mass supply from the infalling envelope onto the rotating disc produces gravitational instabilities resulting in a spiral disc structure, similar to that recently observed by Fukagawa et al. (2004) and simulated with a 3D MHD code by Fromang et al. (2004). I conclude that the continuous replenishment of the AB Aur disc matter by the material from the surrounding envelope provides a straightforward explanation to the observational fact that most of the disc grains are pristine and resemble ISM dust particles even after several Myr of the evolution, which can also be true for other Herbig Ae/Be systems. Another possibility could be that AB Aur is merely younger, $t \sim 2$ Myr.
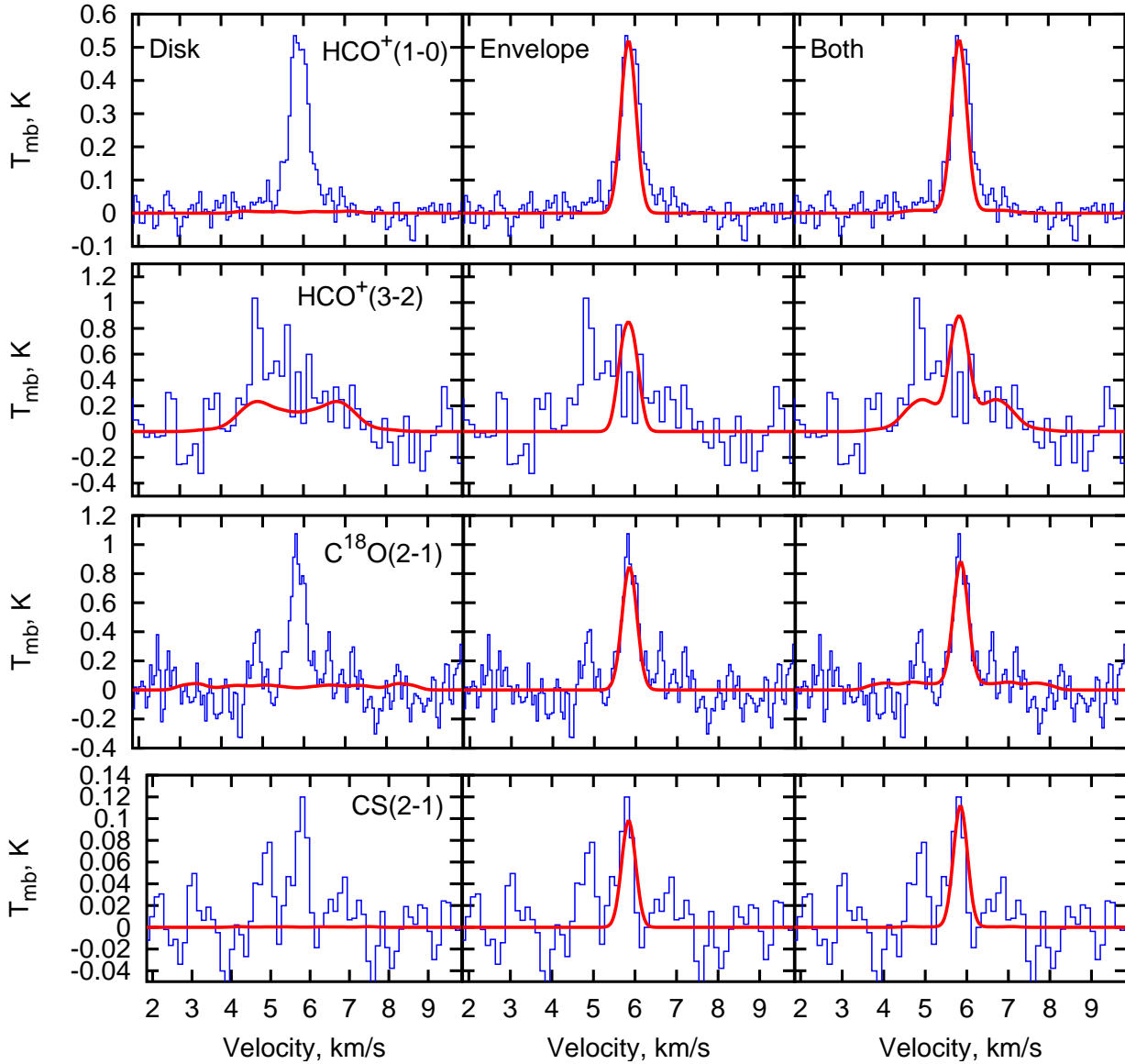
Figure 5.14. Same as in Fig. 5.13 but for the HCO$^+$(1-0) line (top row). In contrast with CO(2-1), this line is optically thin. This is also true for the HCO$^+$(3-2) spectrum, which is shown in the second row from top. Note that the HCO$^+$(3-2) emission generated in the disc contributes much more to the resulting line profile than in the case of the HCO$^+$(1-0) line. The optically thin C^{18}O(2-1) and CS(2-1) lines are depicted in the third and fourth rows from top, respectively. Overall agreement between the observed and modelled spectra is only achieved with the disc-in-envelope model (right panels).

Chapter 6

Conclusions and prospects for the future

In this thesis, I studied the following issues related to the evolution of gas and dust in protoplanetary discs.

First, I modelled the optical characteristics of dust grains expected to be present in Class II discs, ranging from classical homogeneous spheres till complex fractal aggregates and composite porous particles. It was found that the presence of highly absorbing materials, like metallic iron, as well as porosity, affect the optical behaviour of dust grains to a remarkably large degree, especially at $\lambda \gtrsim 100\mu$m. Consequently, it results in various slopes of and a factor of $\lesssim$ 10–100 difference in the computed monochromatic opacities for distinct dust models at (sub-) millimetre wavelengths. Therefore, I conclude that an order-of-magnitude uncertainty in the opacity value must be always kept in mind when one estimates the mass of a disc from the measured continuum flux at $\approx$ 1 mm.

Using these monochromatic values, I calculated the Rosseland and Planck mean dust opacities and unified it with the mean gas opacities in a opacity table which is appropriate for $T \in [5, 10^4]$ K and $\rho \in [10^{-18}, 10^{-7}]$ g cm^{-3}, and freely available in the Internet: `http://www.astro.uni-jena.de/Laboratory/labindex.html`. In addition, I showed that different opacity tables utilised in the same hydrodynamical model lead to different thermal and density structures of the disc, which should be taken into account in interpreting the results of disc chemical modelling.

The opacity project attracted attention of many researchers, studying the evolution of accretion discs. Their feedback was essential to understand what can be done in this area in the coming years. First, it would be important to extend the dust compositional model to other metallicities, and to take into account recent advances in our understanding of the cosmic elemental abundances. Then, much more direct information regarding the dust composition and properties in the Solar system and interstellar medium, and certainly in planet-forming discs at early stages of the evolution will become available after completion of the *Stardust* and particularly *Spitzer* space missions. Thus, this flow of new exciting results and data will certainly require an "update" of the current opacity models.

The next problem I have addressed in the thesis was the possibility to reduce the complexity of chemical networks without loosing accuracy in the time-dependent abundances of pre-selected molecule(s). To do so, I elaborated a rigorous mathematical algorithm and found that significant reduction is possible for some observationally and dynamically important species, but only for a fixed range of physical conditions. This reduction saves computational time and makes the development a coupled and consistent chemo-dynamical models with mixing processes possible. It is also useful for analysing the chemical evolution of particular molecules, since smaller networks can be examined and understood easier than original (larger) ones.

Using this reduction technique, I studied what chemical processes govern the evolution of the ionisation degree in a protoplanetary disc. From a chemical point of view, the disc can be divided in three layers. In the dense and opaque disc midplane the relevant chemistry is simple, as the reduced networks include no more than about 10 species and a similar number of reactions. This is also true for the heavily irradiated surface layer. In contrast, I found that the chemistry in the intermediate layer is controlled by stellar X-rays (inner part) and UV-radiation (outer part) and, thus, has the most

complicated chemistry. In some regions one has to take into account reactions leading to formation and destruction of carbon chains containing up to 6 carbon atoms, as well as sulphur chemistry, which results in reduced networks with over hundred species and reactions.

Also, I computed the location and size of the "dead" zone, where accretion is strongly suppressed due to a too low degree of the fractional ionisation. In many MHD studies of the disc evolution the value of ionisation degree is calculated with a simple equilibrium approach, which, as I have demonstrated, is not appropriate everywhere in the disc. It will be extremely important to investigate how mixing processes (turbulent diffusion, convection, etc.) as well as grain growth and sedimentation may affect these results and if the disc chemical structure has indeed a "layered" appearance.

Despite the value of fundamental theoretical studies, it is always better to confirm their quality by comparison with observations. In this respect, I used for the first time a coherent modelling of the physical structure, chemical evolution, and radiative transfer in molecular lines of the AB Aur system.

The main idea of this study was to determine as many parameters of this system as possible, using available information from the literature before computing the models in a "step-by-step" way and compare the results with modelled line data. This approach also allows defining uncertainties of the model parameters.

First, the AB Aur disc was modelled by the 2D flared passive model with vertical temperature gradient and Keplerian rotation, while the envelope was represented as the infalling isothermal spherical cloud with a central region shadowed by the disc and two wide cones transparent to the stellar radiation. Second, time-dependent molecular abundances were calculated for 3 Myr with the gas-grain chemical network. These abundances were translated to the excitation temperatures, and consequently to the beam-convolved synthetic spectra and a spectral map by the 2D non-LTE line radiative transfer code. These results were compared with the millimetre data *step-by-step*, namely, the orientation of the AB Aur disc was derived first, followed by the disc radius and then its mass, and finally thermal, kinematic, and then the density structures of the envelope were determined.

Overall, it took about 30 iterations (each required $\sim$ 3 days) to constrain all the model parameters and their uncertainties. Given the high number of parameters to be derived and large computational requirements, it could not be done with a χ^2-minimisation technique in the *uv*-plane.

As a result, the best-fit disc model accurately reproduces the observed HCO^+(1-0) interferometric map apart from one corner, where a *local* density enhancement likely affects the observational data. The best-fit envelope model successfully explains the single-dish spectra apart from the CS(5-4) data, which require the presence of small high-density "clumps" in the model. The fact that the AB Aur system looks inhomogeneously on various spatial scales is well established by the visual and especially IR observations.

Therefore, I conclude that from a formal point of view the usual approach to represent a protoplanetary disc or envelope as a homogeneous structure is not valid here, and one has to deal with the full 3D modelling.

The reconstructed infall velocity and density structure of the envelope allowed to estimate an average mass accretion rate in this object, which is close to the measured value. Consequently, the constrained $\lesssim$ 25 Myr lifetime of the AB Aur system is only determined by the initial mass of the envelope matter available for accretion. I argued that such continuous mass supply may be able to drive gravitational instabilities in the outer disc, which in turn regulates accretion and produces the spiral structure, similar to that what has been observed. I conclude that the instantaneous "refinement" of the disc matter by pristine material from the envelope provides a straightforward explanation to the observational fact that the dust in the AB Aur system closely resembles the ISM dust. It will be extremely important to clarify whether the same evolutionary scenario is appropriate for other Herbig Ae/Be systems as well. Another possibility could be that AB Aur is merely younger, $t \sim$ 2 Myr.

Chapter 7

Zusammenfassung

In dieser Dissertation habe ich folgende Sachverhalte untersucht, die eng mit Fragen bezüglich der Entwicklung von Gas und Staub in protoplanetaren Scheiben verbunden sind.

Zunächst habe ich die optischen Eigenschaften von solchen Staubteilchen modelliert, deren Existenz in zirkumstellaren Scheiben bei sogenannten Klasse–II–Quellen allgemein angenommen wird. Dies reicht von klassischen homogenen sphärischen Partikeln bis zu komplexen fraktalen Aggregaten und zusammengesetzten porösen Partikeln. Hierbei zeigte sich, daß durch einen zunehmenden Anteil an hochabsorbierenden Materialien (wie z.B. metallisches Eisen) oder auch durch Porösität die optischen Eigenschaften dieser Staubteilchen in einem beträchtlichen Maße beeinflußt werden, insbesondere im Wellenlängenbereich $\lambda > 100\,\mu$m. Dies führt schließlich zu deutlich unterschiedlichem Wellenlängenverhalten für die berechneten monochromatischen Opazitäten bei den verschiedenen Staubmodellen, wobei die Opazitätswerte im (Sub–)Millimeterbereich um einen Faktor $\lesssim 10-100$ differieren können.

Ausgehend von diesen monochromatischen Werten habe ich die mittleren Rosseland– und Planck–Werte für die Staubopazitäten berechnet. Diese Daten habe ich mit mittleren Gas–Opazitäten kombiniert und eine Opazitätstabelle erstellt, die für den Temperaturbereich $T \in [5, 10^4]$ K und den Dichtebereich $\rho \in [10^{-18}, 10^{-7}]\,\mathrm{g\,cm^{-3}}$ gültig ist. Diese Daten sind frei im Internet verfügbar unter der Adresse: *http://www.astro.uni-jena.de/Laboratory/labindex.html*. Weiterhin konnte ich zeigen, daß die Verwendung verschiedener Opazitätstabellen in (abgesehen davon) identischen hydrodynamischen Modellen zu unterschiedlichen Temperatur– und Dichte–Strukturen in der modellierten Scheibe führt. Dies muß bei der Interpretation von Ergebnissen der chemischen Modellierung solcher Scheiben berücksichtigt werden.

Ein weiteres Problemfeld meiner Dissertation war es, die Möglichkeiten zu untersuchen, wie man die Komplexität von chemischen Netzwerken reduzieren kann, ohne die Genauigkeit bezüglich der zeitabhängigen Häufigkeiten vorher ausgewählter Moleküle einzubüßen. Zu diesem Zweck habe ich einen strengen mathematischen Algorithmus ausgearbeitet, mit dessen Hilfe sich zeigte, daß eine erhebliche Reduzierung für einige beobachtungstechnisch sowie dynamisch wichtige Spezies möglich ist, allerdings nur für jeweils begrenzte Bereiche physikalischer Bedingungen. Unter Zuhilfenahme dieser gefundenen Reduktionstechniken habe ich die chemischen Prozesse untersucht, welche die Entwicklung des Ionisationsgrades in einer protoplanetaren Scheibe bestimmen. Vom chemischen Standpunkt aus gesehen kann die Scheibe in drei Schichten eingeteilt werden. In der dichten und kaum lichtdurchlässigen Scheiben–Mittelebene ist die relevante Chemie einfach, da die reduzierten chemischen Netzwerke nicht mehr als zehn Spezies und nur eine ähnliche Anzahl an Reaktionen enthalten. Zum gleichen Ergebnis komme ich bezüglich der stark vom Zentralstern bestrahlten Oberflächenschicht der zirkumstellaren Scheibe. Im Gegensatz dazu fand ich, daß die Chemie in der Zwischenschicht zwischen Mittelebene und Oberfläche durch stellare Röntgenstrahlung (innerer Teil) und UV–Strahlung (äußerer Teil) bestimmt wird und deshalb von deutlich komplizierterer Natur ist.

In einigen Scheibenbereichen müssen zum einen Reaktionen in Betracht gezogen werden, die zur Ausbildung bzw. Zerstörung von kleinen Kohlenstoff–Ketten mit bis zu sechs Kohlenstoff–Atomen führen, zum anderen Reaktion im Rahmen der Schwefel–Chemie. Somit ergeben sich reduzierte Netzwerke mit über 100 Spezies und Reaktionen.

Ich habe auch die Lage und Größe der sogenannten "toten Zone" berechnet, in welcher die Akkretion von Material stark unterdrückt wird aufgrund eines zu niedrigen Ionisationsgrades. In vielen magneto–hydrodynamischen (MHD) Studien der Scheibenentwicklung wird der Wert des Ionisationsgrades durch einen einfachen Gleichgewichtsansatz berechnet; eine Methode, die, wie ich gezeigt habe, nicht überall in der Scheibe geeignet ist.

Grundsätzliche theoretische Studien haben ihren eigenen Wert. Trotzdem sollte ihre Güte auch durch den Vergleich mit Beobachtungsdaten überprüft werden. Hierfür habe ich, zum ersten Mal, eine Gesamtmodellierung des AB Aur Systems durchgeführt unter Einbeziehung der physikalischen Struktur, der chemischen Entwicklung und des Strahlungstransportes in Moleküllinien in der AB Aur Scheibe.

Zunächst wurde AB Aur als passive, aufgeweitete ("flared") 2D–Scheibe mit vertikalem Temperaturgradienten und Kepler–Rotation modelliert. Die umgebende, einfallende, sphärische Hülle wurde als anfangs isotherm angenommen, wobei eine zentrale Region durch die Scheibe abgeschattet wird, während zwei weite konusförmige Bereiche senkrecht zur Scheibenebene besser durchlässig für die stellare Strahlung sind. Im nächsten Schritt wurden zeitabhängige molekulare Häufigkeiten für einen Zeitabschnitt von 3 Millionen Jahren unter Verwendung eines kombinierten chemischen Netzwerkes für Gas und Staub berechnet. Diese Häufigkeiten wurden in Anregungstemperaturen übersetzt. Schließlich wurden auf dieser Grundlage (unter Berücksichtigung realer Teleskop–Charakteristika) synthetische Spektren sowie eine Spektralkarte mit Hilfe des 2D–Linien–Strahlungstransport–Programms gewonnen. Diese Resultate wurden dann *Schritt für Schritt* mit Beobachtungsdaten im Millimeter–Bereich verglichen. Konkret wurde zunächst die Orientierung der AB Aur–Scheibe abgeleitet, dann der Scheibenradius und die Scheibenmasse. Schließlich wurde die Temperatur– und Dichteverteilung sowie die kinetische Struktur der Hülle bestimmt. Insgesamt wurden 30 Iterationsschritte benötigt (jeweils drei Tage pro Iteration), um alle Modellparameter und deren Unsicherheiten deutlich einzuschränken. Wegen der hohen Zahl von zu bestimmenden Parametern und entsprechend immensen Ansprüchen bei deren Berechnung ist eine einfache χ^2–Minimierung der Parameter–Unsicherheiten nicht möglich.

Als Ergebnis der angewandten Iterationstechnik erhielt ich ein Scheibenmodell, welches zu großen Teilen die existierenden HCO$^+$(1–0)–Interferometrie–Karten reproduzieren kann. In einem Teil der Karte gibt es Abweichungen zwischen Modell und Beobachtung, was sich auf *lokale* Verdichtungen in der realen Scheibe zurückführen läßt. Das am besten angeglichene Hüllenmodell schließlich kann erfolgreich die mit Einzelteleskopen beobachteten CS(5–4)–Daten erklären, wobei dieses spezielle Modell die Anwesenheit von kleinen relativ dichten Klumpen innerhalb der Hülle voraussagt. Die Tatsache, daß das AB Aur–System auf verschiedenen räumlichen Skalen inhomogen aufgebaut erscheint, ist durch optische und insbesondere Infrarot–Beobachtungen bestätigt.

Die rekonstruierten Material–Einfallgeschwindigkeiten und Dichtestrukturen der Hülle erlauben es, eine durchschnittliche Massenakkretionsrate für dieses Objekt anzugeben, welche nahe beim gemessenen Wert ist. Die damit eingegrenzte Lebenszeit des AB Aur Systems von $\lesssim 25$ Millionen Jahren ist somit nur bestimmt durch die Anfangsmasse des für die Akkretion verfügbaren Hüllenmaterials. Ich diskutiere im weiteren die Möglichkeit, daß solch ein kontinuierlicher Massennachschub in der Lage sein kann, gravitative Instabilitäten in der äußeren Scheibe zu erzeugen, was im Gegenzug die Akkretion reguliert und eine Spiralstruktur hervorruft, ähnlich zu den tatsächlich beobachteten Strukturen.

Ich folgere daraus, daß das unverzügliche Nachfüllen von Scheibenmaterie aus dem weiten Reservoir noch nicht veränderten Materials aus der Hülle eine gute Erklärung dafür gibt, daß die beobachteten Staubeigenschaften im AB Aur System recht gut mit denen von interstellarem Staub übereinstimmen. Für die Zukunft wird es sehr wichtig sein herauszufinden, ob das gleiche Entwicklungsszenarium auch für andere Herbig Ae/Be–Sterne zutrifft. Eine andere Möglichkeit könnte darin bestehen, daß das AB Aur–System einfach deutlich jünger ist, nämlich $t \sim 2$ Millionen Jahre.

Bibliography

Adams, N. G., Smith, D., and Millar, T. J.: 1984, The importance of kinetically excited ions in the synthesis of interstellar molecules, *MNRAS* **211**, 857

Adams, W. S.: 1941, What Lies Between the Stars, *PASP* **53**, 73

Aikawa, Y. and Herbst, E.: 1999a, Deuterium Fractionation in Protoplanetary Disks, *ApJ* **526**, 314

Aikawa, Y. and Herbst, E.: 1999b, Molecular evolution in protoplanetary disks. Two-dimensional distributions and column densities of gaseous molecules, *A&A* **351**, 233

Aikawa, Y. and Herbst, E.: 2001, Two-dimensional distributions and column densities of gaseous molecules in protoplanetary disks. II. Deuterated species and UV shielding by ambient clouds, *A&A* **371**, 1107

Aikawa, Y., Miyama, S. M., Nakano, T., and Umebayashi, T.: 1996, Evolution of Molecular Abundance in Gaseous Disks around Young Stars: Depletion of CO Molecules, *ApJ* **467**, 684

Aikawa, Y., van Zadelhoff, G. J., van Dishoeck, E. F., and Herbst, E.: 2002, Warm molecular layers in proto-planetary disks, *A&A* **386**, 622

Alexander, D. R.: 1975, Low-Temperature Rosseland Opacity Tables, *ApJS* **29**, 363

Alexander, D. R., Augason, G. C., and Johnson, H. R.: 1989, An opacity-sampled treatment of water vapor, *ApJ* **345**, 1014

Alexander, D. R. and Ferguson, J. W.: 1994, Low-temperature Rosseland opacities, *ApJ* **437**, 879

Allen, M. and Robinson, G. W.: 1977, The molecular composition of dense interstellar clouds, *ApJ* **212**, 396

Amin, M. Y., Shalabiea, O. M., and Herbst, E.: 1997, New chemical models for dense portions of NGC 7023, *MNRAS* **290**, 347

Anders, E. and Grevesse, N.: 1989, Abundances of the elements - Meteoritic and solar, *Geochim. Cosmochim. Acta* **53**, 197

Armitage, P. J., Clarke, C. J., and Palla, F.: 2003, Dispersion in the lifetime and accretion rate of T Tauri discs, *MNRAS* **342**, 1139

Bacmann, A., Lefloch, B., Ceccarelli, C., Steinacker, J., Castets, A., and Loinard, L.: 2003, CO Depletion and Deuterium Fractionation in Prestellar Cores, *ApJ* **585**, L55

Balbus, S. A. and Hawley, J. F.: 1991, A powerful local shear instability in weakly magnetized disks. I - Linear analysis. II - Nonlinear evolution, *ApJ* **376**, 214

Bates, D. R.: 1951, Rate of formation of molecules by radiative association, *MNRAS* **111**, 303

Bates, D. R. and Herbst, E.: 1988, in T. J. Millar and D. A. Williams (eds.), *ASSL Vol. 146: Rate Coefficients in Astrochemistry*, pp 41–48, Kluwer Academic Publishers, Dordrecht

Bates, D. R. and Spitzer, L. J.: 1951, The Density of Molecules in Interstellar Space., *ApJ* **113**, 441

Bauer, I., Finocchi, F., Duschl, W. J., Gail, H.-P., and Schloeder, J. P.: 1997, Simulation of chemical reactions and dust destruction in protoplanetary accretion disks., *A&A* **317**, 273

Beckwith, S. V. W., Henning, T., and Nakagawa, Y.: 2000, in V. Mannings, A. P. Boss, and S. S. Russell (eds.), *Protostars and Planets IV*, pp 533–558, University of Arizona Press, Tucson

Bell, K. R. and Lin, D. N. C.: 1994, Using FU Orionis outbursts to constrain self-regulated protostellar disk

models, *ApJ* **427**, 987

Bergin, E., Calvet, N., D'Alessio, P., and Herczeg, G. J.: 2003, The Effects of UV Continuum and Lyα Radiation on the Chemical Equilibrium of T Tauri Disks, *ApJ* **591**, L159

Bergin, E. A., Neufeld, D. A., and Melnick, G. J.: 1999, Formation of Interstellar Ices behind Shock Waves, *ApJ* **510**, L145

Bergman, D. J.: 1978, The dielectric constant of a composite material-A problem in classical physics, *Phys. Rep.* **43**, 377

Bernatowicz, T. J., Cowsik, R., Gibbons, P. C., Lodders, K., Fegley, B. J., Amari, S., and Lewis, R. S.: 1996, Constraints on Stellar Grain Formation from Presolar Graphite in the Murchison Meteorite, *ApJ* **472**, 760

Bettens, R. P. A. and Herbst, E.: 1996, The Abundance of Very Large Hydrocarbons and Carbon Clusters in the Diffuse Interstellar Medium, *ApJ* **468**, 686

Biham, O., Furman, I., Pirronello, V., and Vidali, G.: 2001, Master Equation for Hydrogen Recombination on Grain Surfaces, *ApJ* **553**, 595

Black, J. H. and Dalgarno, A.: 1973, The Formation of CH in Interstellar Clouds, *Astrophys. Lett.* **15**, L79

Blaes, O. M. and Balbus, S. A.: 1994, Local shear instabilities in weakly ionized, weakly magnetized disks, *ApJ* **421**, 163

Blum, J., Henning, T., Ossenkopf, V., Sablotny, R., Stognienko, R., and Thamm, E.: 1994, in M. M. Nowak (ed.), *Fractals in the nature and Applied Science (A-41)*, pp 41–59, Elsiever Science

Blum, J., Wurm, G., Poppe, T., Kempf, S., and Kozasa, T.: 2002, First results from the cosmic dust aggregation experiment CODAG, *Advances in Space Research* **29**, 497

Bohren, C. F. and Huffman, D. R.: 1983, *Absorption and scattering of light by small particles*, New York: Wiley

Boogert, A. C. A., Hogerheijde, M. R., and Blake, G. A.: 2002, High-Resolution 4.7 micron Keck/NIRSPEC Spectra of Protostars. I. Ices and Infalling Gas in the Disk of L1489 IRS, *ApJ* **568**, 761

Bourdon, E. B., Prince, R. H., and Duley, W. W.: 1982, An experimental determination of the cross section for photodesorption, *ApJ* **260**, 909

Bouwman, J., Meeus, G., de Koter, A., Hony, S., Dominik, C., and Waters, L. B. F. M.: 2001, Processing of silicate dust grains in Herbig Ae/Be systems, *A&A* **375**, 950

Bouwman, J., Meeus, G., Hony, S., Dominik, C., de Koter, A., and Waters, L. B. F. M.: 2000, in A.-M. L. . S. R. A. Penny, P. Artymowicz (ed.), *IAU Symp. 202: Planetary systems in the universe: observation, formation and evolution*, Astr. Soc. Pacific

Brittain, S. D., Rettig, T. W., Simon, T., Kulesa, C., DiSanti, M. A., and Dello Russo, N.: 2003, CO Emission from Disks around AB Aurigae and HD 141569: Implications for Disk Structure and Planet Formation Timescales, *ApJ* **588**, 535

Brown, P. D., Charnley, S. B., and Millar, T. J.: 1988, A model of the chemistry in hot molecular cores, *MNRAS* **231**, 409

Brown, P. N., Byrne, G. D., and Hindmarsh, A. C.: 1989, VODE: A Variable Coefficient ODE Solver, *J. Sci. Stat. Comput.* **10**, 1038

Brownlee, D. E., Tsou, P., Anderson, J. D., Hanner, M. S., Newburn, R. L., Sekanina, Z., Clark, B. C., Hörz, F., Zolensky, M. E., Kissel, J., McDonnell, J. A. M., Sandford, S. A., and Tuzzolino, A. J.: 2003, Stardust: Comet and interstellar dust sample return mission, *Journal of Geophysical Research (Planets)* **108-E10**, 1

Bruggeman, D. A. G.: 1935, The calculation of various physical constants of heterogeneous substances. I. The dielectric constants and conductivities of mixtures composed of isotropic substances, *Annalen der Physik*

24, 636

Buch, V. and Zhang, Q.: 1991, Sticking probability of H and D atoms on amorphous ice - A computational study, *ApJ* **379**, 647

Bujarrabal, V., Alcolea, J., Neri, R., and Grewing, M.: 1997, The mass and temperature distribution in the protoplanetary nebula M 1-92: ^{13}CO interferometric observations., *A&A* **320**, 540

Burke, J. R. and Hollenbach, D. J.: 1983, The gas-grain interaction in the interstellar medium - Thermal accommodation and trapping, *ApJ* **265**, 223

Butler, P., Vogt, S. S., Marcy, G. W., Fischer, D. A., Wright, J. T., Henry, G. W., Laughlin, G., and Lissauer, J.: 2004, A Neptune-Mass Planet Orbiting the Nearby M Dwarf GJ 436, *ArXiv Astrophysics e-prints*, astro-ph/0408587

Cameron, A. G. W.: 1995, The first ten million years in the solar nebula, *Meteoritics* **30**, 133

Caselli, P., Hasegawa, T. I., and Herbst, E.: 1998, A Proposed Modification of the Rate Equations for Reactions on Grain Surfaces, *ApJ* **495**, 309

Cassen, P. and Moosman, A.: 1981, On the formation of protostellar disks, *Icarus* **48**, 353

Ceccarelli, C., Dominik, C., Lefloch, B., Caselli, P., and Caux, E.: 2004, Detection of H$_2$D$^+$: Measuring the Midplane Degree of Ionization in the Disks of DM Tauri and TW Hydrae, *ApJ* **607**, L51

Charnley, S. B., Hartquist, T. W., Dyson, J. E., and Williams, D. A.: 1990, Chemical evolution in molecular clump-stellar wind interfaces, *MNRAS* **243**, 405

Charnley, S. B., Tielens, A. G. G. M., and Rodgers, S. D.: 1997, Deuterated Methanol in the Orion Compact Ridge, *ApJ* **482**, L203

Chase, Jr, M. W., Davies, C. A., Downey, Jr., J. R., Frurip, D. J., McDonald, R. A., and Syverud, A. N.: 1986, *JANAF Thermochemical Tables*, Part I, American Chemical Society, American Institute of Physics, New York, third edition

Chiang, E. I. and Goldreich, P.: 1997, Spectral Energy Distributions of T Tauri Stars with Passive Circumstellar Disks, *ApJ* **490**, 368

Clary, D. C.: 1988, in T. J. Millar and D. A. Williams (eds.), *ASSL Vol. 146: Rate Coefficients in Astrochemistry*, pp 1–24, Kluwer Academic Publishers, Dordrecht

Clary, D. C., Haider, N., Husain, D., and Kabir, M.: 1994, Interstellar carbon chemistry: Reaction rates of neutral atomic carbon with organic molecules, *ApJ* **422**, 416

Cox, A. N. and Stewart, J. N.: 1970a, Rosseland Opacity Tables for Population i Compositions, *ApJS* **19**, 243

Cox, A. N. and Stewart, J. N.: 1970b, Rosseland Opacity Tables for Population II Compositions, *ApJS* **19**, 261

Crovisier, J., Leech, K., Bockelee-Morvan, D., Brooke, T. Y., Hanner, M. S., Altieri, B., Keller, H. U., and Lellouch, E.: 1997, The spectrum of Comet Hale-Bopp (C/1995 01) observed with the Infrared Space Observatory at 2.9 AU from the Sun, *Science* **275**, 1904

D'Alessio, P., Calvet, N., and Hartmann, L.: 2001, Accretion Disks around Young Objects. III. Grain Growth, *ApJ* **553**, 321

Dalgarno, A. and Black, J. H.: 1976, Molecule formation in the interstellar gas, *Reports of Progress in Physics* **39**, 573

Dalgarno, A. and McCray, R. A.: 1972, Heating and Ionization of HI Regions, *ARA&A* **10**, 375

Dalgarno, A. and Roberge, W. G.: 1979, Collision-induced dissociation of interstellar molecules, *ApJ* **233**, L25

Dalgarno, A. and Stephens, T. L.: 1970, Discrete Absorption and Photodissociation of Molecular Hydrogen, *ApJ* **160**, L107

D'Angelo, D.: 2001, private communication

Dartois, E., Dutrey, A., and Guilloteau, S.: 2003, Structure of the DM Tau Outer Disk: Probing the vertical kinetic temperature gradient, *A&A* **399**, 773

DeWarf, L. E., Sepinsky, J. F., Guinan, E. F., Ribas, I., and Nadalin, I.: 2003, Intrinsic Properties of the Young Stellar Object SU Aurigae, *ApJ* **590**, 357

d'Hendecourt, L. B., Allamandola, L. J., Baas, F., and Greenberg, J. M.: 1982, Interstellar grain explosions - Molecule cycling between gas and dust, *A&A* **109**, L12

d'Hendecourt, L. B., Allamandola, L. J., and Greenberg, J. M.: 1985, Time dependent chemistry in dense molecular clouds. I - Grain surface reactions, gas/grain interactions and infrared spectroscopy, *A&A* **152**, 130

Di Francesco, J., Evans, N. J., Harvey, P. M., Mundy, L. G., and Butner, H. M.: 1998, High-Resolution Far-Infrared Studies of Intermediate-Mass Pre-Main-Sequence Objects, *ApJ* **509**, 324

Di Francesco, J., Evans, N. J., Harvey, P. M., Mundy, L. G., Guilloteau, S., and Chandler, C. J.: 1997, Millimeter and Radio Interferometry of Herbig Ae/Be Stars, *ApJ* **482**, 433

Dolginov, A. Z. and Stepinski, T. F.: 1994, Are cosmic rays effective for ionization of protoplanetary disks?, *ApJ* **427**, 377

Dominik, C., Dullemond, C. P., Waters, L. B. F. M., and Walch, S.: 2003, Understanding the spectra of isolated Herbig stars in the frame of a passive disk model, *A&A* **398**, 607

Draine, B. T.: 1978, Photoelectric heating of interstellar gas, *ApJS* **36**, 595

Draine, B. T. and Bertoldi, F.: 1996, Structure of Stationary Photodissociation Fronts, *ApJ* **468**, 269

Draine, B. T. and Lee, H. M.: 1984, Optical properties of interstellar graphite and silicate grains, *ApJ* **285**, 89

Dubrulle, B., Morfill, G., and Sterzik, M.: 1995, Dust diffusion, sedimentation, and gravitational instabilities in protoplanetary disks, *Icarus* **114**, 237

Dullemond, C. P. and Dominik, C.: 2004, Flaring vs. self-shadowed disks: The SEDs of Herbig Ae/Be stars, *A&A* **417**, 159

Dunham, T.: 1937, Interstellar Neutral Potassium and Neutral Calcium, *PASP* **49**, 26

Dunham, T. and Adams, W. S.: 1941, Iron as an Interstellar Gas, *PASP* **53**, 341

Dutrey, A., Guilloteau, S., and Guelin, M.: 1997, Chemistry of protosolar-like nebulae: The molecular content of the DM Tau and GG Tau disks., *A&A* **317**, L55

Eisner, J. A., Lane, B. F., Akeson, R. L., Hillenbrand, L. A., and Sargent, A. I.: 2003, Near-Infrared Interferometric Measurements of Herbig Ae/Be Stars, *ApJ* **588**, 360

El-Nawawy, M. S., Ateya, B. G., and Aiad, A.: 1992, The charge state in a highly dense molecular cloud, *Ap&SS* **190**, 257

Elia, D., Strafella, F., Campeggio, L., Giannini, T., Lorenzetti, D., Nisini, B., and Pezzuto, S.: 2004, Modeling the Continuum Emission from the Circumstellar Environment of Herbig Ae/Be Stars, *ApJ* **601**, 1000

Feigelson, E. D. and Lawson, W. A.: 2004, An X-Ray Census of Young Stars in the Chamaeleon I North Cloud, *ApJ* **614**, 267

Feigelson, E. D. and Montmerle, T.: 1999, High-Energy Processes in Young Stellar Objects, *ARA&A* **37**, 363

Finocchi, F. and Gail, H.-P.: 1997, Chemical reactions in protoplanetary accretion disks. III. The role of ionisation processes., *A&A* **327**, 825

Finocchi, F., Gail, H.-P., and Duschl, W. J.: 1997, Chemical reactions in protoplanetary accretion disks. II. Carbon dust oxidation., *A&A* **325**, 1264

Fleming, T. and Stone, J. M.: 2003, Local Magnetohydrodynamic Models of Layered Accretion Disks, *ApJ* **585**, 908

Flower, D. R. and Launay, J. M.: 1985, Rate coefficients for the rotational excitation of CO by ortho- and para-H$_2$, *MNRAS* **214**, 271

Fromang, S., Terquem, C., and Balbus, S. A.: 2002, The ionization fraction in α models of protoplanetary discs, *MNRAS* **329**, 18

Fromang, S., Terquem, C., Balbus, S. A., and De Villiers, J.: 2004, Evolution of massive and magnetized protoplanetary disks, *ArXiv Astrophysics e-prints*, astro-ph/0402373

Fuchs, R.: 1975, Theory of the optical properties of ionic crystal cubes, *Phys. Rev. B* **11**, 1732

Fuente, A., Martın-Pintado, J., Bachiller, R., Rodrıguez-Franco, A., and Palla, F.: 2002, The history of mass dispersal around Herbig Ae/Be stars, *A&A* **387**, 977

Fukagawa, M., Hayashi, M., Tamura, M., Itoh, Y., Hayashi, S. S., Oasa, Y., Takeuchi, T., Morino, J., Murakawa, K., Oya, S., Yamashita, T., Suto, H., Mayama, S., Naoi, T., Ishii, M., Pyo, T., Nishikawa, T., Takato, N., Usuda, T., Ando, H., Iye, M., Miyama, S. M., and Kaifu, N.: 2004, Spiral Structure in the Circumstellar Disk around AB Aurigae, *ApJ* **605**, L53

Gail, H.-P.: 2001, Radial mixing in protoplanetary accretion disks. I. Stationary disc models with annealing and carbon combustion, *A&A* **378**, 192

Gail, H.-P.: 2002, Radial mixing in protoplanetary accretion disks. III. Carbon dust oxidation and abundance of hydrocarbons in comets, *A&A* **390**, 253

Gammie, C. F.: 1996, Layered Accretion in T Tauri Disks, *ApJ* **457**, 355

Ghosh, K. and Fuchs, R.: 1991, Critical behavior in the dielectric properties of random self-similar composites, *Phys. Rev. B* **44**, 7330

Glassgold, A. E., Lucas, R., and Omont, A.: 1986, Molecular ions in the circumstellar envelope of IRC+10216, *A&A* **157**, 35

Glassgold, A. E., Najita, J., and Igea, J.: 1997a, X-Ray Ionization of Protoplanetary Disks, *ApJ* **480**, 344

Glassgold, A. E., Najita, J., and Igea, J.: 1997b, X-Ray Ionization of Protoplanetary Disks: Erratum, *ApJ* **485**, 920

Grady, C. A., Perez, M. R., Talavera, A., Bjorkman, K. S., de Winter, D., The, P.-S., Molster, F. J., van den Ancker, M. E., Sitko, M. L., Morrison, N. D., Beaver, M. L., McCollum, B., and Castelaz, M. W.: 1996, The β Pictoris phenomenon among Herbig Ae/Be stars. UV and optical high dispersion spectra., *A&AS* **120**, 157

Grady, C. A., Woodgate, B., Bruhweiler, F. C., Boggess, A., Plait, P., Lindler, D. J., Clampin, M., and Kalas, P.: 1999, Hubble Space Telescope Space Telescope Imaging Spectrograph Coronagraphic Imaging of the Herbig Ae Star AB Aurigae, *ApJ* **523**, L151

Greaves, J. S., Holland, W. S., Moriarty-Schieven, G., Jenness, T., Dent, W. R. F., Zuckerman, B., McCarthy, C., Webb, R. A., Butner, H. M., Gear, W. K., and Walker, H. J.: 1998, A Dust Ring around epsilon Eridani: Analog to the Young Solar System, *ApJ* **506**, L133

Gredel, R., Lepp, S., and Dalgarno, A.: 1987, The C/CO ratio in dense interstellar clouds, *ApJ* **323**, L137

Gredel, R., Lepp, S., Dalgarno, A., and Herbst, E.: 1989, Cosmic-ray-induced photodissociation and photoionization rates of interstellar molecules, *ApJ* **347**, 289

Green, N. J. B., Toniazzo, T., Pilling, M. J., Ruffle, D. P., Bell, N., and Hartquist, T. W.: 2001, A stochastic approach to grain surface chemical kinetics, *A&A* **375**, 1111

Green, S.: 1975, Rotational excitation of molecular ions in interstellar clouds, *ApJ* **201**, 366

Green, S. and Chapman, S.: 1978, Collisional excitation of interstellar molecules - Linear molecules CO, CS, OCS, and HC$_3$N, *ApJS* **37**, 169

Greenberg, J. M.: 1967, Models of Interstellar Grains., *AJ* **72**, 800

Greenberg, J. M.: 1973, in M. Gordon and L. Snyder (eds.), *Molecules in the Galactic Environment*, pp 93–142, New York, John Wiley and Sons

Grevesse, N. and Sauval, A. J.: 1998, Standard Solar Composition, *Space Science Reviews* **85**, 161

Grinin, V. P. and Rostopchina, A. N.: 1996, Orientation of circumstellar disks and the statistics of H$_\alpha$ profiles of Ae/Be Herbig stars, *Astronomy Reports* **40**, 171

Guilloteau, S. and Dutrey, A.: 1998, Physical parameters of the Keplerian protoplanetary disk of DM Tauri, *A&A* **339**, 467

Gurvich, I., Kleiman, M., Shiloah, N., and Oaknin, D.: 2005, *J. Quant. Spec. Radiat. Transf.*, in prep.

Gurvich, I., Shiloah, N., and Kleiman, M.: 2001, Calculations of the Mie scattering coefficients for multilayered particles with large size parameters, *J. Quant. Spec. Radiat. Transf.* **70**, 433

Habing, H. J.: 1968, The interstellar radiation density between 912 A and 2400 A, *Bull. Astron. Inst. Netherlands* **19**, 421

Haisch, K. E., Lada, E. A., and Lada, C. J.: 2001, Disk Frequencies and Lifetimes in Young Clusters, *ApJ* **553**, L153

Hartquist, T. W. and Williams, D. A.: 1990, Cosmic-Ray Induced Desorption and High Depletions in Dense Cores, *MNRAS* **247**, 343

Hasegawa, T. I. and Herbst, E.: 1993, Three-Phase Chemical Models of Dense Interstellar Clouds - Gas Dust Particle Mantles and Dust Particle Surfaces, *MNRAS* **263**, 589

Hasegawa, T. I., Herbst, E., and Leung, C. M.: 1992, Models of gas-grain chemistry in dense interstellar clouds with complex organic molecules, *ApJS* **82**, 167

Hayashi, C.: 1981, Structure of the solar nebula, growth and decay of magnetic fields and effects of magnetic and turbulent viscosities on the nebula, *Progress of Theoretical Physics Supplement* **70**, 35

Hayashi, C., Nakazawa, K., and Nakagawa, Y.: 1985, in D. C. Black and M. S. Matthews (eds.), *Protostars and Planets II*, pp 1100–1153, University of Arizona Press, Tucson

Helling, C.: 1999, *Ph.D. thesis*, TU Berlin

Helling, C., Winters, J. M., and Sedlmayr, E.: 2000, Circumstellar dust shells around long-period variables. VII. The role of molecular opacities, *A&A* **358**, 651

Henning, T., Burkert, A., Launhardt, R., Leinert, C., and Stecklum, B.: 1998, Infrared imaging and millimetre continuum mapping of Herbig Ae/Be and FU Orionis stars, *A&A* **336**, 565

Henning, T. and Stognienko, R.: 1996, Dust opacities for protoplanetary accretion disks: influence of dust aggregates., *A&A* **311**, 291

Herbig, G. H.: 1960, The Spectra of Be- and Ae-TYPE Stars Associated with Nebulosity, *ApJS* **4**, 337

Herbig, G. H. and Goodrich, R. W.: 1986, Near-simultaneous ultraviolet and optical spectrophotometry of T Tauri stars, *ApJ* **309**, 294

Herbst, E.: 1980, An additional uncertainty in calculated radiative association rates of molecular formation at low temperatures, *ApJ* **241**, 197

Herbst, E.: 1985, An update of and suggested increase in calculated radiative association rate coefficients, *ApJ* **291**, 226

Herbst, E.: 1987, Can gas phase reactions produce complex oxygen-containing molecules in dense interstellar

clouds? - A revision of some important radiative association rate coefficients, *ApJ* **313**, 867

Herbst, E.: 1993, in T. Millar and D. Williams (eds.), *Dust and Chemistry in Astronomy*, pp 183–204, Institute of Physics Publishing

Herbst, E. and Klemperer, W.: 1973, The Formation and Depletion of Molecules in Dense Interstellar Clouds, *ApJ* **185**, 505

Hillenbrand, L. A., Strom, S. E., Vrba, F. J., and Keene, J.: 1992, Herbig Ae/Be stars - Intermediate-mass stars surrounded by massive circumstellar accretion disks, *ApJ* **397**, 613

Hinsen, K. and Felderhof, B. U.: 1992, Dielectric constant of a suspension of uniform spheres, *Phys. Rev. B* **46**, 12955

Hogerheijde, M. R.: 2001, From Infall to Rotation around Young Stellar Objects: A Transitional Phase with a 2000 AU Radius Contracting Disk?, *ApJ* **553**, 618

Hogerheijde, M. R.: 2003, in M. Burton, R. Jayawardhana, and T. Bourke (eds.), *IAU Symp. 221: Star formation at high angular resolution*, p. 105, Astr. Soc. Pacific

Hogerheijde, M. R. and van der Tak, F. F. S.: 2000, An accelerated Monte Carlo method to solve two-dimensional radiative transfer and molecular excitation. With applications to axisymmetric models of star formation, *A&A* **362**, 697

Hollenbach, D. and McKee, C. F.: 1979, Molecule formation and infrared emission in fast interstellar shocks. I Physical processes, *ApJS* **41**, 555

Hollenbach, D. and Salpeter, E. E.: 1971, Surface Recombination of Hydrogen Molecules, *ApJ* **163**, 155

Huntress, W. T. and Mitchell, G. F.: 1979, The synthesis of complex molecules in interstellar clouds, *ApJ* **231**, 456

Igea, J. and Glassgold, A. E.: 1999, X-Ray Ionization of the Disks of Young Stellar Objects, *ApJ* **518**, 848

Ilgner, M.: 2003, *Ph.D. thesis*, Universität Jena

Ilgner, M., Henning, T., Markwick, A. J., and Millar, T. J.: 2004, Transport processes and chemical evolution in steady accretion disk flows, *A&A* **415**, 643

Imhoff, C. L. and Appenzeller, I.: 1987, in *ASSL Vol. 129: Exploring the Universe with the IUE Satellite*, pp 295–319, D. Reidel Publishing Co., Dordrecht

Jäger, C., Il'in, V. B., Henning, T., Mutschke, H., Fabian, D., Semenov, D., and Voshchinnikov, N.: 2003, A Database of Optical Constants of Cosmic Dust Analogs, *J. Quant. Spec. Radiat. Transf.* **79**, 765

Jessberger, E. K., Christoforidis, A., and Kissel, J.: 1988, Aspects of the major element composition of Halley's dust, *Nature* **332**, 691

Jones, A. P. and Williams, D. A.: 1985, Time-dependent sticking coefficients and mantle growth on interstellar grains, *MNRAS* **217**, 413

Jones, H. R. A., Paul Butler, R., Tinney, C. G., Marcy, G. W., Penny, A. J., McCarthy, C., Carter, B. D., and Pourbaix, D.: 2002, A probable planetary companion to HD 39091 from the Anglo-Australian Planet Search, *MNRAS* **333**, 871

Jørgensen, U. G.: 2003, in I. Hubeny, D. Mihalas, and K. Werner (eds.), *ASP Conf. Ser. 288: Stellar Atmosphere Modeling*, pp 303–318, San Francisco: Astronomical Society of the Pacific

Jura, M.: 1975, Interstellar clouds containing optically thin H_2, *ApJ* **197**, 575

Jura, M. and Werner, M. W.: 1999, The Detached Dust Shell around the Massive Star HD 179821, *ApJ* **525**, L113

Kant, I.: 1798, *Allgemeine Naturgeschichte und Theorie des Himmels*, Zeitz, Bei W. Webel, 1798. Neue aufl.

Kempf, S., Pfalzner, S., and Henning, T. K.: 1999, N-Particle-Simulations of Dust Growth. I. Growth Driven by Brownian Motion, *Icarus* **141**, 388

Kenyon, S. J. and Hartmann, L.: 1987, Spectral energy distributions of T Tauri stars - Disk flaring and limits on accretion, *ApJ* **323**, 714

Kesselman, V. S.: 1980, Coagulation of interstellar dust in a turbulent gas, *AZh* **57**, 566

Klahr, H. H. and Bodenheimer, P.: 2003, Turbulence in Accretion Disks: Vorticity Generation and Angular Momentum Transport via the Global Baroclinic Instability, *ApJ* **582**, 869

Kuan, Y.-J., Charnley, S. B., Huang, H.-C., Tseng, W.-L., and Kisiel, Z.: 2003, Interstellar glycine, *ApJ* **593**, 848

Kurucz, R.: 1993, ATLAS9 Stellar Atmosphere Programs and 2 km/s grid., *ATLAS9 Stellar Atmosphere Programs and 2 km/s grid. Kurucz CD-ROM No. 13. Cambridge, Mass.: Smithsonian Astrophysical Observatory, 1993.* 13

Lada, C. J.: 1999, in C. J. Lada and N. D. Kylafis (eds.), *NATO ASIC Proc. 540: The Origin of Stars and Planetary Systems*, pp 143–192, Kluwer Academic Publishers

Langer, W. D., Velusamy, T., Kuiper, T. B. H., Peng, R., McCarthy, M. C., Travers, M. J., Kovacs, A., Gottlieb, C. A., and Thaddeus, P.: 1997, First Astronomical Detection of the Cumulene Carbon Chain Molecule H_2C_6 in TMC-1, *ApJ* **480**, L63

Laplace, S.: 1796, *Exposition du Systéme du Monde*

Larson, R. B.: 2003, The physics of star formation, *Reports of Progress in Physics* **66**, 1651

Le Teuff, Y. H., Millar, T. J., and Markwick, A. J.: 2000, The UMIST database for astrochemistry 1999, *A&AS* **146**, 157

Lee, H.-H., Herbst, E., Pineau des Forets, G., Roueff, E., and Le Bourlot, J.: 1996, Photodissociation of H_2 and CO and time dependent chemistry in inhomogeneous interstellar clouds., *A&A* **311**, 690

Lee, H.-H., Roueff, E., Pineau des Forets, G., Shalabiea, O. M., Terzieva, R., and Herbst, E.: 1998, Bistability in large chemical networks: a global view, *A&A* **334**, 1047

Leger, A., Jura, M., and Omont, A.: 1985, Desorption from interstellar grains, *A&A* **144**, 147

Lenzuni, P., Gail, H., and Henning, T.: 1995, Dust Evaporation in Protostellar Cores, *ApJ* **447**, 848

Lepp, S. and Dalgarno, A.: 1996, X-ray-induced chemistry of interstellar clouds., *A&A* **306**, L21

Leung, C.-M. and Liszt, H. S.: 1976, Radiation transport and non-LTE analysis of interstellar molecular lines. I - Carbon monoxide, *ApJ* **208**, 732

Lin, D. N. C. and Papaloizou, J.: 1980, On the structure and evolution of the primordial solar nebula, *MNRAS* **191**, 37

Liszt, H. S. and Leung, C. M.: 1977, Radiation transport and non-LTE analysis of interstellar molecular lines. II - Carbon monosulfide, *ApJ* **218**, 396

Lynden-Bell, D. and Pringle, J. E.: 1974, The evolution of viscous discs and the origin of the nebular variables., *MNRAS* **168**, 603

Maloney, P. R., Hollenbach, D. J., and Tielens, A. G. G. M.: 1996, X-Ray–irradiated Molecular Gas. I. Physical Processes and General Results, *ApJ* **466**, 561

Mannings, V., Boss, A. P., and Russell, S. S. (eds.): 2000, *Protostars and Planets IV*, University of Arizona Press, Tucson

Mannings, V. and Sargent, A. I.: 1997, A High-Resolution Study of Gas and Dust around Young Intermediate-Mass Stars: Evidence for Circumstellar Disks in Herbig Ae Systems, *ApJ* **490**, 792

Marcy, G. W. and Butler, R. P.: 2000, Planets Orbiting Other Suns, *PASP* **112**, 137

Markwick, A. J., Ilgner, M., Millar, T. J., and Henning, T.: 2002, Molecular distributions in the inner regions of protostellar disks, *A&A* **385**, 632

Marsh, K. A., Van Cleve, J. E., Mahoney, M. J., Hayward, T. L., and Houck, J. R.: 1995, Spatially Resolved Mid-Infrared Observations of Circumstellar Dust around AB Aurigae, *ApJ* **451**, 777

Mathis, J. S., Rumpl, W., and Nordsieck, K. H.: 1977, The size distribution of interstellar grains, *ApJ* **217**, 425

Mattera, L.: 1978, *Ph.D. thesis*, University of Waterloo, Canada

McArthur, B. E., Endl, M., Cochran, W. D., Benedict, G. F., Fischer, D. A., Marcy, G. W., Butler, R. P., Naef, D., Mayor, M., Queloz, D., Udry, S., and Harrison, T. E.: 2004, Detection of a NEPTUNE-mass planet in the ρ_1 Cancri system using the Hobby-Eberly Telescope, *ArXiv Astrophysics e-prints*, astro-ph/0408585

McEwan, M. J., Scott, G. B. I., Adams, N. G., Babcock, L. M., Terzieva, R., and Herbst, E.: 1999, New H and H_2 Reactions with Small Hydrocarbon Ions and Their Roles in Benzene Synthesis in Dense Interstellar Clouds, *ApJ* **513**, 287

Meeus, G., Waters, L. B. F. M., Bouwman, J., van den Ancker, M. E., Waelkens, C., and Malfait, K.: 2001, ISO spectroscopy of circumstellar dust in 14 Herbig Ae/Be systems: Towards an understanding of dust processing, *A&A* **365**, 476

Messenger, S.: 2000, Identification of molecular-cloud material in interplanetary dust particles, *Nature* **404**, 968

Meyer, D. M. and Roth, K. C.: 1991, Discovery of interstellar NH, *ApJ* **376**, L49

Mie, G.: 1908, Beiträge zur Optik trüber Medien, speziell kolloidaler Metallösungen, *Ann. Phys.* **25**, 377

Mihalas, D.: 1978, *Stellar atmospheres /2nd edition/*, San Francisco, W. H. Freeman and Co., 1978. 650 p.

Millan-Gabet, R., Schloerb, F. P., and Traub, W. A.: 2001, Spatially Resolved Circumstellar Structure of Herbig Ae/Be Stars in the Near-Infrared, *ApJ* **546**, 358

Millan-Gabet, R., Schloerb, F. P., Traub, W. A., Malbet, F., Berger, J. P., and Bregman, J. D.: 1999, Sub-Astronomical Unit Structure of the Near-Infrared Emission from AB Aurigae, *ApJ* **513**, L131

Millar, T. J.: 2000, The Evolution of Solar Systems, *Contemporary Physics* **41**, 191

Millar, T. J.: 2003, Deuterium Fractionation in Interstellar Clouds, *Space Science Reviews* **106**, 73

Millar, T.-J., Bennett, A., and Herbst, E.: 1989, Deuterium fractionation in dense interstellar clouds, *ApJ* **340**, 906

Millar, T. J., Bennett, A., Rawlings, J. M. C., Brown, P. D., and Charnley, S. B.: 1991, Gas phase reactions and rate coefficients for use in astrochemistry - The UMIST ratefile, *A&AS* **87**, 585

Millar, T. J., Defrees, D. J., McLean, A. D., and Herbst, E.: 1988, The sensitivity of gas-phase models of dense interstellar clouds to changes in dissociative recombination branching ratios, *A&A* **194**, 250

Millar, T. J., Farquhar, P. R. A., and Willacy, K.: 1997, The UMIST Database for Astrochemistry 1995, *A&AS* **121**, 139

Millar, T. J., Nomura, H., and Markwick, A. J.: 2003, in R. J. . T. B. M. Burton (ed.), *IAU Symp. 221: Star formation at high angular resolution*, Astr. Soc. Pacific

Millar, T. J. and Williams, D. A. (eds.): 1988, *Rate coefficients in astrochemistry*, Kluwer Academic Publishers, Dordrecht

Miroshnichenko, A., Ivezić , Ž., Vinković , D., and Elitzur, M.: 1999, Dust Emission from Herbig Ae/Be Stars: Evidence for Disks and Envelopes, *ApJ* **520**, L115

Mizuno, H., Markiewicz, W. J., and Voelk, H. J.: 1988, Grain growth in turbulent protoplanetary accretion

disks, *A&A* **195**, 183

Monteiro, T. S.: 1985, Rotational excitation of HCO$^+$ by collisions with H$_2$, *MNRAS* **214**, 419

Montmerle, T., Feigelson, E. D., Bouvier, J., and Andre, P.: 1993, in E. H. Levy and J. I. Lunine (eds.), *Protostars and Planets III*, pp 689–717, University of Arizona Press, Tucson

Montmerle, T., Koch-Miramond, L., Falgarone, E., and Grindlay, J. E.: 1983, Einstein observations of the Rho Ophiuchi dark cloud - an X-ray Christmas tree, *ApJ* **269**, 182

Najita, J., Bergin, E. A., and Ullom, J. N.: 2001, X-Ray Desorption of Molecules from Grains in Protoplanetary Disks, *ApJ* **561**, 880

Nakajima, T. and Golimowski, D. A.: 1995, Coronagraphic imaging of pre-main-sequence stars: Remnant evvelopes of star formation seen in reflection, *AJ* **109**, 1181

Natta, A., Prusti, T., Neri, R., Wooden, D., Grinin, V. P., and Mannings, V.: 2001, A reconsideration of disk properties in Herbig Ae stars, *A&A* **371**, 186

Neufeld, D. A., Maloney, P. R., and Conger, S.: 1994, Water maser emission from X-ray-heated circumnuclear gas in active galaxies, *ApJ* **436**, L127

Nishi, R., Nakano, T., and Umebayashi, T.: 1991, Magnetic flux loss from interstellar clouds with various grain-size distributions, *ApJ* **368**, 181

Nuth, J. A. and Berg, O.: 1994, in *Lunar and Planetary Institute Conference Abstracts*, pp 1011–1011

Ohishi, M., Irvine, W. M., and Kaifu, N.: 1992, in P. D. Singh (ed.), *IAU Symp. 150: Astrochemistry of Cosmic Phenomena*, pp 171–177, Kluwer Academic Publishers, Dordrecht

Oppenheimer, M. and Dalgarno, A.: 1974, The Fractional Ionization in Dense Interstellar Clouds, *ApJ* **192**, 29

Ossenkopf, V.: 1991, Effective-medium theories for cosmic dust grains, *A&A* **251**, 210

Ossenkopf, V. and Henning, T.: 1994, Dust opacities for protostellar cores, *A&A* **291**, 943

Papaloizou, J. C. B., Terquem, C., and Nelson, R. P.: 1999, in J. A. Sellwood and J. Goodman (eds.), *ASP Conf. Ser. 160: Astrophysical Discs - an EC Summer School*, pp 186–206

Parise, B., Castets, A., Herbst, E., Caux, E., Ceccarelli, C., Mukhopadhyay, I., and Tielens, A. G. G. M.: 2004, First detection of triply-deuterated methanol, *A&A* **416**, 159

Pavlyuchenkov, Y. N. and Shustov, B. M.: 2004, A Method for Molecular-Line Radiative-Transfer Computations and Its Application to a Two-Dimensional Model for the Starless Core L1544, *Astronomy Reports* **48**, 315

Perez, M. R. and Grady, C. A.: 1997, Observational Overview of Young Intermediate-Mass Objects: Herbig Ae/Be Stars, *Space Science Reviews* **82**, 407

Piétu, V., Dutrey, A., and Kahane, C.: 2003, A Keplerian disk around the Herbig Ae star HD 34282, *A&A* **398**, 565

Pietu, V., Guilloteau, S., and Dutrey, A.: 2005, *Sub-arcsec imaging of the AB Aur molecular disk and envelope at millimeter wavelengths*, A&A, submitted

Piskunov, N., Wood, B. E., Linsky, J. L., Dempsey, R. C., and Ayres, T. R.: 1997, Local Interstellar Medium Properties and Deuterium Abundances for the Lines of Sight toward HR 1099, 31 Comae, beta Ceti, and beta Cassiopeiae, *ApJ* **474**, 315

Pollack, J. B., Hollenbach, D., Beckwith, S., Simonelli, D. P., Roush, T., and Fong, W.: 1994, Composition and radiative properties of grains in molecular clouds and accretion disks, *ApJ* **421**, 615

Pollack, J. B., McKay, C. P., and Christofferson, B. M.: 1985, A calculation of the Rosseland mean opacity of dust grains in primordial solar system nebulae, *Icarus* **64**, 471

Prasad, S. S. and Tarafdar, S. P.: 1983, UV radiation field inside dense clouds - Its possible existence and chemical implications, *ApJ* **267**, 603

Qi, C., Ho, P. T. P., Wilner, D. J., Takakuwa, S., Hirano, N., Ohashi, N., Bourke, T. L., Zhang, Q., Blake, G. A., Hogerheijde, M., Saito, M., Choi, M., and Yang, J.: 2004, Imaging the Disk around TW Hya with the Submillimeter Array, *ArXiv Astrophysics e-prints*, astro-ph/0403412

Qi, C.: 2000, *Ph.D. thesis*, California Institute of Technology, Pasadena, California

Rae, J. G. L., Bell, N., Hartquist, T. W., Pilling, M. J., and Ruffle, D. P.: 2002, Reduced networks governing the fractional ionisation in interstellar molecular clouds, *A&A* **383**, 738

Rawlings, J. M. C., Hartquist, T. W., Menten, K. M., and Williams, D. A.: 1992, Direct diagnosis of infall in collapsing protostars. I - The theoretical identification of molecular species with broad velocity distributions, *MNRAS* **255**, 471

Regos, E.: 1997, Magnetic viscosity in weakly ionized protostellar discs, *MNRAS* **286**, 97

Reyes-Ruiz, M.: 2001, The Magnetorotational Instability across the Dead Zone of Protoplanetary Disks, *ApJ* **547**, 465

Rietmeijer, F. J. M. and Nuth, J. A.: 2000, Collected Extraterrestrial Materials: Constraints on Meteor and Fireball Compositions, *Earth Moon and Planets* **82**, 325

Roberge, A., Lecavelier des Etangs, A., Grady, C. A., Vidal-Madjar, A., Bouret, J.-C., Feldman, P. D., Deleuil, M., Andre, M., Boggess, A., Bruhweiler, F. C., Ferlet, R., and Woodgate, B.: 2001, FUSE and Hubble Space Telescope/STIS Observations of Hot and Cold Gas in the AB Aurigae System, *ApJ* **551**, L97

Roberge, W. G., Jones, D., Lepp, S., and Dalgarno, A.: 1991, Interstellar photodissociation and photoionization rates, *ApJS* **77**, 287

Roberts, H. and Herbst, E.: 2002, The abundance of gaseous H_2O and O_2 in cores of dense interstellar clouds, *A&A* **395**, 233

Roberts, H., Herbst, E., and Millar, T. J.: 2002, The importance of new rate coefficients for deuterium fractionation reactions in interstellar chemistry, *MNRAS* **336**, 283

Roberts, H., Herbst, E., and Millar, T. J.: 2003, Enhanced Deuterium Fractionation in Dense Interstellar Cores Resulting from Multiply Deuterated H_3^+, *ApJ* **591**, L41

Roberts, H. and Millar, T. J.: 2000, Modelling of deuterium chemistry and its application to molecular clouds, *A&A* **361**, 388

Ruden, S. P. and Pollack, J. B.: 1991, The dynamical evolution of the protosolar nebula, *ApJ* **375**, 740

Ruffle, D. P., Rae, J. G. L., Pilling, M. J., Hartquist, T. W., and Herbst, E.: 2002, A network for interstellar CO - The first application of objective reduction techniques in astrochemistry, *A&A* **381**, L13

Rybicki, G. B. and Hummer, D. G.: 1991, An accelerated lambda iteration method for multilevel radiative transfer. I - Non-overlapping lines with background continuum, *A&A* **245**, 171

Sano, T., Miyama, S. M., Umebayashi, T., and Nakano, T.: 2000, Magnetorotational Instability in Protoplanetary Disks. II. Ionization State and Unstable Regions, *ApJ* **543**, 486

Schmitt, W., Henning, T., and Mucha, R.: 1997, Dust evolution in protoplanetary accretion disks., *A&A* **325**, 569

Schnabel, K., Helling, C., Woitke, P., and Sedlmayr, E.: 2001, in *Astronomische Gesellschaft Meeting Abstracts*, p. 44

Schramm, L. S., Brownlee, D. E., and Wheelock, M. M.: 1989, Major element composition of stratospheric micrometeorites, *Meteoritics* **24**, 99

Schräpler, R. and Henning, T.: 2004, Dust diffusion, sedimentation, and gravitational instabilities in protoplanetary disks, *ApJ* **614**, 960

Seaton, M. J., Yan, Y., Mihalas, D., and Pradhan, A. K.: 1994, Opacities for Stellar Envelopes, *MNRAS* **266**, 805

Semaniak, J., Minaev, B. F., Derkatch, A. M., Hellberg, F., Neau, A., Rosén, S., Thomas, R., Larsson, M., Danared, H., Paál, A., and af Ugglas, M.: 2001, Dissociative Recombination of HCNH$^+$: Absolute Cross-Sections and Branching Ratios, *ApJS* **135**, 275

Semenov, D., Henning, T., Helling, C., Ilgner, M., and Sedlmayr, E.: 2003, Rosseland and Planck mean opacities for protoplanetary discs, *A&A* **410**, 611

Semenov, D., Pavlyuchenkov, Y., Henning, T., Herbst, E., and van Dishoeck, E.: 2004a, On the feasibility of disk chemical modeling, *Baltic Astronomy* **13**, 454

Semenov, D., Pavlyuchenkov, Y., Schreyer, K., Henning, T., Dullemond, K., and Bacmann, A.: 2005, Millimeter observations and modeling of the AB Aurigae system, *ApJ* 621, (astro-ph/0411653)

Semenov, D., Wiebe, D., and Henning, T.: 2004b, Reduction of chemical networks. II. Analysis of the fractional ionisation in protoplanetary discs, *A&A* **417**, 93

Shakura, N. I. and Sunyaev, R. A.: 1973, Black holes in binary systems. Observational appearance., *A&A* **24**, 337

Shalabiea, O. M. and Greenberg, J. M.: 1994, Two key processes in dust/gas chemical modelling: photo-processing of grain mantles and explosive desorption., *A&A* **290**, 266

Sharp, C. M.: 1992, Molecular opacities for solar and enhanced CNO abundances - Relevance for accretion disks, *A&AS* **94**, 1

Shu, F. H., Tremaine, S., Adams, F. C., and Ruden, S. P.: 1990, Sling amplification and eccentric gravitational instabilities in gaseous disks, *ApJ* **358**, 495

Simon, M., Dutrey, A., and Guilloteau, S.: 2000, Dynamical Masses of T Tauri Stars and Calibration of Pre-Main-Sequence Evolution, *ApJ* **545**, 1034

Smith, I. W. M.: 1988, in T. J. Millar and D. A. Williams (eds.), *ASSL Vol. 146: Rate Coefficients in Astrochemistry*, pp 106–116, Kluwer Academic Publishers, Dordrecht

Smith, I. W. M., Herbst, E., and Chang, Q.: 2004, Rapid neutral-neutral reactions at low temperatures: a new network and first results for TMC-1, *MNRAS* **350**, 323

Spanel, P. and Smith, D.: 1994, A study of electron attachment to C_{70} using the FALP technique, *Chemical Physics Letters* **229**, 262

Stantcheva, T., Caselli, P., and Herbst, E.: 2001, Modified rate equations revisited. A corrected treatment for diffusive reactions on grain surfaces, *A&A* **375**, 673

Stantcheva, T. and Herbst, E.: 2004, Models of gas-grain chemistry in interstellar cloud cores with a stochastic approach to surface chemistry, *A&A* **423**, 241

Stognienko, R., Henning, T., and Ossenkopf, V.: 1995, Optical properties of coagulated particles., *A&A* **296**, 797

Terzieva, R. and Herbst, E.: 1998a, Errata; The Sensitivity of Gas-Phase Chemical Models of Interstellar Clouds to C and O Elemental Abundances and to a New Formation Mechanism for Ammonia, *ApJ* **509**, 932

Terzieva, R. and Herbst, E.: 1998b, The Sensitivity of Gas-Phase Chemical Models of Interstellar Clouds to C and O Elemental Abundances and to a New Formation Mechanism for Ammonia, *ApJ* **501**, 207

The, P. S., de Winter, D., and Perez, M. R.: 1994, A new catalogue of members and candidate members of the Herbig Ae/Be (HAEBE) stellar group, *A&AS* **104**, 315

Thi, W. F., van Dishoeck, E. F., Blake, G. A., van Zadelhoff, G. J., Horn, J., Becklin, E. E., Mannings, V., Sargent, A. I., van den Ancker, M. E., Natta, A., and Kessler, J.: 2001, H$_2$ and CO Emission from Disks around T Tauri and Herbig Ae Pre-Main-Sequence Stars and from Debris Disks around Young Stars: Warm and Cold Circumstellar Gas, *ApJ* **561**, 1074

Tielens, A. G. G. M. and Hagen, W.: 1982, Model calculations of the molecular composition of interstellar grain mantles, *A&A* **114**, 245

Tielens, A. G. G. M.: 1993, in Millar, T. J. and Williams, D. A. (ed.), *Dust and Chemistry in Astronomy*, The Graduate Series in Astronomy, pp 103–142, Institute of Physics

Tsuboi, Y., Hamaguchi, K., Koyama, K., and Yamauchi, S.: 1999, Magnetic activities in young stellar objects, *Astronomische Nachrichten* **320**, 175

Tuthill, P. G., Monnier, J. D., Danchi, W. C., Hale, D. D. S., and Townes, C. H.: 2002, Imaging the Disk around the Luminous Young Star LkH$_\alpha$ 101 with Infrared Interferometry, *ApJ* **577**, 826

Umebayashi, T. and Nakano, T.: 1980, Recombination of Ions and Electrons on Grains and the Ionization Degree in Dense Interstellar Clouds, *PASJ* **32**, 405

Umebayashi, T. and Nakano, T.: 1981, Fluxes of Energetic Particles and the Ionization Rate in Very Dense Interstellar Clouds, *PASJ* **33**, 617

van den Ancker, M. E., Bouwman, J., Wesselius, P. R., Waters, L. B. F. M., Dougherty, S. M., and van Dishoeck, E. F.: 2000, ISO spectroscopy of circumstellar dust in the Herbig Ae systems AB Aur and HD 163296, *A&A* **357**, 325

van den Ancker, M. E., de Winter, D., and Tjin A Djie, H. R. E.: 1998, HIPPARCOS photometry of Herbig Ae/Be stars, *A&A* **330**, 145

van den Ancker, M. E., The, P. S., Tjin A Djie, H. R. E., Catala, C., de Winter, D., Blondel, P. F. C., and Waters, L. B. F. M.: 1997, HIPPARCOS data on Herbig Ae/Be stars: an evolutionary scenario., *A&A* **324**, L33

van Dishoeck, E. F.: 1988, in T. Millar and D. Williams (eds.), *ASSL Vol. 146: Rate Coefficients in Astrochemistry*, pp 49–72, Kluwer Academic Publishers, Dordrecht

van Dishoeck, E. F.: 1994, in R. Cutri and W. Latter (eds.), *ASP Conf. Ser. 58: The First Symposium on the Infrared Cirrus and Diffuse Interstellar Clouds*, pp 319–331, Astr. Soc. Pacific

van Dishoeck, E. F.: 1998, in T. W. Hartquist and D. A. Williams (eds.), *The Molecular Astrophysics of Stars and Galaxies*, pp 53–100, Clarendon Press, Oxford

van Dishoeck, E. F.: 2004, ISO Spectroscopy of Gas and Dust: From Molecular Clouds to Protoplanetary Disks, *ARA&A* **42**, 119

van Dishoeck, E. F. and Black, J. H.: 1988, The photodissociation and chemistry of interstellar CO, *ApJ* **334**, 771

van Dishoeck, E. F. and Blake, G. A.: 1995, Chemical Evolution of Circumstellar Matter around Young Stellar Objects, *Ap&SS* **224**, 237

van Dishoeck, E. F. and Blake, G. A.: 1998, Chemical Evolution of Star-Forming Regions, *ARA&A* **36**, 317

van Zadelhoff, G.-J., Aikawa, Y., Hogerheijde, M. R., and van Dishoeck, E. F.: 2003, Axi-symmetric models of ultraviolet radiative transfer with applications to circumstellar disk chemistry, *A&A* **397**, 789

Vasyunin, A., Sobolev, A. M., Wiebe, D. Z., and Semenov, D.: 2004, Influence of Uncertainties in the Rate Constants of Chemical Reactions on Astrochemical Modeling Results, *Astronomy Letters* **30**, 566

Velusamy, T., Langer, W. D., and Goldsmith, P. F.: 2002, Tracing the Infall and the Accretion Shock in the Protostellar Disk: L1157, *ApJ* **565**, L43

Vinković, D., Ivezić, Ž., Miroshnichenko, A. S., and Elitzur, M.: 2003, Discs and haloes in pre-main-sequence

stars, *MNRAS* **346**, 1151

Voshchinnikov, N. V.: 2004, *Optics of Cosmic Dust*, Part I, Cambridge University Press, Cambridge, first edition

Voshchinnikov, N. V., Il'in, V. B., and Henning, T.: 2004, Modelling the optical properties of composite and porous interstellar grains, *ArXiv Astrophysics e-prints*, astro-ph/0409457

Voshchinnikov, N. V., Il'in, V. B., Henning, T., and Dubkova, D. N.: 2003, in A. N. Witt (ed.), *Astrophysics of Dust*, pp 169–169

Voshchinnikov, N. V. and Mathis, J. S.: 1999, Calculating Cross Sections of Composite Interstellar Grains, *ApJ* **526**, 257

Wahhaj, Z., Koerner, D. W., Ressler, M. E., Werner, M. W., Backman, D. E., and Sargent, A. I.: 2003, The Inner Rings of β Pictoris, *ApJ* **584**, L27

Walmsley, C. M., Pineau des Forêts, G., and Flower, D. R.: 1999, Silicon chemistry in PDRs, *A&A* **342**, 542

Waters, L. B. F. M. and Waelkens, C.: 1998, Herbig Ae/Be Stars, *ARA&A* **36**, 233

Watson, W. D.: 1974, Molecular CH, CH^+, and H in the Interstellar Gas, *ApJ* **189**, 221

Watson, W. D. and Salpeter, E. E.: 1972, Molecule Formation on Interstellar Grains, *ApJ* **174**, 321

Weidenschilling, S. J.: 1980, Dust to planetesimals - Settling and coagulation in the solar nebula, *Icarus* **44**, 172

Weizsäcker, C. F. V.: 1943, Über die Entstehung des Planetensystems. Mit 2 Abbildungen., *Zeitschrift fur Astrophysics* **22**, 319

Westley, M. S., Baragiola, R. A., Johnson, R. E., and Baratta, G. A.: 1995, Photodesorption from Low-Temperature Water Ice in Interstellar and Circumsolar Grains, *Nature* **373**, 405

Wheelock, S., Chillemi, J., Gautier, N., Gregorich, D., Kester, D., McCallon, H., Oken, C., White, J., and Chester, T.: 1991, Second Generation IRAS Sky Intensity Product, *BAAS* **23**, 908

Whittet, D. C. B., Schutte, W. A., Tielens, A. G. G. M., Boogert, A. C. A., de Graauw, T., Ehrenfreund, P., Gerakines, P. A., Helmich, F. P., Prusti, T., and van Dishoeck, E. F.: 1996, An ISO SWS view of interstellar ices: first results., *A&A* **315**, L357

Wiebe, D., Semenov, D., and Henning, T.: 2003, Reduction of chemical networks. I. The case of molecular clouds, *A&A* **399**, 197

Willacy, K., Klahr, H. H., Millar, T. J., and Henning, T.: 1998, Gas and grain chemistry in a protoplanetary disk, *A&A* **338**, 995

Willacy, K. and Langer, W. D.: 2000, The Importance of Photoprocessing in Protoplanetary Disks, *ApJ* **544**, 903

Willacy, K., Rawlings, J. M. C., and Williams, D. A.: 1994, Molecular Desorption from Dust in Star-Forming Regions, *MNRAS* **269**, 921

Williams, D. A.: 1972, Association Reactions, *Astrophys. Lett.* **10**, L17

Williams, D. A.: 1993, in T. Miller and D. Williams (eds.), *Dust and Chemistry in Astronomy*, pp 143–170, Institute of Physics Publishing

Wilner, D. J., Holman, M. J., Kuchner, M. J., and Ho, P. T. P.: 2002, Structure in the Dusty Debris around Vega, *ApJ* **569**, L115

Wilson, T. L. and Rood, R.: 1994, Abundances in the Interstellar Medium, *ARA&A* **32**, 191

Woitke, P. and Helling, C.: 2003, Dust in brown dwarfs. II. The coupled problem of dust formation and sedimentation, *A&A* **399**, 297

Wurm, G. and Blum, J.: 1998, Experiments on Preplanetary Dust Aggregation, *Icarus* **132**, 125

Wurm, G. and Blum, J.: 2000, An Experimental Study on the Structure of Cosmic Dust Aggregates and Their Alignment by Motion Relative to Gas, *ApJ* **529**, L57

Appendix A

Scheme to compute the optical constants of aggregate particles

In this Appendix, I summarise the adopted computational method to calculate the optical constants of homogeneous aggregates.

A convenient physical quantity characterising how a solid particle interacts with electromagnetic field is the so-called refractive index (optical constants):

$$m_\lambda = n_\lambda + k_\lambda \cdot i, \tag{A.1}$$

where λ is the wavelength of the incident light and $k_\lambda \geq 0$ (e.g., Bohren and Huffman, 1983; Voshchinnikov, 2004). For a poor conductors (dielectrics) $k_\lambda \ll 1$, whereas highly conductive materials, like iron, have $k_\lambda \gg 1$ and $n_\lambda \simeq k_\lambda$. Note that vacuum has $m_\lambda = 1 + 0 \cdot i$ at all wavelengths. The dielectric functions of a material can be expressed from the optical constants as

$$\epsilon = \epsilon' + \epsilon'' \cdot i, \ \epsilon' = n^2 - k^2, \ \epsilon'' = 2nk - \frac{4\pi\sigma}{\omega}, \tag{A.2}$$

where σ is the conductivity and $\omega = 2\pi\nu = 2\pi c/\lambda$ is the circular frequency.

Recently, the optical constants of various materials expected to be present in cosmic objects have been compiled by Jäger et al. (2003) in an extended database and published in the Internet: `www.astro.uni-jena.de/Laboratory/Database/jpdoc/index.html`.

Given the fact that dust grains in real astronomical objects are far from being homogeneous (made of one material) and likely have composite (fine mixture of various materials) or layered structure, it is important to have a mathematical tool to combine refractive indices of several dust components in a grain into one effective index that can be used as a representation of the optical constants of such a heterogeneous particle (Effective Medium Theory, EMT). Many such methods (mixing rules) have been proposed over the last century; the most popular one is the classical rule of Bruggeman (1935) that allows to calculate the effective dielectric constant of a two-component medium from the dielectric permittivities ϵ_i and volume fractions f_i of the components:

$$f\frac{\epsilon_1 - \epsilon_{\text{eff}}}{\epsilon_1 + 2\epsilon_{\text{eff}}} + (1 - f)\frac{\epsilon_2 - \epsilon_{\text{eff}}}{\epsilon_2 + 2\epsilon_{\text{eff}}} = 0. \tag{A.3}$$

This rule has been generalised to many components by Ossenkopf (1991). It is applied to compute the effective optical constants of composite aggregates in my opacity model.

To translate the dielectric functions of aggregates into the optical properties, I use the spectral representation of inhomogeneous media (Bergman, 1978), allowing to separate the influence of the topological structure of an aggregate and its optical constants on the resulting optical characteristics in the static limit (Henning and Stognienko, 1996). It can be written as (Ghosh and Fuchs, 1991)

$$\epsilon_{\text{eff}} = \epsilon_2 \left(1 - f \int_0^1 \frac{G(n)}{t - n} dn\right), \ t = \frac{1}{1 - \epsilon_1/\epsilon_2}, \tag{A.4}$$

where n is a depolarisation factor and $G(n)$ is the distribution of these factors associated with the topology of the component 1, which must satisfy the two moment equations:

$$\int_0^1 G(n)dn = 1, \quad \int_0^1 nG(n)dn = \frac{1-f}{3}. \tag{A.5}$$

Eq. (A.4) can be understood as follows. All possible resonanses of a two-phase medium occur if the quantity t is real and $0 \leq t \leq 1$, and is also determined by the spectral function $G(n)$. For astrophysically important materials, which have usually $\Im(m_\lambda) > 0$, t is not a real number, and thus the only resonances contributing to the integral (A.4) occur at $n \sim 0$. Note that a mode at the depolarisation factor $n = 0$ describes the percolation of component 1 in component 2, therby determining the optical behaviour of the entire aggregate particle. This parameter depends on both the number of sub-grains in a particle and its topology. Thus, it differs for BPCA and BCCA aggregates. The physical meaning of this quantity is that it describes a fractional amount of material forming conducting paths inside the aggregate.

The major obstacle of this approach is that there is no simple way to compute the spectral function for a given aggregate topology, and only a limited number of topologies can be studied (e.g., Fuchs, 1975; Hinsen and Felderhof, 1992). I use the discrete multi-pole method (DMM) to calculate the spectral function of the aggregated particles of a special topology, when their sub-grains touch each other only at one point (Hinsen and Felderhof, 1992). Unfortunately, the DMM method is not able to account for the percolation strength g_0. Therefore, I use the upper limit on the percolation strength:

$$g_0 \approx \frac{R_{\mathrm{ex}}}{N}, \tag{A.6}$$

where R_{ex} is the radius of the outermost sphere covering the aggregate particle and N is the amount of sub-grains in an aggregate particle.

The simplest possible spectral function is considered:

$$G_{\mathrm{simp}}(n) = g_0\delta(n) + g_1\delta(n - n_1), \tag{A.7}$$

where g_1 and n_1 are the strength and location of the second resonance, which are defined by the moment equation (A.5): $g_1 = 1 - g_0$ and $n_1 = (1 - f)/3g_1$, respectively. Consequently, the effective dielectric function of an aggregate particle can be written as

$$\epsilon_{\mathrm{eff}} = \epsilon_2\left(1 - \frac{fg_0}{t} - \frac{fg_1}{t - n_1}\right). \tag{A.8}$$

In the aggregate model, it is assumed that the second component of the two-phase medium is vacuum, whereas the first component is any dust constituent from Table 2.1 (homogeneous aggregates) or their EMT mixture (composite aggregates).

According to Henning and Stognienko (1996), the corresponding filling factors f and percolation strengths g_0 for the considered BPCA and BCCA can be parameterised as follows:

$$f = a_1R_{\mathrm{ex}}^{D-3}(1 + b_1R_{\mathrm{ex}}^{c1}), g_0 = a_2R_{\mathrm{ex}}^{1-D}(1 + b_2R_{\mathrm{ex}}^{c2}). \tag{A.9}$$

Here $D = 3.0$ and $D = 1.96$ are the fractal dimensions of BCCA and BPCA aggregates, respectively (Blum et al., 1994), and the fit coefficients are summarised in Table A.1.

Table A.1. Fit coefficients for the filling factors and percolation strengths of aggregates

Aggregate	Parameter	Value	Parameter	Value	Parameter	Value
BCCA	a_1	0.279	b_1	4.01	c_1	-1.34
BCCA	a_2	4.28	b_2	-6.11	c_2	-1.57
BPCA	a_1	0.0457	b_1	696.0	c_1	-3.93
BPCA	a_2	22.2	b_2	-12400	c_2	-5.79

References. — Adopted from Henning and Stognienko (1996).

Appendix B

Surface species and reactions adopted in the disc chemical model

Table B.1. Desorption energies of surface species*

Species	E_{des} [K]	Species	E_{des} [K]	Species	E_{des} [K]	Species	E_{des} [K]	Species	E_{des} [K]
C	800	C_2	1210	C_2H	1460	C_2H_2	2490	C_2H_3	1760
C_2H_4	2010	C_2H_5	2110	C_2H_5OH	3470	C_2H_6	2320	C_2H_6CO	2820
C_2S	2500	C_3	2010	C_3H	2270	C_3H_2	2110	C_3H_3	2220
C_3H_4	2470	C_3N	2720	C_3O	2520	C_3P	3245	C_3S	3000
C_4	2420	C_4H	2670	C_4H_2	2920	C_4P	3452	C_4S	3500
C_5	3220	C_5H	3470	C_5H_2	3730	C_5H_4	4030	C_5N	3930
C_6	3620	C_6H	3880	C_6H_2	4130	C_7	4430	C_7H	4680
C_7H_2	4930	C_7H_4	5240	C_7N	5130	C_8	4830	C_8H	5080
C_8H_2	5340	C_9	5640	C_9H	5890	C_9H_2	6140	C_9N	6340
CCl	2509	CCN	2010	CCO	2010	CCP	2762	CH	654
CH_2	956	CH_2CN	2470	CH_2CO	2520	CH_2NH	1560	CH_2PH	2471
CH_3	1160	CH_3CHO	2870	CH_3CN	2270	CH_3OCH_3	2820	CH_3OH	2060
CH_4	1120	CHOOH	2570	Cl	1216	ClO	2141	CN	1510
CO	1210	CO_2	2690	CP	1950.4	CS	2000	D	450
HDO	3676	OD	1230	Fe	4200	H	350	H_2	450
H_2C_3	1902	H_2CN	1643.2	H_2CO	1760	H_2CS	2250	H_2O	4820
H_2O_2	2520	H_2S	1800	H_2S_2	2600	H_2SiO	6956	H_3C_3N	3270
H_3C_4N	3782	H_3C_6N	5178	H_3C_8N	6238	HC_3N	2970	HC_5N	4180
HC_7N	5390	HC_9N	6590	HCCP	3256.6	HCl	1823	HCN	4280
HCO	1510	$HCOOCH_3$	3002	HCP	1952	HCS	2000	HCSi	8599
HNC	1510	HNO	1510	HNSi	8699	HPO	2399	HS	1500
HS_2	2300	Mg	5300	N	800	N2	750	N2O	2290
Na	11800	NH	604	NH_2	856	NH_3	3080	NO	1210
NO_2	1855	NS	2000	O	800	O_2	1210	O_2H	1510
OCN	2010	OCS	3000	OH	1260	P	1549	PH	1599

continued on next page

continued from previous page

Species	E_{des} [K]	Species	E_{des} [K]	Species	E_{des} [K]	Species	E_{des} [K]	Species	E_{des} [K]
PH_2	1649	PN	2249	PO	2349	S	1100	S_2	2000
Si	2700	SiC	3500	SiC_2	2656	SiC_2H	2656	SiC_2H_2	2706
SiC_3	3206	SiC_3H	3256	SiC_4	3806	$SiCH_2$	2106	$SiCH_3$	2156
SiH	2940	SiH_2	3190	SiH_3	3440	SiH_4	3690	SiN	2105
SiNC	2705	SiO	3500	SiO_2	2726	SiS	3800	SO	2000
SO_2	3070								

* The values that end with a non-zero digit are calculated by Eq. (3.10) in Section 3.2.

Table B.2. Set of the adopted surface reactions

Reaction	α_0 [cm^{-3} s^{-1}]	β	γ [K]	Reaction	α_0 [cm^{-3} s^{-1}]	β	γ [K]
gH + gC → gCH	$1.94 \cdot 10^{12}$	0	0	gH + gN → gNH	$1.94 \cdot 10^{12}$	0	0
gH + gO → gOH	$1.94 \cdot 10^{12}$	0	0	gH + gS → gHS	$1.94 \cdot 10^{12}$	0	0
gH + gSi → gSiH	$1.94 \cdot 10^{12}$	0	0	gH + gCH → gCH$_2$	$1.94 \cdot 10^{12}$	0	0
gH + gNH → gNH$_2$	$1.94 \cdot 10^{12}$	0	0	gH + gOH → gH$_2$O	$1.94 \cdot 10^{12}$	0	0
gH + gSiH → gSiH$_2$	$1.94 \cdot 10^{12}$	0	0	gH + gHS → gH$_2$S	$1.94 \cdot 10^{12}$	0	0
gH + gC$_2$ → gC$_2$H	$1.94 \cdot 10^{12}$	0	0	gH + gCN → gHCN	$1.94 \cdot 10^{12}$	0	0
gH + gCO → gHCO	$2.57 \cdot 10^{6}$	0	1000	gH + gNO → gHNO	$1.94 \cdot 10^{12}$	0	0
gH + gO$_2$ → gO$_2$H	$1.51 \cdot 10^{6}$	0	1200	gH + gCS → gHCS	$5.15 \cdot 10^{6}$	0	1000
gH + gCH$_2$ → gCH$_3$	$1.94 \cdot 10^{12}$	0	0	gH + gNH$_2$ → gNH$_3$	$1.94 \cdot 10^{12}$	0	0
gH + gSiH$_2$ → gSiH$_3$	$1.94 \cdot 10^{12}$	0	0	gH + gH$_2$S → gH$_2$ + gHS	$1.31 \cdot 10^{7}$	0	860
gH + gC$_2$H → gC$_2$H$_2$	$1.94 \cdot 10^{12}$	0	0	gH + gHCO → gH$_2$CO	$1.94 \cdot 10^{12}$	0	0
gH + gO$_2$H → gH$_2$O$_2$	$1.94 \cdot 10^{12}$	0	0	gH + gC$_3$ → gC$_3$H	$1.94 \cdot 10^{12}$	0	0
gH + gCH$_3$ → gCH$_4$	$1.94 \cdot 10^{12}$	0	0	gH + gSiH$_3$ → gSiH$_4$	$1.94 \cdot 10^{12}$	0	0
gH + gH$_2$CO → gHCO + gH$_2$	$5.06 \cdot 10^{4}$	0	1850	gH + gH$_2$O$_2$ → gH$_2$O + gOH	$4.90 \cdot 10^{5}$	0	1400
gH + gC$_2$H$_2$ → gC$_2$H$_3$	$1.43 \cdot 10^{6}$	0	1210	gH + gC$_3$H → gC$_3$H$_2$	$1.94 \cdot 10^{12}$	0	0
gH + gC$_4$ → gC$_4$H	$1.94 \cdot 10^{12}$	0	0	gH + gC$_3$N → gHC$_3$N	$1.94 \cdot 10^{12}$	0	0
gH + gC$_2$H$_3$ → gC$_2$H$_4$	$1.94 \cdot 10^{12}$	0	0	gH + gC$_3$H$_2$ → gC$_3$H$_3$	$1.43 \cdot 10^{6}$	0	1210
gH + gC$_4$H → gC$_4$H$_2$	$1.94 \cdot 10^{12}$	0	0	gH + gC$_5$ → gC$_5$H	$1.94 \cdot 10^{12}$	0	0
gH + gC$_2$H$_4$ → gC$_2$H$_5$	$2.88 \cdot 10^{7}$	0	750	gH + gC$_3$H$_3$ → gC$_3$H$_4$	$1.94 \cdot 10^{12}$	0	0
gH + gC$_5$H → gC$_5$H$_2$	$1.94 \cdot 10^{12}$	0	0	gH + gC$_5$N → gHC$_5$N	$1.94 \cdot 10^{12}$	0	0
gH + gC$_6$ → gC$_6$H	$1.94 \cdot 10^{12}$	0	0	gH + gC$_2$H$_5$ → gC$_2$H$_6$	$1.94 \cdot 10^{12}$	0	0
gH + gC$_6$H → gC$_6$H$_2$	$1.94 \cdot 10^{12}$	0	0	gH + gC$_7$ → gC$_7$H	$1.94 \cdot 10^{12}$	0	0

Reaction	α_0 [cm^{-3} s^{-1}]	β	γ [K]	Reaction	α_0 [cm^{-3} s^{-1}]	β	γ [K]
gH + gC$_7$H → gC$_7$H$_2$	$1.94 \cdot 10^{12}$	0	0	gH + gC$_7$N → gHC$_7$N	$1.94 \cdot 10^{12}$	0	0
gH + gC$_8$ → gC$_8$H	$1.94 \cdot 10^{12}$	0	0	gH + gC$_8$H → gC$_8$H$_2$	$1.94 \cdot 10^{12}$	0	0
gH + gC$_9$ → gC$_9$H	$1.94 \cdot 10^{12}$	0	0	gH + gC$_9$H → gC$_9$H$_2$	$1.94 \cdot 10^{12}$	0	0
gH + gC$_9$N → gHC$_9$N	$1.94 \cdot 10^{12}$	0	0	gH + gHNO → gNO + gH$_2$	$3.68 \cdot 10^{5}$	0	1500
gH + gHCS → gH$_2$CS	$1.94 \cdot 10^{12}$	0	0	gH + gOCS → gCO + gHS	$1.94 \cdot 10^{12}$	0	0
gH + gH$_2$O$_2$ → gO$_2$H + gH$_2$	$5.16 \cdot 10^{4}$	0	1900	gH + gCH$_4$ → gCH$_3$ + gH$_2$	$1.27 \cdot 10^{-1}$	0	5940
gH + gC$_2$H$_6$ → gC$_2$H$_5$ + gH$_2$	1.44	0	4890	gH + gH$_2$CN → gCH$_2$NH	$1.94 \cdot 10^{12}$	0	0
gC + gC → gC$_2$	$3.71 \cdot 10^{3}$	0	0	gC + gN → gCN	$3.57 \cdot 10^{3}$	0	0
gC + gO → gCO	$3.46 \cdot 10^{3}$	0	0	gC + gS → gCS	$1.86 \cdot 10^{3}$	0	0
gC + gCH → gC$_2$H	$1.33 \cdot 10^{5}$	0	0	gC + gNH → gHNC	$5.28 \cdot 10^{5}$	0	0
gC + gOH → gCO + gH	$9.30 \cdot 10^{2}$	0	0	gC + gC$_2$ → gC$_3$	$1.86 \cdot 10^{3}$	0	0
gC + gCN → gCCN	$1.86 \cdot 10^{3}$	0	0	gC + gNO → gOCN	$1.86 \cdot 10^{3}$	0	0
gC + gO$_2$ → gCO + gO	$1.86 \cdot 10^{3}$	0	0	gC + gCH$_2$ → gC$_2$H$_2$	$1.86 \cdot 10^{3}$	0	0
gC + gNH$_2$ → gHNC + gH	$2.16 \cdot 10^{3}$	0	0	gC + gC$_3$ → gC$_4$	$1.86 \cdot 10^{3}$	0	0
gC + gC$_2$H → gC$_3$H	$1.86 \cdot 10^{3}$	0	0	gC + gCCN → gC$_3$N	$1.86 \cdot 10^{3}$	0	0
gC + gOCN → gCO + gCN	$1.86 \cdot 10^{3}$	0	0	gC + gCH$_3$ → gC$_2$H$_3$	$1.86 \cdot 10^{3}$	0	0
gC + gC$_3$H → gC$_4$H	$1.86 \cdot 10^{3}$	0	0	gC + gC$_4$ → gC$_5$	$1.86 \cdot 10^{3}$	0	0
gC + gC$_5$ → gC$_6$	$1.86 \cdot 10^{3}$	0	0	gC + gC$_2$H$_3$ → gC$_3$H$_3$	$1.86 \cdot 10^{3}$	0	0
gC + gC$_6$ → gC$_7$	$1.86 \cdot 10^{3}$	0	0	gC + gC$_7$ → gC$_8$	$1.86 \cdot 10^{3}$	0	0
gC + gC$_8$ → gC$_9$	$1.86 \cdot 10^{3}$	0	0	gC + gC$_4$H → gC$_5$H	$1.86 \cdot 10^{3}$	0	0
gC + gC$_5$H → gC$_6$H	$1.86 \cdot 10^{3}$	0	0	gC + gC$_6$H → gC$_7$H	$1.86 \cdot 10^{3}$	0	0
gC + gC$_7$H → gC$_8$H	$1.86 \cdot 10^{3}$	0	0	gC + gC$_8$H → gC$_9$H	$1.86 \cdot 10^{3}$	0	0
gC + gHS → gCS + gH	$1.86 \cdot 10^{3}$	0	0	gC + gNS → gCN + gS	$1.86 \cdot 10^{3}$	0	0
gC + gSO → gCO + gS	$1.86 \cdot 10^{3}$	0	0	gC + gCCO → gC$_3$O	$1.86 \cdot 10^{3}$	0	0
gN + gN → gN2	$3.43 \cdot 10^{3}$	0	0	gN + gO → gNO	$3.32 \cdot 10^{3}$	0	0
gN + gCH → gHCN	$1.33 \cdot 10^{5}$	0	0	gN + gC$_2$ → gCCN	$1.72 \cdot 10^{3}$	0	0
gN + gC$_3$ → gC$_3$N	$1.72 \cdot 10^{3}$	0	0	gN + gC$_3$H → gHC$_3$N	$1.72 \cdot 10^{3}$	0	0
gN + gC$_5$ → gC$_5$N	$1.72 \cdot 10^{3}$	0	0	gN + gC$_5$H → gHC$_5$N	$1.72 \cdot 10^{3}$	0	0
gN + gC$_7$ → gC$_7$N	$1.72 \cdot 10^{3}$	0	0	gN + gC$_7$H → gHC$_7$N	$1.72 \cdot 10^{3}$	0	0
gN + gC$_9$ → gC$_9$N	$1.72 \cdot 10^{3}$	0	0	gN + gC$_9$H → gHC$_9$N	$1.72 \cdot 10^{3}$	0	0
gN + gS → gNS	$1.72 \cdot 10^{3}$	0	0	gN + gHS → gNS + gH	$1.72 \cdot 10^{3}$	0	0
gN + gNS → gN2 + gS	$1.73 \cdot 10^{3}$	0	0	gN + gCH$_2$ → gH$_2$CN	$1.73 \cdot 10^{3}$	0	0
gN + gO$_2$H → gO$_2$ + gNH	$1.72 \cdot 10^{3}$	0	0	gO + gO → gO$_2$	$3.21 \cdot 10^{3}$	0	0
gO + gS → gSO	$1.61 \cdot 10^{3}$	0	0	gO + gCH → gHCO	$1.33 \cdot 10^{5}$	0	0
gO + gNH → gHNO	$5.28 \cdot 10^{5}$	0	0	gO + gOH → gO$_2$H	$1.61 \cdot 10^{3}$	0	0

continued from previous page

Reaction	α_0	β	γ	Reaction	α_0	β	γ
	[cm^{-3} s^{-1}]		[K]		[cm^{-3} s^{-1}]		[K]
gO + gCN → gOCN	$1.61 \cdot 10^3$	0	0	gO + gCO → gCO$_2$	$2.13 \cdot 10^{-3}$	0	1000
gO + gCS → gOCS	$1.61 \cdot 10^3$	0	0	gO + gSO → gSO$_2$	$1.61 \cdot 10^3$	0	0
gO + gHCO → gCO$_2$ + gH	$1.61 \cdot 10^3$	0	0	gO + gCH$_2$ → gH$_2$CO	$1.61 \cdot 10^3$	0	0
gO + gC$_3$ → gC$_3$O	$1.61 \cdot 10^3$	0	0	gO + gHS → gSO + gH	$1.61 \cdot 10^3$	0	0
gO + gC$_2$ → gCCO	$1.61 \cdot 10^3$	0	0	gO + gNS → gNO + gS	$1.61 \cdot 10^3$	0	0
gO + gNH$_2$ → gHNO + gH	$1.91 \cdot 10^3$	0	0	gO + gO$_2$H → gO$_2$ + gOH	$1.61 \cdot 10^3$	0	0
gO + gHNO → gNO + gOH	$1.61 \cdot 10^3$	0	0	gS + gCH → gHCS	$1.31 \cdot 10^5$	0	0
gS + gNH → gNS + gH	$5.26 \cdot 10^5$	0	0	gS + gCH$_3$ → gH$_2$CS + gH	$2.05 \cdot 10^{-1}$	0	0
gCH + gCH → gC$_2$H$_2$	$2.63 \cdot 10^5$	0	0	gCH + gOH → gH$_2$CO	$1.31 \cdot 10^5$	0	0
gCH + gC$_2$ → gC$_3$H	$1.31 \cdot 10^5$	0	0	gCH + gC$_2$H → gC$_3$H$_2$	$1.31 \cdot 10^5$	0	0
gCH + gHNO → gNO + gCH$_2$	$1.31 \cdot 10^5$	0	0	gCH + gCH$_3$ → gC$_2$H$_4$	$1.31 \cdot 10^5$	0	0
gCH + gC$_3$ → gC$_4$H	$1.31 \cdot 10^5$	0	0	gCH + gC$_4$ → gC$_5$H	$1.31 \cdot 10^5$	0	0
gCH + gC$_5$ → gC$_6$H	$1.31 \cdot 10^5$	0	0	gCH + gC$_6$ → gC$_7$H	$1.31 \cdot 10^5$	0	0
gCH + gC$_7$ → gC$_8$H	$1.31 \cdot 10^5$	0	0	gCH + gC$_8$ → gC$_9$H	$1.31 \cdot 10^5$	0	0
gCH + gNH → gH$_2$CN	$2.19 \cdot 10^5$	0	0	gCH + gNH → gHCN gH	$2.19 \cdot 10^5$	0	0
gCH + gNH → gHNC gH	$2.19 \cdot 10^5$	0	0	gCH + gNO → gHCN gO	$1.31 \cdot 10^5$	0	0
gCH + gO$_2$ → gHCO gO	$1.31 \cdot 10^5$	0	0	gCH + gNH$_2$ → gCH$_2$NH	$1.32 \cdot 10^5$	0	0
gCH + gC$_3$H → gC$_4$H$_2$	$1.31 \cdot 10^5$	0	0	gCH + gC$_4$H → gC$_5$H$_2$	$1.31 \cdot 10^5$	0	0
gCH + gC$_5$H → gC$_6$H$_2$	$1.31 \cdot 10^5$	0	0	gCH + gC$_6$H → gC$_7$H$_2$	$1.31 \cdot 10^5$	0	0
gCH + gC$_7$H → gC$_8$H$_2$	$1.31 \cdot 10^5$	0	0	gCH + gC$_8$H → gC$_9$H$_2$	$1.31 \cdot 10^5$	0	0
gCH + gC$_2$H$_3$ → gC$_3$H$_4$	$1.31 \cdot 10^5$	0	0	gNH + gCH$_2$ → gCH$_2$NH	$5.26 \cdot 10^5$	0	0
gOH + gOH → gH$_2$O$_2$	$3.97 \cdot 10^{-3}$	0	0	gOH + gCO → gCO$_2$ + gH	$1.02 \cdot 10^{-12}$	0	300
gOH + gHCO → gCHOOH	$1.99 \cdot 10^{-3}$	0	0	gOH + gCH$_3$ → gCH$_3$OH	$4.27 \cdot 10^{-2}$	0	0
gOH + gH$_2$CO → gHCO + gH$_2$O	$1.99 \cdot 10^{-3}$	0	0	gH$_2$ + gOH → gH$_2$O + gH	$2.20 \cdot 10^{-2}$	0	2600
gH$_2$ + gCN → gHCN + gH	1.33	0	2070	gH$_2$ + gNH$_2$ → gNH$_3$ + gH	$2.49 \cdot 10^{-8}$	0	6300
gH$_2$ + gCH$_2$ → gCH$_3$ + gH	$1.58 \cdot 10^{-3}$	0	3530	gH$_2$ + gCH$_3$ → gCH$_4$ + gH	$1.82 \cdot 10^{-8}$	0	6440
gH$_2$ + gC$_2$ → gC$_2$H + gH	$3.39 \cdot 10^{-5}$	0	4200	gH$_2$ + gC$_2$H → gC$_2$H$_2$ + gH	$3.21 \cdot 10^{-5}$	0	4200
gH$_2$ + gC$_3$ → gC$_3$H + gH	$2.13 \cdot 10^{-5}$	0	4200	gH$_2$ + gC$_3$H → gC$_3$H$_2$ + gH	$2.07 \cdot 10^{-5}$	0	4200
gH$_2$ + gC$_4$ → gC$_4$H + gH	$1.67 \cdot 10^{-5}$	0	4200	gH$_2$ + gC$_4$H → gC$_4$H$_2$ + gH	$1.65 \cdot 10^{-5}$	0	4200
gH$_2$ + gC$_5$ → gC$_5$H + gH	$1.44 \cdot 10^{-5}$	0	4200	gH$_2$ + gC$_5$H → gC$_5$H$_2$ + gH	$1.43 \cdot 10^{-5}$	0	4200
gH$_2$ + gC$_6$ → gC$_6$H + gH	$1.31 \cdot 10^{-5}$	0	4200	gH$_2$ + gC$_6$H → gC$_6$H$_2$ + gH	$1.30 \cdot 10^{-5}$	0	4200
gH$_2$ + gC$_7$ → gC$_7$H + gH	$1.22 \cdot 10^{-5}$	0	4200	gH$_2$ + gC$_7$H → gC$_7$H$_2$ + gH	$1.21 \cdot 10^{-5}$	0	4200
gH$_2$ + gC$_8$ → gC$_8$H + gH	$1.15 \cdot 10^{-5}$	0	4200	gH$_2$ + gC$_8$H → gC$_8$H$_2$ + gH	$1.14 \cdot 10^{-5}$	0	4200
gH$_2$ + gC$_9$ → gC$_9$H + gH	$1.11 \cdot 10^{-5}$	0	4200	gH$_2$ + gC$_9$H → gC$_9$H$_2$ + gH	$1.10 \cdot 10^{-5}$	0	4200
gCH$_2$ + gCN → gCH$_2$CN	17.1	0	0	gCH$_2$ + gHNO → gCH$_3$ + gNO	17.1	0	0

continued from previous page

Reaction	α_0 $[\mathrm{cm^{-3}\,s^{-1}}]$	β	γ [K]	Reaction	α_0 $[\mathrm{cm^{-3}\,s^{-1}}]$	β	γ [K]
gCH$_3$ + gCN → gCH$_3$CN	$4.08 \cdot 10^{-2}$	0	0	gCH$_3$ + gHNO → gCH$_4$ + gNO	$4.08 \cdot 10^{-2}$	0	0
gCH$_3$ + gHCO → gCH$_3$CHO	$4.08 \cdot 10^{-2}$	0	0	gCH$_3$ + gC$_3$N → gH$_3$C$_4$N	$4.08 \cdot 10^{-2}$	0	0
gCH$_3$ + gC$_5$N → gH$_3$C$_6$N	$4.08 \cdot 10^{-2}$	0	0	gCH$_3$ + gC$_7$N → gH$_3$C$_8$N	$4.08 \cdot 10^{-2}$	0	0
gCH$_4$ + gC$_2$H → gC$_2$H$_2$ + gCH$_3$	$2.16 \cdot 10^{-13}$	0	250				

Adopted from Hasegawa et al. (1992) and Hasegawa & Herbst (1993).

Appendix C

Acknowledgements

Appendix D

Cirriculum vitae

Name: Semenov Dmitry Alexandrovich,
                   borned 20 February 1978 in S.-Petersburg (Leningrad), USSR

1985-1993:   Graduate studies in the school N93

1993-1995:   Graduate studies in the special phys.-mathematical school N239

1995-2000:   Undergraduate studies at the Astronomical Department of
                   St. Petersburg University, Russia

1999-2000:   Scientific work at the Astrophysical Institute of
                   Friedrich-Schiller-University, Jena, Germany

07/2000:   Degree in Astronomy, St. Petersburg University,
                   "Modelling of polarization properties of cometary dust grains",
                   scientific adviser – Prof. Dr. N.V. Voshchinnikov

2000-2003:   PhD study at the Astrophysical Institute of
                   Friedrich-Schiller-University, Jena,
                   "Astrophysical modelling - the chemical evolution of protoplanetary discs",
                   scientific adviser – Prof. Dr. Th. Henning

2003-2004:   PhD study at the Max Planck Institute for Astronomy, Heidelberg

Heidelberg, December 6, 2004

Ehrenwörtliche Erklärung

Ich erkläre hiermit ehrenwörtlich, daß ich die vorliegende Arbeit selbständig, ohne unzulässige Hilfe Dritter and ohne Benutzung anderer als der angegebenen Hilfsmittel und Literatur angefertigt habe. Die aus andere Quellen direkt oder inderekt Daten und Konzepte sind unter Angabe der Quelle gekennzeichnet.

Insbesondere habe ich hierfür nicht die entgeltliche Hilfe von Vermittlungs – bzw. Beratungs-diensten (Promotionsberater oder andere Personen) in Anspruch genommen. Niemand hat von mir unmittelbar oder mittelbar geldwerte Leistungen für Arbeiten erhalten, die im Zussammenhang mit dem Inhalt der vorgelegten Dissertation stehen.

Die geltende Promotionsordnung der Physikalisch-Astronomisch Fakultät ist mir bekannt.

Ich versichere ehrenwörtlich, daß ich nach bestem Wissen die reine Wahrheit gesagt und nichts verschwiegen habe.

Heidelberg, den 6 Dezember 2004